Hypersonic Aeroelastic Analysis

Lockheed Missiles & Space Co., Inc.

September 30, 1975

243088

ADA 028794

D D C

AUG 17 1976

D

LOCKHEED

MISSILES & SPACE COMPANY, INC. • SUNNYVALE, CALIFORNIA

A SUBSIDIARY OF LOCKHEED AIRCRAFT CORPORATION

30 September 1975

LMSC-D056746

HYPERSONIC AEROELASTIC ANALYSIS

Final Report

Approved for public release; distribution unlimited

Prepared by:

Lars E. Ericsson
Consulting Engineer, Engineering Technology

Bo O. Almroth
Senior Member, Engineering Sciences

John A. Bailie
Staff Engineer, Loads/Structures & Dynamics

Francis A. Brogan
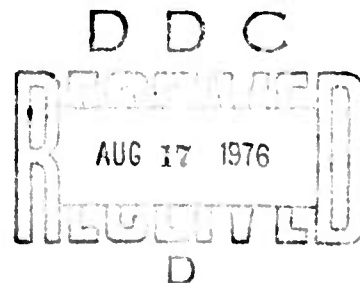Research Scientist, Structural Mechanics Lab

Gary M. Stanley
Scientist

Prepared under Contract N62269-73C-0713
for
Naval Air Development Center
Warminster, Pennsylvania

ABSTRACT

The aerothermoelastic characteristics of a tactical missile operating at near zero angle of attack in the low hypersonic speed range have been studied. An integrated digital computer program has been developed for the aeroelastic response of sharp-edge aerodynamically heated, cantilevered lifting surfaces representative of tactical missile fins. The nonuniform flow generated by a spherically blunted missile nose is accounted for. Based upon the application of the computer program to selected cases, recommendations are made regarding the analysis procedures. It is found to be best from the standpoint of computer economy to run a full nonlinear quasi-static analysis for each trajectory, and to perform flutter analyses only at discrete times along the trajectory, selected by the analyst. Appropriate prestress conditions are obtained from the quasi-static solution. In a nonlinear flutter analysis the solution is obtained by direct numerical integration of the coupled nonlinear equations. However, in its present form this solution is markedly more time consuming (on the computer) than standard type linear flutter analyses.

An analytic theory is developed which can predict the nonuniform flow effects of nose bluntness in the complete hypersonic speed range $M \geq 3$. The predicted adverse effects of missile nose bluntness on vehicle dynamics are in excellent agreement with available experimental results. On a tactical missile the nonuniform flow field generates large spanwise dynamic pressure gradients over the fins. At nonzero angle of attack this inviscid shear flow makes the fin forces displacement sensitive. Simple viscous perturbation methods are developed which can predict the viscous induced effects on the unsteady fin aerodynamics with the desired accuracy.

Thermostructural numerical results are compared with existing closed form solutions and show how nonlinear coupling effects cause a deviation from the idealized cases considered in closed form solutions. Typical results illustrate the thermally induced stiffness changes in wings and demonstrate the importance of boundary conditions, temperature sensitive elastic moduli, initial imperfections, planform and thickness variations.

CONTENTS

ILLUSTRATIONS

Section 1
INTRODUCTION

When considering the aerothermoelastic characteristics of a finned tactical missile operating in the low hypersonic speed range, which is the subject of the present study, one encounters several problem areas. The aerodynamic heating causes a degradation of structural properties and, in combination with thermally induced stresses, accentuates nonlinear structural behavior. Aerodynamically the usual nonlinear airfoil characteristics of the fins are complicated by the nonuniform flow field generated by the slight nose bluntness necessary for the survival of the missile nose cone. The goal of the present study is to combine these nonlinear features in one computer program that will be able to predict divergence and flutter speeds for the fins on a tactical missile flying at near zero angle of attack at Mach numbers between $M_\infty = 3$ and $M_\infty = 6$.

One of the features that distinguishes the aeroelastic behavior of lifting surfaces at subsonic and low supersonic speeds is that isothermal, linear theories generally suffice to define both structural and aerodynamic behavior. There are exceptions such as the nonlinear flow behavior at transonic speeds and nonlinearities at all speeds caused by separated flow. In most cases, however, the equations can be linearized making it possible to conduct the different phases of aeroelastic analyses independently. Because the effects of prestress and small geometric imperfections are ignored in the linearization process, both strength and stiffness are invariant with time. This leads to a rather simple definition of critical loading conditions by means of the dynamic pressure and the velocity normal load factor, and the response to gusts and turbulence can be considered separately. Above all, it is the removal of time as a variable in the definition of the aerothermoelastic environment which results in a greatly simplified analysis.

Once the flight regime is extended to high supersonic speeds, aerodynamic heating must be included and the analysis becomes more complicated. The temperatures vary with time, and since thermal stresses change the structural stiffness, the aeroelastic problem cannot be formulated in terms of the current flight condition even if one assumes linear structural behavior. The classic aeroelastic triangle of interacting Inertial, Elastic, and Aerodynamic forces used by Collar (Ref. 1) becomes the aeroelastic rectangle shown by Rogers (Ref. 2) and reproduced here as Figure 1.1 with only the strong couplings indicated.

In the mid-fifties numerous studies were initiated on the influence of aerodynamic heating on aeroelastic behavior in the low supersonic speed range. Usually these studies were based on linearized theories. The thermal, aerodynamic, or structural effects of the problem were usually considered separately. Only a few investigations were devoted to their interactions. These included a wide ranging study on static phenomena at Bell Aircraft which took full advantage of the digital computer capability existing at that time (Refs. 3-7). With the aid of an early model digital computer, significant progress was also made at M.I.T. toward the understanding of the nonlinear effects of thermally induced stresses (Refs. 8-10). In addition to these and other similar studies with very limited distribution, numerous closed form solutions have been published. They are all based on simplifying assumptions such as infinite aspect ratio, zero chordwise flexibility, and idealized boundary conditions. Such solutions are satisfactory for demonstration of certain phenomena but their usefulness for analysis of practical flight structures is limited. Harder et al (Ref. 11) used a combination of digital and analog methods to investigate the flutter of heated monocoque wing structures.

With the extension of the flight regime to hypersonic speeds nonlinear effects become dominant. Over the past decade many studies have been made of the aeroelastic behavior of a wide range of vehicle configurations operating at hypersonic speeds. These include studies of static aerodynamics and vehicle dynamics of reentry vehicles and manned spacecraft, flutter analyses of lifting surfaces accounting for body flexibility, and panel flutter analyses. By the early nineteen fifties, the nonlinear relationship between the local

1-2

angles of attack of a body and the pressure distribution was well understood for inviscid flow. The importance of thermal stresses was appreciated. It was also common knowledge that for thin platelike lifting surfaces, transverse deflections of the same order as the thickness result in nonlinear force-deflection relationships. It was possible to evaluate the effects of each of these complications separately, but the state of technology did not allow the inclusion of all facets of the aeroelastic problem in a realistic analysis of the flight vehicle.

An important paper by Ashley and Zartarian (Ref. 12) demonstrates the use of piston theory in various applications to lifting surfaces with infinitely sharp leading edges. Although the thickness of the airfoil has been shown to have significant nonlinear effects on the pressure distribution, the equations of motion can still be linearized and the classical method of solving linear equations can be used. This is done for simple chordwise rigid sections in a series of MIT reports which are based on the unsteady shock expansion method and the unsteady Newtonian theory (Refs. 13-17). It was found that for a "typical section" with sharp leading edge the effect of the aerodynamic nonlinearity on the flutter speed was small. During the late fifties and early sixties, the Bell Aerospace Corporation, under Air Force Systems Command sponsorship, produced a series of reports on static aero-thermoelastic phenomena at hypersonic speeds (Refs. 18-20). In Ref. 20, geometrically nonlinear structural behavior and thermal stresses are accounted for. Various inviscid aerodynamic theories are presented in simple form, such as tangent wedge, modified Newtonian, shock expansion, and blast wave theories. Simple means to correct for leading edge sweep, nose bluntness, and boundary layer effects are provided.

This sampling of the literature has been made to show what types of analyses are available. They are all for highly idealized conditions and are, therefore, insufficient for determination of the aeroelastic characteristics of a tactical missile in the low hypersonic flight regime ($(3 \leq M_\infty \leq 6)$, the objective of the present study. Even if one considers only the fins, the aerodynamics can become rather complicated for a typical geometry (see Fig. 1.2). A nonuniform inviscid flow field, the "entropy wake", is generated by the curved bow shock,

1-3

causing the vehicle aerodynamics to become highly nonlinear. The entropy gradients in the "entropy wake" have large adverse effects on the vehicle dynamics due to the convective time lag associated with the "entropy wake" effects (Refs. 21-23). When only the local strip-aerodynamics on the fin are considered, the "entropy wake" effect is to introduce a spanwise dynamic pressure variation and, at non-zero angle of attack, a locally nonuniform flow in the "2-D strip planes" (see Fig. 1.2). In the present study an already developed hypersonic theory (Refs. 21-23) is extended down to $M_\infty = 3$.

Viscous effects are usually important in hypersonic flow. The large effects of boundary layer transition on reentry vehicles are well known (Refs. 24 and 25). The transition effects are of special concern when local temperature is important, such as is the case on an ablating vehicle (Refs. 21 and 26) or on thermally distorted surfaces (Ref. 25). The fin shock will cause the fuselage boundary layer to separate, generating complex aero-thermodynamic interactions (Ref. 27), which can have profound effects on the unsteady aerodynamics of the fins. Within the scope of the present study only an exploratory analysis of the viscous flow effects is possible.

It is desirable to develop an aeroelastic analysis capability for the hypersonic range that includes all important nonlinear effects. Experience indicates that below hypersonic speeds mechanically induced stress can be neglected, as the geometric changes are small for flight velocities significantly below those that cause aeroelastic instability. This makes the structural and aeroelastic analyses relatively independent of each other, contrary to what is the case at hypersonic speeds.

The nonlinear coupling between structural deformation and aero-thermodynamic behavior is probably the most important interaction which can be neglected only at subsonic and low supersonic speeds. For example, in a symmetric airfoil section the inplane stresses do not produce any out-of-plane distortions, and hence no change in distribution of aerodynamic pressures, until thermal buckling or aeroelastic instability is encountered. In practical applications a number of complications arise. Symmetric profiles with imperfections, as well as nonsymmetric, cambered, or deliberately warped sections, experience

thermally induced lateral deformations, which cause the lift distribution to become dependent upon the vehicle flight history. The fact that any plate-like wing subjected to bending will exhibit chordwise curvature due to the Poisson effect also provides thermoelastic coupling not considered in linear theory.

Since in the hypersonic domain larger deformations must be allowed, the non-linear interdependence between deformation, aerodynamic forces, and temperatures becomes continually stronger as the Mach number is increased. This makes it necessary to include thermal, aerodynamic, and structural analyses in the same program for evaluation of aeroelastic stability. Here such a program is de-veloped for the analysis of a lifting surface on a tactical missile. The computer program is built around the STAGS code (Ref. 28), which includes geometrically nonlinear structural effects. A modified STAGS code constitutes the heart of the program package, with the other programs attached to it. In what follows, the analyses leading to the different computer codes used in the integrated aerothermoelastic computer program are described first. After that the numerical results obtained with the integrated program are discussed and compared with the limited amount of pertinent data that is available. Using these results, an optimum procedure is formulated for aeroelastic analysis of a hypersonic tactical missile, based upon current state of the art. Recom-mendations are made for further improvement of this analytic capability. In-structions for the use of the aerothermoelastic computer program are given in Appendix B.
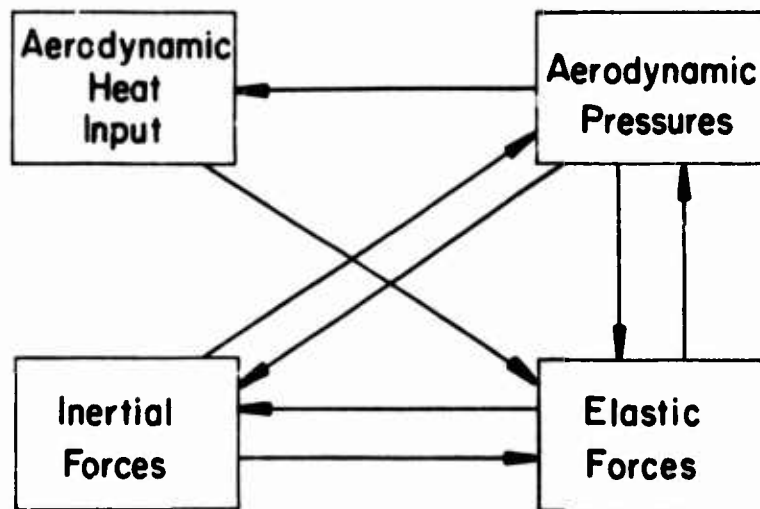
Fig. 1.1 Aerothermoelastic Rectangle (from Ref. 2)
Arrows denote strong coupling.
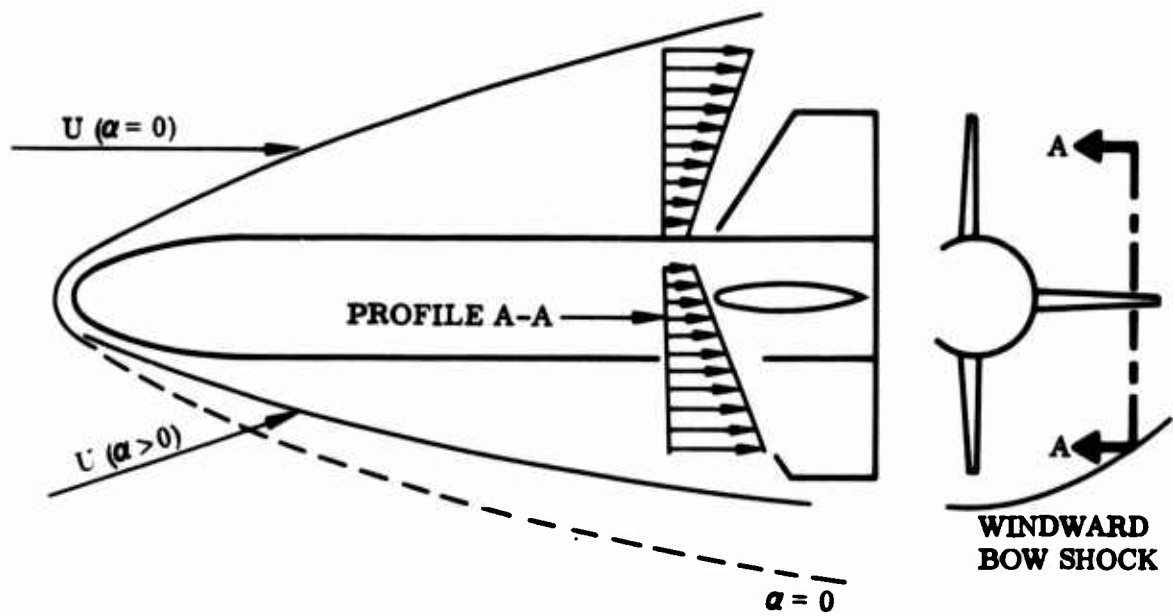
Figure 1. 2 Hypersonic missile flow field

Section 2
STRUCTURAL ANALYSIS

The thermoelastic analysis in the computer program is carried out by use of a combination of the STAGS program for elastic analysis and a program for determination of the temperature history in the structure. These two codes are briefly described in the following. Specific numerical results are presented to verify that these codes are suitable for aeroelastic analysis of tactical missiles.

2.1 The STAGS Code

STAGS is intended for analysis of shell or plate type structures. The structure to be considered may consist of up to 30 different shell branches, each treated by use of finite difference discretization. In addition, the structure may include some finite elements: elastic bars, shear panels, beams, and nonlinear plate elements. The computer code is discussed in detail in Ref. 28. Only a brief description is given here.

The analysis in STAGS is based on a finite difference energy method. That is, the total potential energy is expressed in terms of the applied mechanical or thermal loads and the displacement components at a number of node points. This is possible after derivatives occurring in the expression for the strain energy have been substituted by their finite difference equivalents and the energy has been numerically integrated over the entire structure. The total potential energy is minimized with respect to the degrees of freedom of the system

$$\partial V / \partial X_i = \partial / \partial X_i (U - \Omega) \qquad (2.1)$$

Here U is the strain energy, Ω the work done by external (or thermal) forces, and the X_i represent the displacement unknowns. The minimization leads to a set of equations of the form

$$K(X) = \{F\} \qquad (2.2)$$

where K is a <u>nonlinear</u> algebraic operator (of the third order). The force vector $\{F\}$ consists of thermal and mechanical loads, and also contains the strains caused by inelastic deformation. The equilibrium equations for a system in motion are obtained through the addition of the effects of inertia and damping.

$$[M]\{\ddot{X}\} + [D]\{\dot{X}\} + K(X) = \{F\} \qquad (2.3)$$

Options are given in the program that allow for omission or inclusion of the dynamic terms. The perturbation technique is used to formulate the eigen-value problems for bifurcation buckling and small amplitude vibrations.

Consequently, the code can be used for:

- o Linear stress analysis
- o Geometrically nonlinear elastic stress analysis
- o Inelastic stress analysis, geometrically linear or nonlinear
- o Bifurcation buckling analysis with linear or geometrically nonlinear prestress (elastic)
- o Small amplitude vibration analysis with prestress based on linear or geometrically nonlinear analysis (elastic)
- o Transient response analysis, linear or geometrically non-linear, elastic or inelastic

Any combination of point forces, line loads, and distributed surface tractions can be applied. Loading by specification of displacements or thermal gradients (through the shell wall and over the shell surface) is also permitted. Any set of boundary conditions or other displacement constraints can be included.

Restart capability exists both in the nonlinear static analysis and in the transient analysis. Intermediate data can be saved on tape or file, permitting the analysis to be continued at a later time. The input data is automatically checked for certain types of errors and for inconsistencies. If so desired, the user can suppress execution of the program in order to obtain a check on

the input. The output from such a preliminary run may include a graphic pre-sentation of the shell geometry with a display of the grid lines. The results of a STAGS run can be transferred to tape or disk file to be used as input for a postprocessor to obtain contour- or cross-plots of displacements, stress re-sultants, and stresses. Displacement histories can also be plotted in the case of transient or nonlinear static analysis.

The STAGS code accepts the input in two different forms, regular data cards and user written subroutines. The latter type of input may sometimes be more demanding on the user. However, it makes possible the definition of input parameters such as loads, temperatures, etc. by functional relationships. This tends to increase the generality of the computer code and also, in many cases, results in a more compact input deck. User-written subroutines can be used for

- o Initial imperfections
- o Loads
- o Load factor history (for transient analysis)
- o Shell wall properties and temperatures
- o Reference surface geometry
- o Grid generation
- o Boundary conditions and other constraints
- o Stiffener geometry and temperature
- o External damping

The shell configuration is described by use of a reference surface. The shell itself can be offset from this reference surface by a small amount that is allowed to vary over the surface. The location of any point on the reference surface can be uniquely defined by use of a set of two independent parameters, X, Y. The geometry of the surface is given after a functional relationship has been established that defines the coordinates in a Cartesian system x,y,z as functions of the values of these two parameters.

$$x = x(X, Y), \quad y = y(X, Y), \quad z = x(X, Y) \qquad (2.4)$$

The parameters X and Y defining the position of a point on the surface are referred to as surface coordinates. For shell geometries not included as standards in STAGS the user must define the relation given in Eq. (2.4) in a user-written subroutine.

If one of the surface coordinates is held constant and the other is varied over its range, a trace is obtained on the surface. Such a trace is referred to as a coordinate line. Coordinate lines have a two-fold purpose in the analysis. The directions of the in-plane displacements are defined by the coordinate lines. In addition, a set of coordinate lines are used to define the surface grid that is needed in a finite difference analysis. In most cases the two sets of coordinate systems are identical, but sometimes the natural coordinates for the shell are not suitable for grid generation. In that case a separate set of surface coordinates, denoted ξ, η, can be used to define the grid through a user-written subroutine. It is also possible to define directly the X, Y coordinates for the grid points, without use of an additional coordinate system, either by use of regular input data cards or by a user-written subroutine.

For definition of shell geometry a Cartesian system x,y,z (see Eq. (2.4)) is defined for each shell branch. One Cartesian system x_g, y_g, z_g is chosen as a global coordinate system. Orientation parameter cards define the orientation of the individual coordinate systems of each of the branches with respect to the global system. The global system is not defined explicitly by input cards but is given implicitly by the values of the orientation parameters.

Stiffeners are defined as structural elements attached to the shell surface. Effects of stiffener cross section warping or deformation are neglected. Stiffeners can either be considered as discrete, in which case they are defined one by one, or their contribution to the shell wall stiffness can be "smeared" over the shell surface. Smeared stiffeners are used for convenience

(to reduce the number of data cards) or in order to suppress the local deformation between the stiffeners. Present constraints in the computer program are as follows: inelastic analysis can only be used with an initially isotropic material. It cannot be used with material properties that vary with the surface coordinates. The yield stress must be independent of temperature. Bifurcation buckling and small amplitude vibration analyses cannot include plasticity.

2.2 The TRR1D Program

For computation of temperatures in the shell the code TRR1D developed by Compton and Schultz (Refs. 29,30) computes the transient thermal response of a body subject to arbitrary aerodynamic heating. The shell or plate under consideration is divided into a number of layers (called nodes). Individual layers can be of different materials. Temperature varient thermal properties can be included for all layers. The mid-surface of the geometry is assumed to be adiabatic, and the exterior surface is subjected to time-varient aerodynamic heating. Heat conduction into the body is one-dimensional, and radiation from the surface to the surroundings can be taken into account. The finite difference equations are derived by conventional energy balance considerations for each layer using an implicit difference scheme. The temperature response is determined by a tri-diagonal matrix solution at each time step.

The calculation of the aerodynamic heat transfer coefficient is performed at each time step based on updated ambient conditions. In summary, the aerothermodynamic techniques used are:

1. Stagnation point - Fay-Riddel method.
2. Flat plate - Blasius method for laminar flow and the Spalding-Chi method for turbulent flow.
3. Conical flow - Flat-plate methods modified for conical flow as given by VanDriest in Ref. 31.

Transition from laminar to turbulent flow is assumed to occur instantaneously at a boundary layer edge Reynold's number of 500,000, which is very much on the

2-5

conservative side for the Mach number range of interest. No effort is made
to compute a transition zone or to compute a virtual origin for the turbulent
boundary layer. It is highly desirable that a code be developed which gives
a better estimate of the temperature field.

2.3 Code Verification

A few examples follow here in which results from STAGS are compared to re-
sults obtained by other means. The first of these excludes temperature effects.
The next series of examples includes a temperature field defined in the STAGS
input as varying parabolically in the chordwise direction. The last few
examples are obtained by use of STAGS and TRR1D. The temperature field is
determined internally and thermal degradation of material properties is in-
cluded.

2.3.1 Small Amplitude Vibrations of Stress Free Plate

An important function of STAGS in the aeroelastic analysis is to determine
modes and frequencies of small amplitude vibration. The capability to perform
such analyses has been included recently. In order to verify this new capa-
bility, STAGS results were obtained and compared with results from FLUENC,
which is a sub-program of the MOFA system of computer programs (Ref. 32).

The analysis was performed for a plate of rectangular planform with a 10-in.
chord and an 8-in. span as shown in Fig. 2.1. The grid has 11 node points along
the chord and 5 along the span. The plate was clamped over a portion of the
root chord as shown in the figure. The grid is rather coarse and the results
will not be very accurate. However, it has been used throughout the program
development for reasons of computer economy. It is sufficiently fine to indi-
cate the gross behavior of the plate. As with decreasing grid size the STAGS
results converge from below and the FLUENC results from above we can expect
some discrepancy. First STAGS and FLUENC were applied to a plate with constant
thickness, 0.2 in. The mode shapes from the two programs were very close.
The frequencies corresponding to this coarse grid are shown in Table 2.1.

2-6

Table 2.1

Comparison of Frequencies for Constant Thickness Plate

Mode Number	FREQUENCY (Hz)		
	FLUENC Grid (5x11)	STAGS Grid (5x11)	STAGS Refined Grid (15x21)
1	63.65	57.12	61.67
2	122.14	106.29	111.82
3	287.41	266.84	281.29
4	523.27	466.10	498.76

The relatively good agreement between the results indicates that with diminishing grid size they would agree in the limit. This impression is reinforced by the fact that with a refined grid (3 times denser in the most critical spanwise direction) STAGS gives the results shown in the last column of Table 2.1.

In another example a plate with variable thickness is considered. The chordwise section has a "diamond profile" (double wedge). The section properties, independent of the spanwise coordinate, correspond to 0.05-in. thickness at the leading and trailing edges and a maximum thickness of 0.45-in. at midchord. The same grid was used as in the previous case. We may expect somewhat larger discrepancy in this case since the plate is very thin at the leading and the trailing edges, and thus a finer spacing is required for convergence. Results are shown in Table 2.2. The last column shows results obtained by use of a grid with variable spacing. These results verify the validity of the program and underscore the usefulness of a variable spacing grid for this type of plate. It shoud be noticed that with constant thickness elements in FLUENC we expect the frequencies to be somewhat high.

Table 2.2

Mode Number	FREQUENCY (Hz)		
	FLUENC Grid (5x11)	STAGS Grid (5x11)	STAGS Grid (9x11)
1	125.99	103.40	117.97
2	272.47	237.07	238.87
3	644.58	570.95	604.02
4	1044.34	782.05	798.10

2.3.2 Influence of Temperature Gradients

For minimum drag many plate-like wing structures subjected to hypersonic flow
are designed so that they are very thin at the leading and trailing edges
(the diamond shaped profile). This results in temperature distributions with
markedly higher temperatures at the edges and a minimum at mid-chord. The
thermal expansion results in that case in spanwise compression at the edges
and tension in the cooler midsection. Such temperature distributions can
have a profound effect on the aeroelastic behavior of the wing. Consequently,
the effect has been studied in the past and several research papers have been
published (Refs. 33-40). These papers were published before the high speed
computer had made detailed analysis of more complex configurations possible.
In the following we will compare results obtained from STAGS with the closed
form solutions of Ref. 34 for constant thickness plates. The temperature dis-
tribution, however, will be one that is typical of a wing with a diamond
shaped profile.

2.3.3 Thermal Buckling

With the temperature distribution discussed above, compressive stresses at
the edges are increasing with the temperature. At some temperature level
thermal buckling will occur. According to Ref. 34, the critical value of
the difference between edge and mid-chord temperature is

$$\Delta T_{crit} = 18.5 \frac{D}{E \alpha t c^2} \cdot \frac{(\xi + 1)(\xi + 3)}{\xi} \tag{2.5}$$

For parabolic temperature variation, with a minimum at mid-chord, $\xi = 2$. In that case, a square aluminum plate with a 20 in. side and 0.5 in. thickness will buckle at $\Delta T_{crit} = 153°F$. With a discretized analytical model, as in the STAGS code, the results are accurate only if a sufficiently fine grid spacing is used. Therefore, for comparison with the analytical results in Ref. 34 STAGS results were obtained for various grid sizes. With a relatively coarse grid spacing, 2.0 in., the critical temperature difference is $118°F$, far below the analytical results, $153°F$. The primary reason for the discrepancy is that the temperature gradient is large at leading and trailing edges and the thermal stresses are therefore not well represented in the prebuckling solution with this coarse grid size. As the grid is refined, values of ΔT_{crit} closer to the value of Ref. 34 are obtained. Thus, with a grid spacing of 1.0 in., $\Delta T_{crit} = 142°F$.

With a sufficiently fine grid the STAGS results should be more accurate than those of Ref. 34. The reason for this is that Eq. (2.5) is based on the assumption that in the buckling mode the chord remains straight. The STAGS results show some chordwise bending in the buckling mode. If essentially the same restriction is introduced in STAGS (by increasing the chordwise bending stiffness by a factor of 10^4) ΔT_{crit} increases to $147°F$. Thus, the validity of the STAGS code is verified for this type of application. The model with coarse grid spacing, 2.0 in., although somewhat inaccurate, reflects correctly the basic structural behavior. In the interest of computer economy, subsequent results were obtained with this grid size.

The temperature field under consideration here is symmetric about the mid-plane of the plate. Consequently, for a perfectly flat plate there will be no out of plane deformation in the prebuckling stage, $\Delta T < \Delta T_{crit}$. Above the critical temperature this equilibrium configuration becomes unstable. With the temperature difference increasing above ΔT_{crit}, a new deformation mode gradually develops. This mode is essentially represented by pure twisting of the wing.

The value of the twist at the wing tip is shown as a function of the temperature in Fig. 2.2. The temperature difference is normalized with respect to ΔT_{crit}, so that thermal buckling occurs at $\lambda = 1.0$. The twist parameter $\emptyset$ is defined in Ref. 34. The results for the perfectly flate plate, as obtained in Ref. 34, are shown by the curve marked $\emptyset_i = 0$.

If the plate contains an imperfection in shape that is not orthogonal to the buckling mode, no equilibrium can exist without lateral displacements. By use of a nonlinear analysis it is possible to determine the growth of this lateral displacement with increasing values of λ. An initial imperfection in the form of a uniform twist of the wing was introduced in Ref. 34. The amplitude of the twisting mode was then determined as a function of λ. Results were obtained for different values of the initial twist as shown in Fig. 2.2.

For two values of the initial twist, $\emptyset = 0.05$ and 0.20, results were obtained by use of STAGS and are also shown in Fig. 2.2. At any finite value of λ the STAGS results indicate a lower value of the twist. It should be noted that the curves with STAGS results are normalized with respect to a lower value of ΔT_{crit}, $118^{o}F$. STAGS results normalized with respect to the critical load of Ref. 34 would indicate higher values of the twist than those shown in Ref. 34. This reflects the fact that the discrete model is weaker due to the coarser spacing and also due to the inclusion of chordwise bending. The occurrence of chordwise bending was pointed out in Ref. 35.

The twist, defined as the rotation of an element of the chord around a spanwise axis, is constant in the analysis of Ref. 34, but is allowed to vary along the chord in the STAGS analysis. STAGS results for the local twist are shown in Fig. 2.3 .

The variation of the torsional stiffness of the lifting surface with temperature and initial twist is also discussed in Ref. 34. STAGS results for the torsional stiffness are compared to those from Ref. 34 in Figure 2.4. The agreement between results from the two methods provides additional verification of the STAGS code. For a perfect plate the torsional stiffness (or the

square of the corresponding vibration frequency) decreases linearly with increasing temperature, so that it becomes equal to zero at $\lambda = 1.0$. The imperfect plate retains a finite stiffness. The explanation of the fact that the imperfect shell retains a finite stiffness at $\lambda = 1.0$ is that the edges are stretching as the wing twists. This reduces the temperature induced spanwise compression stress.

Less information is available on the effect of the temperature distribution on the bending stiffness of the plate. Kochanski and Argyris (Ref. 36) and Mansfield (Ref. 37) consider the problem for wings of infinite aspect ratio. While those results do not apply to the low aspect ratio wing considered in the STAGS analysis, it is still possible to compare certain trends. It is explained in Ref. 37 how a temperature field with higher temperatures at the leading and trailing edges reduces the bending stiffness of the plate. When the plate is subjected to spanwise bending, the Poisson effect results in chordwise bending as well. Due to this chordwise bending, the higher temperatures are on one side of the neutral axis and the lower temperatures on the other side. This introduces "thermal bending" of the plate in the same direction as the applied "mechanical bending". Hence, with increasing temperature the plate bending stiffness should be decreasing. This trend is shown by the STAGS results presented in Figure 2.5. Again, the imperfection is in the twisting mode.

The ratio between the fundamental bending and torsional frequencies is one of the important parameters in flutter analysis. This ratio can readily be obtained from the results of the stiffness calculations with STAGS discussed above. Results are presented in Figure 2.6. As is to be expected, the frequency ratio changes markedly with the temperature and its behavior is strongly dependent on the initial imperfection amplitude. For a perfectly flat plate the frequency ratio becomes infinite at $\lambda = 1.0$ because the frequency of the torsional mode vanishes.

In conclusion, STAGS numerical results agree well with the analytical results of Ref. 34. Whenever differences occur, these can be traced to the restriction imposed in the analysis of Ref. 34 in order to make a closed form solution possible.

2.3.4 Lifting Surfaces with Diamond Shaped Profile

It was demonstrated above how the thermal stresses induced by aerodynamic heating dramatically reduce the torsional stiffness of the lifting surface. The example discussed illustrates a basic trend, although it is somewhat less than realistic, since a plate of uniform thickness is used in the elastic analysis with a temperature distribution typical of a surface with a diamond profile.

In other attempts at analysis (Refs. 33, 35-40)) the variable thickness was accounted for in the elastic analysis. These publications consider the effect on the torsional stiffness of spanwise thermal stresses in wings of rectangular planform. The wing, treated as a simple beam, is clamped at the root chord and generally considered to have an infinite aspect ratio. Singer (Ref. 39) is among those who introduces an approximate correction for finite aspect ratio.

Material property degradation with the temperature is another complication that cannot easily be accounted for in the analytic solutions. Only through use of a numerical solution procedure is it possible to obtain reasonably accurate results. Nevertheless, the analytic solutions are useful since they give an indication of what trends to expect in a computer solution of the governing partial differential equations.

With thin leading and trailing edges on the lifting surface it appears necessary also to consider local deformation modes. Mansfield (Ref. 40) presents a closed form solution for the thermal bifurcation buckling of a lifting surface with a sharp leading edge. The critical load in that case depends only on the temperature gradient at the edge, the thermal expansion coefficient α, and the wedge angle $(2\theta_w)$. A parabolic temperature distribution discussed earlier is assumed. The critical temperature at the sharp edge is

$$\Delta T_{crit} = \frac{3 \, (2\theta_w)^2}{5 \, \alpha \, (1+\nu)} \tag{2.6}$$

This simple closed form solution cannot take into account the effects of property degradation, nose bluntness, finite aspect ratio, or boundary conditions at the wing root. Neither is it possible to evaluate wing behavior when the critical temperature is exceeded. However, the formula should be useful for a first estimate.

The STAGS program with the thermal analyzer TRR1D was used to study the behavior of rectangular wings with diamond shaped cross-section under hypersonic flight conditions. The cross-section of the wing is shown in Fig. 2.2. The edges are somewhat blunted so that the thickness varies from 0.05 in. at the leading and trailing edges to 0.45 in. at mid-chord. For comparison with the analytical solutions (Ref. 40) the spatial temperature distribution should be held constant in time also in the STAGS analysis. The temperature distribution shown in Fig. 2.7 is typical for results obtained by use of TRR1D. The four lowest vibration frequencies and corresponding modes were determined for different values of the amplitude of this distribution. The results are shown in Fig. 2.7 both for a wing clamped along the entire length of the root chord and for one in which the displacements are constrained only at the node points 7,8,9.

For the wing with complete root chord constraint the trends of the lowest frequencies agree with that of the analytic solutions at the lower edge temperatures. The torsional stiffness, represented by the square of the frequency of the second mode, decreases with the temperature. Extrapolation of the results obtained indicate that the stiffness would vanish at a temperature of about $680^{\circ}F$. Analytic solutions, valid only for longer wings, indicate a higher critical temperature of about $760^{\circ}F$. The lowest frequency, corresponding to the first bending mode, is less sensitive to the temperature. The elementary beam theory does not predict any influence of thermal stress on the bending stiffness. However, higher order theories, such as those by Mansfield (Ref. 37) or Kochanski and Argyris (Ref. 36) show the same trend as the STAGS solution.

The frequencies of the wing with only partial root chord constraint shows very little dependence on the temperature. This result is to be expected

since the thermal stresses at the leading and trailing edges will be less
significant if points on the root chord are free to move in the spanwise
direction. Thermal stresses computed for the rectangular wing are shown for
three different boundary conditions in Fig. 2.8. The results in Fig. 2.7
also include the reduction in stiffness that is due to material property
degradation. Since the thicker midsection of the wing stays relatively cool,
the reduction is moderate.

The frequencies of the third and fourth modes are also shown in Fig. 2.7 as
functions of temperature. At all temperatures at which results were obtained,
the mode corresponding to the four lowest eigenvalues are clearly identified
as the first and second bending modes, and the first and second torsion modes.
However, at a temperature of 690°F the solution indicated in addition one
negative eigenvalue. This, of course, represents the mode corresponding to
leading edge buckling. The critical load then is exceeded at $T = 690^{\circ}$F but
not at $T = 460^{\circ}$F (the second highest temperature for which results were obtained).

It is clear that the 5x11 finite difference grid used is too coarse to give
a good estimate of the critical load when the buckling mode is localized.
With 1.0 in. chordwise grid spacing the critical temperature for bifurcation
buckling is found to be 570°F. However, examination of the buckling mode
indicates that a much finer grid is needed near the leading edge. A grid
with variable spacing was introduced (Fig. 2.9), and with this grid the
critical leading edge temperature was found to be 370°F. The corresponding
buckling mode is shown in Fig. 2.10.   Beyond the 5th row, 0.75 in. from
the leading edge, the lateral displacements are very small. According to
Eq. (2.6) with $\beta = 0.08$, and a sharp edge, the critical temperature is 230°F.

The behavior of the plate in the postcritical temperature range was also de-
termined. The nonlinear analysis does not distinguish between stable and
unstable equilibrium configurations. True bifurcation modes are orthogonal
to the precritical deformation pattern. Therefore, if buckled configurations
are to be computed, it is necessary to introduce a small disturbance as a
trigger. In this case a couple of lateral loads of one pound each and with
opposite direction were applied at the leading edge near the root chord (rows

3 and 4). It is found that the amplitude of the buckle grows gradually with the temperature, so that the deformation still is very moderate at temperatures well beyond the critical. Modulus degradation with the temperature does not have a detrimental effect. In fact, the increase in the buckle amplitude is somewhat retarded through property degradation, probably because a reduced shear modulus allows the leading edge to expand more freely in comparison to the cooler material in the interior. It is also found that a leading edge buckle has little effect on the overall stiffness of the wing.

As an additional check on the overall behavior of this wing in response to thermal gradients, the analysis was repeated for the quadratic chordwise temperature distribution. Figure 2.11 demonstrates the precipitous degradation of stiffness for the fully clamped wing. The detailed behavior is rather different from a temperature distribution computed by use of TRR1D. The instability in that case was connected with the localized leading edge buckling, while for the parabolic temperature variation four thermal bifurcation modes are predicted for leading edge temperatures of 683.7, 687.0, 869.8, and 901.1°F. All the associated modes involve large overall deformation as opposed to the localized buckling in the previous case.

Results obtained for a clipped delta wing show similar trends as shown in Fig. 2.12.

In order to verify that STAGS and TRR1D work properly in combination, other cases were executed in which the spatial temperature distribution was allowed to vary with time as prescribed by the results from TRR1D. It was observed that in that case the solution of the nonlinear equations (in STAGS) converged considerably slower. This is tentatively attributed to the fact that presently used extrapolated initial estimates are good only if the temperatures vary proportionally with the aerodynamic pressure. This deficiency should be relatively easy to remedy.

It should be emphasized that the temperatures for leading edge buckling and, to a lesser degree, the degradation of the torsional stiffness are determined in a conservative way by the STAGS-TRR1D combination. The reason for this is

that the relief through heat transfer in the chordwise direction has been neglected. A two-dimensional thermal analysis would certainly result in more realistic, less conservative results. A more realistic treatment of the boundary layer transition will probably work in the same direction.

Finally, the results obtained for wings with different support at the root-chord indicate that deformation of the missile body may have a substantial effect on the stiffness of a heated wing and consequently on its aeroelastic performance. (The aerodynamic coupling between missile body and fin may have an even larger effect on the aeroelastic characteristics, as will be discussed in the following section.)
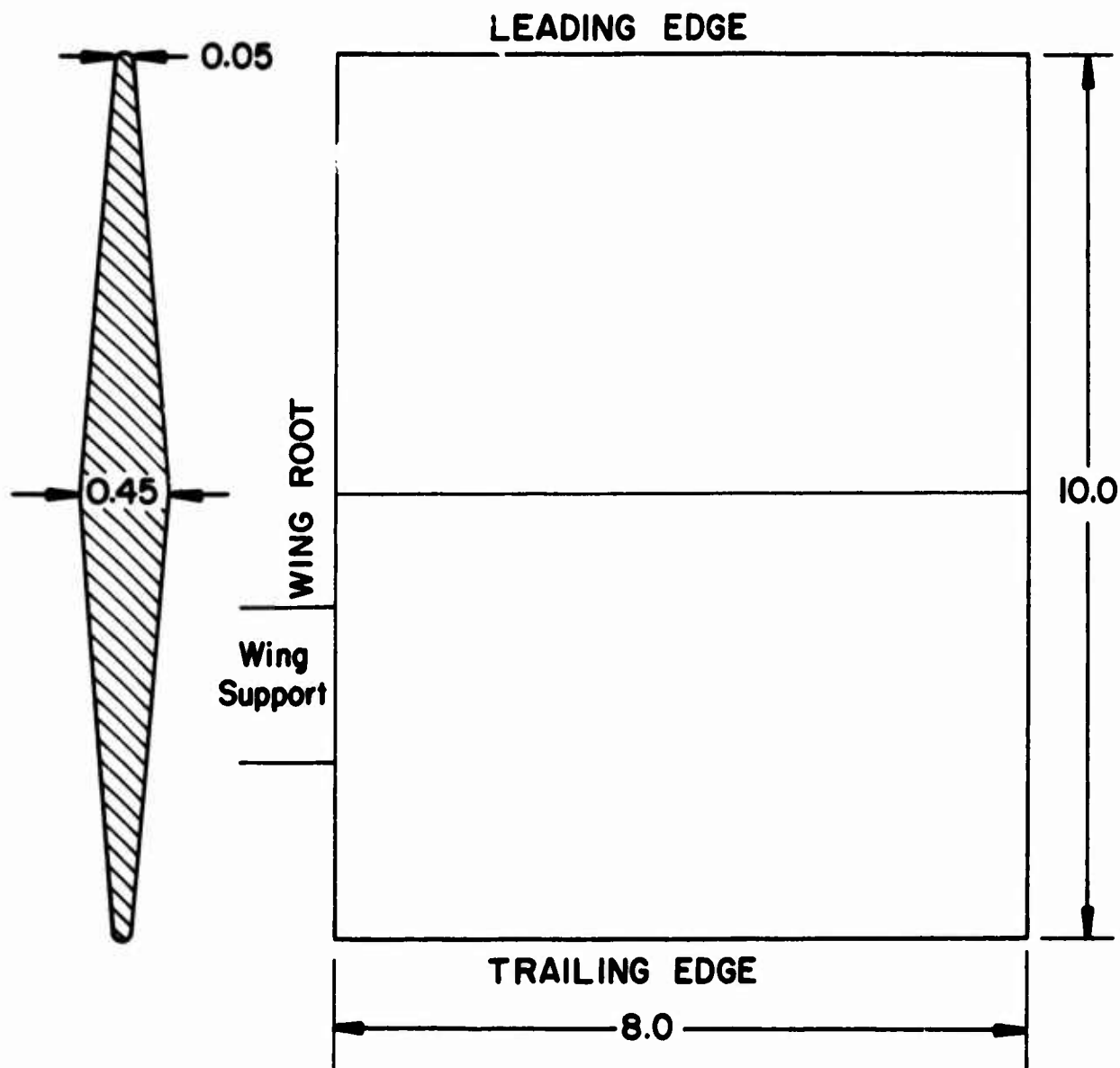
Fig. 2.1   Rectangular Wing with Diamond Profile
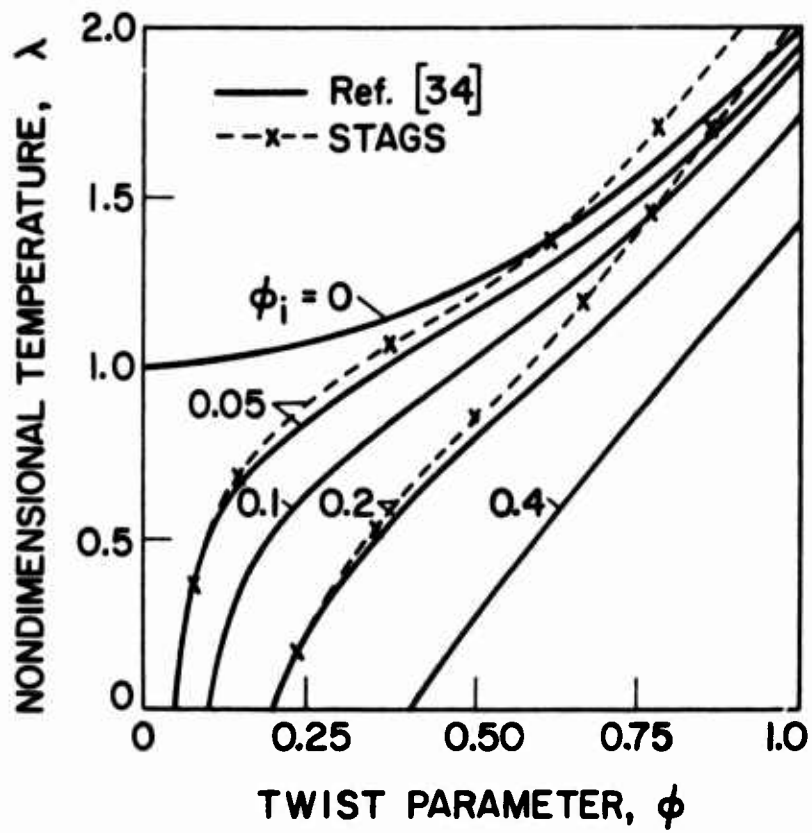
Figure 2.2 Tip Twist as a Function of Temperature
Ratio & Initial Imperfection Amplitude
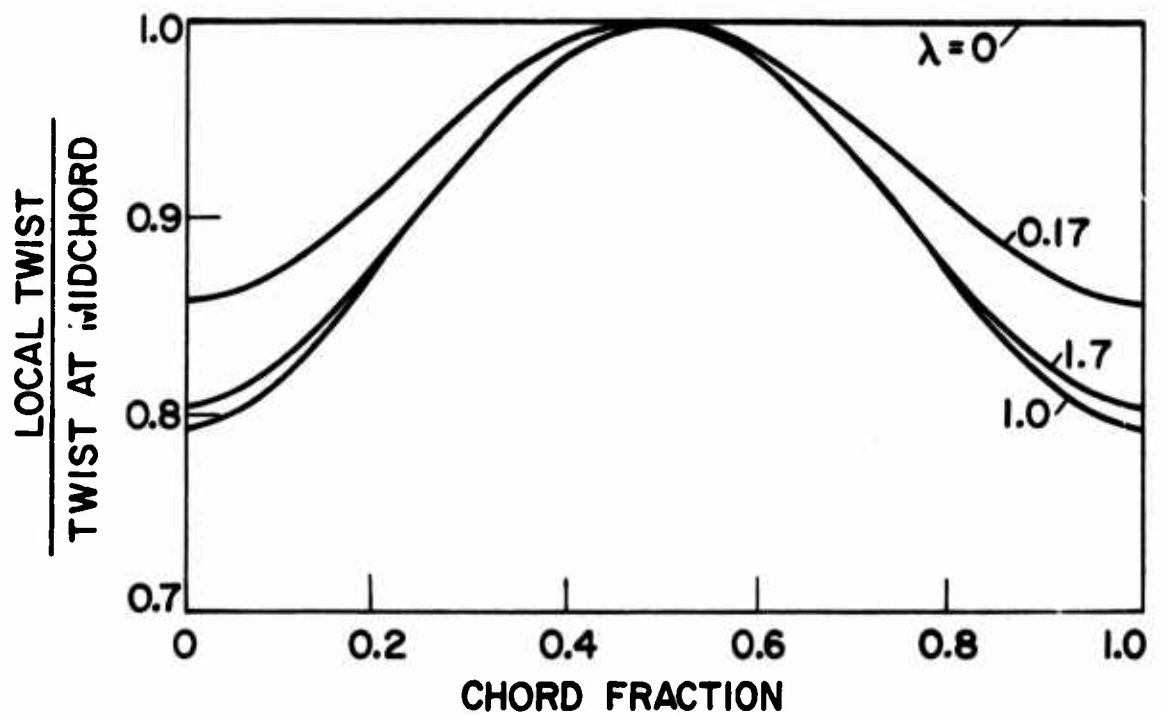
Figure 2.3 Variation of Local Twist along Chord, STAGS Results.
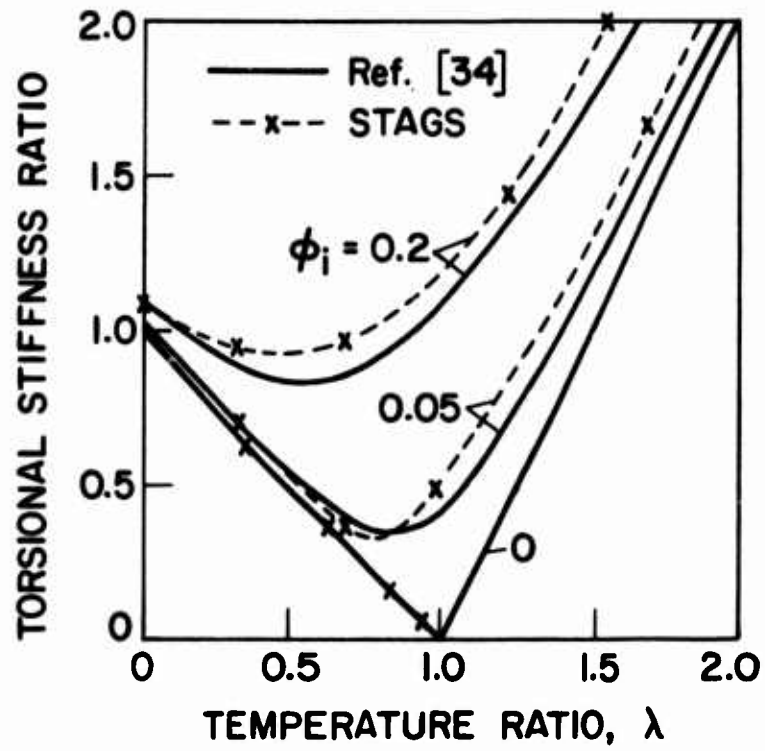
Figure 2.4   Torsional Stiffness as a Function
of Temperature and Initial Imperfection
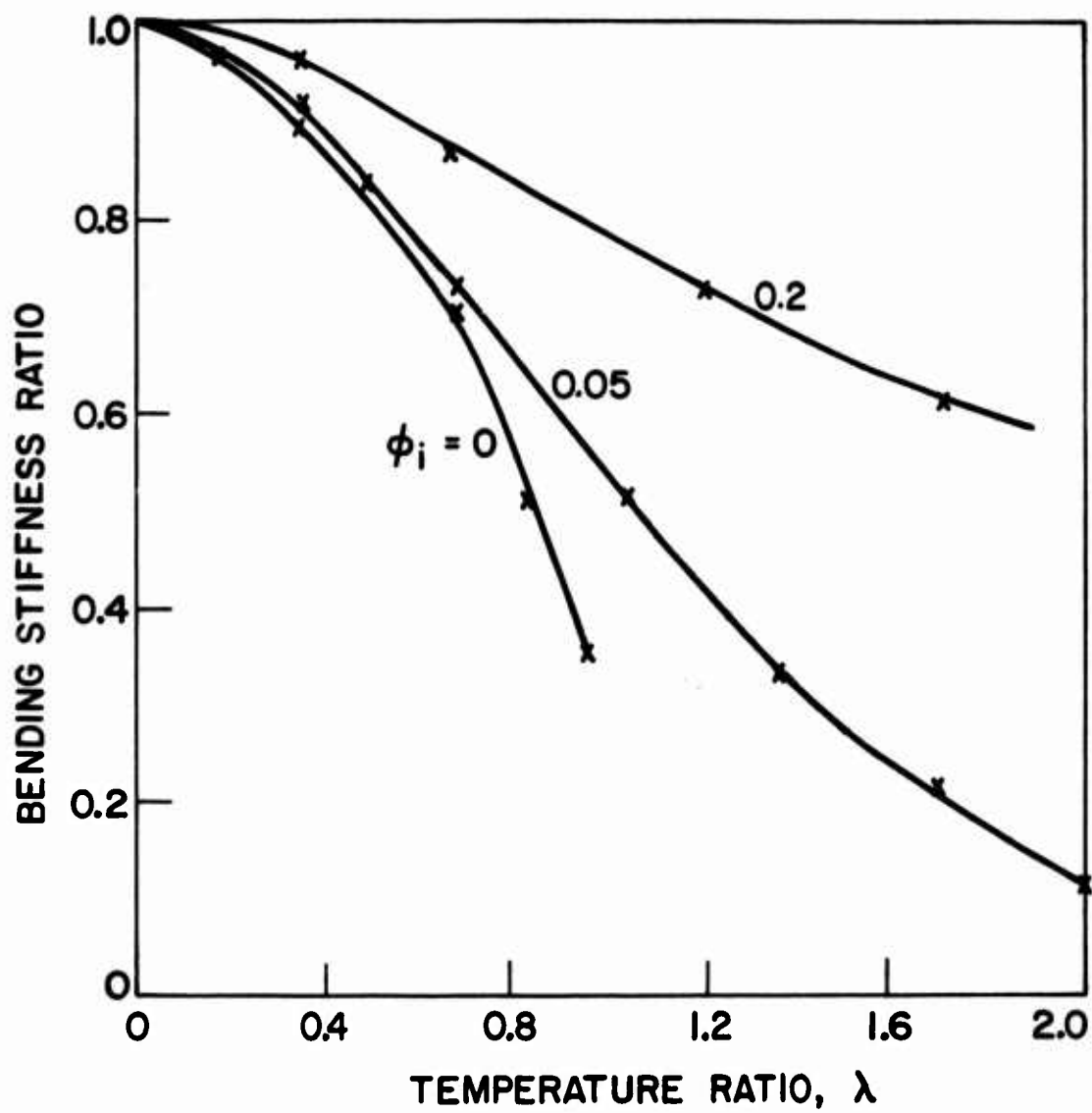
Figure 2.5 Bending Stiffness as a Function of Temperature and
Initial Imperfections, STAGS Results.
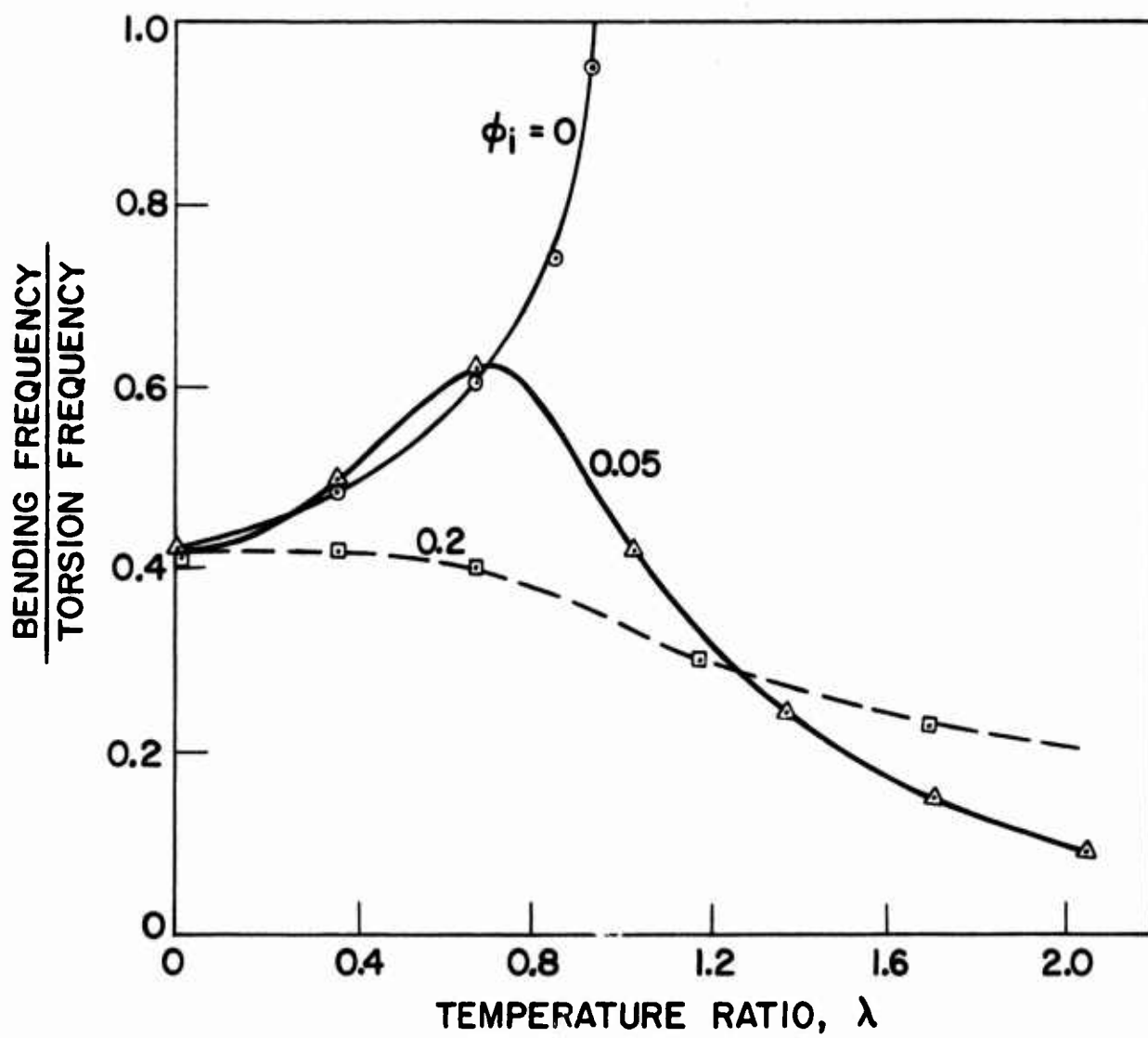
Figure 2.6   Bending to Torsion Frequency Ratio,   STAGS Results.
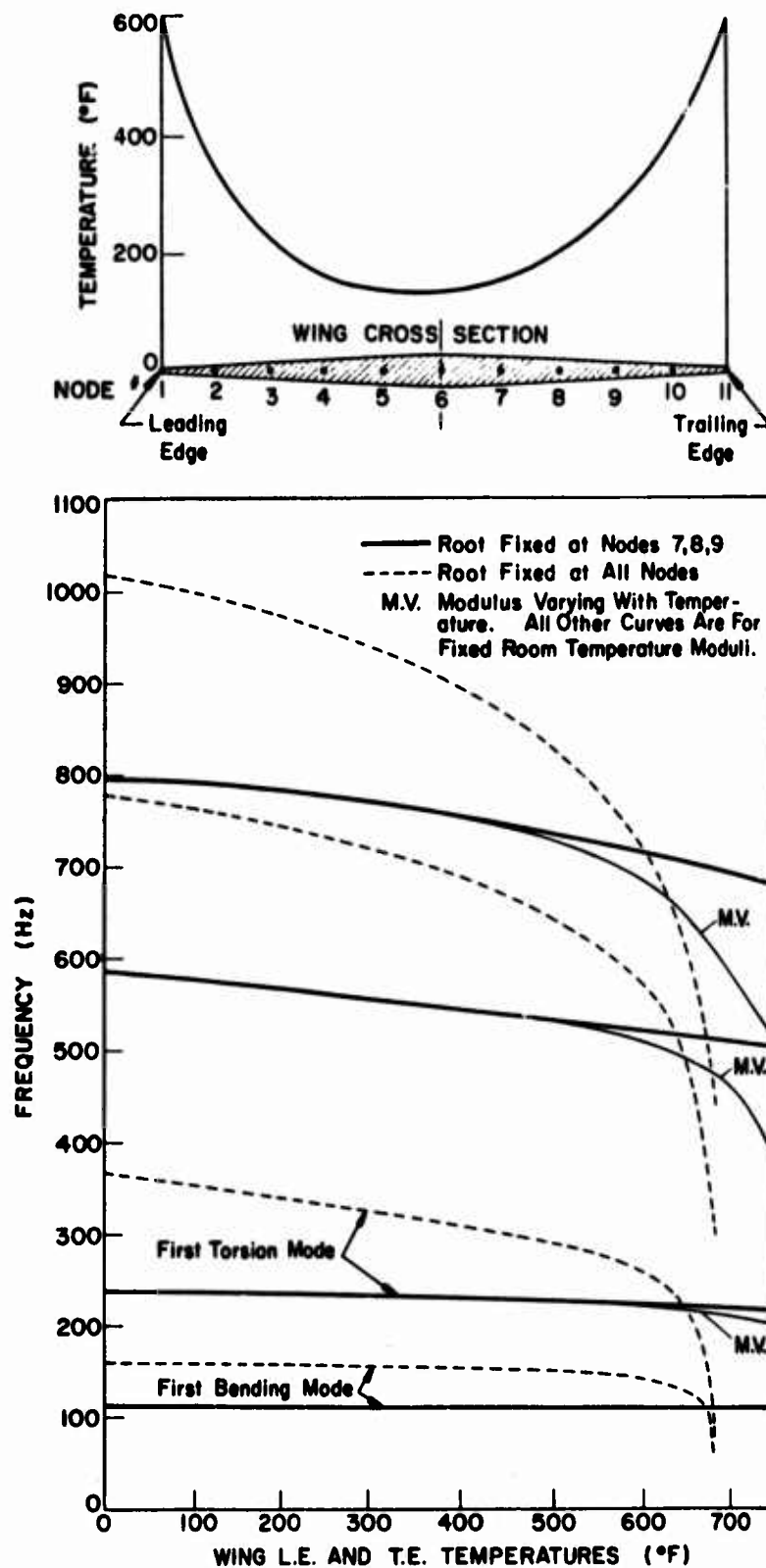
Figure 2.7   Influence of Root Boundary Conditions &
Temperature on Natural Frequencies
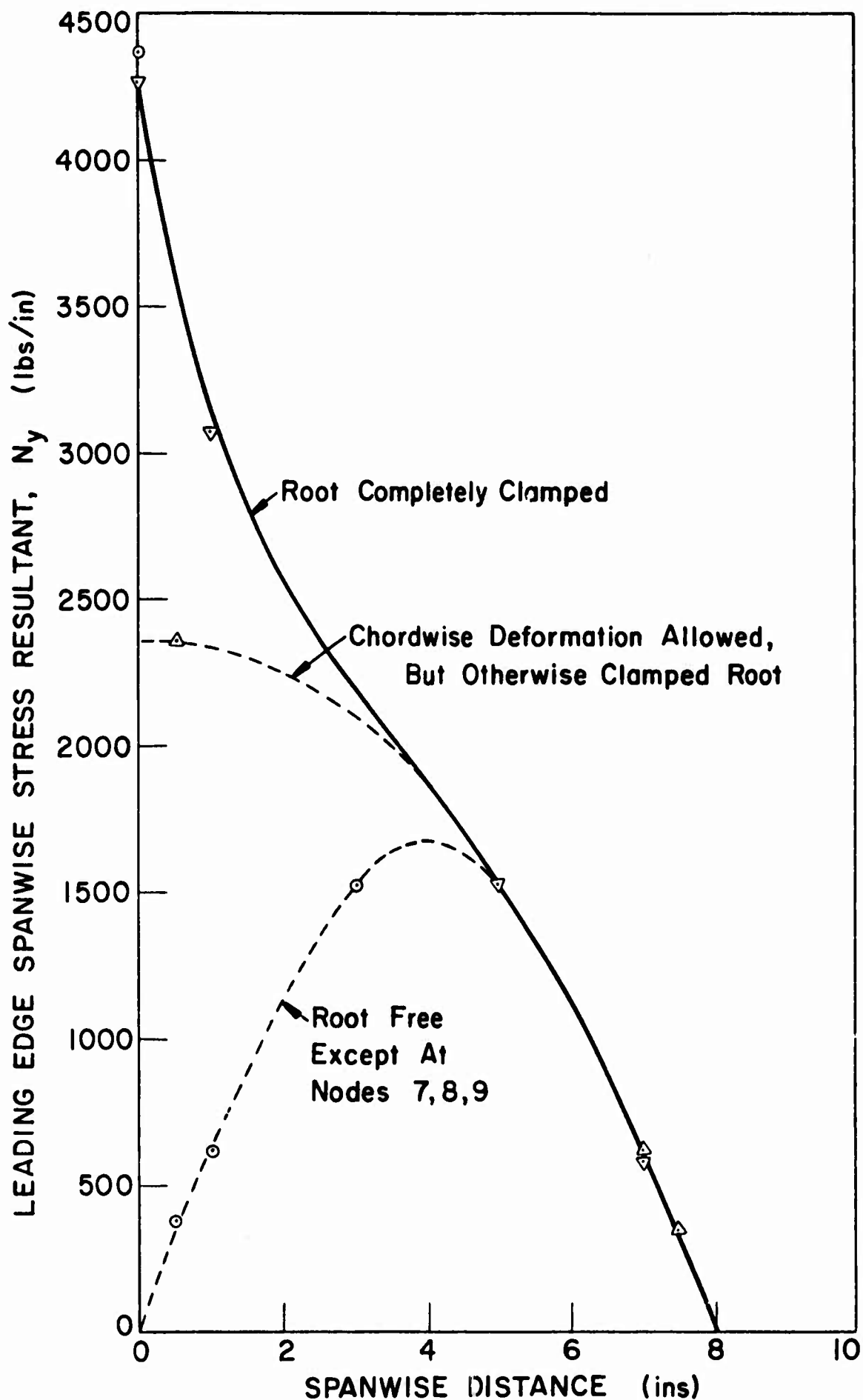
Fig. 2.8 Stress Resultants in Rectangular Planform Diamond Profile Leading Edge Temperature 600°F

2-24
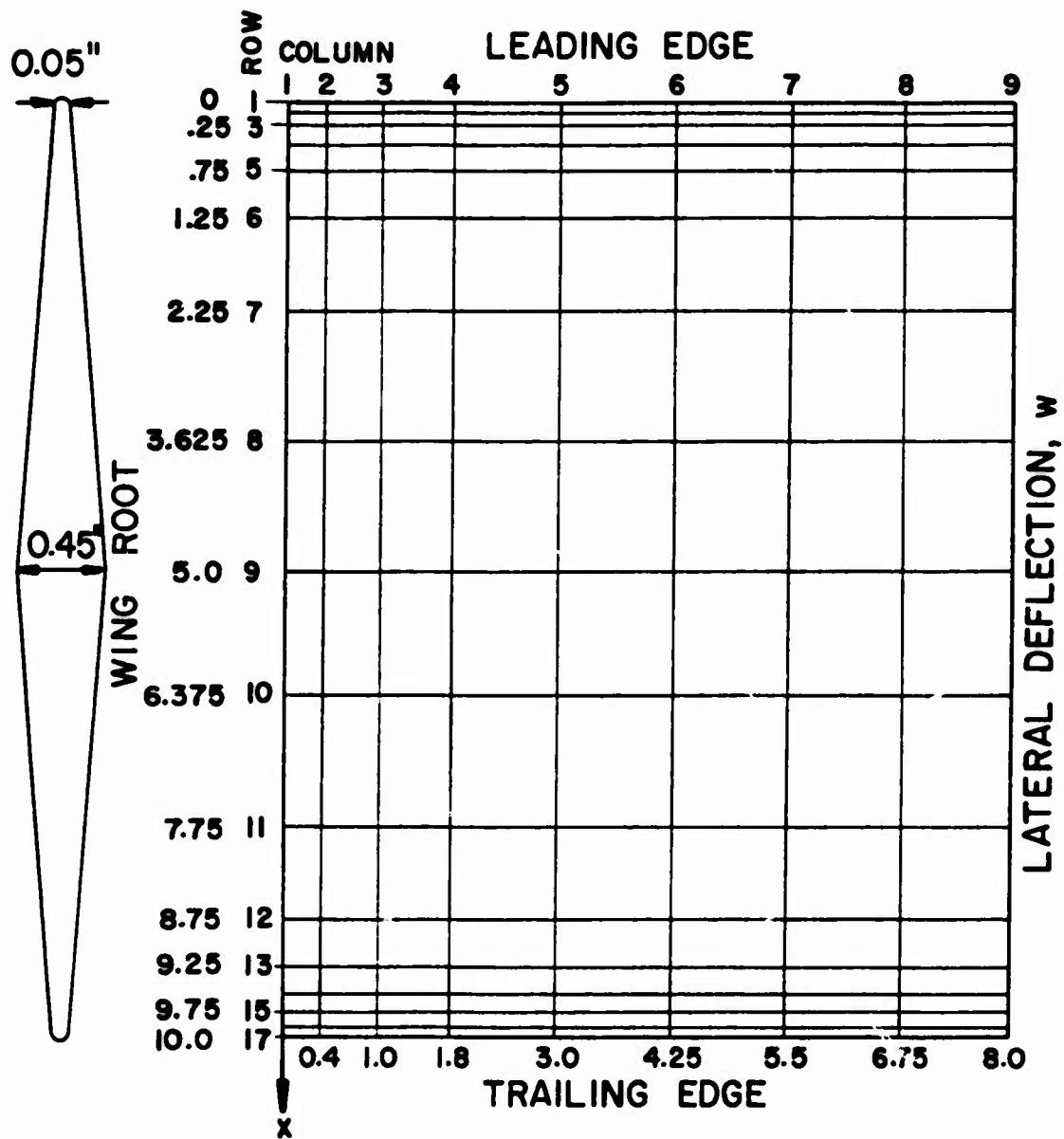
Figure 2.9 Rectangular Wing with Variable Grid
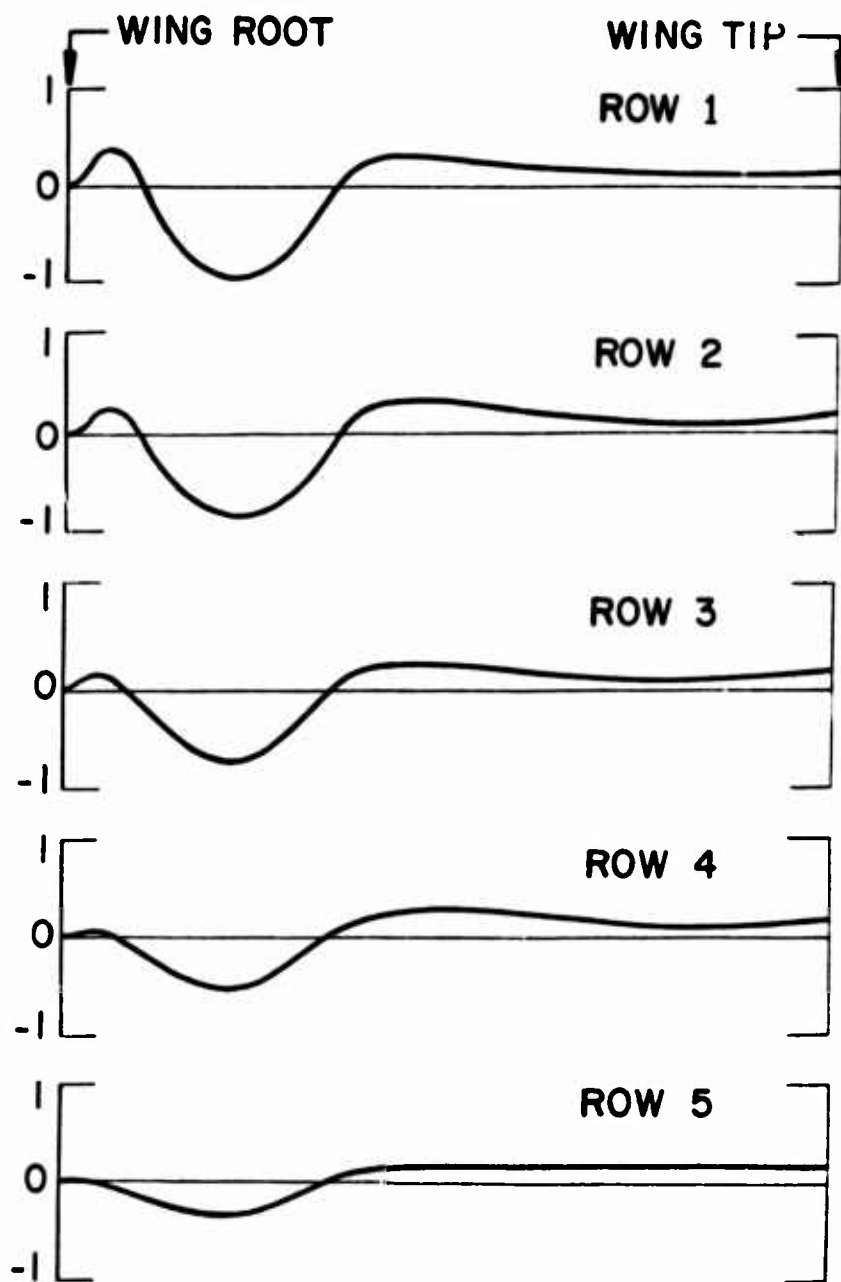
Figure 2.10   Thermal Buckling Mode
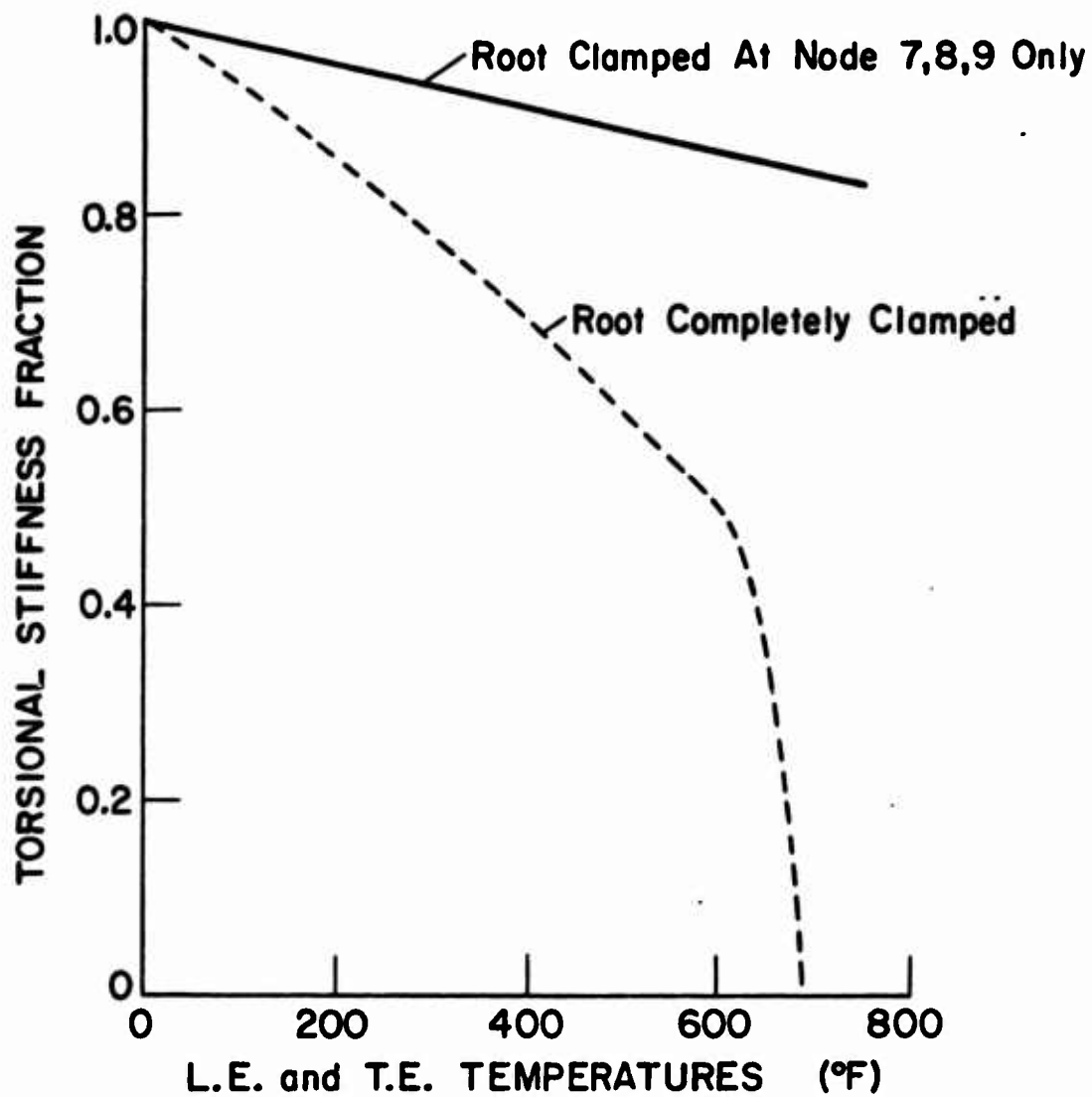
Fig. 2.11 Decrease in Torsional Stiffness for the Rectangular Planform, Diamond Section Wing Subjected to Quadratic Chordwise Temperature Distribution
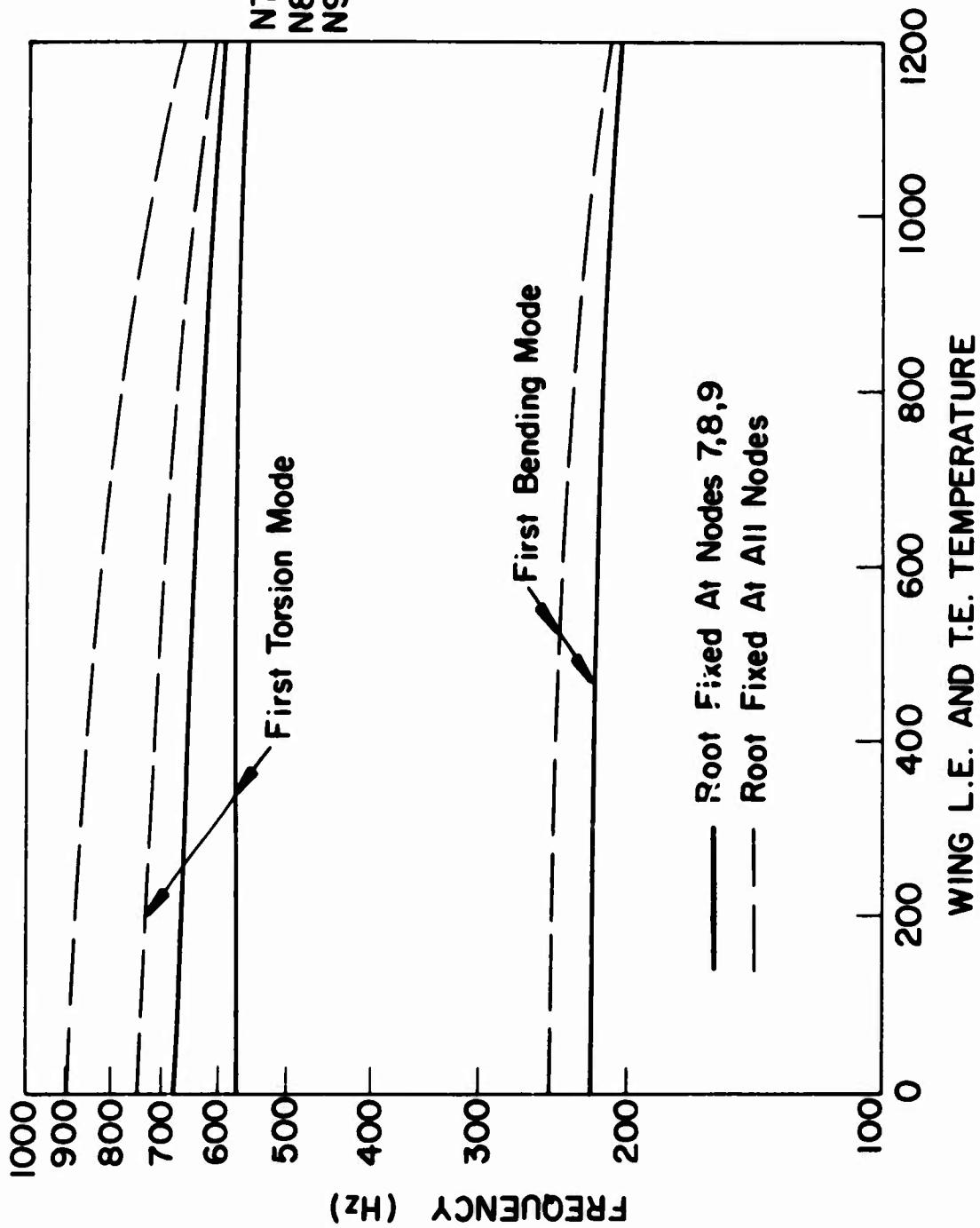
Figure 2.12 Influence of Temperature on Frequencies of Rectangular Planform Diamond Wing Subjected to Quadratic Chordwise Temperature Distribution

Section 3
AERODYNAMIC ANALYSIS

It was indicated in the Introduction, Section 1, that numerous theoretical methods exist through which the hypersonic steady and unsteady aerodynamics of simple geometries can be determined. However, the methods are almost without exception too idealized to be of much help in the design of hypersonic vehicles. This is because the following flow phenomena are not adequately simulated:

1. The inviscid shear flow or entropy gradients generated by the small amount of nose bluntness that is required for thermodynamic survival in hypersonic flow.

2. The viscid-inviscid flow interactions which become important at hypersonic speed, especially in the lower part of the atmosphere where boundary layer transition greatly complicates the physical flow simulation.

The main efforts of the aerodynamic analysis presented here are concentrated on removing these two deficiencies and provide analytic means that can produce realistic predictions of the hypersonic steady and unsteady aerodynamics. In the analysis to be presented only small perturbations from zero angle of attack will be considered, i.e., $\alpha = 0$ if not stated otherwise.

3.1 INVISCID FLOW OVER AXISYMMETRIC BODIES

3.1.1 Bluntness-Induced Effects

Nose bluntness effects play an important role in aerodynamics of bodies at high supersonic and hypersonic speeds. A simple analytic theory has been developed earlier which describes the unsteady aerodynamic characteristics of slender blunted cones at hypersonic speeds (Refs. 22 and 23). In the present analysis the theory is examined

3-1

in regard to existing limitations. It is found that when the Mach number decreases much below $M_\infty = 20$ or the cone angle becomes less than the Mach angle, the unsteady embedded Newtonian theory (Ref. 23) is not applicable in its original form. The needed modifications are simple, however, and a more general embedded Newtonian theory has been formulated.

3.1.2 Embedded Newtonian Flow

The simple Newtonian theory (Ref. 41) has provided an indispensible tool for hypersonic vehicle design. It works well as long as the bow shock follows the body contour relatively closely, such as is the case for pointed bodies and for very blunt geometries. However, when the bow shock cannot follow the body contour, as is the case for blunt nose cylinder-flare bodies, for example, the Newtonian theory gives prohibitively large errors. Severe loss of flare efficiency in the reduced velocity flow field behind a strong bow shock has been noted (Refs. 42 and 43). Less emphasis has been placed on the effect of the entropy gradient created behind a curved bow shock (Ref. 44), and the tendency has been to "average out" the velocity variation over the flare (Ref. 45). In the present analysis the complete entropy gradient effects are considered.

In the embedded Newtonian flow concept first proposed by Seiff (Ref. 45), Newtonian theory is used in the non-uniform, inviscid flow field defined by the bow shock (Refs. 44 and 46). The shock shape is defined by the nose bluntness and can be related to the nose drag (Refs. 47 and 48). The pressure coefficient on the "embedded" body element ΔA in Figure 3.1 can be written:

$$C_p = C_{p_o} + C_{p_{max}} \left(\frac{V_\perp}{U}\right)^2 \frac{\rho U^2}{\rho_\infty U_\infty^2} \tag{3.1}$$

where $C_{p_{max}}$ is well approximated by the stagnation pressure behind a normal shock ($C_{p_{max}} \approx 1.8$)[*] for blunt-bodies and by the Newtonian value ($C_{p_{max}} \approx 2$) for slender

---

[*] For $M_\infty \geq 3$ this gives less than 3 percent deviation from the modified Newtonian value of Ref. 49, which is

$$C_{p_{max}} = \frac{\gamma + 3}{\gamma + 1} \left(1 - \frac{2}{\gamma + 3} \frac{1}{M_\infty^2}\right)$$

geometries. $V_\perp$ is the local velocity component normal to the surface of the body element, and U is the local axial velocity component in the inviscid shear flow. that is, $V_\perp/U$ is determined geometrically and, for the body element in Figure 3.1, pitching with the rate of q radians/sec, it is

$$V_\perp/U = \cos\alpha\,\sin\theta + \sin\alpha\,\cos\theta\,\sin\phi + \frac{(x - x_{CG} + r\tan\theta\,)q}{U}\cos\theta\,\sin\phi \quad (3.2)$$

The dynamic pressure ratio is a function of radial position in the inviscid shear flow profile. If similar profiles are assumed,[#] it can be expressed in the following form

$$\frac{\rho U^2}{\rho_\infty U_\infty^2} = f^*(R/R_{sh}) \quad (3.3)$$

R_{sh} is determined by the nose drag (Refs. 47 and 50)

$$\frac{R_{sh}}{d_N} = K_{sh} C_{D_N}^{1/4}\left(\frac{x - x_{sh}}{d_N}\right)^{1/2} \quad (3.4)$$

where, for $M_\infty \to \infty$, $x_{sh} \approx x_N$, $0.8 < K_{sh} \le 1.0$. For hemisphere-cylinders, $K_{sh} = 1.0$ is found to correlate experimental data (Ref. 47).

R is obtained from Figure 3.1 and is simply

$$\left.\begin{aligned}
\left(\frac{R}{d_N}\right)^2 &= \left(\frac{\Delta z}{d_N}\right)^2 + 2\frac{\Delta z}{d_N}\cos\alpha\left(\frac{1}{2} + \frac{x}{d_N}\tan\beta\right)\sin\phi \\
&\quad + \left(\frac{1}{2} + \frac{x}{d_N}\tan\beta\right)^2\left[\cos^2\alpha\,\sin^2\phi + \cos^2\phi\right] \\[2ex]
\frac{\Delta z}{d_N} &= \frac{x}{d_N}\sin\alpha + \left(\frac{\Delta z}{d_N}\right)^{##}_{elastic}
\end{aligned}\right\} \quad (3.5)$$

$f^*(R/R_{sh})$ in Eq. (3.3) is of parabolic shape and can be written

$$f^*(R/R_{sh}) = f_0^* + A_1 X^* + A_2 X^{*2} \quad (3.6)$$

[#]This should be a good assumption except for the flow region close to the shock, e.g., the near nose region for small α.

[##]Deflection at x relative to the nose, x_o, due to body deformation.

$$X^* = \left(\frac{R}{d_N} - \frac{1}{2}\right)^2 \bigg/ \left(\frac{R_{sh}}{d_N}\right)^2 \qquad (3.7)$$

Seiff's data for a hemisphere-cylinder (Refs. 44 and 47) show that the dynamic pressure data can be fitted by the following polynomial

$$\frac{\bar{q}}{q_\infty} = \frac{\rho U^2}{\rho_\infty U_\infty^2} = f^*(X^*) = 0.17 + 2.75\, X^* + 4 X^{*2} \qquad (3.8)$$

The blast wave pressure is constant over the inner half of a cylindrical shock (Refs. 45 and 50). The pressure coefficient C_{p_o} in Eq. (3.1) is, therefore, assumed to be constant over the radial extent of a submerged flare. This assumption is consistent with the assumption of similar flow profiles, Eq. (3.3). Kuehn (Ref. 51) gives the following correlation formula for the axial distribution of the blast wave pressure p_o (0) on the blast wave centerline (also measured on the surface of a hemisphere-cylinder).[#]

$$\left.\begin{aligned}
\frac{p_o(0)}{p_\infty} &= 0.85\,\frac{k(\gamma)}{\Lambda} + 0.55 \\[2mm]
\Lambda &= C_{D_N}^{-1/2}\, M_\infty^{-2} \left(\frac{x}{d_N} - \frac{x_N}{d_N}\right) \\[2mm]
k(\gamma) &= 0.098\,(\gamma - 1)^{0.395} = 0.067 \text{ for } \gamma = 1.4
\end{aligned}\right\} \qquad (3.9)$$

Equations (3.1)-(3.9) give the following embedded-Newtonian formulation for the aerodynamic pressure coefficient on a surface "embedded" in the "entropy wake" generated by a blunt nose at hypersonic speed ($M_\infty = \infty$, $\gamma = 1.4$).

$$C_p = \frac{0.081\, C_{D_N}^{1/2}}{\left(\dfrac{x}{d_N} - \dfrac{x_N}{d_N}\right)} + C_{p_{NEWT}}\, f^*(X^*) \qquad (3.10)$$

[#]The pressure given by second order blast wave theory is (Ref. 52).

$$p_o(0)/p_\infty = k(\gamma)/\Lambda + 0.44$$

3-4

For $\alpha = 0$ and small β and θ , the pressure on an embedded flare is defined by Eq. (3.10) as

$$
\left.
\begin{aligned}
C_p &= \frac{0.081\ C_{D_N}^{1/2}}{\dfrac{x}{d_N}\left(1 - \dfrac{x_N}{x}\right)} + C_{p_{NEWT}}\ f^*\ (X^*) \\[1em]
X^* &= X\left(1 - \frac{x_N}{x}\right)^{-1} \\[1em]
X &= \beta^2\ C_{D_N}^{-1/2}\ \frac{x}{d_N}
\end{aligned}
\right\} \qquad (3.11)
$$

3.1.3 Generalized Embedded Newtonian Flow

It has been shown that through an appropriate modification the blast-wave parameters can be extended to the correlation of bluntness-induced pressures on cones and wedges (Refs. 53-56). For cones, where $\beta = \theta_c$, the result is (Refs. 22 and 23)

$$
\left.
\begin{aligned}
C_p/2\ \theta_c^2 &= f^*\ (X) \\[1em]
X &= C_{D_N}^{-1/2}\ \theta_c^2\ (x - x_0)/d_N
\end{aligned}
\right\} \qquad (3.12)
$$

The theoretical pressure distributions computed by the M(ethod) 0(f) C(haracteristics) (Ref. 57) at $M_\infty = 20$ for spherically blunted 5°, 10°, and 15° cones are shown in this form in Figure 3.2**. Also plotted are the blast wave pressures for hemisphere-cylinders using Kuehn's correlation (Ref. 51). The difference between cone pressures and blast wave pressures is a measure of the dynamic pressure profile in the "entropy wake" (Refs. 22 and 23).

$$
f^*(X)\ =\ \bar{q}/\bar{q}_\infty\ =\ (\Delta p_c)_{BLUNT}\Big/(\Delta p_c)_{SHARP} \qquad (3.13)
$$

$$
**(p_c)_{BLUNT}\Big/(p_c)_{SHARP}\ =\ (C_{pc})_{BLUNT}\Big/(C_{pc})_{SHARP}\ =\ C_p/2\theta_c^2 \text{ for slender cones}
$$
where $\tan\theta_c = \theta_c$.

The f*-function defined in this manner is shown in Fig. 3.3 for $2.5° \leq \theta_c \leq 20°$, $3 \leq M_\infty \leq 20$. The expected collapse of the pressure distribution curves occurs only for cone angles above a critical value. Closer examination reveals that the critical value is the freestream Mach angle. Including the Mach angle in the shock-angle/cone-angle chart of Ref. 58 indicates that when the cone angle "dips below" μ the shock angle remains more or less insensitive to θ_c (see Figure 3.4). In the limit, when $\theta_c \ll \mu$, the shock angle is completely independent of θ_c. Figure 3.3 shows that the entropy profile is becoming steeper as θ_c is decreased. A steepening of the profile is also observed when going from blunted cones to blunted cylinder-flare bodies (Ref. 23). At hypersonic speeds the f*-function for blunted cylinder flare bodies is (Ref. 21)

$$f* = 0.17 + 2.75\, X* + 4\, X*^2 \tag{3.8}$$

and for blunted cones (Ref. 22)#

$$f* = \begin{cases} 0.17 + 1.375\, X* & : X* \leq 0.49 \\ 1 - 3.43\,(0.7 - X*)^2 & : 0.49 < X* < 0.7 \\ 1 & : 0.7 \leq X* \end{cases} \tag{3.14}$$

For $\alpha = 0$ the similarity parameter $X*$ can be written

$$X* = \left| (x - x_0)/d_N \right| \left[\tan^2 \sigma / C_{D_N}^{1/2} \right] \tag{3.15}$$

Where $\sigma = \beta$ for the cylinder-flare configuration and $\sigma = \theta_c$ for the blunted cone (see Fig. 3.5). Comparing Figures 3.3 and 3.5 one easily arrives at the picture sketched in Figure 3.6, which leads to the following "analytic curve fit" for blunted slender cones (see also Figure 3.7).

#Note that $f = 2f*$

$$\theta_c/\mu \geq 1 \;:\; f^* = \begin{cases} f_o^* + B \chi^* & : \chi^* \leq \chi_1^* \\ 1 - k_f (\chi_o^* - \chi^*)^2 & : \chi_1^* < \chi^* < \chi_o^* \\ 1 & : \chi_o^* \leq \chi^* \end{cases}$$

$$\theta_c/\mu < 1 \;:\; f^* = \begin{cases} f_o^* + AB \chi^* & : \chi^* \leq \chi_2^* \\ 1 - b \left\{ 1 - \left[1 - \left(\dfrac{\chi_o^* - \chi^*}{a} \right)^2 \right]^{1/2} \right\} & : \chi_2^* < \chi^* < \chi_o^* \\ 1 & : \chi_o^* \leq \chi^* \end{cases}$$

$$\chi_o^* = 0.7 \;;\quad \chi_1^* = 2 \chi_{crit}^* - \chi_o^* \;;\quad \chi_{crit}^* = (1 - f_o^*)/AB$$

$$\chi_2^* = (f_1^* - f_o^*)/AB \;;\quad f_1^* = 0.9 - \frac{3.33 - A}{2.33}(0.9 - f_2^*)$$

$$f_2^* = f_o^* + AB \chi_3^* \;;\quad \chi_3^* = \chi_1^* + 0.01$$

$$k_f = B/2 (\chi_o^* - \chi_1^*)$$

$$f_o^* = 0.165 + [\, 9.65/(M_\infty + 8.7)\,]^3 : M_\infty \geq 3$$

$$B = \begin{cases} 1.375 - 0.5 [0.17 (10 - M_\infty)]^3 : & 3 \leq M_\infty < 10 \\ 1.375 & : M_\infty \geq 10 \end{cases}$$

$$A = \begin{cases} 3.33 & : \theta_c^*/\mu \leq 0.23 \\ 3.33 - 3.03 \left| (\theta_c^*/\mu) - 0.23 \right| & : 0.23 < \theta_c^*/\mu < 1 \\ 1 & : 1 \leq \theta_c^*/\mu \end{cases}$$

$$a = (\chi_o^* - \chi_2^*) \left\{ 1 + \left[\frac{(1 - f_1^*)}{(\chi_o^* - \chi_2^*)\, AB} \right]^2 \middle/ \left[1 - \frac{2(1 - f_1^*)}{(\chi_o^* - \chi_2^*)\, AB} \right] \right\}^{1/2}$$

$$b = (1 - f_1^*) \left\{ 1 + \frac{(1 - f_1^*)}{(\chi_o^* - \chi_2^*)\, AB} \middle/ \left[1 - \frac{2(1 - f_1^*)}{(\chi_o^* - \chi_2^*)\, AB} \right] \right\}$$

$$\theta_c^* = \theta_c \text{ for } \alpha = 0$$

(3.16)

For $\theta_c/\mu \geq 1$ and $M_\infty = \infty$, Eq. (3.16) reduces to Eq. (3.14), as it should.

A comparison between predictions through Eq. (3.16) and MOC-computations is made in Figure 3.8 for $M_\infty = 5$ and $M_\infty = 8$. In addition to the dynamic pressure profile given by Eq. (3.16) the velocity profile is needed. Through reasoning analogous to that for hypersonic flow conditions (see Refs. 22 and 23), the velocity ratio is defined as follows:

$$
\left.
\begin{aligned}
g^*(X^*) \;=\; U/U_\infty \;&=\; \begin{cases} g_0^* + k_g\, X^{*1/2} & : X^* < X^*_{crit} \\ 1 & : X^*_{crit} \leq X^* \end{cases} \\[2mm]
k_g \;&=\; \left| 0.304\, B / \left| 1 + (3.33 - A)/2.33 \right| \right|^{1/2} \\[2mm]
g_0^* \;&=\; 1 - k_g\, X^*_{crit}
\end{aligned}
\right\} \qquad (3.17)
$$

When $\alpha \neq 0$ the similarity parameter X^* is not given by Eq. (3.15) but by Eqs. (3.4), (3.5), and (3.7) using the tangent cone approximation.

$$
\left.
\begin{aligned}
\theta_c^* \;&=\; \sin^{-1} (V_\perp/U) \\[2mm]
V_\perp/U \;&=\; \cos\alpha\, \sin\theta_c + \sin\alpha\, \cos\theta_c\, \sin\phi
\end{aligned}
\right\} \qquad (3.18)
$$

Incorporating Eqs. (3.16)-(3.15) in the embedded Newtonian analysis of Reference 23 gives the results shown in Figure 3.9. It can be seen that the stability derivatives of slender blunted cones show sensitivity to Mach number even for $M_\infty > 10$. However, the effect is probably too small to be discernible from the data scatter in dynamic tests. This is indicated by the comparison with experimental data (Refs. 59-61) made in Figure 3.10. The agreement with experimental data is very good, as good (at least) as for the much more time consuming numerical flow field theory of Rie et al (Ref. 62). Note that the opposite effect of nose bluntness on static and dynamic stability derivatives is well predicted. That the experimentally observed effects of Mach number is well predicted by the present theory is documented by Figure 3.11.

By representing the nose bluntness effect as the fractional change of sharp cone characteristics the following advantages are gained: Tangent cone methods can be used even at supersonic Mach numbers, and predictions made by inviscid theory can be compared with viscous experimental data. The justification for this statement is simply that in using this ratio between blunted and sharp cone characteristics the inviscid and viscous crossflow effects that are common to sharp and blunted cones are eliminated. The same is true about sting interference effects which often plague dynamic wind tunnel tests (Ref. 63). Thus, realistic comparisons between inviscid predictions and experimental results can be made as long as nose bluntness has negligible influence on cross flow effects and sting interference. This would certainly be the case for tests with completely turbulent flow. However, hypersonic testing is usually done in laminar flow with a relatively thick boundary layer, and nose bluntness may significantly influence the viscous effects. Orlik-Rückemann (Refs. 64 and 65) has shown that the "boundary-layer-cushioning" effect usually is small on cones, at least for standard C.G. locations. The effect of nose bluntness on viscous crossflow with associated convective time lag effects should also be small as long as boundary layer transition does not occur on the (aft) body* (Refs. 24 and 25). The most difficult problem by far is the effect of nose bluntness on dynamic support interference (Ref. 63), especially in presence of aft body transition effects (Ref. 66). There is experimental evidence (Ref. 67) indicating that nose bluntness could have a significant effect on sting interference. Fortunately, Walchner and Clay made sure that dynamic support interference did not distort their experimental results (Refs. 59 and 68), and also Ward's data (Ref. 61) can be expected to be relatively free of sting interference effects (Ref. 23). Thus, the comparisons made in Figure 3.10 should be valid indicating that the present analytic inviscid flow theory can adequately predict the effect of nose bluntess on slender cone stability characteristics. The comparison made in Figure 3.11 is also valid as far as sting interference goes. However, boundary layer transition effects have distorted the low Mach number comparisons somewhat in the manner described in Ref. 22. The $M_\infty = 5$ data have been corrected for asymmetric transition effects but not the results for $M_\infty = 3$. At $M_\infty = 10$ no asymmetric transition effects were present

---

*Experiments indicate the effect to be less than 10 percent.

Comparing Eqs. (3.8) and (3.14) in view of the trends shown in Figure 3.5 leads to the following definition of the generalized embedded Newtonian flow field over a blunt-nose cylinder.

$$f^* = f_o^* + 2 B X^* + (1.45 B X^*)^2 \leq 1 \qquad (3.19)$$

where f_o^* and B are obtained from Eq. (3.16) and X^* is obtained from Eqs. (3.4), (3.5) and (3.7) by allowing for the spanwise coordinate y/d_N (see insert in Figure 3.13) when computing R/d_N, Eq. (3.5).

This formulation is consistent with the $\sqrt{2}$ ratio between shock radii for cones and cylinders used in Ref. 69. That is, it is assumed that the dynamic pressure profiles remain similar. The dynamic pressure profile above the cylinder surface six (6) nose diameters downstream of a hemispherical nose tip is shown in Figure 3.12 for $M_\infty = 6$. Also shown are the positions of the conic frustum for the two cone angles between which the entropy wake changes from cylindrical to fully conical. If one places fins of unit aspect ratio with their leading edge at $(x - x_o)/d_N = 5.5$, they will be exposed to this dynamic pressure distribution, as is illustrated in Figure 3.13. In one case the missile body is a simple hemisphere-cylinder, in the other case shown the same hemispherical nosetip is followed by a shallow conic frustum, $\theta_c = 0.4 \mu$, and a cylindrical aft body. The figure illustrates how nonlinear the dynamic pressure profiles are, and how a subtle change of body geometry can double the experienced dynamic pressure gradients.

That the nonlinear aerodynamics are real is illustrated by the data in Figure 3.14. The present theory predicts the measured nonlinear $C_m (\alpha)$ characteristics up to $\alpha = 20°$. At higher angles of attack, bow shock-flare shock interactions cause a loss of flare lift (Ref. 70). At some angle of attack the windward fin of the missile configurations in Figure 3.13 will start to interact with the bow shock. At $M_\infty = 6$ this will happen when $\alpha \geq 9°$ for the sphere-cylinder geometry and at $\alpha \geq 7°$ for the sphere-cone-cylinder geometry. At these higher angles of attack it is the shock-induced heating, the "blow-torch-effect" described by Edney (Ref. 71), that is of over-riding concern rather than the aerodynamic effects. It would be highly advisable to design the missile such that this often catastrophic shock-induced heating is avoided. This can be accomplished by careful design. It would be more difficult to do anything about

shock-induced heating on forward canard surfaces. The only recourse designwise will then probably be to sweep the leading edge back until the shock-induced heating predicted by Edney (Ref. 71) becomes tolerable.

3.2 INVISCID TWO-DIMENSIONAL FLOW

3.2.1 Sharp Leading Edge

At hypersonic speeds the unsteady aerodynamics of an airfoil with sharp leading edge is often given with satisfactory accuracy by the simple piston theory. When the piston velocity is so small that no shocks are generated the pressure on an infinitely thin airfoil is given by the "simple wave" equation (Ref. 72).

$$\frac{p}{p_\infty} = \left(1 + \frac{\gamma - 1}{2} \frac{W}{a_\infty}\right)^{\frac{2\gamma}{\gamma - 1}} \tag{3.20}$$

which in expanded form becomes

$$\frac{p}{p_\infty} = 1 + \gamma \frac{W}{a_\infty} + \frac{\gamma(\gamma + 1)}{4} \left(\frac{W}{a_\infty}\right)^2 + \frac{\gamma(\gamma + 1)}{12} \left(\frac{W}{a_\infty}\right)^3 + \ldots \tag{3.21}$$

Piston theory, like the pure Newtonian theory, considers only the local instantaneous flow conditions. Thus, both theories are of quasi-steady nature and can be compared in regard to accuracy using static conditons. With υ denoting the surface inclination to the free stream, W/a_∞ is

$$W/a_\infty = M_\infty \sin \upsilon \cos \upsilon \tag{3.22}$$

For the small disturbance assumption on which the piston theory is based, the angle υ is small[#] and

$$W/a_\infty = K = M_\infty \upsilon$$

With $C_p = 2(p - p_\infty)/\gamma M_\infty^2 p_\infty$ Eq. (3.21) together with Eq. (3.22) gives

$$\left(\frac{C_p}{\upsilon^2}\right)_{PT} = \frac{2}{K}\left[1 + \frac{\gamma+1}{4}K + \frac{\gamma+1}{12}K^2\right] \tag{3.24}$$

As $C_p/\upsilon^2 = 2$ according to pure Newtonian theory, Eq. (3.24) indicates that piston theory and Newtonian theory should give very different results depending upon the Mach number (and flow deflection angle). Figure 3.15 shows that the differences indeed are large. This is puzzling in view of the relatively close agreement between the two theories found by Yates and Bennet (Ref. 76) in their hypersonic flutter calculations. The reason for this will soon become evident.

The static pressure ratio through a "tangent wedge" compression or expansion is (See Refs. 41 and 77).[##]

$$\left(\frac{p}{p_\infty}\right)_{TW} = \begin{cases} 0 & ;\quad K < -\frac{2}{\gamma-1} \\[2ex] \left(1 + \frac{\gamma-1}{2}K\right)^{\frac{2\gamma}{\gamma+1}} & ;\quad -\frac{2}{\gamma-1} < K < 0 \\[2ex] 1 + \gamma K\left[\frac{\gamma+1}{4}K + \sqrt{1 + \left(\frac{\gamma+1}{4}K\right)^2}\right] & ;\quad K \geq 0 \end{cases} \tag{3.25}$$

[#]The thickness effects which are present in supersonic flow (Ref. 73) disappear already at $M_\infty > 2$ (Refs. 74 and 75).

[##]The expression for $K > 0$ is equal to the so-called strong shock piston theory when $K > 1$ (Ref. 78).

The pressure ratios given by piston theory and Newtonian theory are

$$\left(\frac{p}{p_\infty}\right)_{PT} = 1 + \gamma K \left[1 + \frac{\gamma + 1}{4} K + \frac{\gamma + 1}{12} K^2\right] \quad ; \quad -1 \leq K \leq 1 \qquad (3.26)$$

$$\left(\frac{p}{p_\infty}\right)_N = 1 + \begin{cases} 0 & ; \quad K < 0 \\ \\ \gamma K^2 & ; \quad K \leq 0 \end{cases} \qquad (3.27)$$

The pressure ratios given by Eqs. (3.25) through (3.27) are shown in Figure 3.16 for air ($\gamma = 1.4$). One can see that there is a substantial K-range for which the slopes $\partial (p/p_\infty)/\partial K$ given by Eqs. (3.25) - (3.27) will not differ much, indicating that stability derivatives and flutter boundaries would not be very different either, in agreement with the results obtained by Yates and Bennet (Ref. 76). Figure 3.16 also shows that Newtonian and tangent wedge pressure ratios approach different limits for large Mach numbers ($M_\infty \to \infty$). This can be seen directly from Eq. 3.25 which gives

$$\lim_{K \to \infty} \left(\frac{p}{p_\infty}\right)_{TW} = 1 + \frac{\gamma(\gamma + 1)}{2} K^2 \qquad (3.28)$$

This agrees with the Newtonian value $1 + \gamma K^2$, given by Eq. (3.27), only for $\gamma = 1$. In order for the Newtonian theory to give the "correct" limit also for other γ-values, the following "gamma-correction" has to be made.

$$\left(\frac{p}{p_\infty}\right)_{\gamma N} = 1 + \frac{\gamma(\gamma + 1)}{2} K^2 \qquad (3.29)\#$$

#This corresponds to the value $C_{p_s} = \gamma + 1$ used in Ref. 76 .

3-13

For stability and flutter considerations the pressure derivatives are more interesting. They are

$$
\left(\frac{\partial (p/p_\infty)}{\partial K}\right)_{TW} = \begin{cases} 0 & ;\ K \le -\dfrac{2}{\gamma-1} \\[3mm] \gamma\left(1 + \dfrac{\gamma-1}{2}K\right)^{\frac{\gamma+1}{\gamma-1}} & ;\ -\dfrac{2}{\gamma-1} < K < 0 \\[5mm] \gamma\left[\dfrac{\gamma+1}{2}K + \dfrac{1 + 2\left(\dfrac{\gamma+1}{4}K\right)^2}{\sqrt{1 + \left(\dfrac{\gamma+1}{4}K\right)^2}}\right] & ;\ K \ge 0 \end{cases} \tag{3.30}
$$

$$
\left(\frac{\partial (p/p_\infty)}{\partial K}\right)_{PT} = \gamma\left[1 + \frac{\gamma+1}{2}K + \frac{\gamma+1}{4}K^2\right] \qquad ;\ -1 \le K \le 1 \tag{3.31}
$$

$$
\left(\frac{\partial (p/p_\infty)}{\partial K}\right)_{\gamma N} = \begin{cases} 0 & ;\ K < 0 \\[3mm] \gamma(\gamma+1)K & ;\ K \ge 0 \end{cases} \tag{3.32}
$$

Figure 3.17 shows the derivatives given by Eqs. (3.30) through (3.32) for $\gamma = 1.4$. It appears that piston theory can be used for $-1 < K < 1$ and "gamma-corrected" Newtonian theory for $K > 2$. The hypersonic similarity results above can be extended down to (low) supersonic Mach numbers by substituting the Prandtl-factor $\sqrt{M_\infty^2 - 1}$ for M_∞ in the definition of K in Eq. (3.23) (Refs. 41 and 79). Eq. (3.31) shows that for $\gamma = 1.4$ the quadratic term (cubic in Eq. (3.26)) increases the linear slope (obtained at $K = 0$) with 60 percent at the limit ($K = \pm 1$) for the piston theory. Thus, as Lighthill pointed out (Ref. 72), it is important to include this last term of the piston theory, and the so called third order piston theory should be used. However, if the piston theory is used only to describe the unsteady perturbation from the steady local flow condition, one needs only the linear term, as long as the unsteady perturbation is small, e.g., for $(\dot\theta c/U_\infty)^2 \ll 1$ (see Ref. 76).

For a rigid airfoil describing oscillations of low reduced frequency, $(c\omega/U_\infty)^2 \ll 1$, the hypersonic similarity parameter can be written

$$K = M_\infty V_\perp /U \qquad (3.33)$$

where from Figure 3.18 a $V_\perp /U$ is defined as follows for lower and upper surfaces.

$$\left.\left(\frac{V_\perp}{U}\right)\right._L = \sin(\upsilon_L + \alpha_0 + \theta) + \frac{(x - x_{CG} + y_L \tan \upsilon_L)\, q}{U} \cos \upsilon_L$$

$$\left.\left(\frac{V_\perp}{U}\right)\right._U = \sin(\upsilon_U - \alpha_0 - \theta) - \frac{(x - x_{CG} + y_U \tan \upsilon_U)\, q}{U} \cos \upsilon_U \qquad (3.34)$$

$$\upsilon = \tan^{-1}(\partial y/\partial x)$$

θ is the perturbation in pitch around the trim angle of attack α_0 . For

$\alpha_0 = \theta = q = 0$ this definition of K agrees with that given earlier in Eq. (3.23).

The surface pressure coefficient is determined as follows:

$$
C_p = \begin{cases}
0 & ; K < -\dfrac{2}{\gamma - 1} \\[2em]
\dfrac{2}{\gamma M_\infty^2}\left[(1 + \dfrac{\gamma - 1}{2} K)^{\frac{2\gamma}{\gamma - 1}} - 1\right] & ; -\dfrac{2}{\gamma - 1} < K < 0 \\[2em]
\dfrac{2K}{M_\infty^2}\left[\dfrac{\gamma + 1}{4} K + \sqrt{1 + (\dfrac{\gamma + 1}{4} K)^2}\right] & ; K \geq 0
\end{cases}
\qquad (3.35)
$$

3-15

In the case of the elastically deforming airfoil, Eq (3.34) becomes

$$\left(\frac{V_\perp}{U}\right)_L = \sin\left(\upsilon_L + \alpha_o + \frac{\partial h}{\partial x}\right) + \frac{1}{U}\frac{\partial h}{\partial t}\cos\upsilon_L$$

$$\left(\frac{V_\perp}{U}\right)_U = \sin\left(\upsilon_U - \alpha_o - \frac{\partial h}{\partial x}\right) - \frac{1}{U}\frac{\partial h}{\partial t}\cos\upsilon_U$$

(3.36)

h is the centerline displacement normal to the rigid wing chord (see Figure 3.18b). In the aeroelastic analysis to be discussed later the deflection h is the sum of the deformations in a large number of elastic degrees of freedom. A special case which has been treated extensively is the so called binary flutter in which the wing is deforming in bending and torsion only; i.e., the airfoil section is undeformed (see Figure 3.18c). For this case Eq. (3.36) becomes

$$\left(\frac{V_\perp}{U}\right)_L = \sin\left(\upsilon_L + \alpha_o + \theta\right)$$

$$+ \frac{x - x_{CG} + y_L \tan\upsilon_L}{U}\frac{\partial\theta}{\partial t} + \frac{1}{U}\frac{\partial h_{CG}}{\partial t}\cos\upsilon_L$$

$$\left(\frac{V_\perp}{U}\right)_U = \sin\left(\upsilon_U - \alpha_o - \theta\right)$$

$$+ \frac{x - x_{CG} + y_U \tan\upsilon_U}{U}\frac{\partial\theta}{\partial t} + \frac{1}{U}\frac{\partial h_{CG}}{\partial t}\cos\upsilon_U$$

(3.37)

h_{CG} is the bending deformation of the airfoil elastic axis (see Figure 3.18c).

The chordwise load distribution is in coefficient form

$$\partial c_N/\partial\xi = \left(c_P\right)_L - \left(c_P\right)_U$$

(3.38)

3-16

At $\alpha_0 = 0$ Eqs. (3.33) - (3.38) define the following derivatives for a symmetric, sharp wedge ($\upsilon_L = \upsilon_U = \theta_w$)

$$\partial c_{N\theta}/\partial \xi = 2 M_\infty C_{p_K} \cos \theta_w \qquad (3.39)$$

$$\partial c_{Nq}/\partial \xi = 2 M_\infty C_{p_K} \left[\xi(1 + \tan^2 \theta_w) - \xi_{CG} \right] \cos \theta_w \qquad (3.40)$$

where C_{pK}, obtained from Eq. (3.30), is

$$C_{pK} = \begin{cases} 0 & ; \quad K < -\dfrac{2}{\gamma - 1} \\[4mm] \dfrac{2}{M_\infty^2} \left(1 + \dfrac{\gamma - 1}{2} K \right)^{\frac{\gamma + 1}{\gamma - 1}} & ; \quad -\dfrac{2}{\gamma - 1} < K < 0 \quad (3.41) \\[5mm] \dfrac{2}{M_\infty^2} \left[\dfrac{\gamma - 1}{2} K + \dfrac{1 + 2\left(\dfrac{\gamma + 1}{4} K\right)^2}{\sqrt{1 + \left(\dfrac{\gamma + 1}{4} K\right)^2}} \right] & ; \quad K \geq 0 \end{cases}$$

For a thin wedge ($\tan^2 \theta_w \ll 1$ and $\cos \theta_w \approx 1$) the following stability derivatives are obtained at $\alpha_0 = 0$

$$\left. \begin{aligned} c_{n\theta} &= 2 M_\infty C_{pK} \\[3mm] c_{m\theta} &= -c_{n\theta} \left(\tfrac{1}{2} - \xi_{CG} \right) \\[3mm] c_{mq} &= -c_{n\theta} \left[\left(\tfrac{1}{2} - \xi_{CG} \right)^2 + \tfrac{1}{12} \right] \end{aligned} \right\} \qquad (3.42)$$

where C_{pK} is given by Eq. (3.41) with $K = M_\infty \theta_w$ (or $K = \theta_w \sqrt{M_\infty^2 - 1}$ for low supersonic Mach numbers).

For a double-wedge, diamond airfoil shape, the result at $\alpha_o = 0$ is

$$
\left.
\begin{aligned}
c_{n\theta} &= (c_{n\theta})_F + (c_{n\theta})_A \\[1em]
(c_{n\theta})_F &= M_\infty C_{pK} \\[1em]
(c_{n\theta})_A &= M_\infty C_{pK-} \\[1em]
c_{m\theta} &= -(c_{n\theta})_F \left(\frac{1}{4} - \xi_{CG}\right) - (c_{n\theta})_A \left(\frac{3}{4} - \xi_{CG}\right) \\[1em]
c_{mq} &= -(c_{n\theta})_F \left|\left(\frac{1}{4} - \xi_{CG}\right)^2 + \frac{1}{48}\right| - (c_{n\theta})_A \left|\left(\frac{3}{4} - \xi_{CG}\right)^2 + \frac{1}{48}\right|
\end{aligned}
\right\} \tag{3.43}
$$

where C_{pK-} is obtained from Eq. (3.41) with $K = -M_\infty \theta_w$ (or $-\theta_w \sqrt{M_\infty^2 - 1}$)

Equations (3.41) - (3.43) show that $M_\infty c_{n\theta}$, $M_\infty c_{m\theta}$ and $M_\infty c_{mq}$ are functions of K only. This is illustrated in Figure 3.19 for single and double wedges Figures 3.19a and 3.19b, respectively). As expected the tangent wedge values are well represented by third order piston theory for low K - values, $K < 1$, and by the gamma-corrected Newtonian theory for high K - values, $K > 1$. Orlik-Rückemann's experimental pitch damping data for a double wedge (Ref. 80) fall well above the inviscid prediction (see Figure 3.19b). The Helium data point ($\gamma = 5/3$) has been corrected for γ-effects using Eq. (3.43). One feels inclined to agree with the authors that the observed 50 percent overshoot of inviscid predictions cannot be explained by pure boundary layer effects (Refs. 64 and 65), but that some other effects, e.g., shock wave-boundary layer interaction at the trailing edge, must have caused it. One such mechanism has been demonstrated by Hulcher and Behrens (Ref. 81). They showed that at $\alpha = 15°$ the leeside laminar flow on a flat plate at $M_\infty = 6$ was separated

from 70 percent chord to the trailing edge due to the wake recompression (shock). Thus, one can also expect the 9° double wedge to have a trailing edge separation (at α = 0), especially in view of the higher Mach number. It has, in fact, been shown that a biconvex airfoil experiences laminar separated flow on the leeside aft half chord (Ref. 82). The loss of leeside expansion due to separation will generate a negative, statically destabilizing tail load. The dynamic effect will be stabilizing due to the convective time lag effects associated with this wake-induced separation (Refs. 83-85), and could easily cause the observed 50 percent increased damping. The method presented in Reference 82 for prediction of the separation induced pressure increase at supersonic Mach numbers can possibly be applied also in the region of present interest, $3 \leq M_\infty \leq 6$. Thus, with the information contained in References 82 through 85 as a basis, analytic methods could be developed for prediction of the separated flow effect on the unsteady aerodynamic characteristics of double-wedge or lenticular shape airfoils. This is, however, beyond the scope of the present study.

For a single wedge no trailing edge separation is present and the deviations between inviscid predictions and preliminary experimental results (Ref. 86) seem to be accounted for by the attached flow boundary layer effect described by Orlik-Rückemann (see Fig. 3.20). However, one should be careful not to interpret the results as proof positive because of the inherent difficulties in performing a two-dimensional dynamic test, as the authors of Reference 86 point out. The peculiar frequency effects observed in the test could well have been caused by wind tunnel interference as there is no known reason for the effects to be present in the free flight case. Possibly the only way to obtain the desired strip-data (two-dimensional airfoil data) would be to test a half model of the missile-fin configuration varying the aspect ratio of the fin (Ref. 87). In such a test the effect of missile nose bluntness on the unsteady fin aerodynamics could also be investigated to check out the prediction techniques described in Section 3.1.

3.2.2 Bluntness Induced Effects

The blast wave pressure in two-dimensional flow, as it would be measured on a flat plate with blunted leading edge (the 2-D equivalent to Eq. (3.9)), is as follows (Refs. 50-53).[#]

$$\left(\frac{p_o(0)}{p_\infty}\right)_{2D} = 0.85 \frac{k'(\gamma)}{\Lambda'} + 0.56$$

$$\Lambda' = c_{dN}^{-2/3} M_\infty^{-2} \left(\frac{x}{d'_N} - \frac{x_N}{d'_N}\right)^{2/3}$$

$$k'(\gamma) = 0.121 \text{ for } \gamma = 1.4$$

(3.44) [##]

Thus, the following two-dimensional embedded-Newtonian formulation is obtained for the aerodynamic pressure coefficient on a surface "embedded" in the "entropy wake" at hypersonic speeds ($M_\infty \to \infty$)

$$\left(C_P\right)_{2D} = \frac{0.147 \, c_{dN}^{2/3}}{\left(\frac{x}{d'_N} - \frac{x_N}{d'_N}\right)^{2/3}} + C_{P\,NEWT} \, f^*_{2D} \left(\chi^*_{2D}\right)$$

(3.45)

[#]Subscript 2D or a prime superscript is used to indicate two-dimensional quantities equivalent to those used earlier in the three-dimensional case.

[##]The pressure given by second order blast wave theory is (Ref. 52)

$$p_o(0)/p_\infty = k'(\gamma)/\Lambda' + 0.56$$

That is, the same 85 percent "efficienty factor" measured by Kuehn for hemisphere-cylinders (Ref. 51) is applied here. No attempt is made to modify the constant 0.56 as it is unimportant for the determination of aerodynamic force derivatives.

For $\alpha = 0$ the similarity parameter X^*_{2D} that correlates the pressures on a slender, blunted wedge is (see Chernyi, Ref. 53).

$$X^*_{2D} = X_{2D} \left(1 - \frac{x_N}{x}\right)$$

$$X_{2D} = \tan^3 \theta_w \ c_{dN}^{-1} \ \frac{x}{d'_N}$$

(3.47)

That is, the parameter X^*_{2D} at $\alpha \neq 0$, corresponding to the parameter X^* defined by Eq. (3.7) for the 3-D case, is

$$X^*_{2D} = \left(\frac{R}{d'_N} - \frac{1}{2}\right)^3 \bigg/ \left(\frac{R_{sh}}{d'_N}\right)^3_{2D}$$

(3.48)

Here d'_N is the thickness of the blunted leading edge and $(R_{sh}/d_N)_{2D}$ is defined as follows (Ref. 52)

$$\left(\frac{R_{sh}}{d_N}\right)_{2D} = K_{sh} \ c_{dN}^{1/3} \left(\frac{x - x_{sh}}{d'_N}\right)^{2/3}$$

(3.49)

It is assumed, now as before, that $x_{sh} = x_N$ and $K_{sh} = 1$[#]. For a slender wedge with (semi) cylindrical leading edge the results shown in Figure 3.21 are obtained, which give $f^*_{2D} = 1$. That is, the pressure on a wedge with semi-cylindrical leading

---

[#]Using another value would give a different definition of f^*_{2D}. It would, however, give the same C_p-value, Eq. (3.45), because f^*_{2D} is defined as the difference between the surface pressure, computed by M O C (Ref. 57) and the blast wave pressure, given by Eg. (3.44).

edge bluntness is simply the sum of the blast wave pressure and the pressure measured on a sharp wedge.

$$(C_p)_{2D} = C_{po} + (C_p)_{SHARP}$$

$$C_{po} = \frac{0.147\ c_{dN}^{2/3}}{\left(\dfrac{x}{d'_N} - \dfrac{x_N}{d'_N}\right)}$$

$$\left.\right\} \quad (3.50)$$

$(C_p)_{SHARP}$ is given by Eq. (3.35)

That there is no velocity deficit effect on the wedge pressures, only on the cone pressures, is explained by the differences in flow fields. For the wedge all flow turning occurs at the shock, whereas substantial flow turning occurs downstream of the shock on the cone. For a slender blunted wedge ($\tan^2 \theta_w \ll 1$ and $\cos \theta_w \approx 1$) the derivatives corresponding to the sharp wedge derivatives given in Eq. (3.42) are

$$c_{n\theta} = (c_{n\theta})_M + (c_{n\theta})_N$$

$$(c_{n\theta})_M = 2 M_\infty C_{pK} (1 - \xi_o)$$

$$c_{m\theta} = (c_{n\theta})_M \left[\frac{1 + \xi_o}{2} - \xi_{CG}\right] - (c_{n\theta})_N (\xi_o - \xi_{CG})$$

$$c_{mq} = -(c_{n\theta})_M \left[\frac{1 + \xi_o}{2} - \xi_{CG}\right]^2 + \frac{1}{12} (1 - \xi_o)^2$$
$$- (c_{n\theta})_N (\xi_o - \xi_{CG})^2$$

$$\left.\right\} \quad (3.51)$$

for a (semi) cylindrical leading edge

$$(c_{n\theta})_N = 2 \xi_o c_{dN} = 2.4 \xi_o$$

$$\xi_o = \frac{d'_N}{d'_B} \Bigg/ \left[\left(1 - \frac{d'_N}{d'_B}\right) \cot \theta_w + \frac{d'_N}{d'_B}\right]$$

$$\left.\right\} \quad (3.52)$$

3-22

In Figure 3.22 these inviscid predictions, Eqs. (3.51) and (3.52), are compared with East's experimental data (Ref. 78). The static data seem to agree with predictions, considering the data scatter, whereas the dynamic experimental data do not. For completeness, sharp wedge data are also shown. East shows how the wedge shock caused substantial separation of the sidewall boundary layer, as would be expected (see Figure 3.23 and Ref. 88). It can be seen that for $\xi_{CG} = 0$ the side plate boundary layer separates well upstream of the wedge, and as much as 35 percent of the wedge surface lies within the influence of the sidewall shock according to East. For $\xi_{CG} = 1.0$ the corresponding value is 15 percent. Thus, the wall interference varies with ξ_{CG}. It will also be different for the sharp and blunted wedge. Already at low speeds, these sidewall effects cause dynamic simulation problems (Ref. 89), problems which will become even greater at hypersonic speeds with its complicated "corner-flow" (see Figure 3.24 and Refs. 27, 90, 91, and 92). Thus, the deviations between present predictions and East's experimental data could be caused by this side plate interference. East used experimental wedge data to obtain a dependence of the blast wave pressure, C_{po} in Eq. (3.50), on the "tangent wedge" angle. As the inclusion of this wedge slope dependence of C_{po} did not give any more significant effect of nose bluntness on the predicted stability derivatives than the present simpler formulation, no refinements of Eq. (3.50) are contemplated at this time. It should probably be pointed out that the viscous interaction effects, which will be discussed later, are negligible in East's test, mainly because of the relatively cool wall, $T_w/T_t = 0.33$.

Although East's data are somewhat difficult to use when checking two-dimensional theoretical estimates because of the large interference effects from the side plate boundary layer, they are very valuable in that they point out what the effect from the missile body boundary layer could be on the fin stability derivatives. If one wants to use all-movable fins with some margin of static stability one could end up with an axis position in the range $0.2 < \xi_{CG} < 0.4$; i.e., the very range in which East measured negative aerodynamic damping. Viscous crossflow affects on the missile body could possibly aggravate the situation. Thus, one will have to study this side wall effect further if one wants to design a finned, hypersonic missile. If one, instead of movable fins, decides to use flap controls, one will encounter other problems. Although the velocity deficit effect is absent for a blunted wedge, $f^*_{2D} = 1$ in Eq. (3.45), a deflected

flap downstream of a blunted leading edge will experience entropy-wake-induced non-uniform flow effects as illustrated by the curved flap shock on a lifting reentry vehicle (Refs. 93, 94, and Figure 3.23). At high angles of attack bow shock - flap shock interaction presents additional problems (Ref. 70).

3.3 VISCOUS FLOW EFFECTS

The boundary layer on the fins of a tactical missile operating in the speed range $3 \leq M_\infty \leq 6$ will vary from being completely laminar at the high Mach number - high altitude end of the operating range to being mainly turbulent at low Mach numbers and altitudes. That is, at some intermediate region of the operating range boundary layer transition will have a dominating influence on the aerothermodynamics of the fins. In regard to the boundary layer on the missile body transition will play a role throughout the whole operating range, and will significantly affect the unsteady aerodynamics (Refs. 24 and 25), effects that may become adverse if the missile tip has even a small amount of nose bluntness (Refs. 95 and 96).

As the characteristic time of the thermal response usually will be orders of magnitude larger than the periods of structural vibrations one can neglect any coupling between thermodynamic and elastic response. When considering the rigid body response thermodynamic coupling effects may not be negligible. However, this problem will not be addressed in the present study which only is concerned with the aero-thermo-elastic response of the missile fins. Thus, only the viscous effects on the unsteady aero-dynamics of the fins will be considered here.

3.3.1 Two-Dimensional Viscous Flow

Viscous flow effects in low density hypersonic flow have been widely investigated by both theoreticians and experimentalists. This is at least true in regard to static aerodynamics where the so-called viscid-inviscid interaction effects are well established (see Reference 97 for a summary of the present state of the art). The dynamic effects of this hypersonic viscid-inviscid interaction have received much less attention, the

only well known work being that by Orlik-Rückeman et al (Refs. 64, 65, 80, 86, and 98). In the present study a simplified approach is used, tailored to the particular flow conditions of interest for a tactical missile operating in the low hypersonic flow regime.

3.3.1.1 <u>Static Aerodynamics</u>. The boundary layer displacement surface will increase the local inviscid wedge angle θ_w by an amount $d\delta^*/dx$. Figure 3.19 shows how this will increase the normal force derivative.

The displacement thickness for a laminar boundary layer is (Ref. 41)

$$P_r = 1 \quad ; \quad \delta^* = \left[0.332 \, (\gamma - 1) + \frac{1.730}{M_e^2} \frac{T_w}{T_e} \right] \frac{x M_e^2 \sqrt{C^*}}{\sqrt{Re_x}} \tag{3.53a}$$

$$P_r = 0.725 \quad ; \quad \delta^* = \left[0.289 \, (\gamma - 1) + \frac{1.973}{M_e^2} \frac{T_w}{T_e} \right] \frac{x M_e^2 \sqrt{C^*}}{\sqrt{Re_x}} \tag{3.53b}$$

$C^* = 1$ for $T^* \le 200°R$ and $C^* = \dfrac{T^*}{T_t} \left(1 + \dfrac{\gamma - 1}{2} M_e^2 \right)^{-0.24}$ for reference

temperatures in the range $200°R < T^* < 1000°R$,
where $T^*/T_t = (1 + 3 \, T_w/T_t) / 6$ (Ref. 97)

Alternatively Eq. (3.53) can be written as follows:

$$P_r = 1 \quad ; \quad \delta^* = \left[(\gamma - 1) \left(0.865 \frac{T_w}{T_t} + 0.332 \right) + \frac{1.730}{M_e^2} \frac{T_w}{T_t} \right] \frac{x M_e^2 \sqrt{C^*}}{\sqrt{Re_x}} \tag{3.54a}$$

$$P_r = 0.725 \quad ; \quad \delta^* = \left[(\gamma - 1) \left(0.9685 \frac{T_w}{T_t} + 0.289 \right) \right.$$

$$\left. + \left(1.937 \frac{T_w}{T_t} - 0.207 \right) \frac{1}{M_e^2} \right] \frac{x M_e^2 \sqrt{C^*}}{\sqrt{Re_x}} \tag{3.54b}$$

For the isolated wall $T_w/T_t = \sqrt{P_r}$

The thickness slope is simply

$$\partial \delta^*/dx = \delta^*/2x \qquad (3.55)$$

The slope $\partial \delta^*/dx$ will be very small compared to the angular changes of the inviscid flow, at least in the present study, and the effect of $\partial \delta^*/dx$ can be simulated by a small wedge embedded in the flow aft of the bow shock. Thus, Eq. (3.26) can be used to give for $M_e^2 \gg 1$

$$\Delta p_v/p_e = \gamma K_v = \gamma M_e \, d\delta^*/dx \qquad (3.56)$$

Combining Eqs. (3.53) through (3.56) gives

$$\Delta p_v/p_e = \gamma K_v$$

$$K_v = M_e \, d\delta^*/dx = \bar{B}\bar{\chi}$$

$$\bar{B} = \bar{B}_1 + \bar{B}_2/M_e^2 \qquad (3.57)$$

$$\chi = M_e^3 \, \sqrt{C^*}/\sqrt{Re_x}$$

where $2\bar{B}$ can be identified with the bracket in the equations describing δ^*, Eqs. (3.53) and (3.54).

For $M_e^2 \gg 1$ Eq. (3.57) simplifies to

$$\Delta p_v/p_e = \gamma \bar{B}_1 \, \bar{\chi} \qquad (3.58)$$

Predictions of $p_v/p_e = 1 + \Delta p_v/p_e$ using Eq. (3.58) agree well with experimental wedge data for $M_\infty = 10$ (Ref. 97 and Figure 3.26). The agreement persists up to large

$\bar{X}$ -values (outside the range of interest for the present study). It should be pointed out, however, that when the wedge angle goes to zero, and all the flow change is of viscous nature, Eq. (3.58) no longer predicts the measured pressures. In this case viscid-inviscid coupling effects have to be included (see Refs. 41 and 97). However, on the finite chord airfoil of consideration in the present study, trailing edge and separated flow effects will often dominate when these higher order viscous effects should be considered; e.g., at $\alpha \neq 0$ for finite wedge angles $(\theta_w > 0)$. Eq. (3.57), or Eq. (3.58) for $M_e^2 \gg 1$, is especially convenient when using the local linearization approach in flutter analysis as was done by Yates and Bennet (Ref. 76). As the self-induced pressure does not change the boundary layer slope $d\delta^*/dx$ up to second order accuracy (Ref. 41), the viscous induced effect on the surface pressure derivative is solely a function of inviscid flow parameters. The following simple result is obtained.

$$
\frac{d(\Delta C_{pv})}{d\theta} = \frac{2}{M_\infty^2} \frac{d}{d\theta} \left[\frac{p_e}{p_\infty} \frac{\Delta p_v}{p_e} \right]
$$

$$
= \frac{2}{M_\infty^2} \frac{d(p_e/p_\infty)}{d\theta} \left[\frac{\Delta p_v}{p_e} + \frac{p_e}{p_\infty} \frac{\partial(\Delta p_v/p_e)}{\partial(p_e/p_\infty)} \right]
$$

$$
= \frac{dC_{pe}}{d\theta} \frac{\Delta p_v}{p_e} \left\{ 1 + \frac{p_e}{p_\infty} \frac{\partial \left| \log(\Delta p_v/p_e) \right|}{\partial(p_e/p_\infty)} \right\} \qquad (3.59)
$$

p_e/p_∞ is obtained from Eq. (3.25). The derivative $\partial \left|\log (\Delta p_v/p_e)\right| \Big/ \partial (p_e/p_\infty)$ is obtained from Eq. (3.57) using the oblique shock relations given in Ref. 58. The result is as follows:

$$\frac{\partial \left|\log (\Delta p_v/p_e)\right|}{\partial (p_e/p_\infty)} = \frac{\gamma}{(\Delta p_v/p_e)} \left[\bar{B}_1 \quad \frac{\partial \bar{\chi}}{(p_e/p_\infty)} + \bar{B}_2 \quad \frac{\partial \bar{\nu}}{\partial (p_e/p_\infty)} \right]$$

$$\frac{\partial \bar{\chi}}{\partial (p_e/p_\infty)} = \bar{\chi} \left\{ \frac{5}{4} \quad \frac{1}{M_e^2} \quad \frac{\partial (M_e^2)}{\partial (p_e/p_\infty)} + \frac{1}{4} \quad \frac{1}{(p_e/p_\infty)} \right.$$

$$\left. - \frac{3\gamma}{(\gamma + 1)^2} \quad \frac{1}{\left[\left(\frac{p_e}{p_\infty}\right) + \frac{\gamma - 1}{\gamma + 1}\right] \left[1 + \frac{\gamma - 1}{\gamma + 2}\left(\frac{p_e}{p_\infty}\right)\right]} \right\}$$

$$\frac{\partial \bar{\nu}}{\partial (p_e/p_\infty)} = \bar{\nu} \left\{ \frac{1}{4} \quad \frac{1}{M_e^2} \quad \frac{\partial (M_e^2)}{\partial (p_e/p_\infty)} + \frac{1}{4} \quad \frac{1}{(p_e/p_\infty)} \right.$$

$$\left. - \frac{3\gamma}{(\gamma + 1)^2} \quad \frac{1}{\left[\left(\frac{p_e}{p_\infty}\right) + \frac{\gamma - 1}{\gamma + 1}\right] \left[1 + \frac{\gamma - 1}{\gamma + 1}\left(\frac{p_e}{p_\infty}\right)\right]} \right\} \qquad (3.60)$$

$$\frac{\partial (M_e^2)}{\partial (p_e/p_\infty)} = - \frac{2}{\gamma + 1} \left(1 + \frac{\gamma - 1}{2} M_\infty^2\right) \frac{\left(\frac{p_e}{p_\infty}\right)^2 + 2 \frac{\gamma - 1}{\gamma + 1}\left(\frac{p_e}{p_\infty}\right) + 1}{\left(\frac{p_e}{p_\infty}\right)^2 \left[1 + \frac{\gamma - 1}{\gamma + 1}\left(\frac{p_e}{p_\infty}\right)\right]^2}$$

$$\bar{\nu} = \bar{\chi}/M_e^2$$

Combining (Eqs. (3.59) and (3.60) gives

$$\frac{d(\Delta C_{pv})/d\theta}{dC_{pe}/d\theta} = \frac{\Delta p_v}{p_e}\left\{\frac{5}{4} - \left(\frac{5}{4} - \frac{\bar{B}_2}{\bar{B} M_e^2}\right) G_1 - G_2\right\}$$

$$G_1 = \frac{1 + \frac{\gamma-1}{2} M_\infty^2}{\frac{\gamma+1}{2} M_e^2} \cdot \frac{\left(\frac{p_e}{p_\infty}\right)^2 + 2 \frac{\gamma-1}{\gamma+1}\left(\frac{p_e}{p_\infty}\right) + 1}{\left(\frac{p_e}{p_\infty}\right)\left[1 + \frac{\gamma-1}{\gamma+1}\left(\frac{p_e}{p_\infty}\right)\right]^2}$$

$$G_2 = \frac{3\gamma}{(\gamma+1)^2} \cdot \frac{\left(\frac{p_e}{p_\infty}\right)}{\left[\left(\frac{p_e}{p_\infty}\right) + \frac{\gamma-1}{\gamma+1}\right]\left[1 + \frac{\gamma-1}{\gamma+1}\left(\frac{p_e}{p_\infty}\right)\right]}$$

$$M_e^2 = \frac{M_\infty^2\left[(\gamma+1)\left(\frac{p_e}{p_\infty}\right) + (\gamma-1)\right] - 2\left[\left(\frac{p_e}{p_\infty}\right)^2 - 1\right]}{\left(\frac{p_e}{p_\infty}\right)(\gamma+1)\left[1 + \frac{\gamma-1}{\gamma+1}\left(\frac{p_e}{p_\infty}\right)\right]}$$

$$\hspace{12cm}(3.61)$$

$\Delta p_v/p_e$ and $\bar{B} = \bar{B}_1 + \bar{B}_2/M_e^2$ are defined in Eq. (3.57), and p_e/p_∞ is given by Eq. (3.25), substituting K with K $\sqrt{1 - M_\infty^2}$ at lower supersonic Mach numbers (Ref. 79). The relative change of inviscid aerodynamic derivatives due to viscous first order perturbation effects can be obtained for arbitrary thin airfoils using Eq. (3.61). For a wedge the result becomes particularly simple, as M_e = constant and $\bar{X} = \bar{X}_{TE} \, \xi^{-1/2}$. Integration of Eq. (3.61) gives then for upper and lower surfaces the following relationship.

$$\frac{(\Delta C_{n\theta})_v}{(Cp\theta)_e} = 2\left[\frac{d(\Delta C_{pv})/d\theta}{d(C_{pe})/d\theta}\right]_{TE}$$

$$\hspace{12cm}(3.62)$$

$$\frac{(\Delta C_{m\theta})_v}{(\Delta C_{n\theta})_v} = -\left(\frac{1}{3} - \xi_{CG}\right)$$

Noticing that $(C_{p\theta})_e = (c_{n\theta})_i$, Eq. (3.62) gives the viscous induced increment of upper and lower surface inviscid aerodynamic derivatives. At $\alpha = 0$ it gives the total result for both surfaces. That is

$$\frac{(\Delta C_{n\theta})_v}{(C_{n\theta})_e} = 2 \left[\frac{d\,(\Delta C_{pv})/d\theta}{d(C_{pe})/d\theta}\right]_{TE} \tag{3.63}$$

Within the linear α-range Eq. (3.63) also expresses the ratio $\Delta c_{nv}/c_{ni}$. In Figures 3.27 and 3.28 predictions through Eq. (3.63) are compared with available experimental data (Refs. 99 and 100). The good agreement for the 5° wedge (Fig. 3.27) was expected, but the good agreement with the flat plate data (Fig. 3.28) was a surprise in view of the failure of Eq. (3.58) to predict Sliski's flat plate data (Ref. 97). The experimental data were underpredicted by 30 percent. This may also be the lift loss on a finite chord flat plate due to the trailing edge effect discussed by the authors of Ref. 100. (See inset in Figure 3.28). Thus, fortuitously Eq. (3.63) will give the correct viscous effect on the lift even for the limiting case when $\theta_w \to 0$. However, the moment contribution will not be predicted as well, and neither will the viscous effect on unsteady aerodynamics. However, as was discussed before, a very accurate prediction of the pure viscous interaction for zero inviscid flow inclination to the surface is not essential for prediction of the airfoil aerodynamics. Judging by the good agreement between predicted and measured viscous influence on the moment of the 5° wedge, it does not seem to experience much of this trailing edge effect (see Figure 3.27). This is probably to a large extent due to the modest value ($X_{TE} = 1.3$) of the hypersonic viscous similarity parameter. As this parameter X_{TE} is increased, the strong interaction region near the leading edge and the near wake effect at the trailing edge both become more important. For a finite base height, e.g., for $\theta_w > 0$, the wake recompression effects are fed upstream through the near wake adding complexity to the trailing edge effect (Refs. 84 and 85). For the X_{TE}-range of interest in the present study these effects are, however, unlikely to become important. The viscous effects are likely to be small, as is illustrated by Figure 3.29, at least for steady state flight conditions, $T_w/T_e = 1.0$. When the tactical missile is maneuvering, it may be possible for the fins to reach soak temperatures as high as those expected on the straight wing space shuttle during

reentry; i.e., $T_W/T_e = 2.5$ (Ref. 101). It is interesting to note that for $M_\infty = 6$ this condition comes close to the adiabatic wall case existing in most wind tunnel tests. Even in this case, however, the viscous induced increment of the inviscid lift will not exceed 20 percent. Consequently, inviscid aerodynamic characteristics have been used in the present aeroelastic analysis.

3.3.1.2 Unsteady Aerodynamics. The change of effective airfoil geometry produced by the boundary layer displacement surface and the corresponding effect on static stability derivatives were considered in the previous section. There is, of course, a similar effect on the dynamic stability derivative. Equation (3.61) defines the following strip load derivative distribution.

$$\frac{d(\Delta C_{n\theta})_v}{d\xi} = \left[\frac{d(\Delta C_{pv})}{d\theta}\right]_L - \left[\frac{d(\Delta C_{pv})}{d\theta}\right]_U \tag{3.64}$$

And the running load increment due to viscous wedge thickening is

$$\frac{d(\Delta c_n)_v}{d\xi} = \frac{d(\Delta c_{n\theta})_v}{d\xi} \frac{V_\perp}{U_\infty} \tag{3.65}$$

For a wedge describing rigid body oscillations in pitch around $x = x_{CG}$ Eqs.(3.34), (3.61), (3.64) and (3.65) give for $\alpha_o = 0$

$$\frac{d(\Delta c_{nq})_v}{d\xi} = 2 \left[\frac{d(\Delta C_{pv})}{d\theta}\right]_{TE} \xi^{-1/2} (\xi - \xi_{CG}) \tag{3.66}$$

Integrating Eq. (3.66) and its moment contribution gives

$$\Delta(c_{nq})_v = -\Delta(c_{m\theta})_v = \Delta(c_{n\theta})_v \left(\frac{1}{3} - \xi_{CG}\right) \tag{3.67}$$

$$\Delta(c_{mq})_v = -\Delta(c_{n\theta})_v \left[\frac{4}{45} + \left(\frac{1}{3} - \xi_{CG}\right)^2\right] \tag{3.68}$$

3-31

The ratio $\Delta(c_{N\theta})_v/(c_{n\theta})_i$ is given by Eq. (3.61), as was discussed earlier (See Figures 3.27 - 3.29). Equation (3.68) shows that the viscous induced thickening of the wedge increases the aerodynamic damping, the effect being minimum for $\xi_{CG} = 1/3$. Orlik-Rückeman has shown that in addition to this static interaction, it is important to consider the "dynamic interaction" resulting from the fact that the boundary layer displacement thickness does not remain constant during the oscillation (Ref. 98). The boundary layer becomes thinner on the windward side. On the oscillating airfoil this boundary layer "cushioning" decreases the "piston effectiveness" by changing the inviscid velocity ratio $(V_\perp/U_e)_i$ by an amount $(d\delta^*/dt)/U_e$. This local reaction can be assumed to occur instantaneously for the structural and rigid body frequencies of practical interest. At large χ_{TE} one may have to consider downstream effects of changes occurring at an earlier time instant in the strong interaction region near the leading edge, as well as upstream effects of changes in the near wake recirculatory flow (also occurring at an earlier time instant). These effects are not considered in the present analysis.

For most applications it can be assumed that the missile velocity changes slowly compared to structural and rigid body frequencies. Thus, the time derivative $d\delta^*/dt$ is solely the result of the perturbations of the relative piston velocity V $V_\perp/U_\infty$ defined by Eqs. (3.34), (3.36), or (3.37). That is

$$\frac{d\delta^*}{dt} = \frac{\partial\delta^*}{\partial\theta} \frac{d}{dt}\left(\frac{V_\perp}{U_\infty}\right) \tag{3.69}$$

Whereas the boundary layer slope, $d\delta^*/dx$, is relatively insensitive to the ambient pressure gradient, the boundary layer thickness itself is not, but becomes thinner for increasing pressures (Ref. 41). Bertram et al (Ref. 102) have shown that this fact can be represented by assuming the boundary layer thickness to be inversely proportional to $\sqrt{p_v/p_\infty}$. Consistent with the perturbation approach used here p_v/p_∞ is represented by the inviscid pressure ratio p_e/p_∞. Thus, Eq. (3.55) is modified as follows:

$$\frac{\delta^*}{2x} = \left(\frac{d\delta^*}{dx}\right)_{FP} \Bigg/ \sqrt{\frac{p_e}{p_\infty}} \tag{3.55a}$$

When $p_e/p_\infty \to 1$ the flat plate value, Eq. (3.55), is recovered.

From Eqs. (3.55a), (3.57), and (3.60) is obtained

$$\frac{1}{x} \frac{d\delta^*}{d\theta} = - \frac{dC_{pe}}{d\theta} \frac{\Delta p_v}{p_e} \left(\frac{p_e}{p_\infty}\right)^{-3/2} \frac{M_\infty^2}{M_e}$$

$$\left\{ \frac{3}{4} - \frac{\overline{B}_2}{\overline{B}M_e^2} G_1 + G_2 + \frac{1}{4} \right\}$$

(3.70)

The change of piston effectiveness δ^*/U_e can be written

$$\frac{\dot{\delta}^*}{U_e} = \frac{\dot{\delta}^*}{U_\infty} \frac{U_\infty}{U_e} = \frac{\dot{\theta} c}{U_\infty} \xi \frac{M_\infty}{M_e} \left[\frac{1 + \frac{\gamma - 1}{2} M_e^2}{1 + \frac{\gamma - 1}{2} M_\infty^2}\right]^{1/2} \left(\frac{1}{x} \frac{d\delta^*}{d\theta}\right)$$

(3.71)

Again, using the embedded formulation, Eq. (3.56), gives

$$\Delta p_v (\dot{\delta}^*)/p_e = \gamma M_e \dot{\delta}^*/U_e$$

(3.72)

Combining Eqs. (3.70, (3.71), and (3.72) gives finally

$$\frac{d \Delta C_{pv} (\dot{\delta}^*)}{d \left(\frac{c\dot{\theta}}{U_\infty}\right)} = - 2 \xi \frac{\Delta p_v}{p_e} \left(\frac{p_e}{p_\infty}\right)^{-1/2} \frac{M_\infty}{M_e} \left[\frac{1 + \frac{\gamma - 1}{2} M_e^2}{1 + \frac{\gamma - 1}{2} M_\infty^2}\right]^{1/2}$$

$$\left\{ \frac{3}{4} - \frac{\overline{B}_2}{\overline{B}M_e^2} G_1 + G_2 + \frac{1}{4} \right\}$$

(3.73)

In general M_e and $\Delta p_v/p_e$ are functions of ξ. However, for a wedge Eq. (3.73) simplifies to

$$\frac{d\left[\Delta C_{pv} (\dot{\delta}^*)\right]}{d\left(\frac{c\dot{\theta}}{U_\infty}\right)} = \frac{d\left[\Delta C_{pv}(\dot{\delta}^*)\right]_{TE}}{d\left(\frac{c\dot{\theta}}{U_\infty}\right)} \xi^{1/2}$$

(3.74)

Integrating Eq. (3.74) gives the following result for pitch oscillations around $x = x_{CG}$ at $\alpha = 0$.

$$\left(\Delta c_{n\dot\theta}\right)_v = \frac{d\left[\Delta c_{nv}(\dot\delta^*)\right]}{d\left(\frac{c\dot\theta}{U_\infty}\right)} = \frac{4}{3}\frac{d\left[\Delta C_p(\dot\delta^*)\right]_{TE}}{d\left(\frac{c\dot\theta}{U_\infty}\right)}$$

$$\left(\Delta c_{m\dot\theta}\right)_v = -\left(\Delta c_{n\dot\theta}\right)_v\left(\frac{3}{5} - \xi_{CG}\right)$$

$$\frac{d\left[\Delta C_p(\dot\delta^*)\right]_{TE}}{d\left(\frac{c\dot\theta}{U_\infty}\right)} = -\left(\frac{\Delta p_v}{p_e}\right)_{TE}\frac{\left(c_{n\theta}\right)_i}{\sqrt{p_e/p_\infty}}\frac{M_\infty}{M_e}\sqrt{\frac{1 + \frac{\gamma-1}{2}M_e^2}{1 + \frac{\gamma-1}{2}M_\infty^2}}$$

$$\left\{\left(\frac{}{4} - \frac{\bar B_2}{\bar B M_e^2}\right)G_1 + G_2 + \frac{1}{4}\right\}$$

(3.75)

Combining Eqs. (3.61), (3.62), (3.63), (3.68), and (3.75) with Eq. (3.42) gives the damping ratios

$$\frac{\left(\Delta c_{mq}\right)_v}{c_{mq}}\bigg/\frac{\left(\Delta c_{n\theta}\right)_v}{\left(c_{n\theta}\right)_i} = \frac{\left(\frac{1}{3} - \xi_{CG}\right)^2 + \frac{4}{45}}{\left(\frac{1}{2} - \xi_{CG}\right)^2 + \frac{1}{12}}$$

(3.76)

$$\frac{\left(\Delta c_{m\dot\theta}\right)_v}{c_{mq}}\bigg/\frac{\left(\Delta c_{n\theta}\right)_v}{\left(c_{n\theta}\right)_i} = -G_e\frac{\frac{3}{5} - \xi_{CG}}{\left(\frac{1}{2} - \xi_{CG}\right)^2 + \frac{1}{12}}$$

$$G_e = \frac{2}{3}\left(\frac{p_e}{p_\infty}\right)^{-1/2}\frac{M_\infty}{M_e}\left(\frac{1 + \frac{\gamma-1}{2}M_e^2}{1 + \frac{\gamma-1}{2}M_\infty^2}\right)^{1/2}\frac{\left(\frac{3}{4} - \frac{\bar B_2}{\bar B M_e^2}\right)G_1 + G_2 + \frac{1}{4}}{\frac{5}{4} - \left(\frac{5}{4} - \frac{\bar B_2}{\bar B M_e^2}\right)G_1 - G_2}$$

(3.77)

3-34

and the following viscous-induced forward shift of the aerodynamic center.

$$\left(\Delta\xi_{AC}\right)_v = -\frac{1}{6}\frac{\left(\Delta c_{n\theta}\right)_v}{\left(c_{n\theta}\right)_i}\bigg/\left[1+\frac{\left(\Delta c_{n\theta}\right)_v}{\left(c_{n\theta}\right)_i}\right] \tag{3.78}$$

G_e varies according to the wall temperature ratio. Figure 3.30 illustrates the results for a 5 degree wedge at $M_\infty = 6$. With $\left(\Delta c_{n\theta}\right)_v/\left(c_{n\theta}\right)_i$ from Figure 3.29 one notes that although the viscous induced effect on the lift will not exceed 20 percent, the viscous effect on unsteady aerodynamics can be as high as 50 percent for aft cg or elastic axis locations.

As $\Delta p_v/p_e$ is known, the estimate of $\left(\Delta c_{m\dot\theta}\right)_v$ in Eq. (3.77) can be improved by substituting $\left(p_e/p_\infty\right)^{-1/2}$ in the expression for G_e with $\left(p_v/p_\infty\right)^{-1/2}$, where $p_v/p_\infty = \left[1+\left(\Delta p_v/p_e\right)_{TE}\right]\left(p_e/p_\infty\right)$.

Seeing these large effects of pure viscous interaction one must be concerned about what the effects of transition might be. It is not within the scope of the present study to investigate this, but it is a problem that needs future attention, especially in view of the associated thermal effects. The present predictions are compared with Orlik-Rückeman's theoretical and experimental data (Ref. 86) in Figure 3.31. The agreement between the present first order theory and Orlik-Rückeman's higher order theory is very satisfying and assures that the present embedded viscous perturbation method will be sufficiently accurate for the tactical missile under study. Figure 3.32 shows a more detailed comparison between Orlik-Rückeman's theory (Ref. 98) and the present perturbation method. The difference in inviscid characteristics is the difference between piston theory used by Orlik-Ruckemann and the tangent wedge formulation used in the present analysis.

3.3.1.3 Non-Viscous Applications. The perturbation analysis performed for viscous flow can easily be applied to other surface perturbations, e.g., those caused by elastic deflections.

Mandl (Refs. 103-105) has investigated numerically the effect of one particular type of surface deformation (see inset in Figure 3.33). In this case the following equivalence holds.

$$d\delta^*/dx = \kappa\,\theta_w\,\xi \tag{3.79}$$

where $\kappa = c/R.\theta_w$; $\kappa^2 \ll 1$. $\kappa > 0$ for concave and $\kappa < 0$ for convex surface deformation. Again using the embedded flow approach, the equation corresponding to Eq. (3.56), giving the deformation-induced relative pressure increase, is

$$\Delta p_d/p_e = \gamma M_e\,\kappa\,\theta_w\,\xi \tag{3.80}$$

and the following equation corresponding to Eqs. (3.59)−(3.61) is obtained,

$$\frac{d(\Delta C_{pd})/d\theta}{d(C_{pe})/d\theta} = \frac{\Delta p_d}{p_e}\,(1 - G_1/2) \tag{3.81}$$

The equation corresponding to Eqs. (3.62) and (3.63) is

$$\left.\begin{aligned}
\frac{(\Delta c_{n\theta})_d}{(c_{n\theta})_i} &= \frac{1}{2}\left[\frac{d(\Delta C_{pd})/d\theta}{d(C_{pe})/d\theta}\right]_{TE}\\[2mm]
\frac{(\Delta c_{m\theta})_d}{(\Delta c_{n\theta})_d} &= -\left(\frac{2}{3} - \xi_{CG}\right)
\end{aligned}\right\} \tag{3.82}$$

The effect on the dynamic derivatives is obtained equally simply, the equation corresponding to Eq. (3.66) being

$$\frac{d(c_{nq})_d}{d\xi} = 2\left[\frac{d(\Delta c_{pd})}{d\theta}\right]_{TE}\xi\left(\xi - \xi_{CG}\right) \tag{3.83}$$

which after integration gives

$$(\Delta c_{nq})_d = -(\Delta c_{m\theta})_d = (\Delta c_{n\theta})_d \left(\frac{2}{3} - \xi_{CG}\right) \tag{3.84}$$

$$(\Delta c_{mq})_d = -(\Delta c_{n\theta})_d \left[\left(\frac{2}{3} - \xi_{CG}\right)^2 + \frac{1}{18}\right] \tag{3.85}$$

As the piston is solid in this case $(\Delta c_{n\dot\theta})_d = (\Delta c_{m\dot\theta})_d = 0$ and the total effect on damping is the C_{mq} - change. That is

$$\frac{\left(\Delta c_{mq\ d}\right)}{(c_{mq})_i} \Bigg/ \frac{\left(\Delta c_{n\theta\ d}\right)}{(c_{n\theta})_i} = \frac{\left(\frac{2}{3} - \xi_{CG}\right)^2 + \frac{1}{18}}{\left(\frac{1}{2} - \xi_{CG}\right)^2 + \frac{1}{12}} \tag{3.86}$$

Instead of moving the aerodynamic center forward, as in Eq. (3.78), an equally large aft moment is obtained.

$$\left(\Delta \xi_{AC}\right)_d = \frac{1}{6} \frac{\left(\Delta c_{n\theta}\right)_d}{\left(c_{n\theta}\right)_i} \Bigg/ \left[1 + \frac{\left(\Delta c_{n\theta}\right)_d}{\left(c_{n\theta}\right)_i}\right] \tag{3.87}$$

In Figure 3.33 the κ-derivatives obtained from Eqs. (3.80)−(3.87) are compared with Mandl's numerical results (Refs. 103−105). The agreement is satisfactory for axis locations of interest, $\xi_{CG} < 0.75$, and indicates that the present perturbation method is sufficiently accurate for the small elastic deformation to be considered in the present aeroelastic analysis.

3.4 CENTRIFUGAL PRESSURE CORRECTION

When the surface has a longitudinal curvature, the pressure formulas derived earlier have to be corrected for the curvature effect (Ref. 41). With Busemann's centrifugal pressure correction included, the Newtonian pressure is (Ref. 41)

$$\left(\frac{p}{p_\infty}\right)_{NB} = 1 + \frac{\gamma K^2}{1 - \varepsilon} - \gamma M_\infty^2 \frac{y_b(x)}{R_b(x)} \tag{3.88}$$

ε is the density ratio through the (bow) shock and $R_b(x)$ is the (longitudinal) radius of curvature. For the present analysis of thin airfoils $(1 - \varepsilon) \approx 2/(\gamma + 1)$ and $1/R_b(x) \approx - \partial^2 y_b / \partial x^2$. From Figure 3.18 is obtained

$$(y_b)_{\substack{L \\ U}} = h(x) - h(0) \pm (y)_{\substack{L \\ U}} \tag{3.89}$$

For a thin airfoil the pressure coefficient given by Eq. (3.88) is

$$\left.\begin{aligned}
\left(C_p\right)_{NB} &= \left(C_p\right)_{\gamma N} + \left(\Delta C_p\right)_c \\[2mm]
\left(C_p\right)_{\gamma N} &= \left(\gamma + 1\right)\left(V_\perp / U\right)^2 \\[2mm]
\left(\Delta C_p\right)_c &= -2 y_b / R_b \approx 2 y_b \, \partial^2 y_b / \partial x^2
\end{aligned}\right\} \tag{3.90}$$

$V_\perp / U$ is given by Eq. (3.36) or Eq. (3.37). This centrifugal pressure correction $(\Delta C_p)_c$ should also be added to the tangent wedge pressure, Eq. (3.35).

3-38

3.4.1 Effect of Airfoil Camber.

An infinitely thin airfoil with circular arc camber is sketched in Figure 3.34. The following relationships between geometric parameters hold for $\left(h_o/R_b\right)^2 \ll 1$.

$$\frac{h_o}{R_b} = \frac{1}{2}\left(\frac{x}{R_b}\right)^2$$

$$\frac{h_o}{x} = \frac{1}{2}\frac{x}{R_b}$$

$$\upsilon(x) - \upsilon(0) = \frac{x}{R_b} = 2\frac{h_o}{x}$$

$$\left.\rule{0pt}{110pt}\right\} \quad (3.91)$$

According to Newtonian theory only the windward side has non-zero pressures. For a small angle of attack Eq. (3.89) becomes

$$(\upsilon_b)_L = h_o + x\alpha \tag{3.92}$$

And Eq. (3.81) gives

$$(C_p)_{\gamma N} = (\gamma + 1)\left|\left(\frac{x}{R_b}\right) + \alpha\right|^2$$

$$(\Delta C_p)_c = \left(\frac{x}{R_b}\right)^2\left[1 + 2\alpha \bigg/ \frac{x}{R_b}\right]$$

$$\left.\rule{0pt}{60pt}\right\} \quad (3.93)$$

The α-derivative is

$$\frac{\partial (C_p)_{\gamma N}}{\partial \alpha} = 2(\gamma + 1)\left[\frac{x}{R_b} + \alpha\right]$$

$$\frac{\partial (\Delta C_p)_c}{\partial \alpha} = 2\frac{x}{R_b}$$

(3.94)

Finally, the effect of camber on the α-derivative at $\alpha = 0$ is

$$\frac{\partial \left|\partial (C_p)_{\gamma N}/\partial \alpha\right|}{\partial (h_o/x)} = 4(\gamma + 1)$$

$$\frac{\partial \left|\partial (\Delta C_p)_c/\partial \alpha\right|}{\partial (h_o/x)} = 4$$

(3.95)

Thus, the centrifugal pressure correction increases the Newtonian pressure curvature derivatives by the factor $\left|1 + (\gamma + 1)^{-1}\right|$. In the case of the pure Newtonian theory, $\gamma + 1 = 2$, and Busemann's correction increases the Newtonian pressure by 50 percent (see Ref. 41).

3.4.2 Effect of Surface Curvature

If one turns Figure 3.34 around 180 degrees and reverses the free stream flow direction, the figure can represent the windward side of a circular arc (bicusped) airfoil. In that case, Eqs. (3.93) through (3.95) will represent the pressure derivatives if the sign for the $(\Delta C_p)_c$ -term is reversed. That is, the strip normal force derivative $dC_{N\alpha}/d\xi$, is decreased by the ratio $\left[1 - (1 + \gamma)^{-1}\right]$ from the Newtonian value. Note that $2h_o/x$ represents the change in surface slope between the leading edge and station x (see Eq. (3.91)).

Mandl (Refs. 103–105) investigated the effect of constant surface curvature on the aerodynamic characteristics of a wedge-shaped airfoil (see inset in Figure 3.33 for a definition of geometry). In this case Eqs. (3.93)–(3.95) become (for the windward side)

$$(C_p)_{\gamma N} = (\gamma + 1) \left| \theta_w (1 + \kappa \xi) + \alpha \right|^2$$

$$(\Delta C_p)_c = 2 \kappa \theta_w \xi \left| \theta_w (1 + \kappa/2\xi) + \alpha \right|$$

$$\left. \right\} \quad (3.96)$$

$$\left(\frac{\partial C_p}{\partial \alpha} \right)_{\gamma N} = 2 (\gamma + 1) \left| \theta_w (1 + \kappa \xi) + \alpha \right|$$

$$\frac{\partial (\Delta C_p)_c}{\partial \alpha} = 2 \kappa \theta_w \xi$$

$$\left. \right\} \quad (3.97)$$

For $\alpha = 0$

$$\frac{\partial \left| \partial C_p / \partial \alpha \right|_{\gamma N}}{\partial \kappa} = 2 (\gamma + 1) \theta_w \xi$$

$$\frac{\partial \left| \partial (\Delta C_p)_c / \partial \alpha \right|}{\partial \kappa} = 2 \theta_w \xi$$

$$\left. \right\} \quad (3.98)$$

Again the derivatives at $\alpha = 0$ are increased by the factor $\left| 1 + (\gamma + 1)^{-1} \right|$ above the Newtonian value due to concave curvature effect. (Convex curvature has, of course, the opposite effect, the factor then being $\left| 1 - (\gamma + 1)^{-1} \right|$. For the standard Newtonian theory with Busemann's centrifugal correction Eq. (3.98) becomes (Ref. 41).

$$\frac{\partial \left| \partial C_p / \partial \alpha \right|_N}{\partial \kappa} = 4\theta_w \xi$$

$$\frac{\partial \left| \partial (\Delta C_p)_c / \partial \alpha \right|_B}{\partial \kappa} = 2\theta_w \xi$$

(3.98a)

That is, the centrifugal pressure correction increases the Newtonian value by 50 percent.

3.4.3 Viscous Curvature Effects

For the wedge analyzed earlier in Section 3.3 the viscous curvature parameters are as follows.

$$y_b / c = \xi (\theta_w + \alpha) + \delta^* / c$$

$$\frac{\partial^2 y_b}{\partial x^2} = \frac{\partial^2 \delta^*}{\partial x^2} = \frac{\partial}{\partial x} \left(\frac{\partial \delta^*}{\partial x} \right)_{FP}$$

$$\frac{\delta^*}{c} = 2\xi \left(\frac{\partial \delta^*}{\partial x} \right)_{FP} \bigg/ \sqrt{\frac{p_v}{p_\infty}}$$

$$\left(\frac{\partial \delta^*}{\partial x} \right)_{FP} = \bar{B}\bar{\chi} / M_e \quad \text{where} \quad \bar{B} \approx \bar{B}_1 \quad \text{for} \quad M_e^2 \gg 1$$

$$\bar{B}\bar{\chi} = \frac{1}{\gamma} \frac{\Delta p_v}{p_e} = \frac{1}{\gamma} \left(\frac{\Delta p_v}{p_e} \right)_{TE} \xi^{-1/2}$$

(3.99)

Equation (3.90) gives with the above Eq. (3.99)

$$\left(\Delta C_{pv}\right)_c = - \frac{(\theta_w + a)}{\gamma M_e} \frac{\Delta p_v}{p_e} \left[1 + \frac{2}{\gamma M_e (\theta_w + a)} \frac{\Delta p_v}{p_e} \middle/ \sqrt{\frac{p_v}{p_e}}\right] \qquad (3.100)$$

As

$$\Delta C_{pv} = \frac{2}{\gamma M_\infty^2} \frac{\Delta p_v}{p_e} \frac{p_e}{p_\infty} = \frac{\Delta p_v}{p_e} \left(1 + C_{pe}\right) \qquad (3.101)$$

one obtains

$$\frac{\left(\Delta C_{pv}\right)_c}{\Delta C_{pv}} = - \frac{\theta_w + a}{\gamma M_e \left(1 + C_{pe}\right)}$$

$$- \frac{2}{\left(\gamma M_e\right)^2} \frac{1}{\left(1 + C_{pe}\right)^{3/2}} \frac{\dfrac{\Delta p_v}{p_e}}{\left(1 + \dfrac{\Delta p_v}{p_e}\right)^{1/2}} \qquad (3.102)$$

The magnitude of the first term is always less than $\theta_w/\gamma M_e$ and the magnitude of the second term never exceeds $\left|2/\left(\gamma M_e\right)^2\right| \left(\Delta p_v/p_e\right) \left(1 + \Delta p_v/p_e\right)^{-1/2}$.

In the present analysis it has been shown that viscid-inviscid interaction is not of any real concern unless $M_e^2 \ll 1$ and $\theta_w^2 \ll 1$. For $\theta_w < 0.2$ (11.4°) and $\gamma M_e > 5$ the first term is always less than 4 percent, and the second term would not exceed 6 percent for $\Delta p_v/p_e \leq 1$. Thus, it appears that the viscous curvature effect can be neglected, at least in a first order analysis such as the perturbation method developed earlier.

3.4.4 Elastic Perturbations

For a thin, symmetric airfoil the elastic deflection is represented by the deformation of the center chord line (see Figure 3.18b). In this case the following equivalence with the viscous analysis is obtained

$$d\delta^{*}/dx = dh/dx \qquad (3.103)$$

The deformation-induced relative pressure increase, given by Eq. (3.56), is

$$\left(\Delta p_{E}/p_{e}\right)_{L}^{U} = \pm \gamma M_{e} \, dh/dx \qquad (3.104)$$

To this should be added the curvature effect from Eq. (3.90). That is

$$\left|\left(\Delta C_{pE}\right)_{c}\right|_{L}^{U} = \pm 2 \left(v_{b}\right)_{L}^{U} \, d^{2}h/dx^{2} \qquad (3.105)$$

where $\left(v_{b}\right)_{L}^{U}$ is defined by Eq. (3.89).

For a wedge describing parabolic elastic deformations one can write $h(x)$ as follows

$$\left.\begin{array}{l} dh/dx = \alpha + \bar{\kappa}\theta_{w}\xi \\[2mm] h/c = h(0)/c + \left(\bar{\kappa}\theta_{w}/2\right)\xi^{2} \end{array}\right\} \qquad (3.106)$$

The equations corresponding to Eqs. (3.104) and (3.105) become

$$\left(\frac{\Delta P_E}{P_e}\right)_L = \gamma M_e \left(\alpha + \overline{\kappa}\theta_w \xi\right)$$

$$\left|\left(\Delta C_{pE}\right)_c\right|_L = 2\overline{\kappa}\theta_w \left|\alpha\xi + (\overline{\kappa}\theta_w/2)\xi^2\right|$$

(3.107)

The $\overline{\kappa}$-derivatives are in angular measure

$$\frac{\partial\left(\Delta C_{pE}\right)}{\partial\left(\overline{\kappa}\theta_w \xi\right)} = 2\frac{P_e}{P_\infty}\frac{M_e}{M_\infty^2}$$

$$\frac{\partial\left(\Delta C_{pE}\right)_c}{\partial\left(\overline{\kappa}\theta_w \xi\right)} = 2\left(\alpha + \theta_w\overline{\kappa}\xi\right)$$

(3.108)

That is, for $\alpha = 0$ and $\overline{\kappa} \to 0$ the centrifugal pressure correction goes to zero. Consequently, for the elastic analysis in the present study the formulation expressed through Eqs. (3.34), (3.35), and (3.38) is sufficient.

3.4.5 Surface Curvature Perturbations

For a wedge with a parabolic surface curvature superimposed (see inset in Figure 3.33) the following equivalence holds

$$d\delta^*/dx = \kappa\theta_w \xi$$

(3.109)

$\kappa^2 \ll 1$: $\kappa > 0$ for concave and $\kappa < 0$ for convex surface curvature.

The relative pressure increase given by Eq. (3.56) is for the windward side

$$\left(\Delta p_c/p_e\right)_L = \gamma M_e \kappa\theta_w \xi$$

(3.110)

Through the steps corresponding to those leading to Eq. (3.61) one obtains

$$\left| \frac{d\left(\Delta C_{pc}\right)}{d\theta} \right|_L = \left(\frac{\partial C_{pe}}{\partial \theta}\right)_L \left(\frac{\Delta P_c}{P_e}\right)_L \left(1 - \frac{G_1}{2}\right) \qquad (3.111)$$

To this should be added the centrifugal pressure correction from Eq. (3.97).

$$\left[\frac{d\left(\Delta C_{pc}\right)_c}{d\theta}\right]_L = 2\kappa\,\theta_w\,\xi \qquad (3.112)$$

From Eqs. (3.110) and (3.111) one obtains

$$\frac{\partial}{\partial \kappa} \left| \frac{\partial\left(\Delta C_{pc}\right)}{\partial \theta} \right|_L = \left(\frac{\partial C_{pe}}{\partial \theta}\right)_L \gamma M_e\,\theta_w\,\xi \left(1 - \frac{G_1}{2}\right) \qquad (3.113)$$

From the earlier discussion of Eq. (3.98) it is obvious that for $\alpha = 0$ modifying Eq. (3.110) as follows will include the centrifugal pressure term

$$\frac{\partial}{\partial \kappa} \left[\frac{\partial\left(\Delta C_{pc}\right)}{\partial \theta} + \frac{\partial\left(\Delta C_{pc}\right)_c}{\partial \theta} \right]_L$$

$$= \frac{\gamma(\gamma + 2)}{\gamma + 1} \left(1 - \frac{G_1}{2}\right) M_e\,\theta_w\,\xi \left(\frac{\partial C_{pe}}{\partial \theta}\right)_L \qquad (3.114)$$

Integrating Eq. (3.114) gives the normal force and pitching moment derivatives at $\alpha = 0$

$$\frac{\partial}{\partial \kappa} \left[\frac{d(\Delta c_{nc})}{d\theta} + \frac{d(\Delta c_{nc})_c}{d\theta} \right] \bigg/ \frac{d c_{ne}}{d\theta}$$

$$= \frac{1}{2} \frac{\gamma(\gamma + 2)}{\gamma + 1} M_e \theta_w \left(1 - \frac{G_1}{2} \right)$$

$$\frac{\dfrac{\partial}{\partial \kappa} \left[\dfrac{d(\Delta c_{mc})}{d\theta} + \dfrac{d(\Delta c_{mc})_c}{d\theta} \right]}{\dfrac{\partial}{\partial \kappa} \left[\dfrac{d(\Delta c_{nc})}{d\theta} + \dfrac{d(\Delta c_{nc})_c}{d\theta} \right]} - \left(\frac{2}{3} - \xi_{CG} \right)$$

$$\frac{d c_{ne}}{d\theta} = 2 \left(\frac{\partial c_{pe}}{\partial \theta} \right)_L$$

(3.115)

As there is no "piston cushioning" in this case, the total effect on the damping is the c_{mq} - change. The equation corresponding to Eq. (3.66) is as follows

$$\frac{d}{d\xi} \left\{ \frac{\partial}{\partial \kappa} \left[\frac{d(\Delta c_{nc})}{d\left(\frac{cq}{U_\infty}\right)} + \frac{d(\Delta c_{nc})_c}{d\left(\frac{cq}{U_\infty}\right)} \right] \right\}$$

$$= \frac{2\gamma(\gamma + 2)}{\gamma + 1} \left(1 - \frac{G_1}{2} \right) M_e \theta_w \left(\frac{\partial c_{pe}}{\partial \theta} \right)_L \xi \left(\xi - \xi_{CG} \right)$$

(3.116)

Integration gives

$$\frac{\dfrac{\partial}{\partial \kappa} \left[\dfrac{d(\Delta c_{mc})}{d\left(\frac{cq}{U_\infty}\right)} + \dfrac{d(\Delta c_{mc})_c}{d\left(\frac{cq}{U_\infty}\right)} \right]}{\dfrac{\partial}{\partial \kappa} \left[\dfrac{d(\Delta c_{nc})}{d\left(\frac{cq}{U_\infty}\right)} + \dfrac{d(\Delta c_{nc})_c}{d\left(\frac{cq}{U_\infty}\right)} \right]} = \left(\frac{2}{3} - \xi_{CG} \right)^2 + \frac{1}{18}$$

(3.117)

3-47

In Figure 3.35, the results from Eqs. (3.115) and (3.117) are shown for $M_\infty \theta_w = 1.25$ and $M_e^2 \gg 1$. Also shown are the predictions through Newtonian, Newtonian-Busemann, and Mandl's theory. The agreement between present prediction and Newtonian-Busemann theory is very good, which, of course, it should be for this case, i.e., for $M_\infty \rightarrow \infty$. The centrifugal pressure correction increases the Newtonian value by at most 20 percent. The figure shows that concave surface curvature increases the dynamic stability for all cg locations and increases the static stability for cg locations forward of $\xi_{CG} = 2/3$. The effect of convex curvature is exactly the opposite. Whereas the agreement with experimental data has been found to be good for the Busemann correction of concave surface curvature effects (Ref. 106), no experimental verification of the convex curvature effects have been obtained. Thus, in the present analysis which considers only convex airfoil shapes, the centrifugal pressure correction is neglected.

This is true also in regard to the effect of camber-inducing elastic deflections. We believe that before including surface curvature effects in the aeroeleastic analysis, efforts should be made to account for the effects of boundary layer transition and flow separation.[#] Only when the more fundamental viscous flow effects have been included, can one justify the inclusion of higher order inviscid flow effects, such as the curvature effect discussed above or the bow shock interaction considered by McIntosh (Ref. 107), both being of comparable magnitudes (see Fig. 3.35 and Ref. 108).

[#] Regular viscid-inviscid interaction effects are insignificant for the operating range of the tactical missile under study.
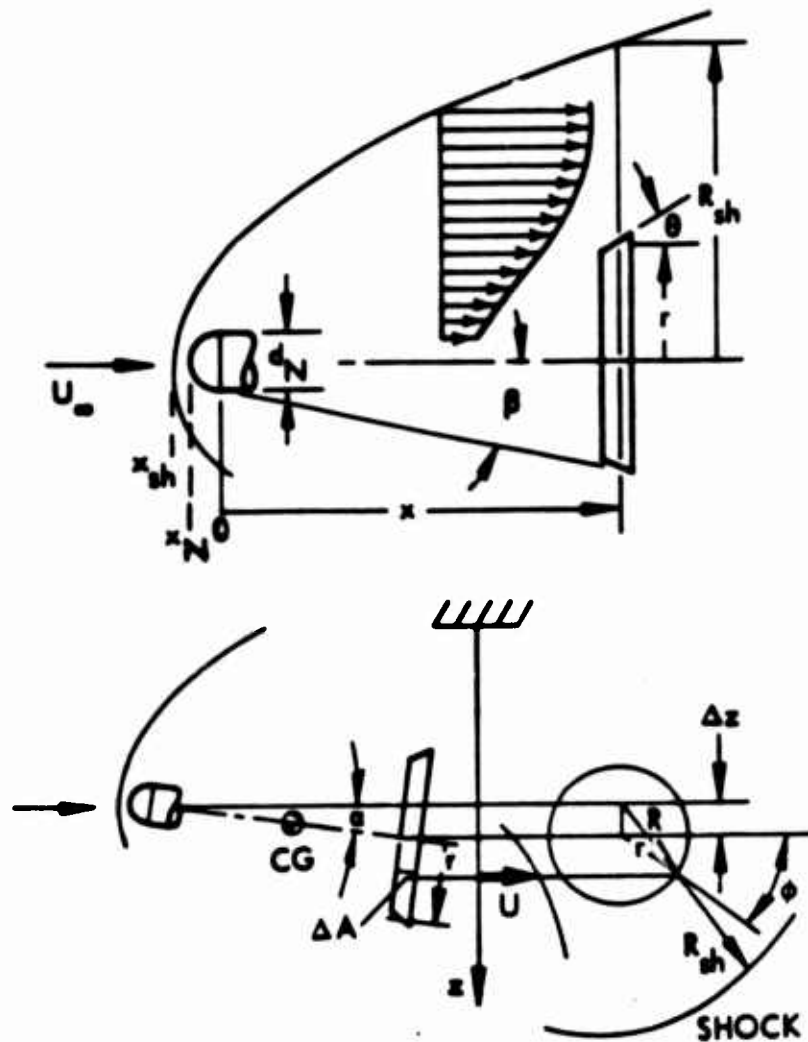
Figure 3.1 Bow-Shock Induced Inviscid Shear Flow at Near Zero Angle
of Attack
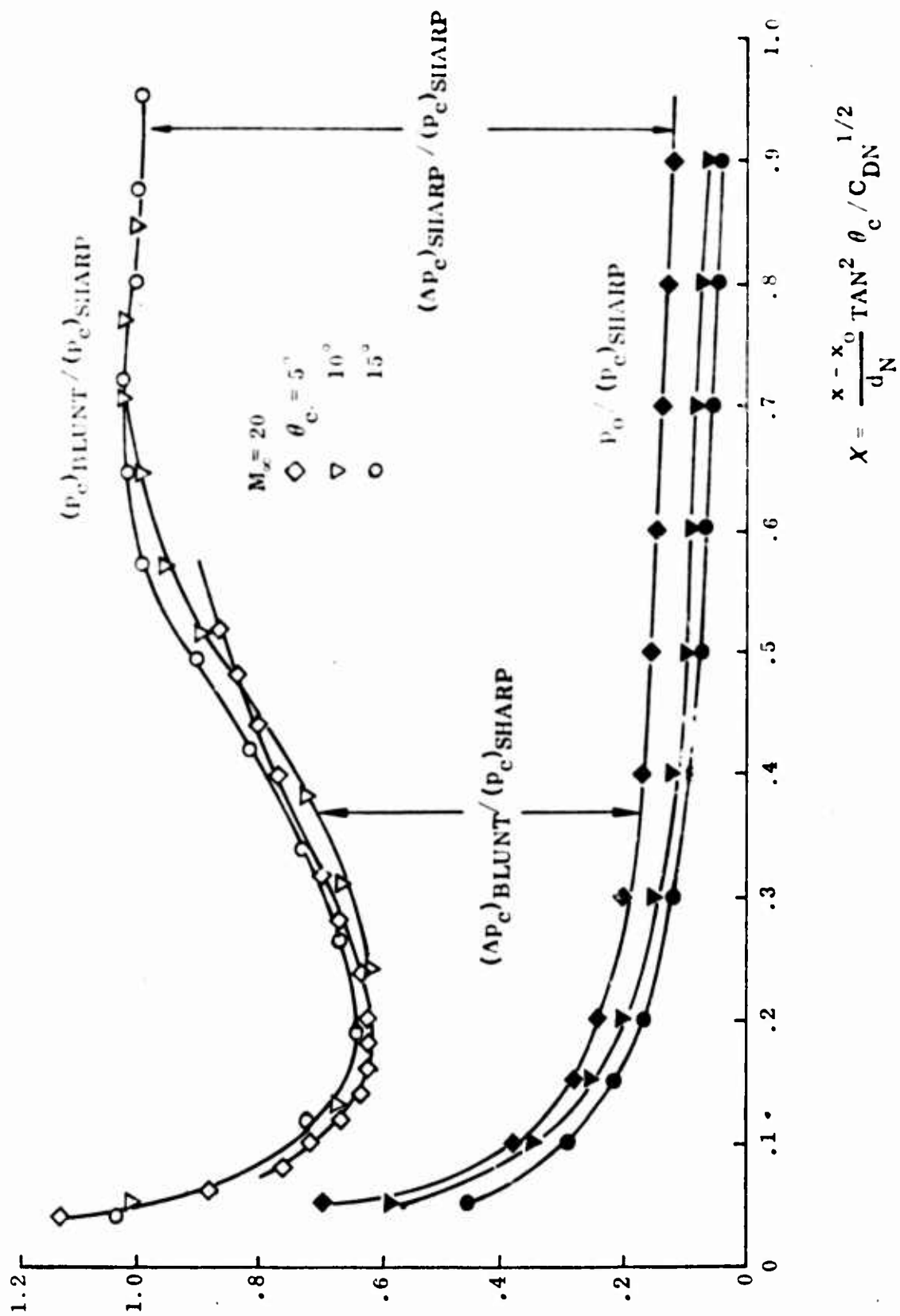
Figure 3.2   Pressure distribution over blunted slender bodies of revolution at $M_\infty = 20$
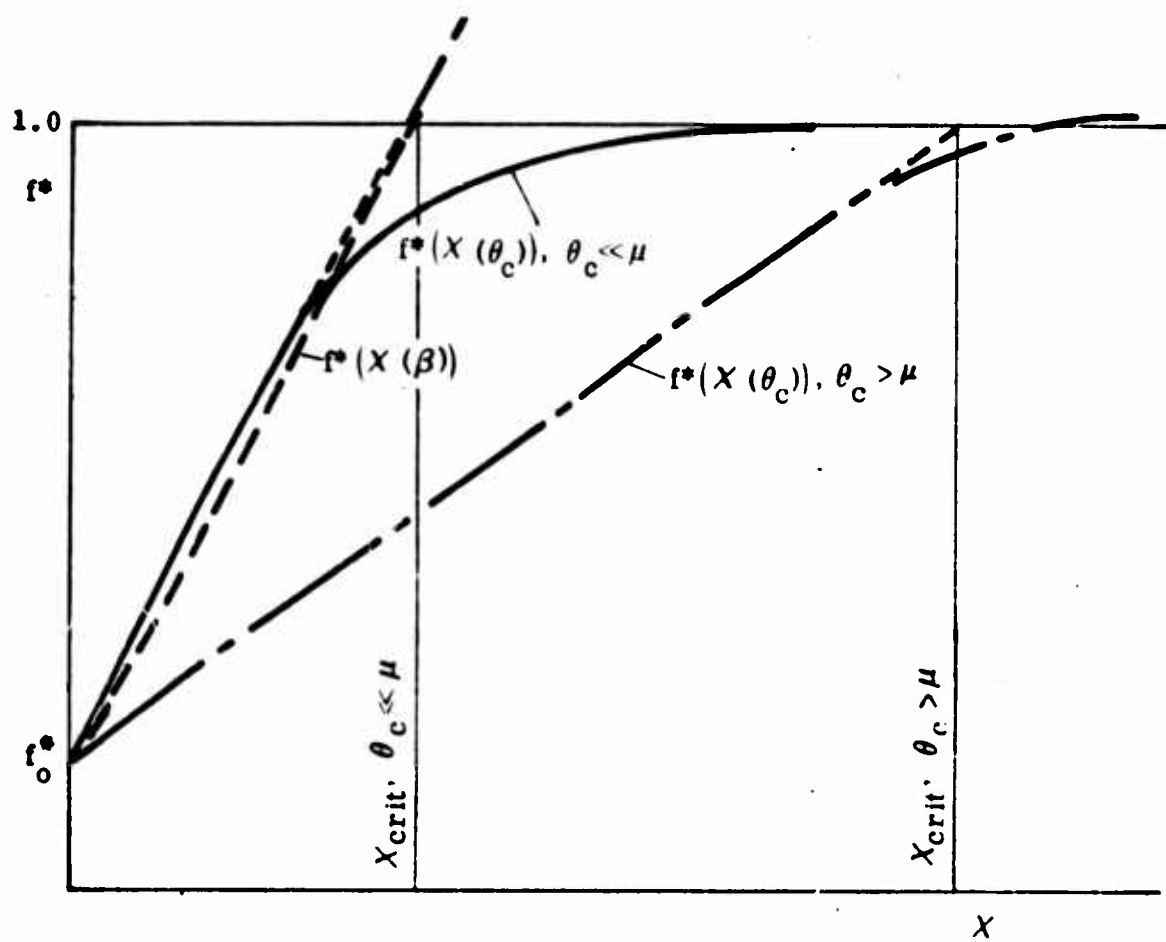
Figure 3.3   Dynamic pressure function for blunted cones at $M_\infty = 20$

Figure 3.4 Variation of Shock-Wave Angle with Cone Semivertex Angle for Various Upstream Mach Numbers, Perfect Gas, $\gamma = 1.405$ (Ref. 33)
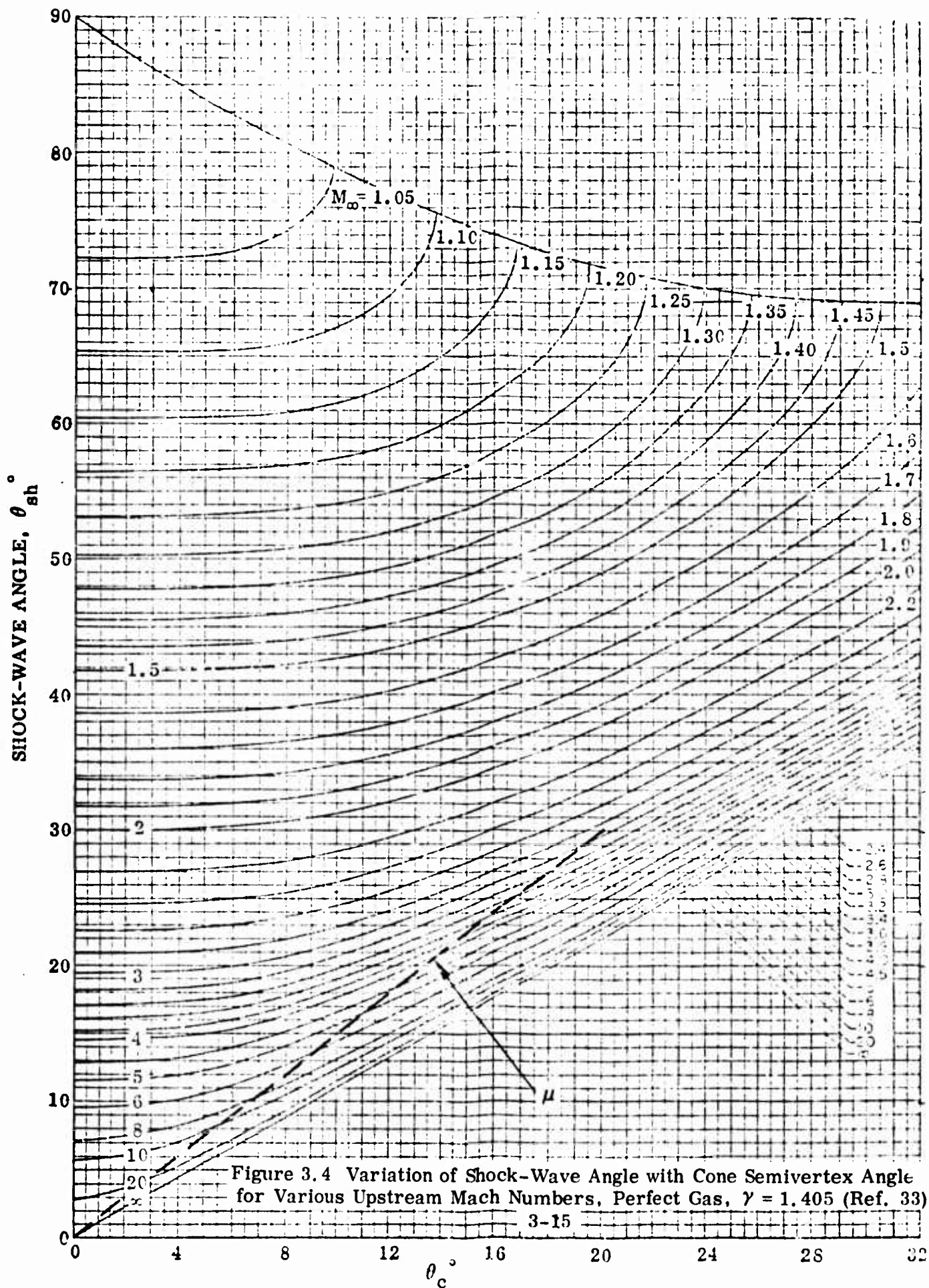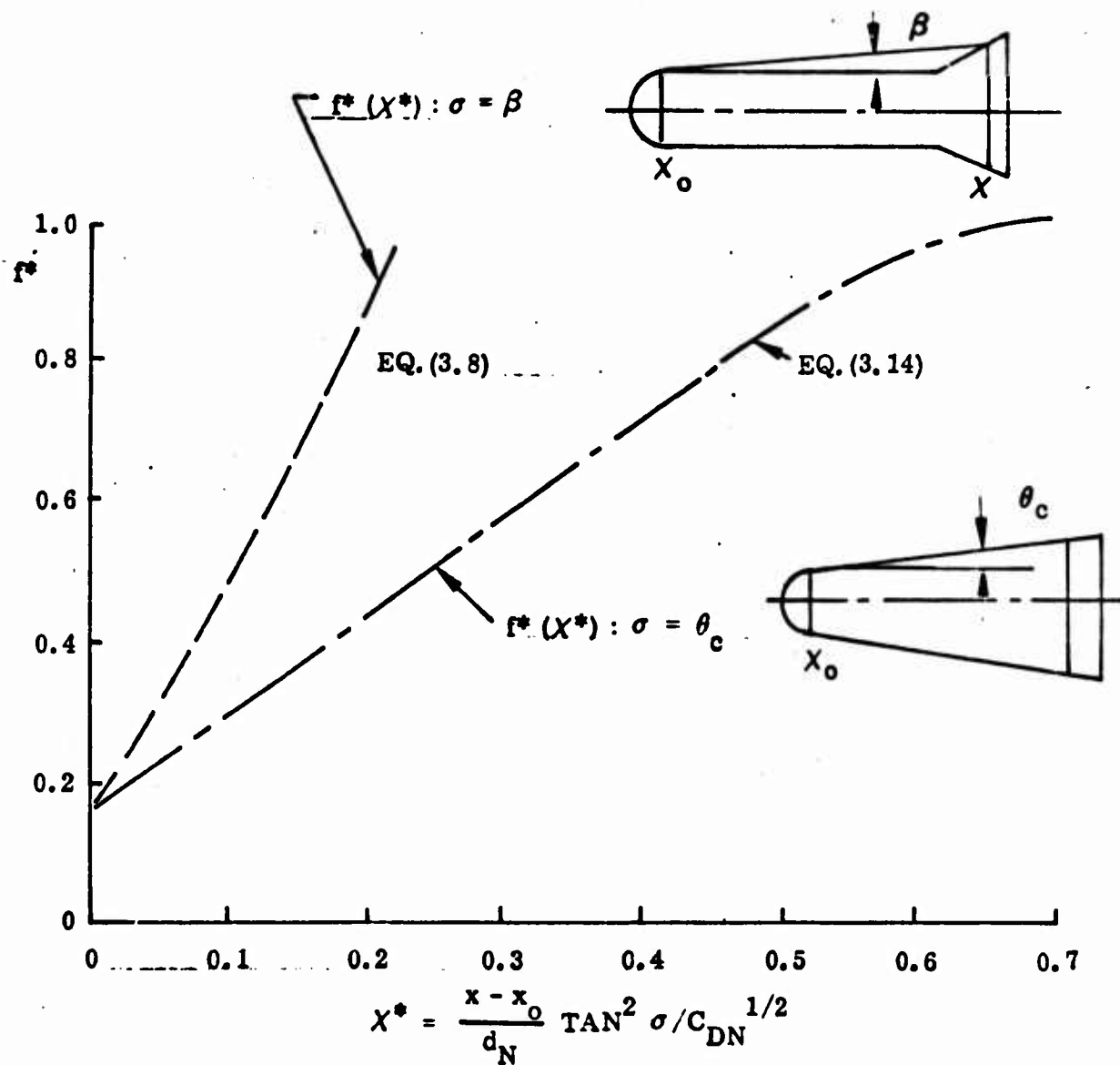
Figure 3.5 Dynamic Pressure Functions for Blunted Cones and Cylinder-Flare Bodies

$$X^* = \frac{x - x_o}{d_N} \, TAN^2 \, \sigma / C_{DN}^{1/2}$$
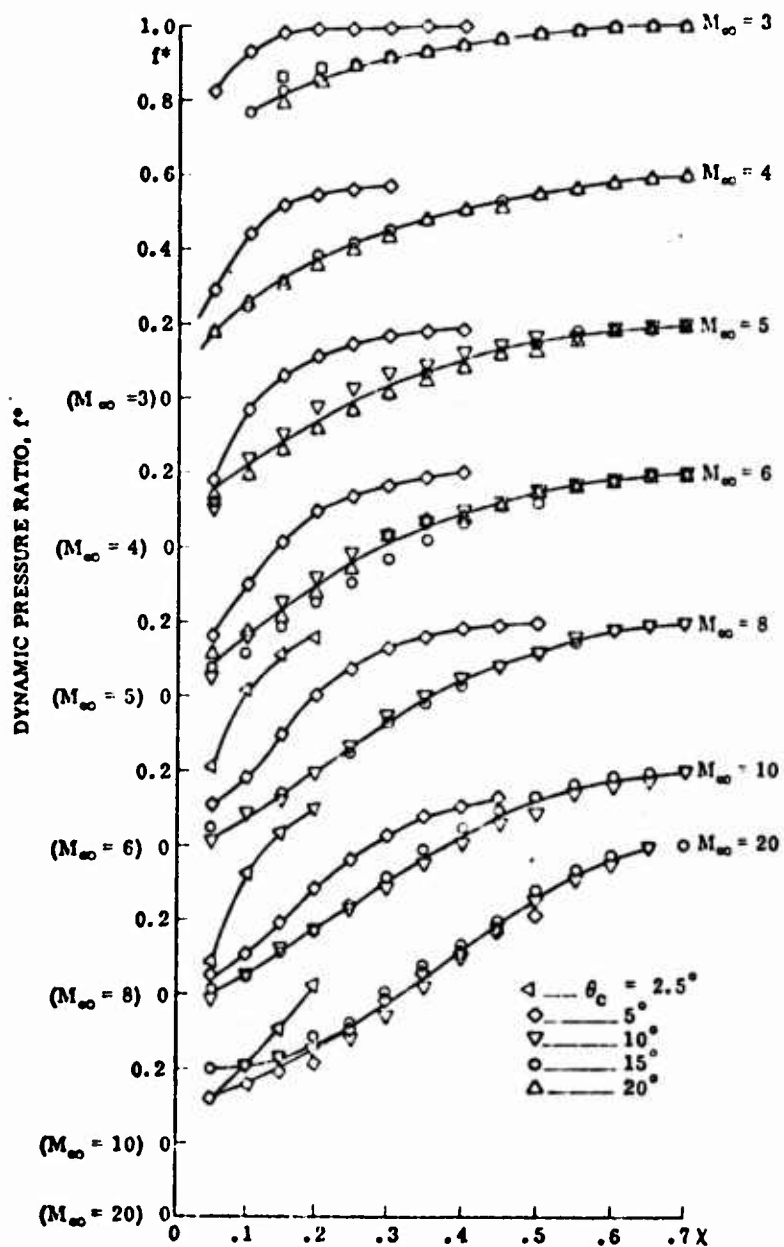
Figure 3.6 Dynamic Pressure Function for Shallow Blunted Cones

3-54
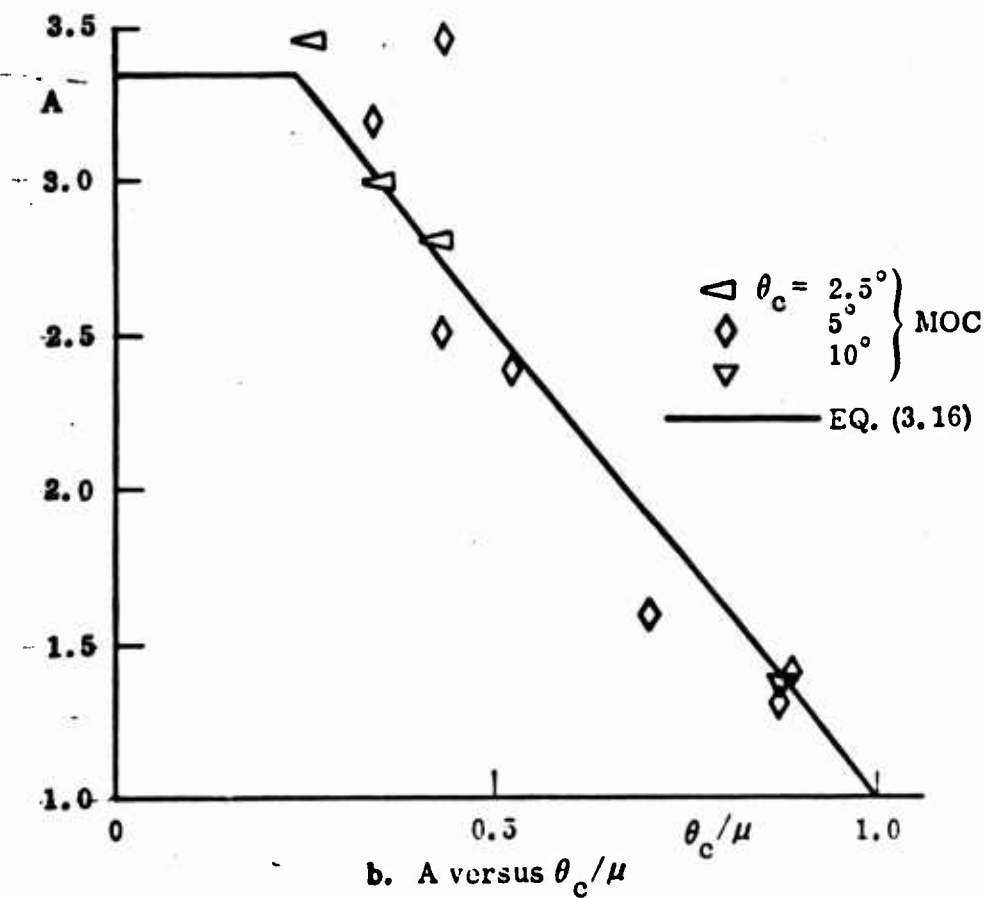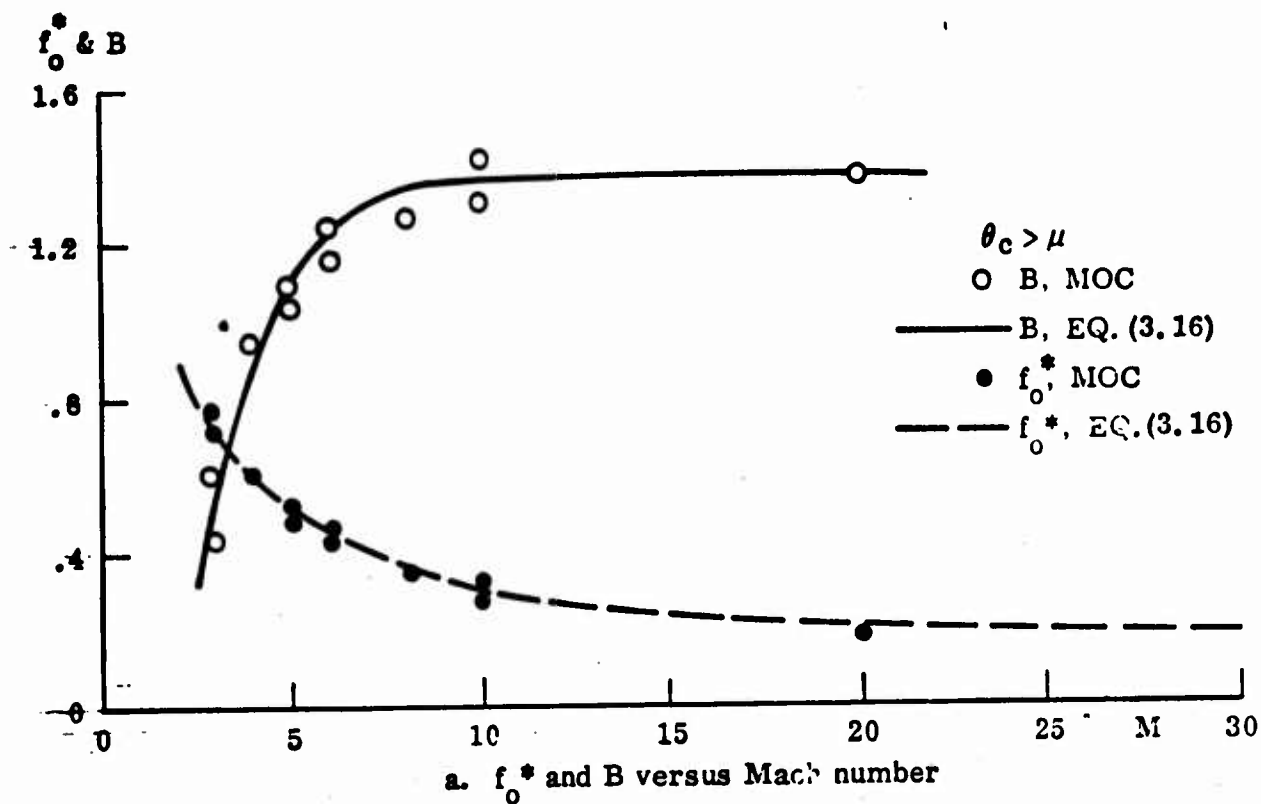
Figure 3.7 Effect of Mach Number on Dynamic Pressure Parameters for Blunted Cones
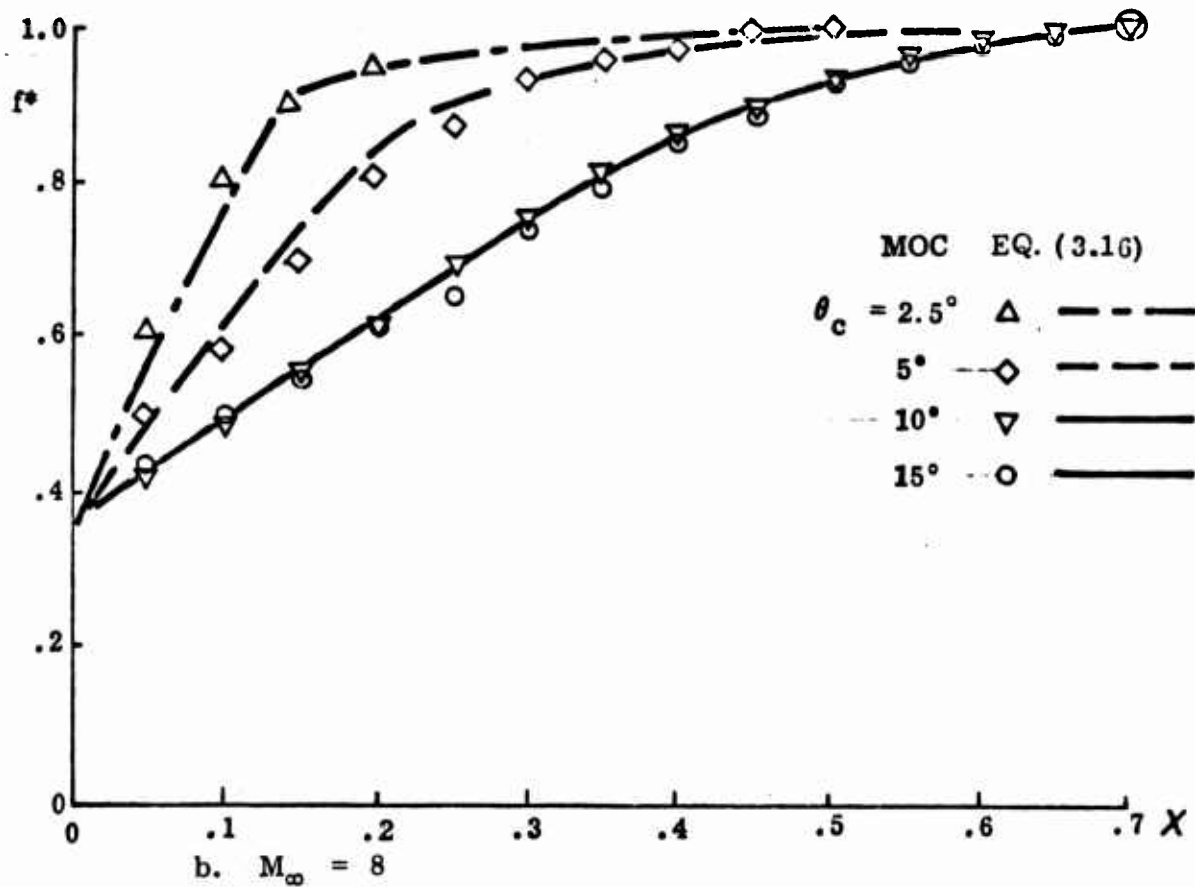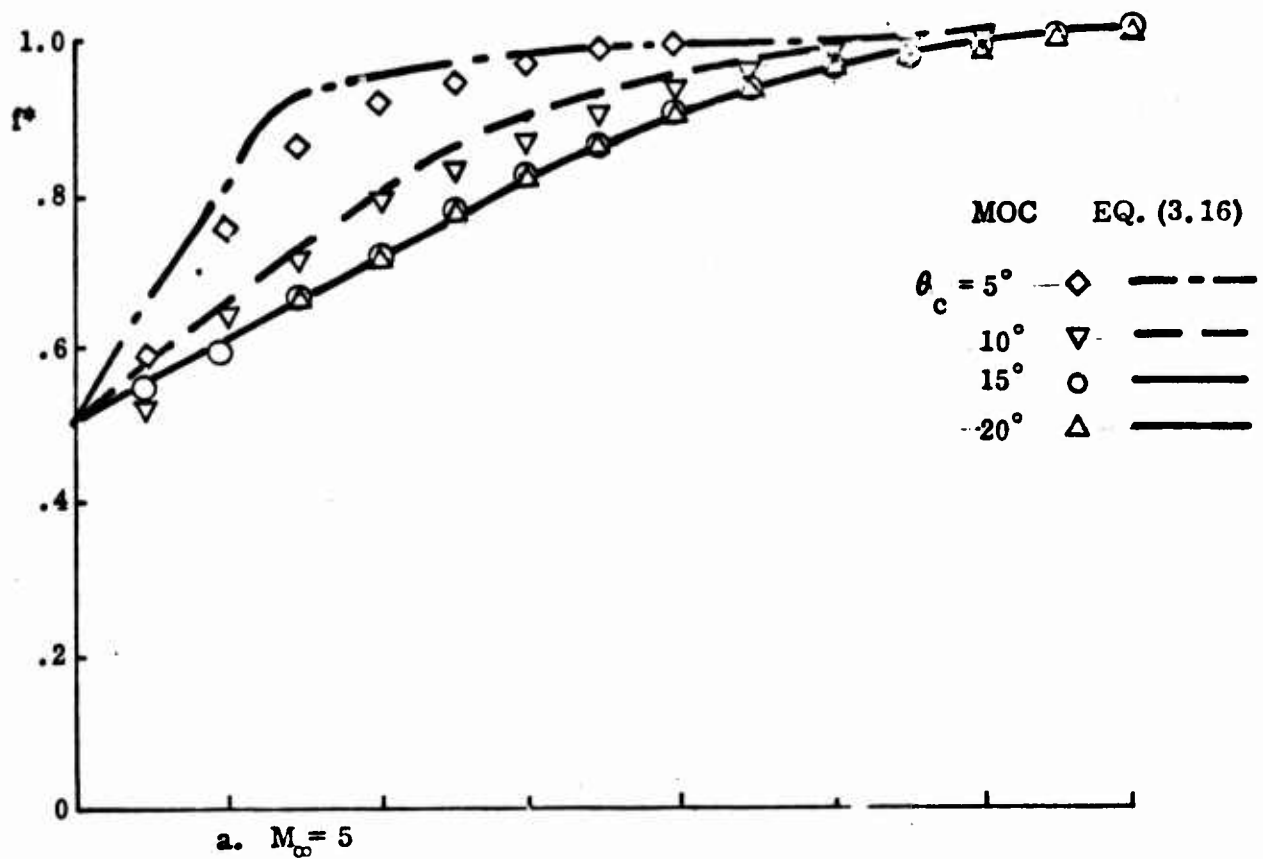
Figure 3.8 Comparison between dynamic pressure functions for blunted slender cones as determined by analytic approximation and method of characteristics
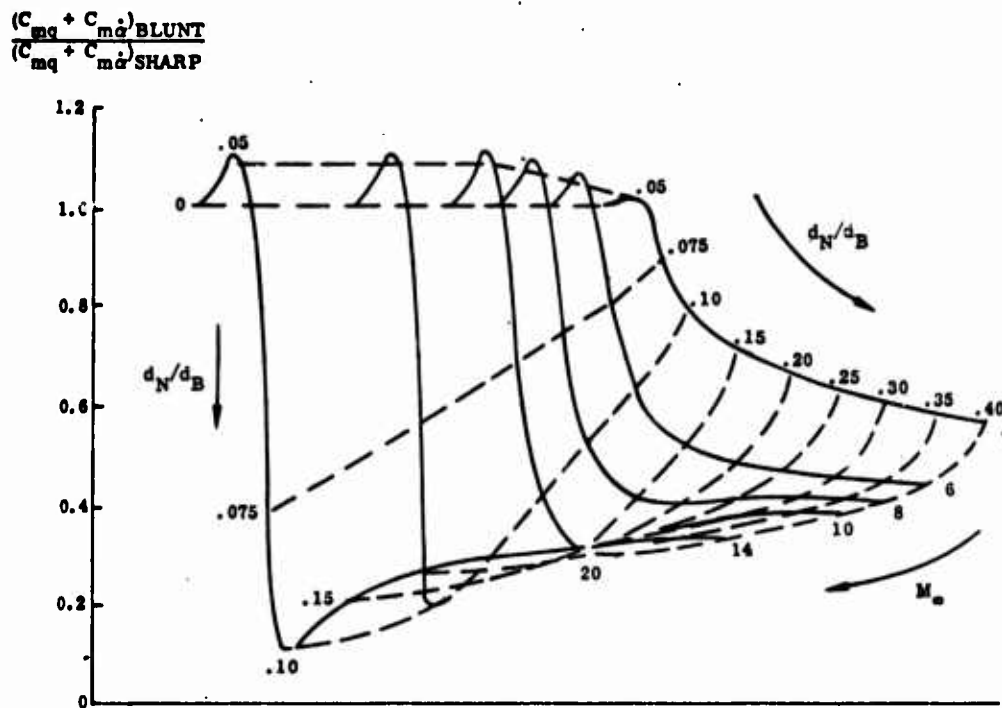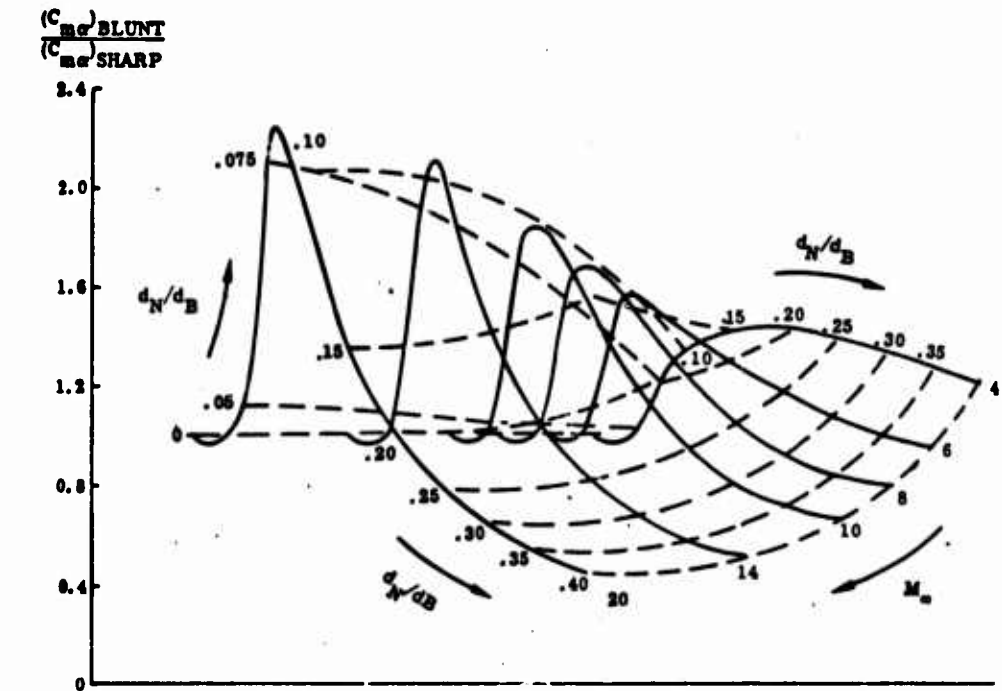
Figure 3.9   Effect of Mach Number on Static and Dynamic Stability
Derivatives of Blunted Slender Cones (Sheet 1 of 2)
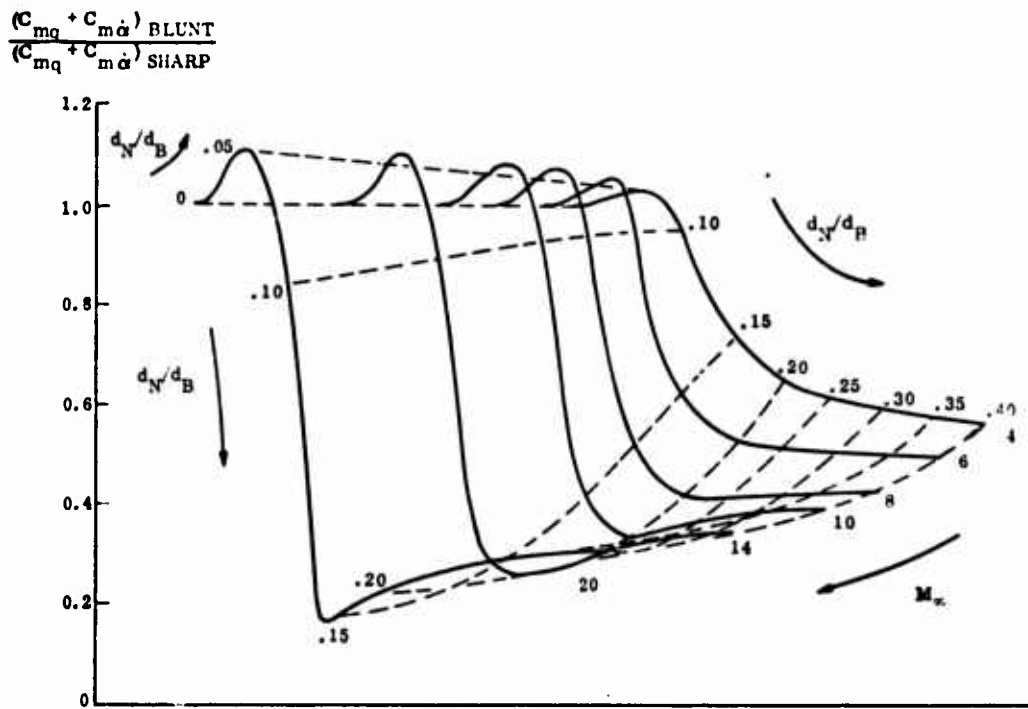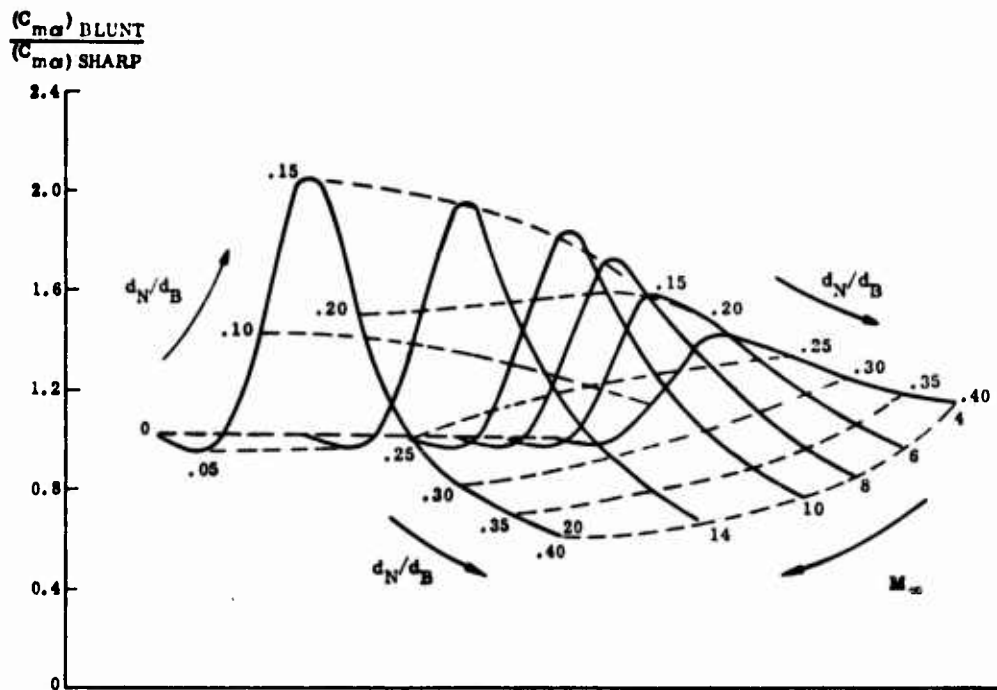
b. $\theta_c = 10°$

Figure 3.9   Effect of Mach Number on Static and Dynamic Stability
Derivatives of Blunted Slender Cones (Sheet 2 of 2)
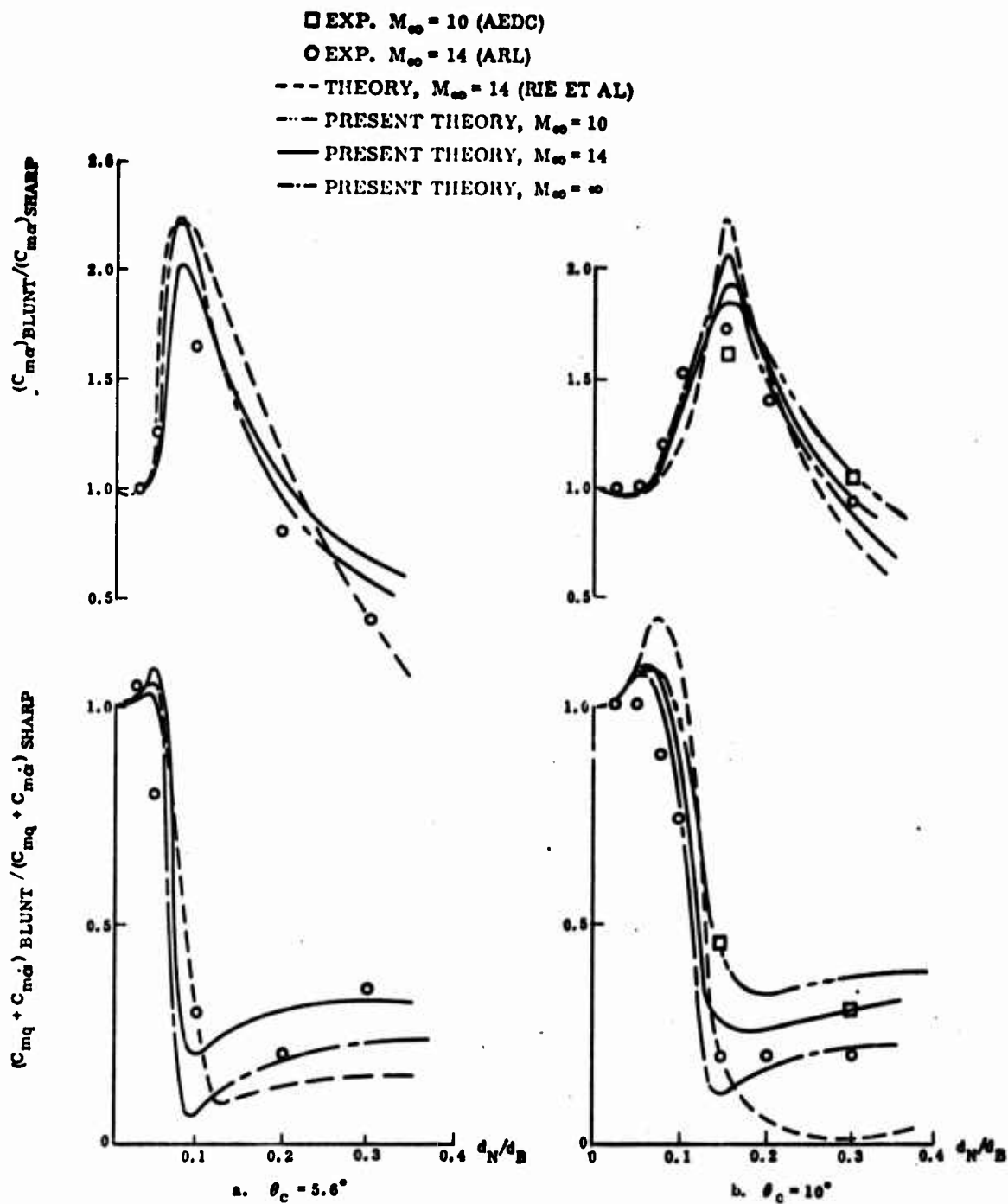
Figure 3.10 Predicted and Measured Stability Derivates of Slender Blunted Cones
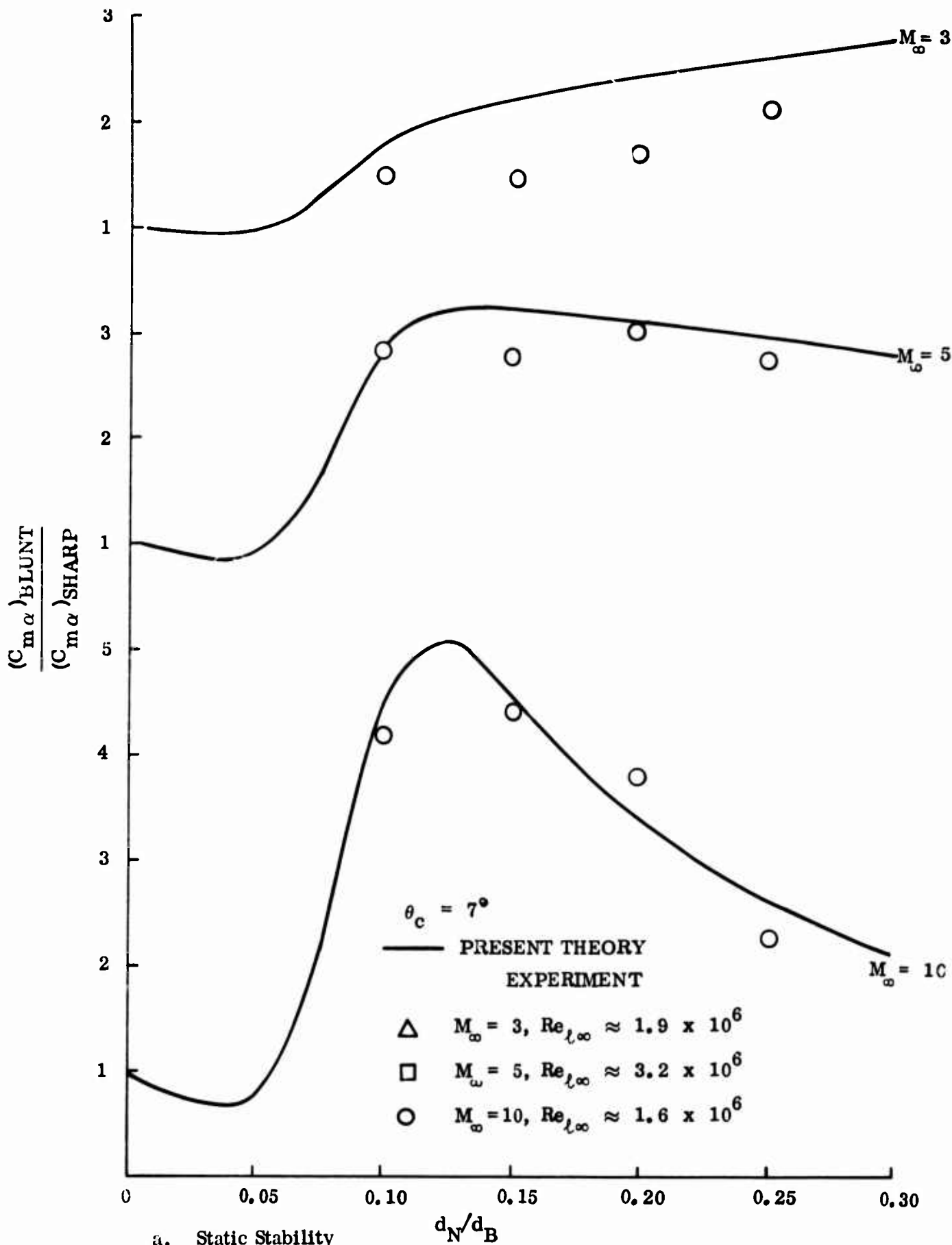
Figure 3.11 Comparison between predicted and measured effects of nose bluntness and mach number on the dynamic stability of a 7° cone (Sheet 1 of 2)
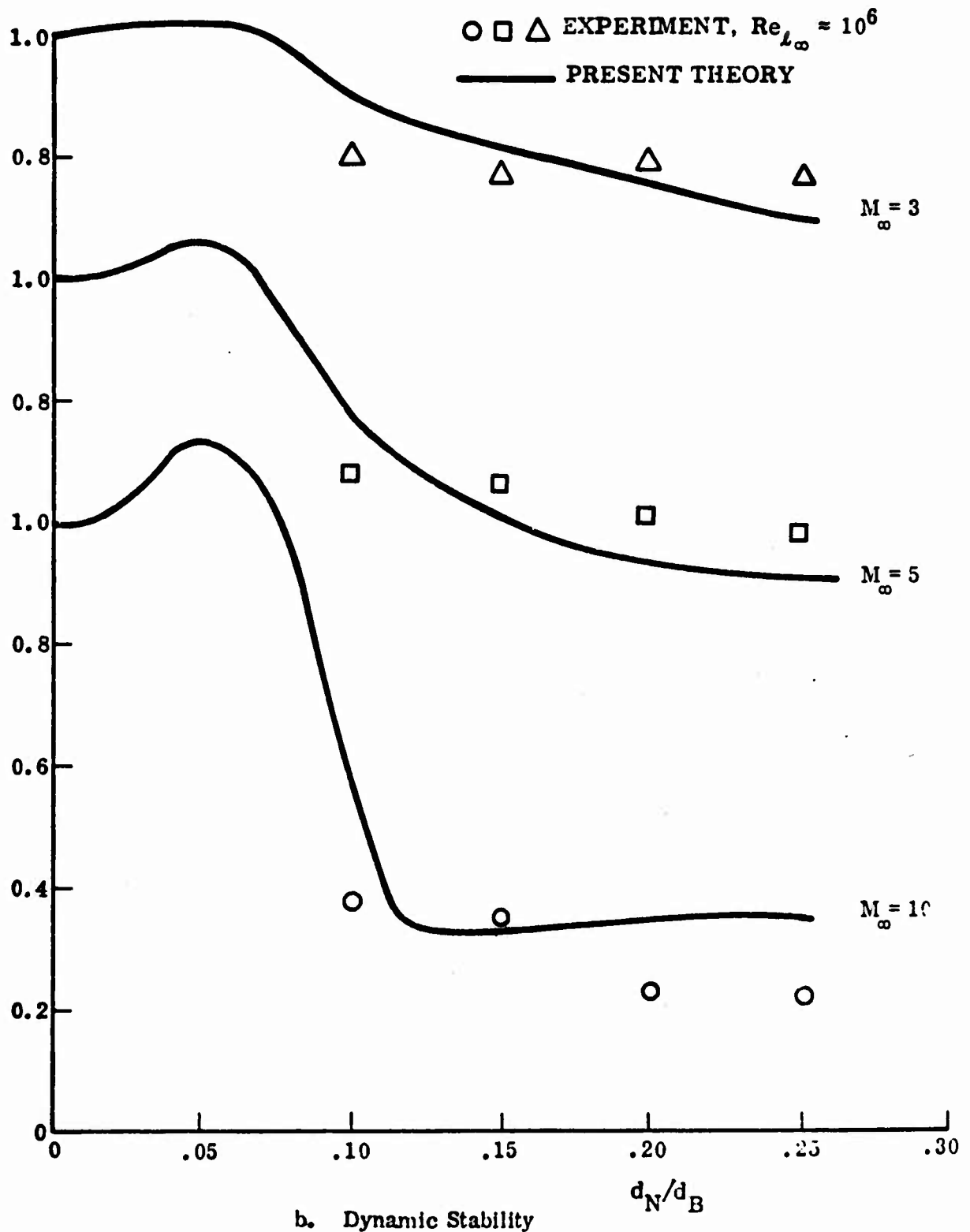
a. Static Stability

Figure 3.11 Comparison between predicted and measured effects of
nose bluntness and mach number on the dynamic stability of a 7° cone
(sheet 2 of 2)
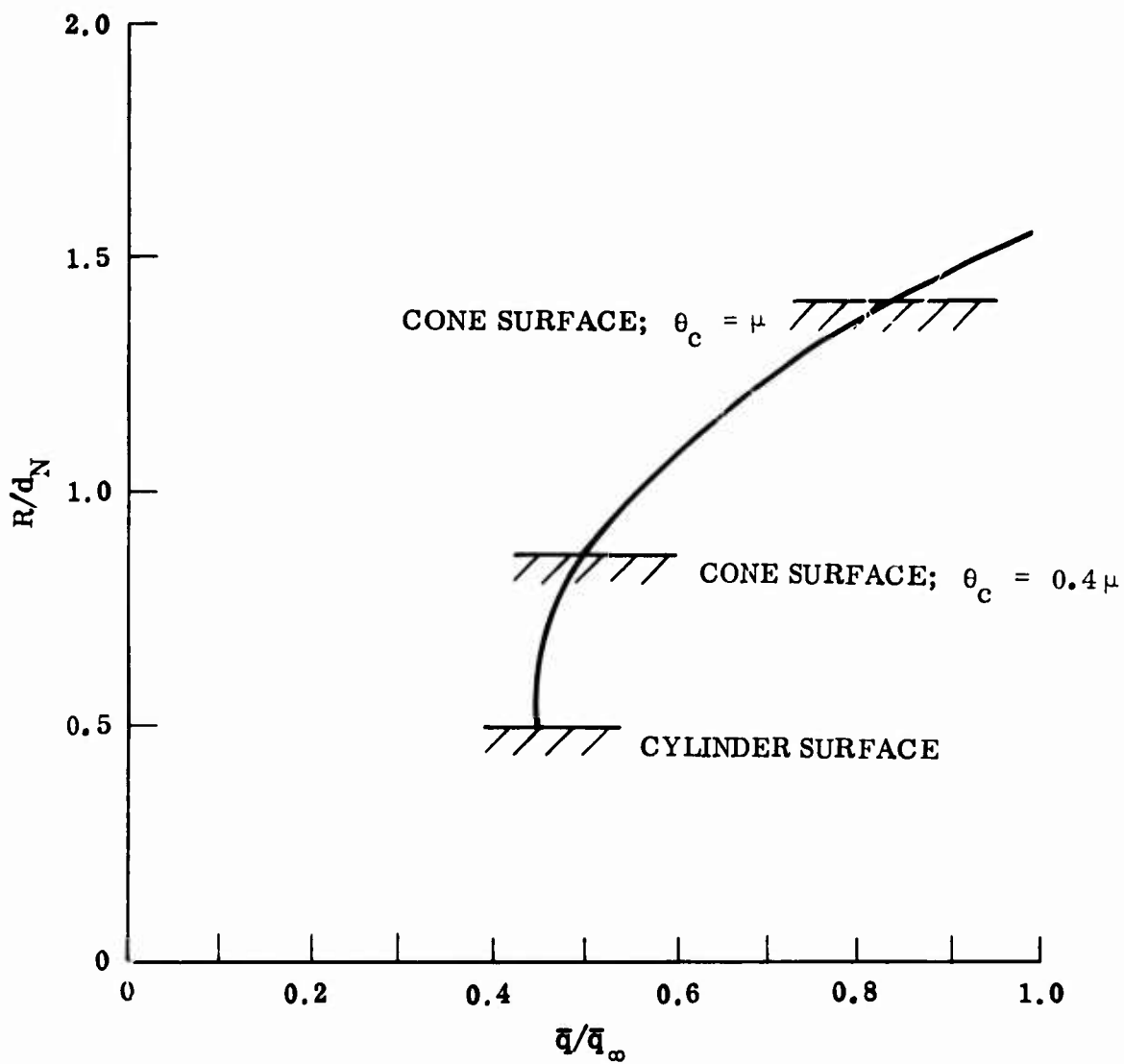
Figure 3.12 Dynamic pressure ratio six nose diameters downstream
of the tip of a hemisphere-cylinder at M_∞ = 6
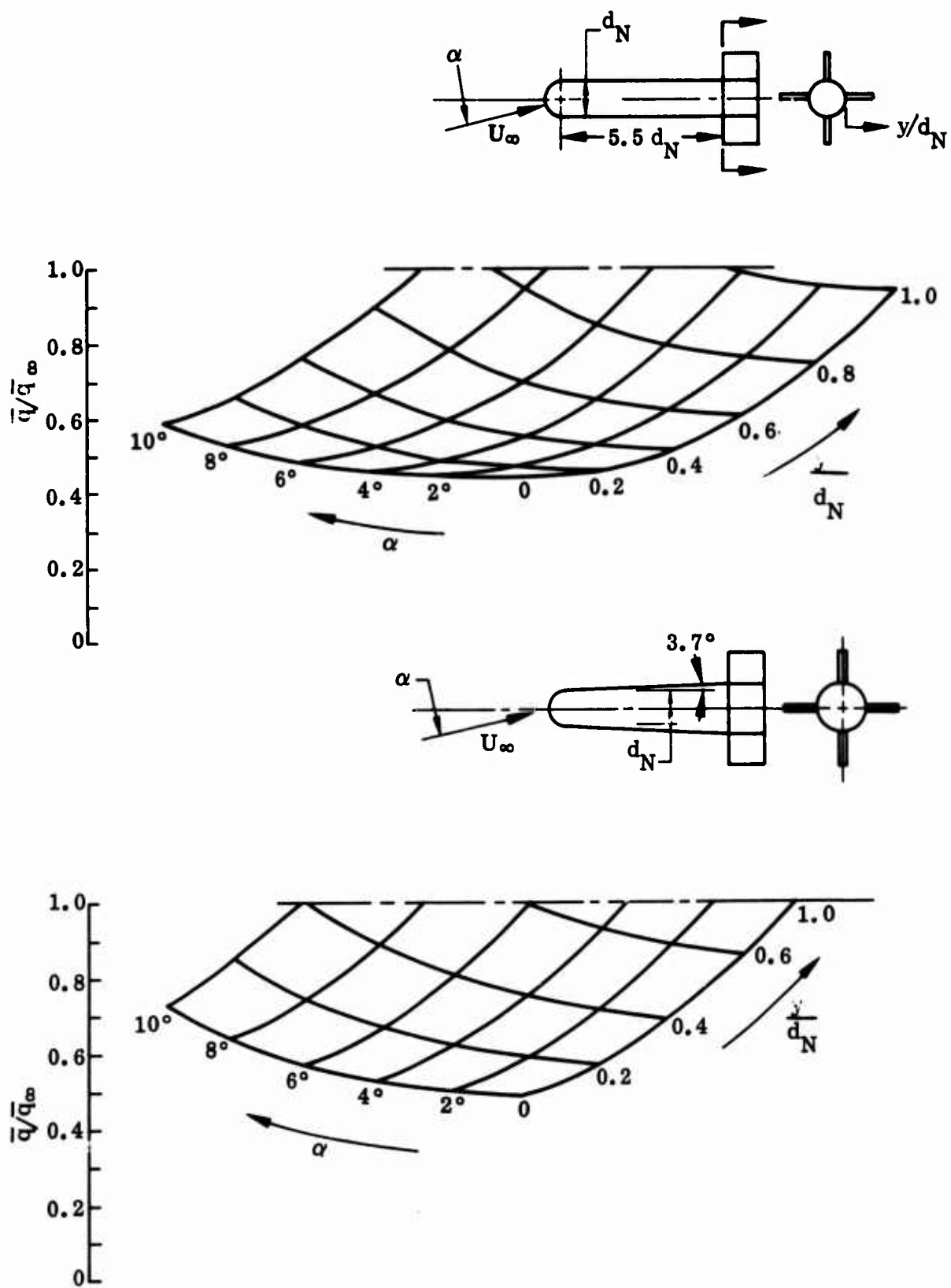
Figure 3.13   Dynamic pressure distribution over aft fins on two
hemisphere-nose missile bodies at $M_\infty = 6$
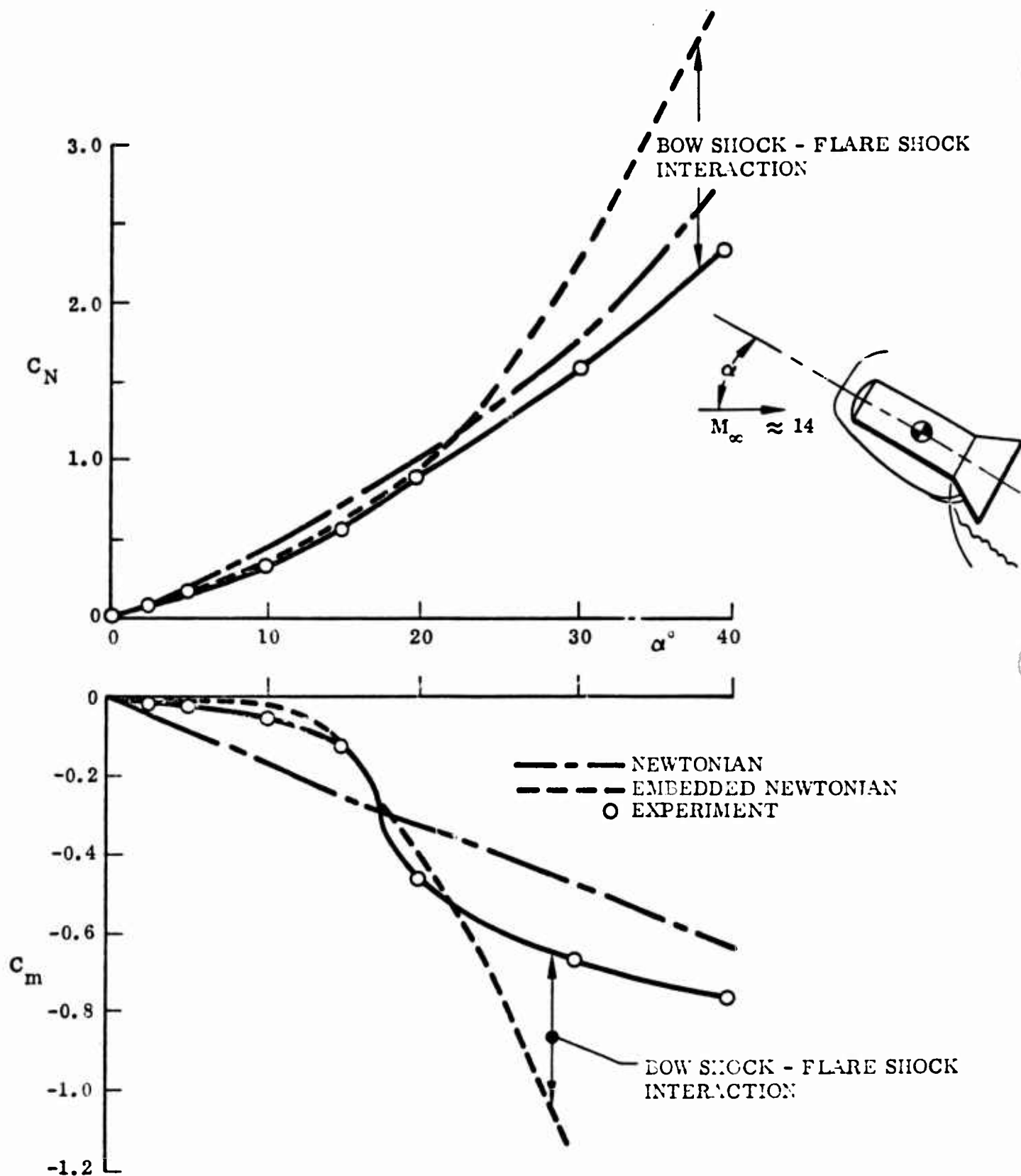
Figure 3.14   Aerodynamic characteristics of a blunt cylinder–flare body at $M_\infty \approx 14$
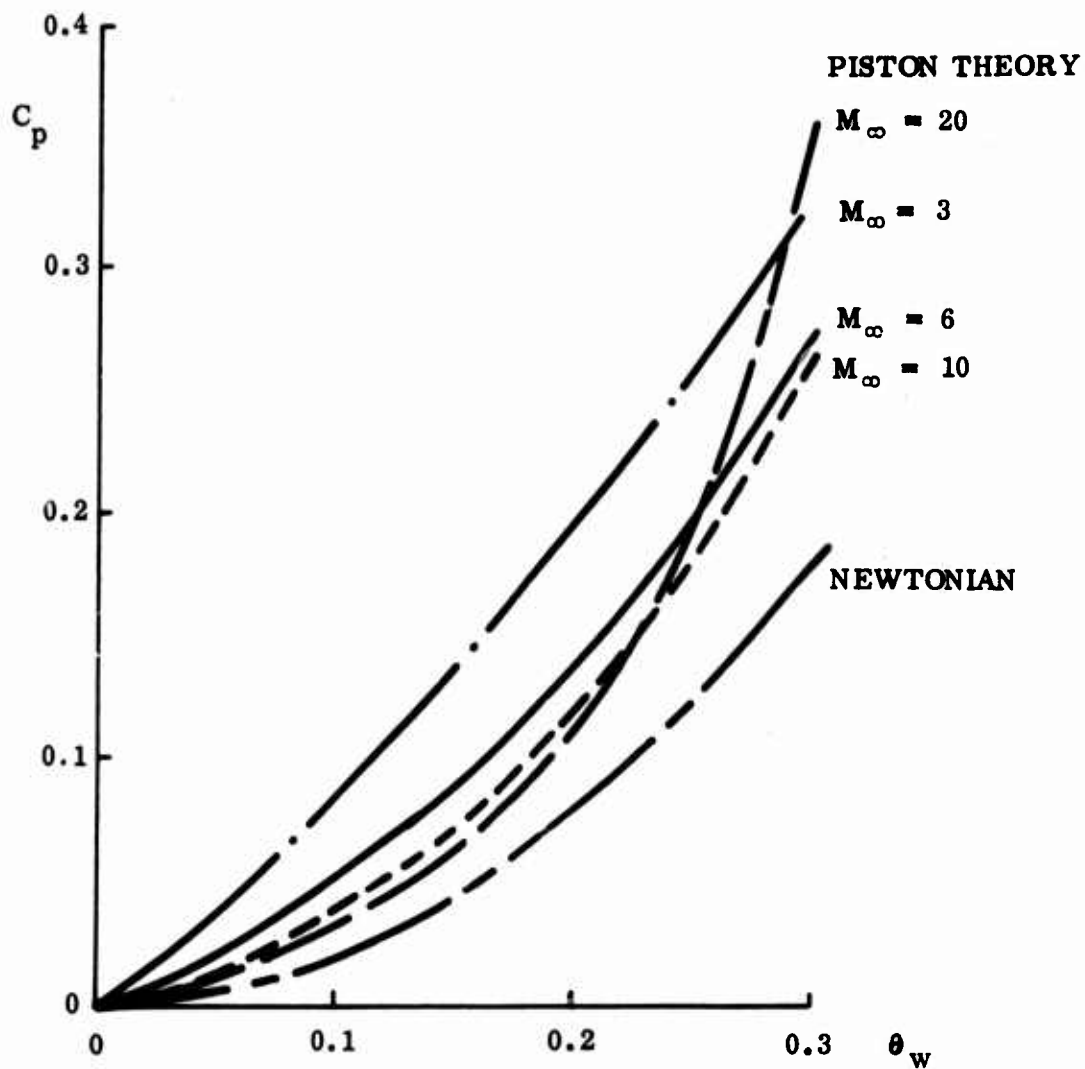
Figure 3.15   Wedge pressure coefficient predicted by piston theory
compared to Newtonian prediction
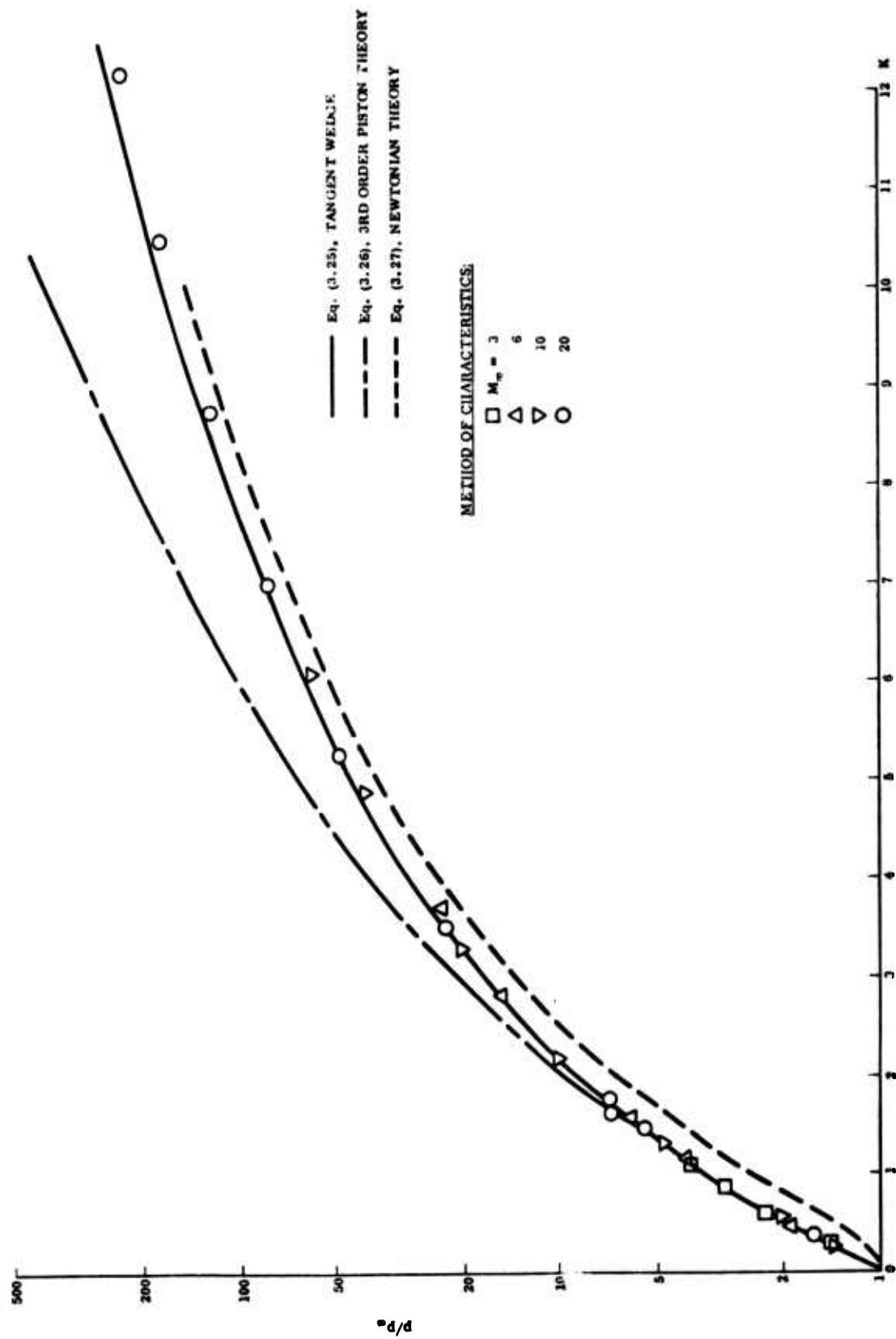
Figure 3.16 Comparison of wedge pressures predicted by method of characteristics, tangent wedge method, 3rd order poston theory, and Newtonian theory

Figure 3.17 Comparison of wedge pressure derivatives predicted by tangent wedge method, 3rd order piston theory, and gamma-corrected Newtonian theory

a. RIGID AIRFOIL PITCH OSCILLATIONS

b. ELASTIC AIRFOIL OSCILLATIONS

c. BINARY FLUTTER

Figure 3.18 Definition of oscillatory parameters
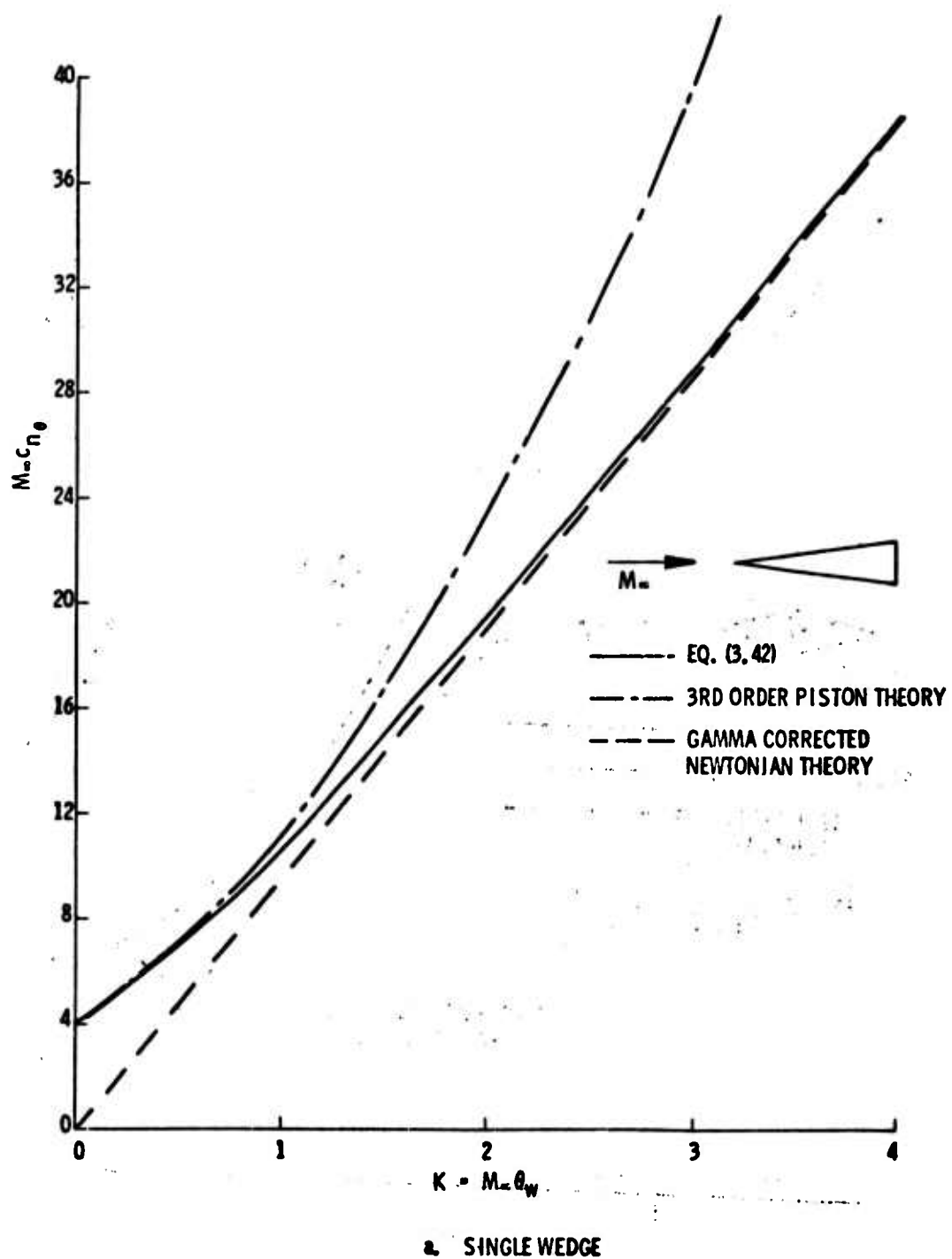
Figure 3.19   Hypersonic aerodynamic derivatives
(Sheet 1 of 2)
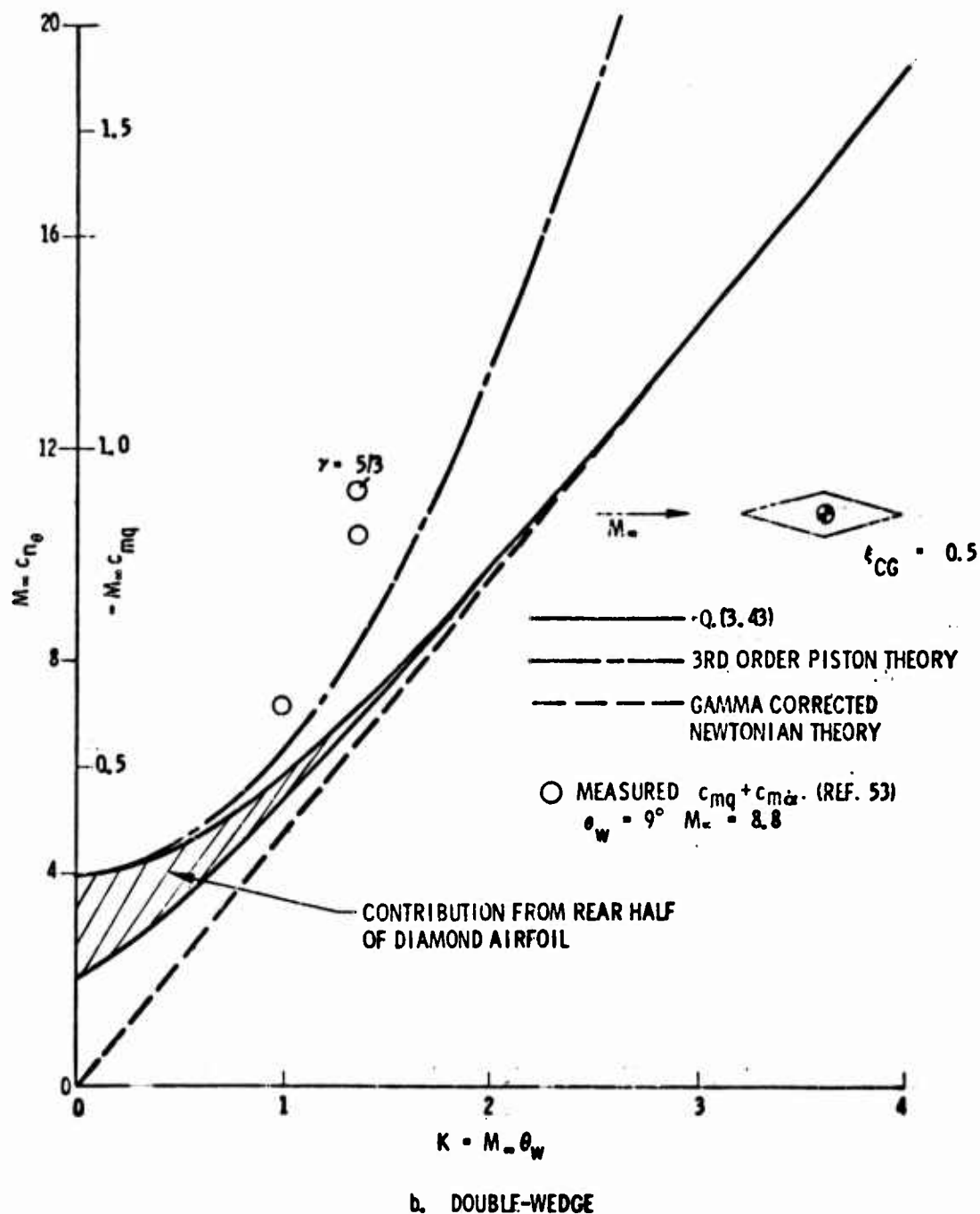
Figure 3.19 Hypersonic aerodynamic derivatives
(Sheet 2 of 2)
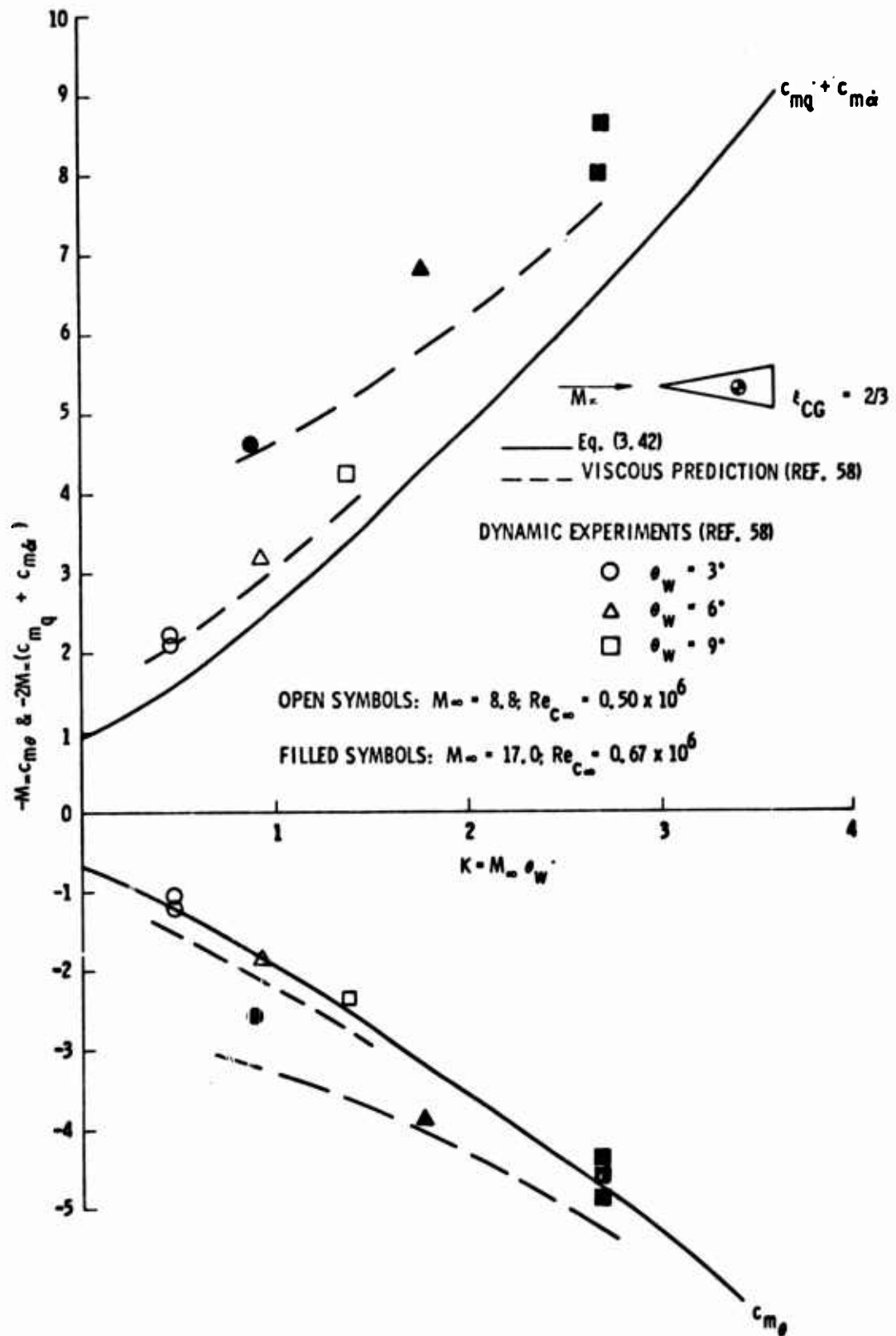
Figure 3.20 Comparison between predicted and measured stability derivatives of a single wedge
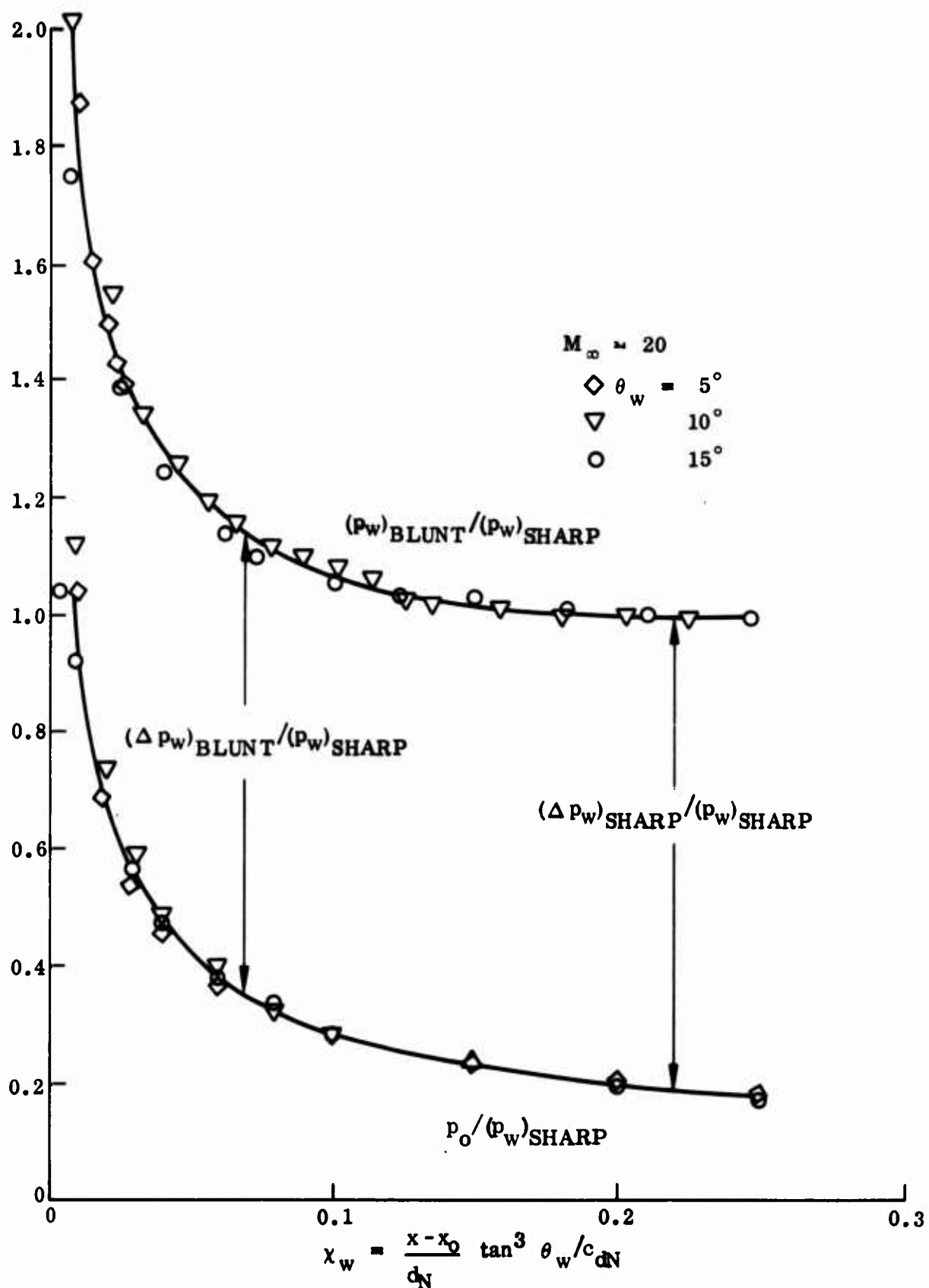
Figure 3.21 Pressure distribution over blunted wedges at $M_\infty = 20$
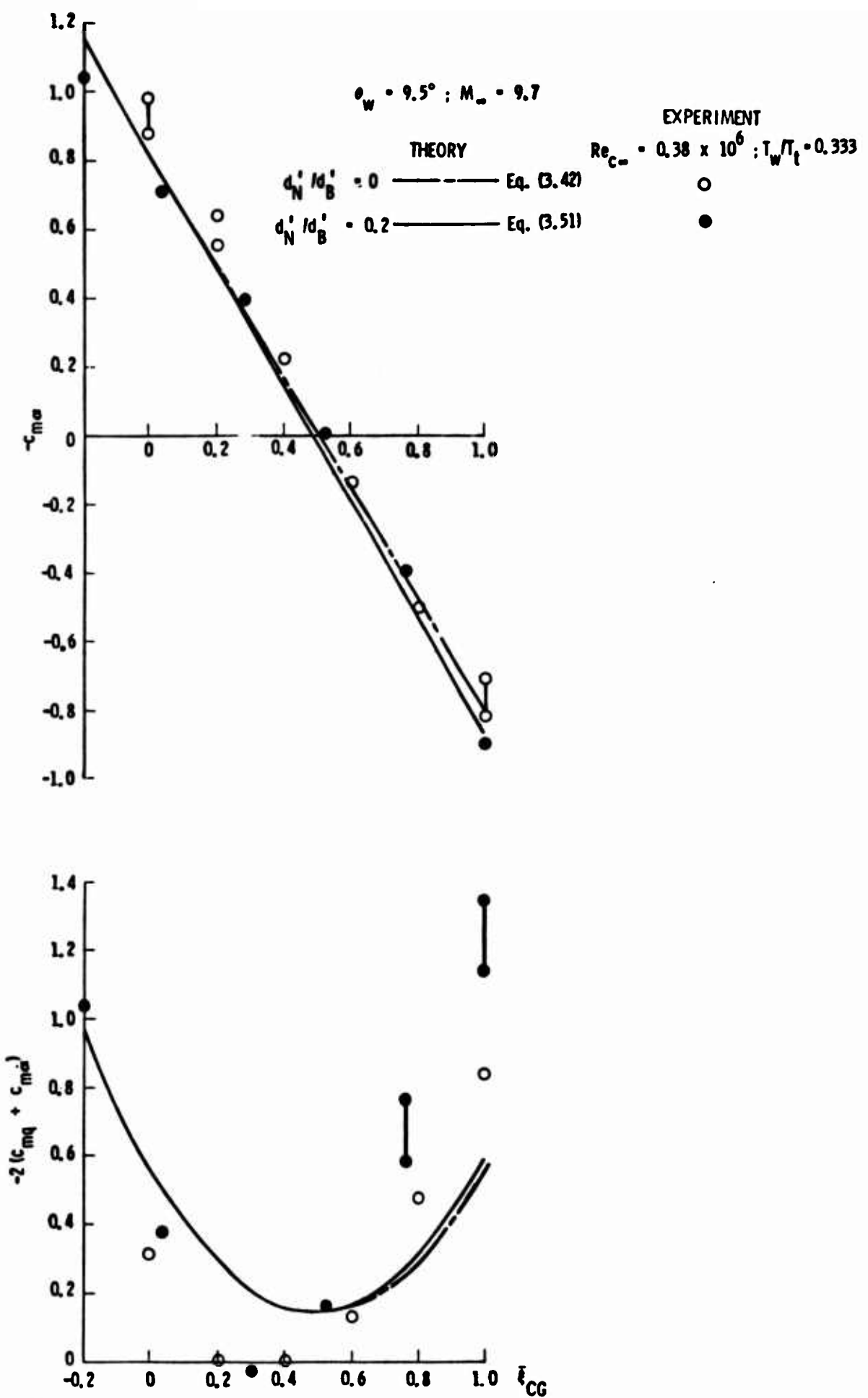
Figure 3.22   Comparison between predicted and measured viscous effects
on the aerodynamic characteristics of a 9.5° wedge

a. View normal to surface
Sidewalls as for $\xi_{CG} = 0$

b. View normal to surface
Sidewalls as for $\xi_{CG} = 1.0$

Figure 3.23 Wedge-side wall boundary layer interference (Ref. 78)

$$M_\infty = 15.8$$
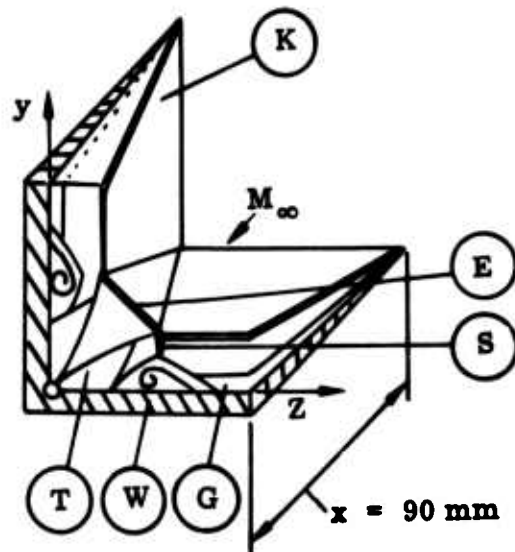
T Trennungsschicht

G Keilgrenzschicht

W Wirbel
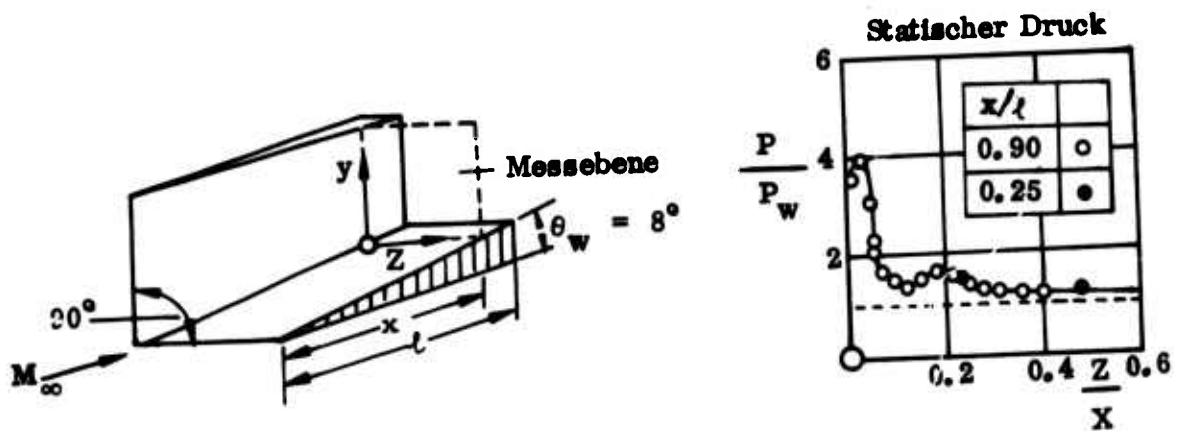
Figure 3.24 Wedge-wall corner flow (Ref. 90)
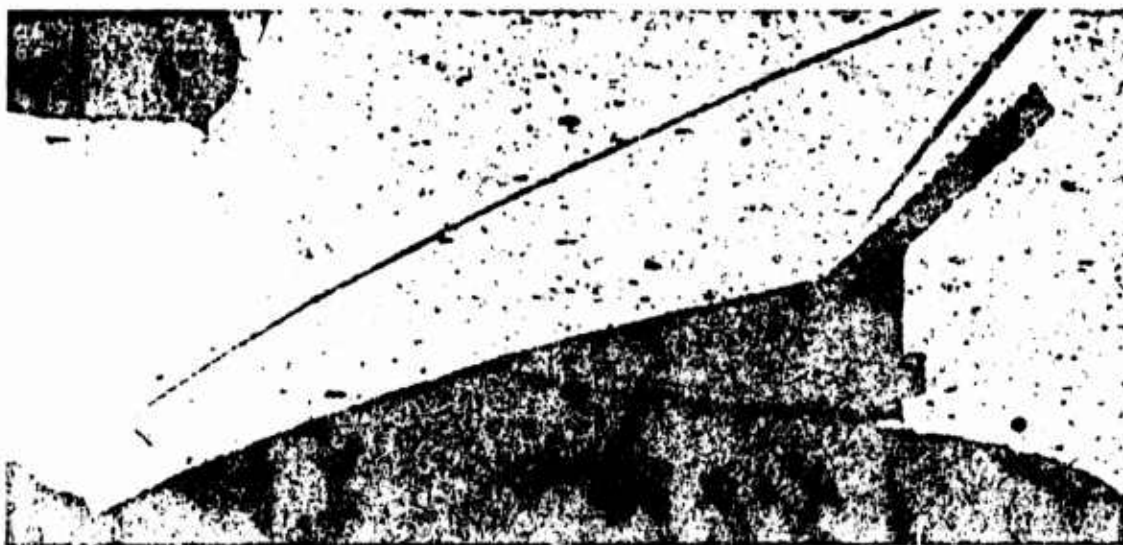
Figure 3.25   Flap shock in non uniform flow (Ref. 94)
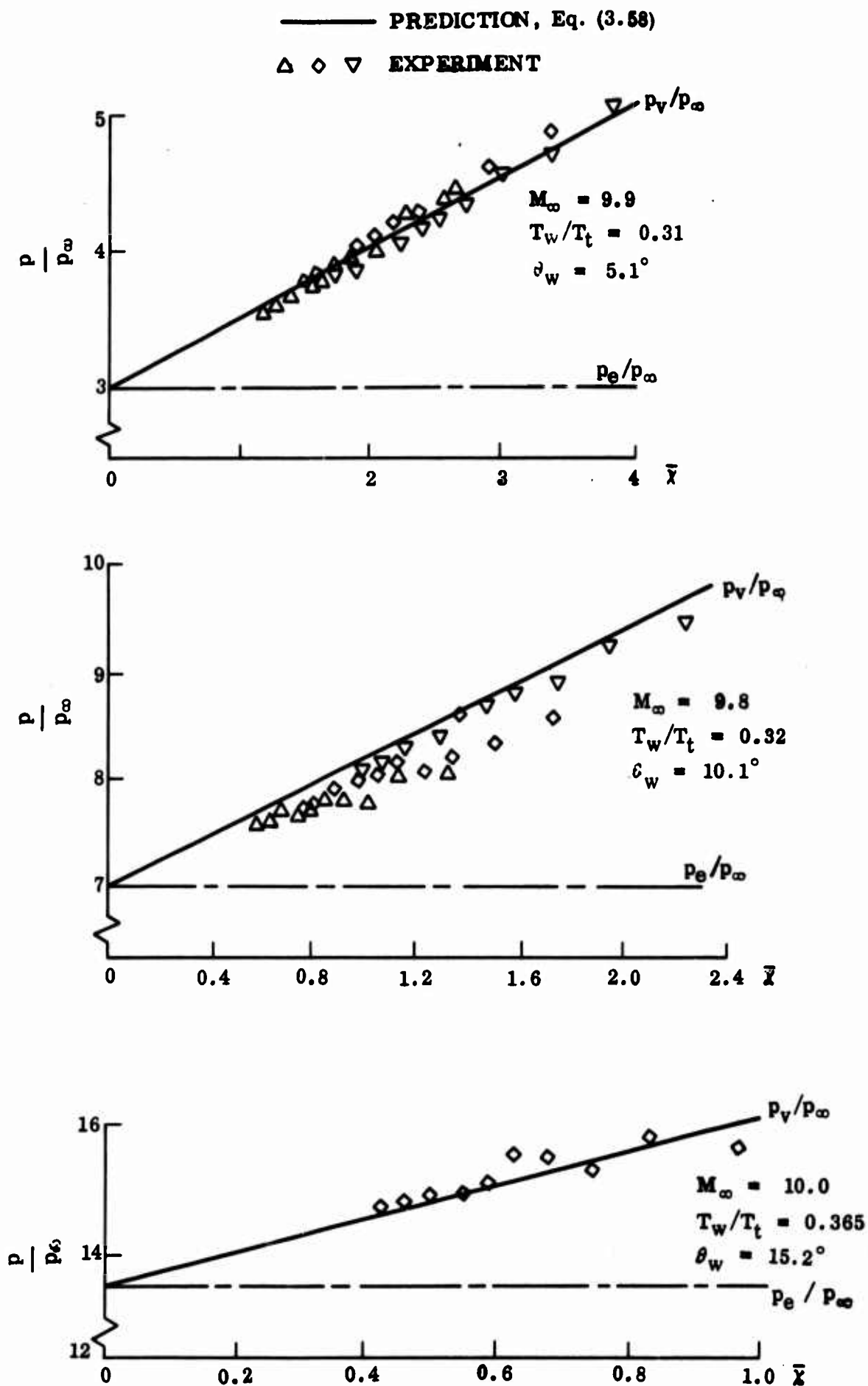
Figure 3.26 Comparison between predicted and measured pressure increase on a wedge due to viscid-inviscid interaction
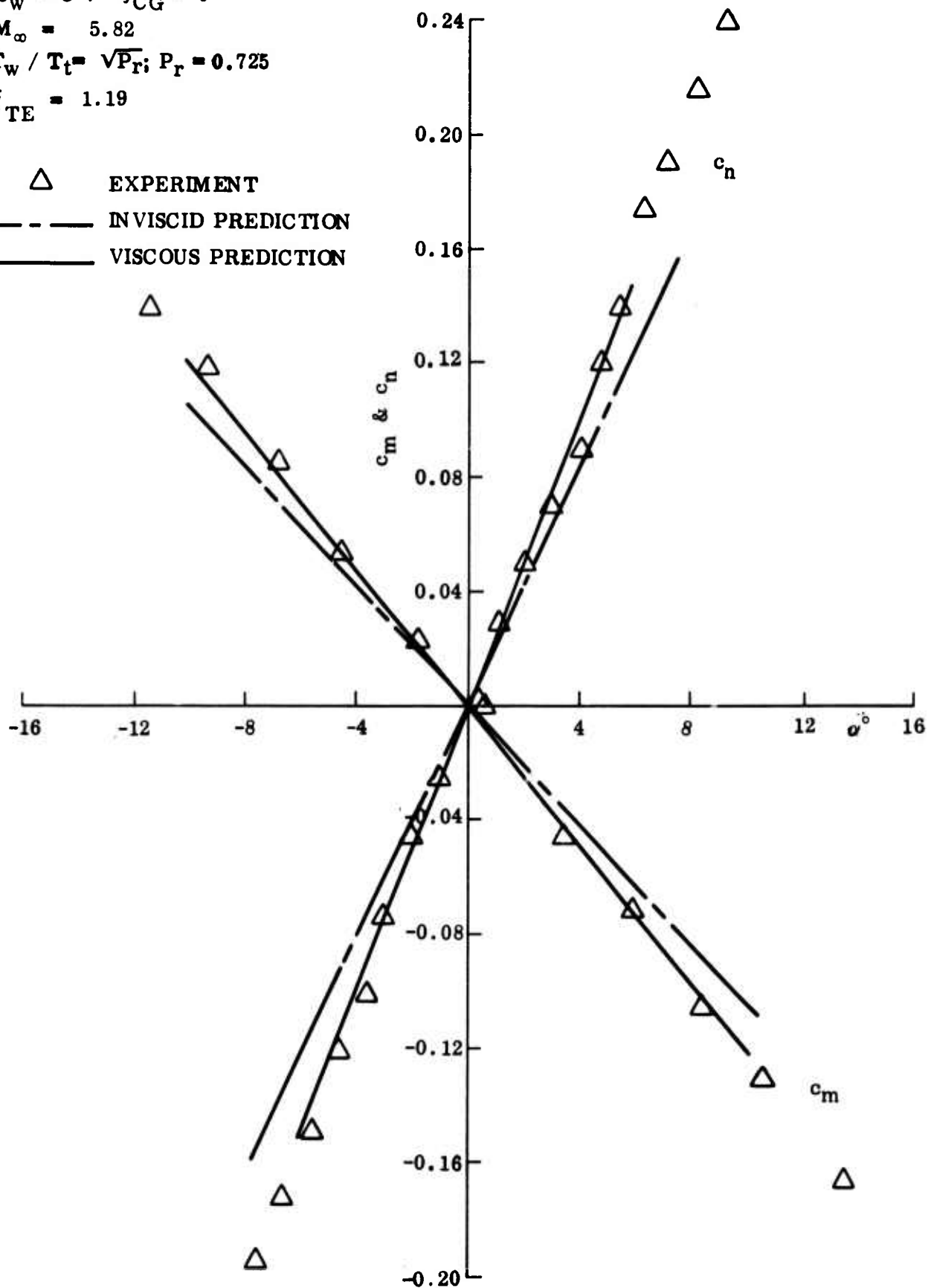
Figure 3.27 Comparison between predicted and measured viscous effects on the aerodynamic characteristics of a 5° wedge
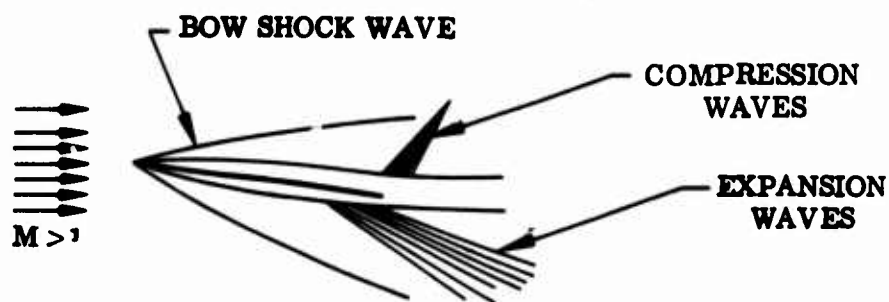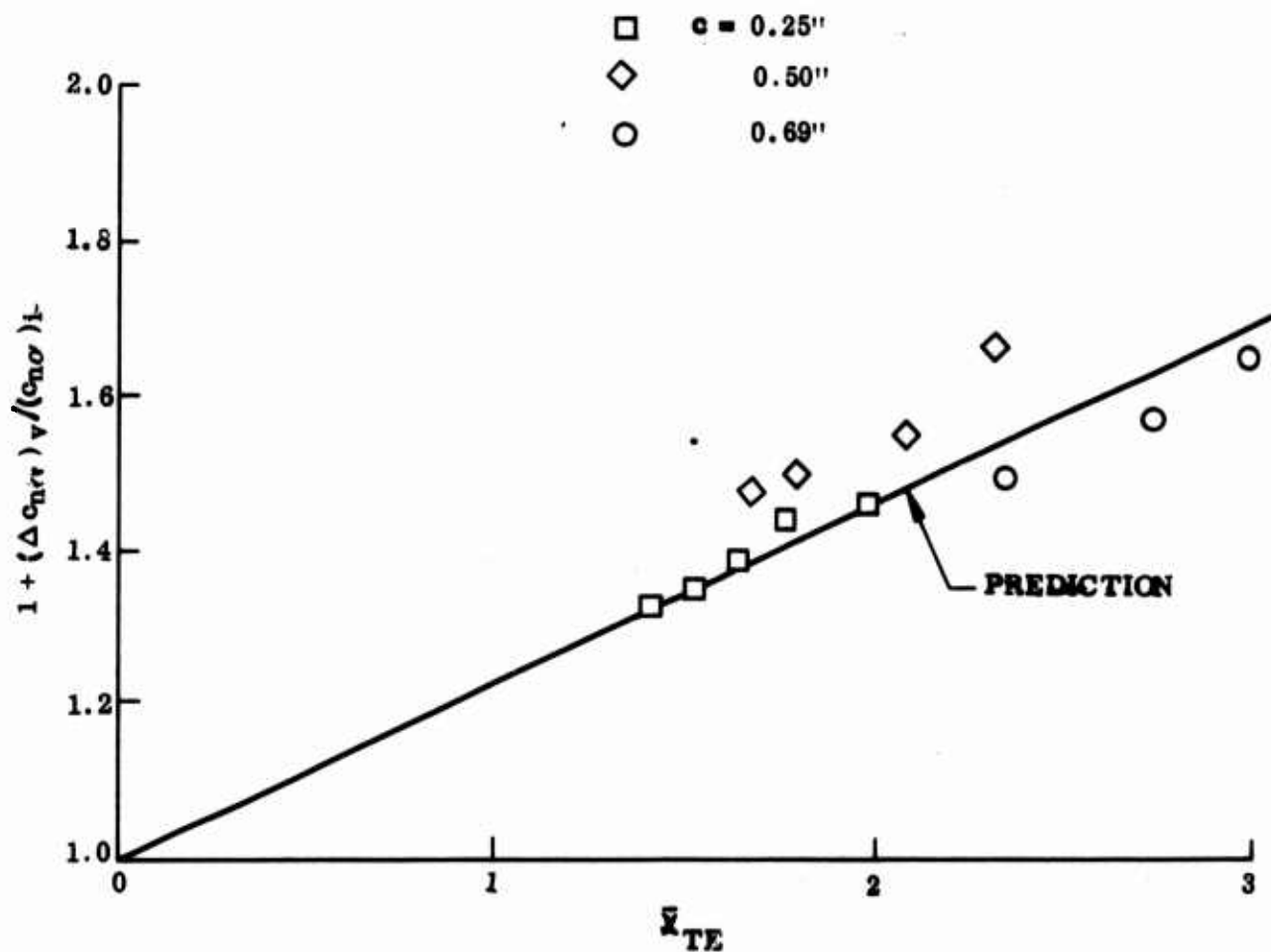
Figure 3.28 Comparison between predicted and measured viscous effects on C_{j_α} of a flat plate

3-79
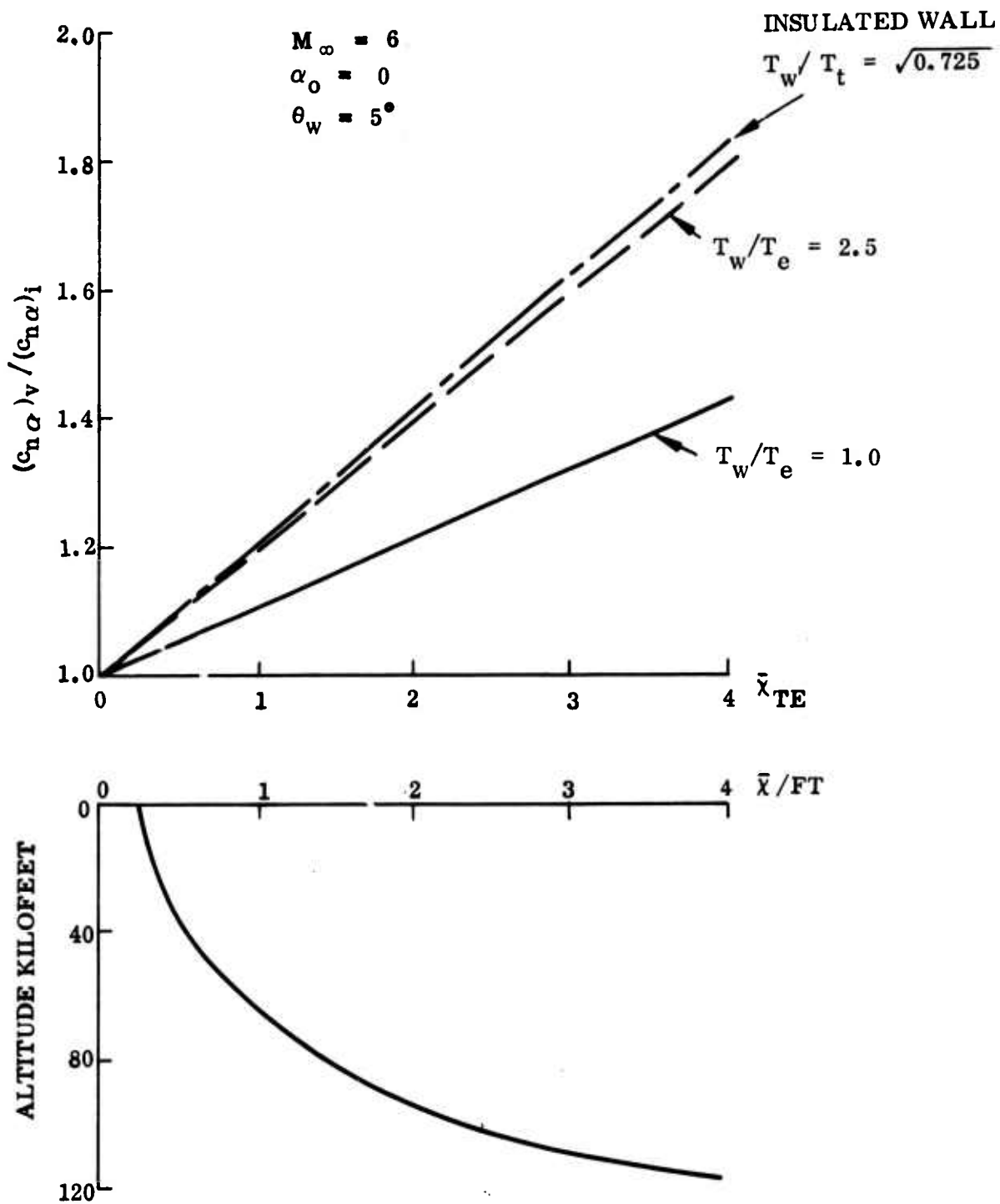
Figure 3.29 Effect of altitude and wall temperature on viscous effects on the normal force of a 5° wedge at $M_\infty = 6$
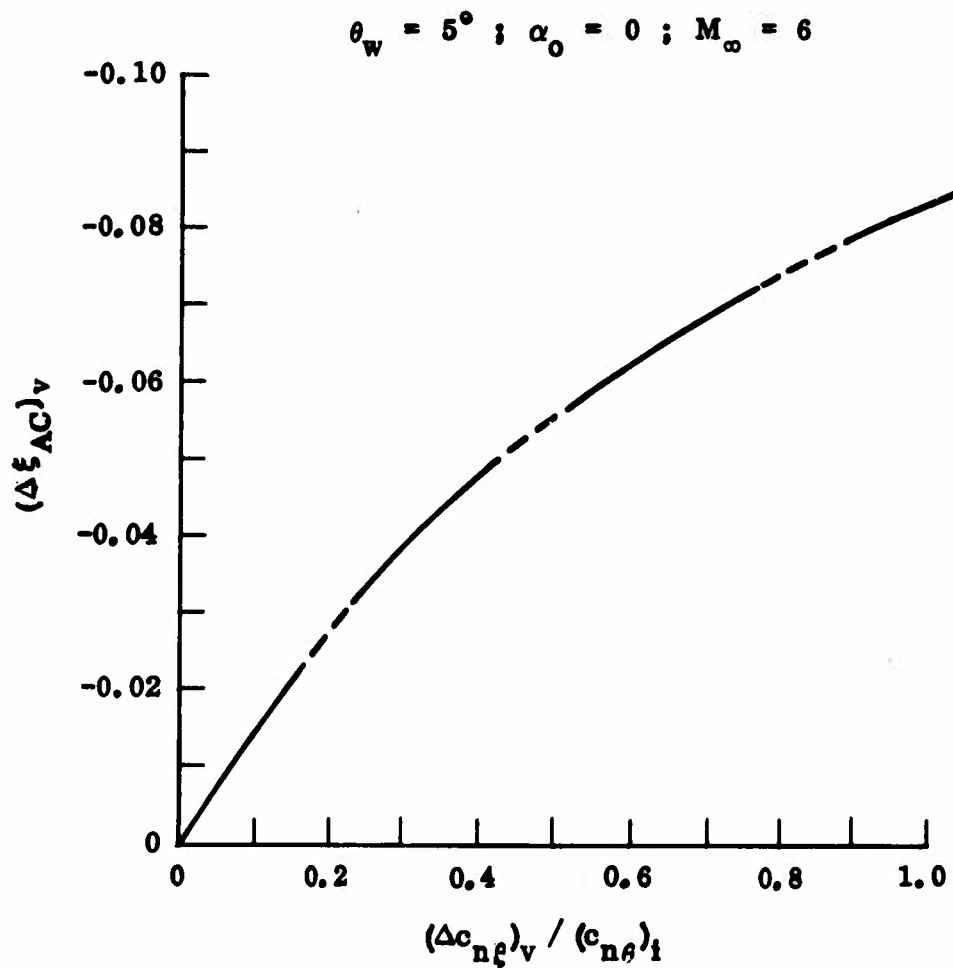
$\theta_W = 5°$; $\alpha_0 = 0$; $M_\infty = 6$

a. Viscous Induced Forward Movement of the Aerodynamic Center

Figure 3.30 Viscous effects on static and dynamic stability derivatives of a 5° wedge at $M_\infty = 6$ (Sheet 1 of 2)

$$\theta_w = 5°\ ;\ \alpha_0 = 0\ ;\ M_\infty = 6$$

$$--\ \cdot\ --\quad \frac{(\Delta c_{mq})_v}{(c_{mq})_i}\ \Bigg/\ \frac{(\Delta c_{n\theta})_v}{(c_{n\theta})_i}$$

$$\begin{array}{l} --\ \cdot\ --\\ ---\\ ——— \end{array}\quad \frac{(\Delta c_{mq})_v + (\Delta c_{m\dot\theta})_v}{(c_{mq})_i}\ \Bigg/\ \frac{(\Delta c_{n\theta})_v}{(c_{n\theta})_i}\ ;\quad \begin{array}{l} T_w / T_t = \sqrt{0.725}\\ T_w / T_e = 2.5\\ T_w / T_e = 1.0 \end{array}$$
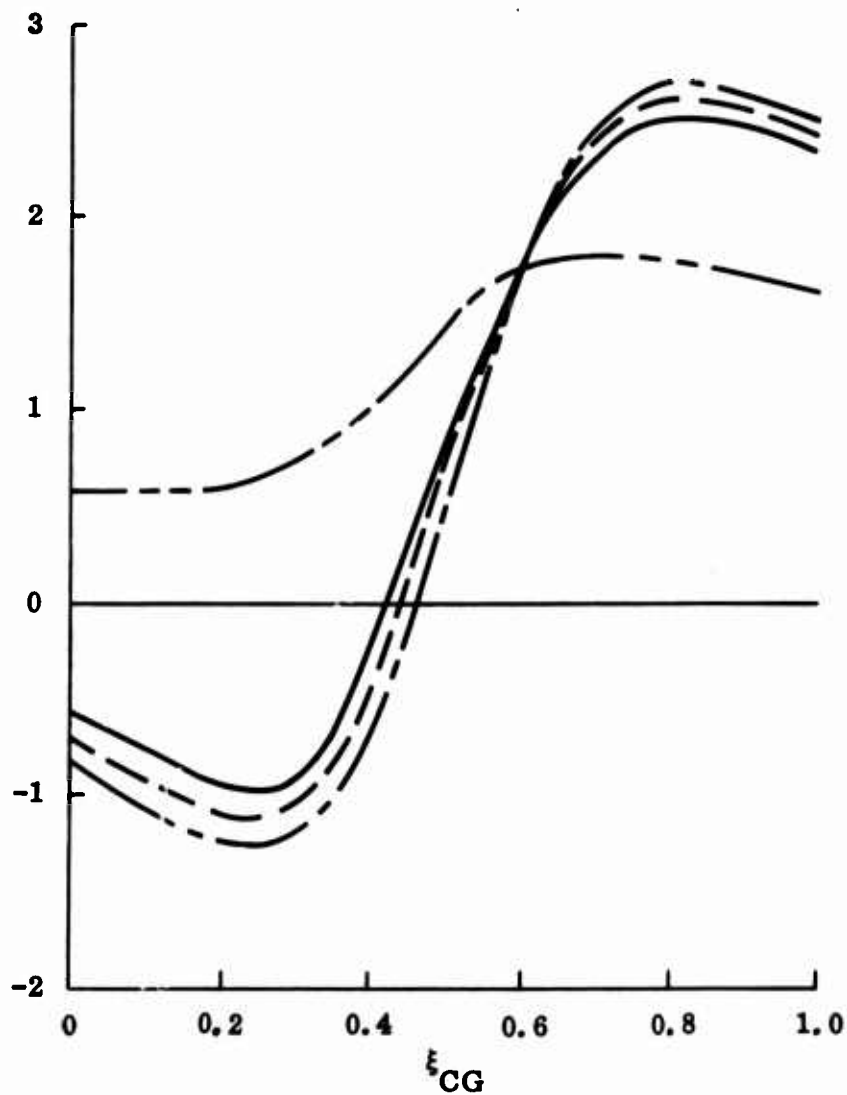
b. Normalized Viscous Induced Dynamic Effects

Figure 3.30 Viscous effects on static and dynamic stability derivatives of a 5° wedge at $M_\infty = 6$ (Sheet 2 of 2)
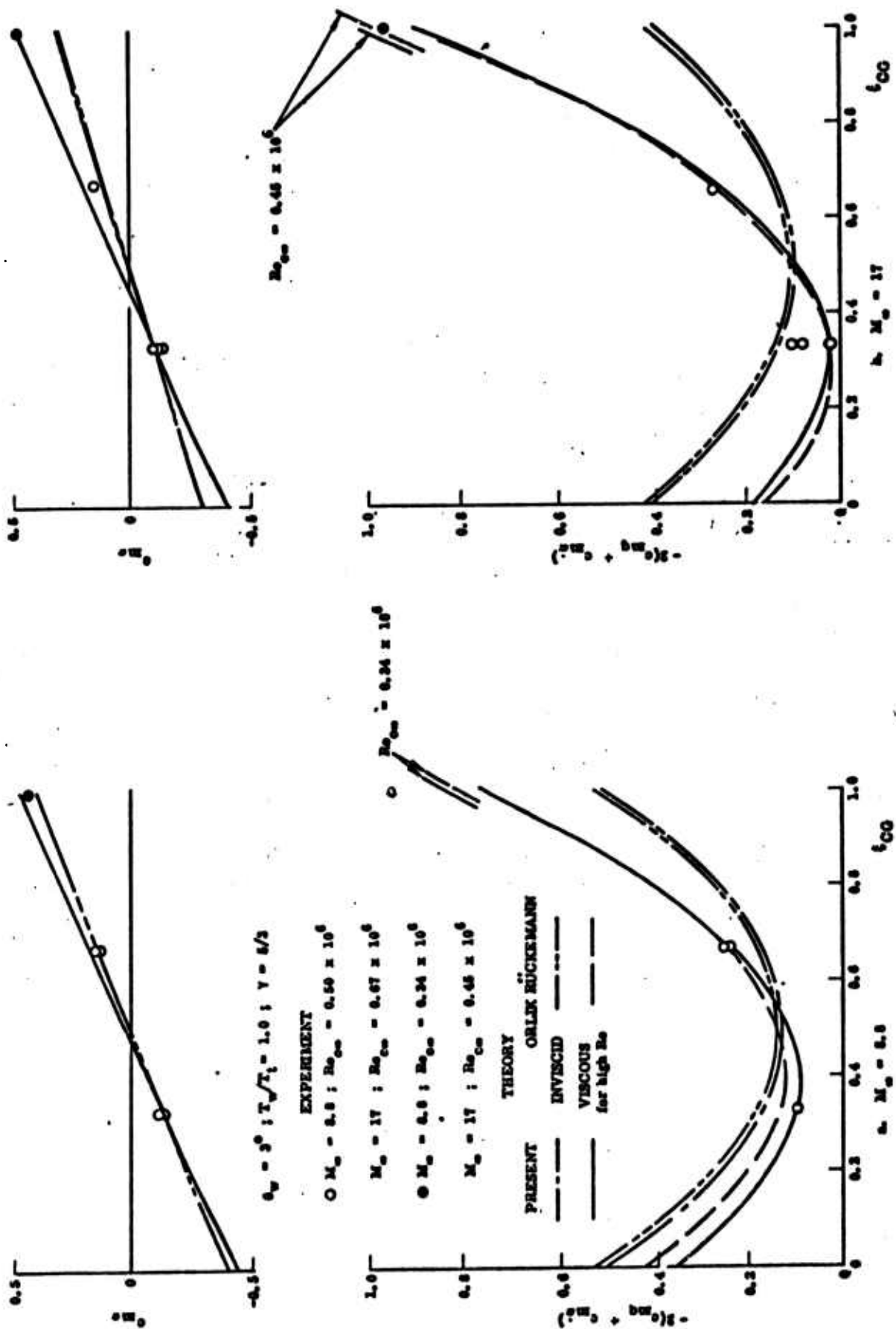
Figure 3.31 Comparison between predicted and measured viscous effects on static and dynamic stability derivatives of a 3° wedge for heated wall conditions
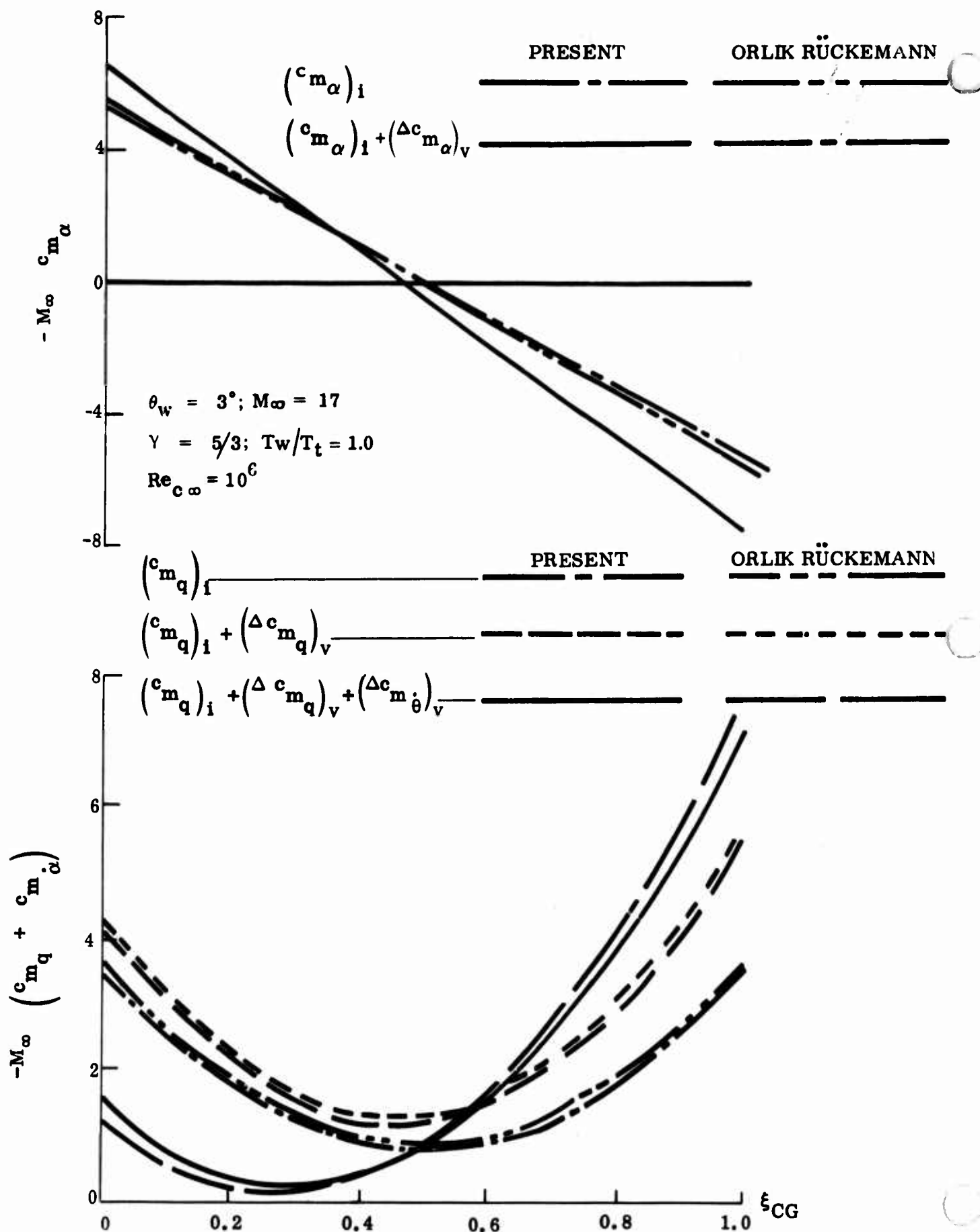
Figure 3.32   Detailed comparison between the present theory and Orlik-Rückemann's theory
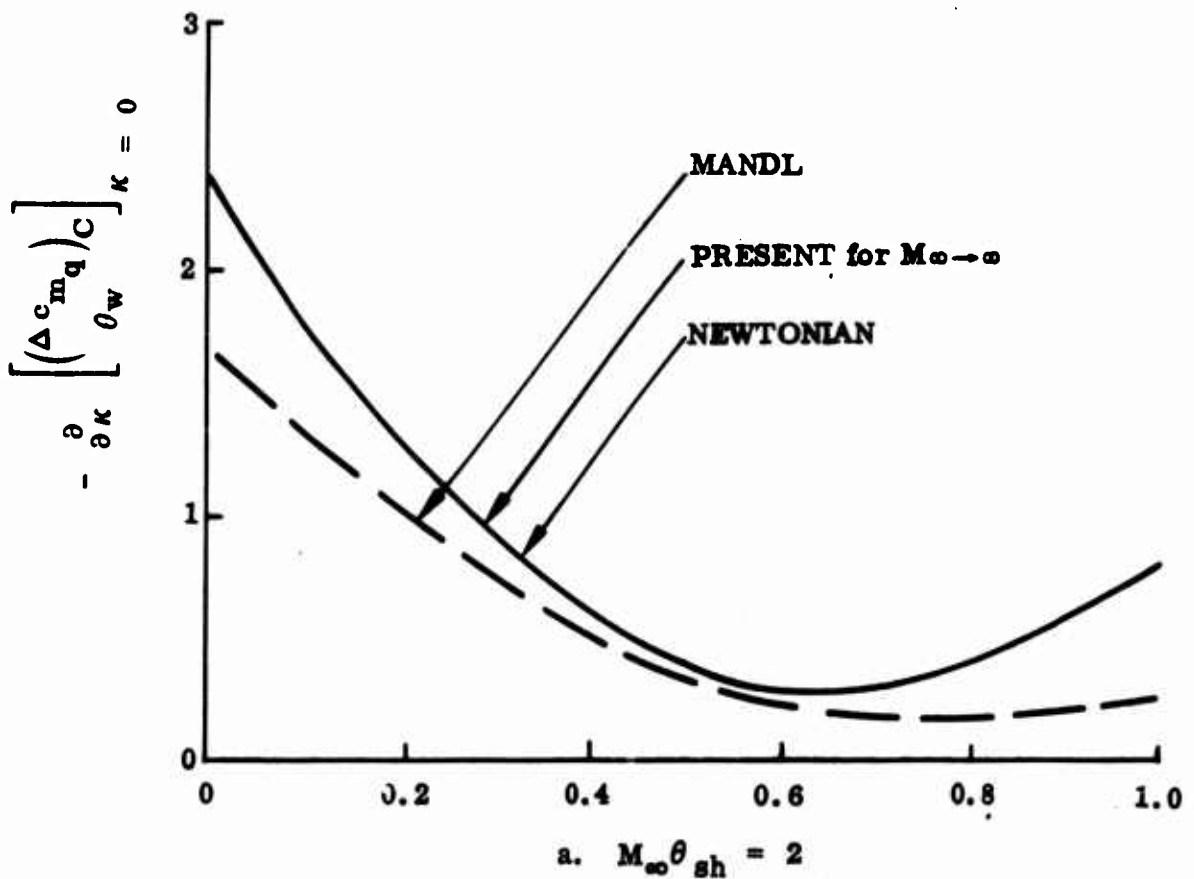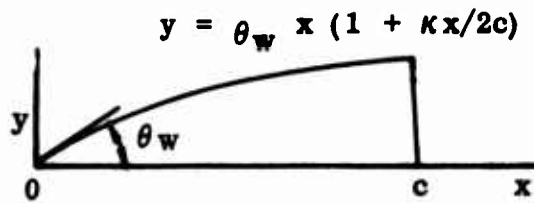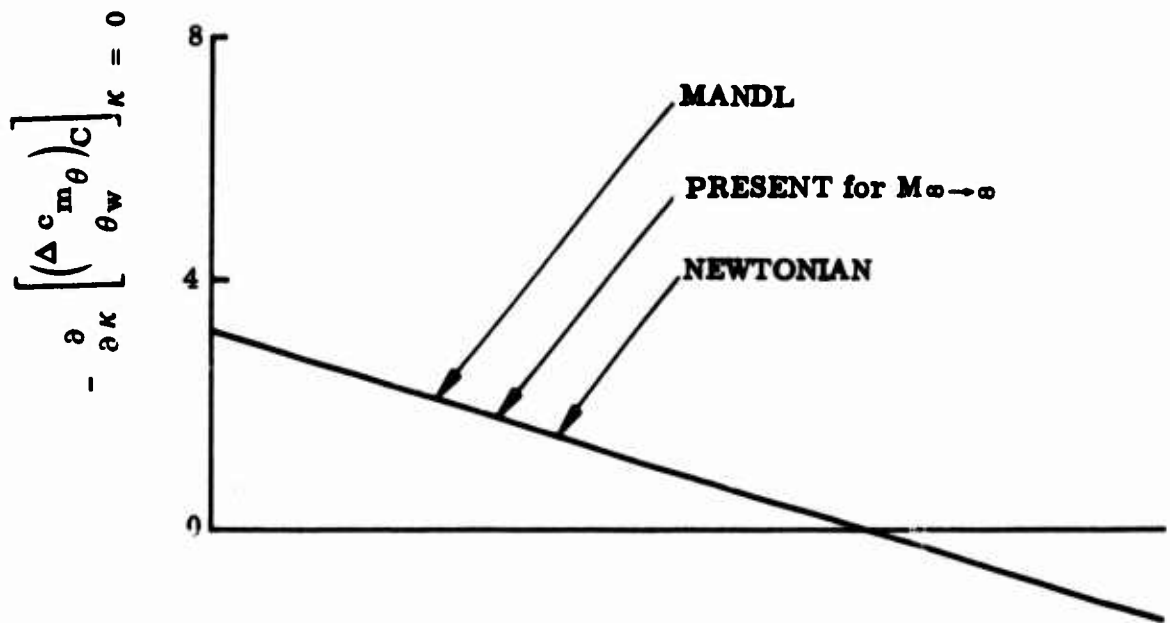
Figure 3.33 Comparison of present results with other theories
(Sheet 1 of 2)
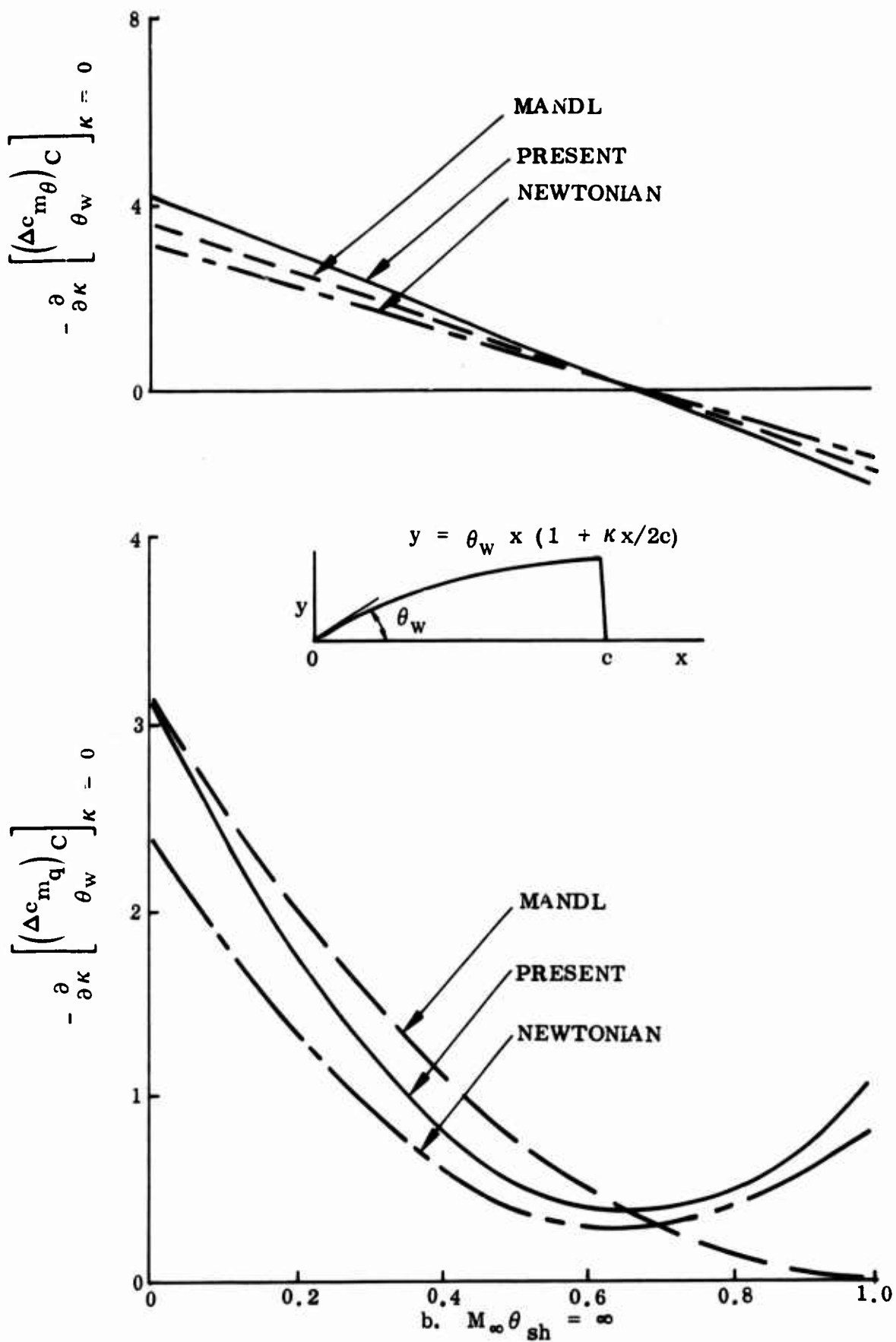
Figure 3.33 Comparison of present results with other theories
(Sheet 2 of 2)
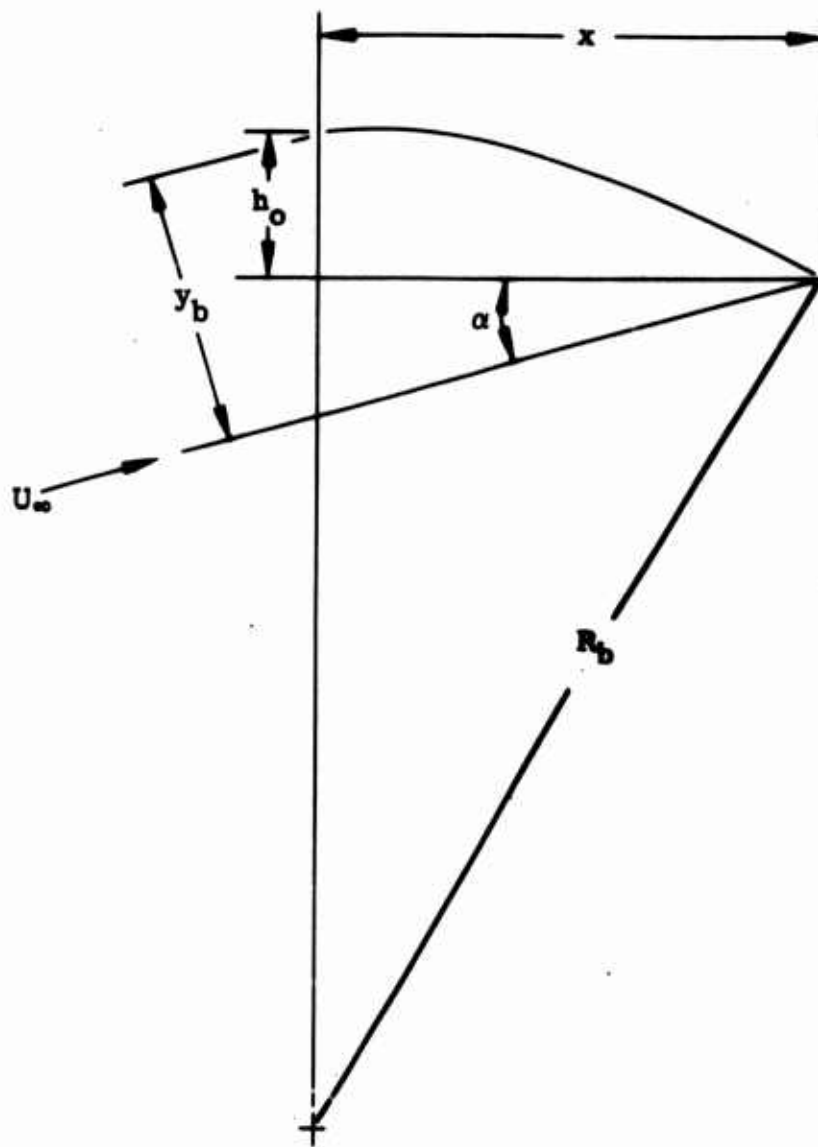
Figure 3.34 Cambered thin plate geometry
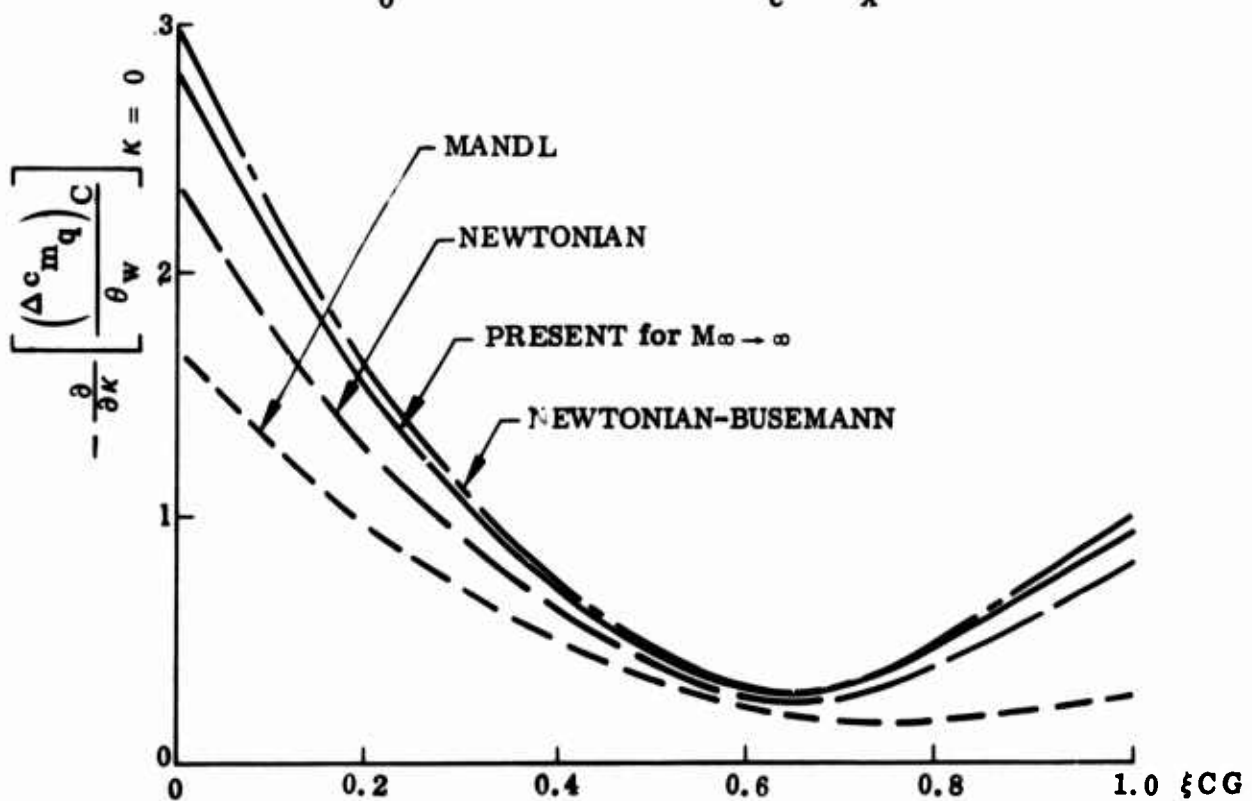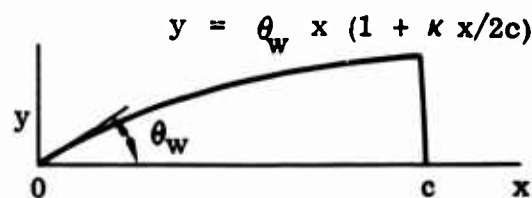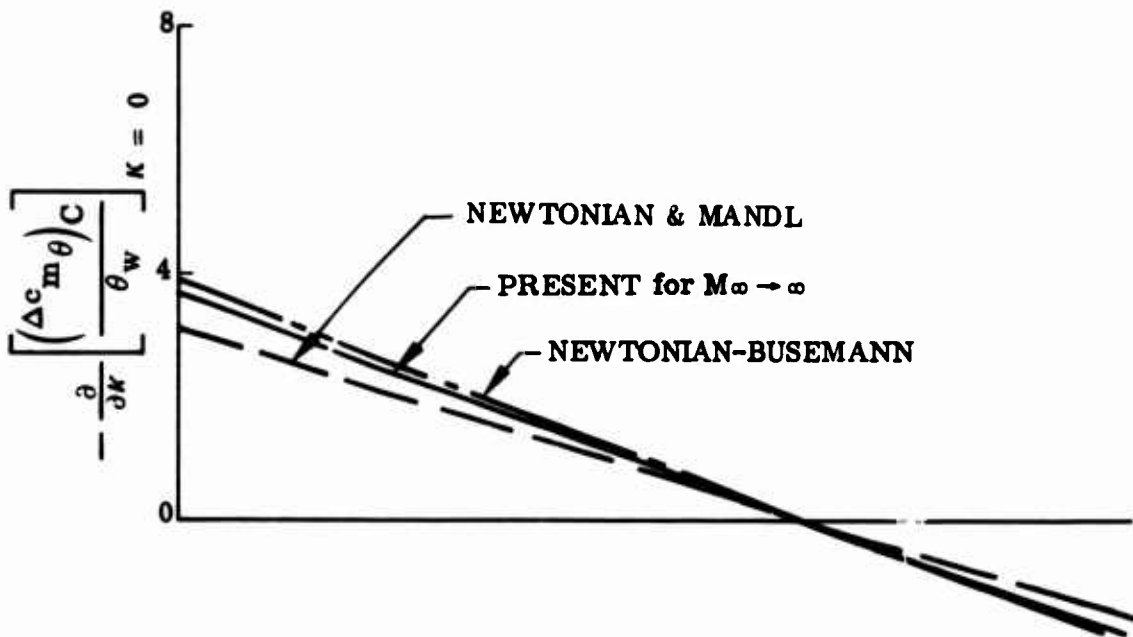
Figure 3.35   Effect of longitudinal surface curvature and centrifugal pressure correction at $M_\infty \theta_w = 1.25$

Section 4
AEROELASTIC ANALYSIS

4.1 Approach

Over the past decade many studies have been made of the aeroelastic behavior
of a wide range of vehicle configurations operating at hypersonic speed. Some
of these are referred to in Section 1 which gives a brief summary of the state
of the art in the field. Here an aeroelastic analysis system is presented for
lifting surfaces on tactical missiles. Previously existing codes for aero-
dynamic, thermal, and elastic analysis with modifications as necessary have
been utilized as much as possible. The system of computer codes is intended
to provide a well tested analytical method for solving a wide range of hyper-
sonic aeroelastic problems for lifting surfaces in the Mach number range of
roughly 3 to 6.

The equations governing a vehicle under flight conditions can, after reduction
to a finite number of degrees of freedom, be written in the form

$$[M] \{ \ddot{u} \} + [D] \{ \dot{u} \} + P (\dot{u}) + K(u) + Q(u) = \{ F \} \qquad (4.1)$$

Here the vector u represents the "discretized" displacement field, $[M]$ and
$[D]$ represent structural inertia and damping matrices. The operators P
and Q determine the components of aerodynamic forces caused by structural
deformation. In the linear case the operator K corresponds to the stiffness
matrix. It determines internal forces in terms of the displacement unknowns.
Finally, $\{F\}$ is a vector representing other than displacement dependent
forces on the structure, including the effects of aerodynamic heating. The
components of $\{F\}$ generally vary with time. Even when stationary flight
conditions are reached, temperatures will continue to vary until thermal
equilibrium is obtained.

A straightforward numerical integration of Eq. (4.1) over the trajectory or over pertinent parts of it, is in principle feasible. Such a solution would yield the answers to all questions about structural integrity, including possible aeroelastic instability. However, the time period over which the integration must be carried out is large in comparison to the period of free vibrations of a typical wing. Therefore, the procedure will in general not be economically feasible, and even in the presence of our days' high-speed digital computers, the classical methods of aeroelastic analysis survive as viable options.

The force vector $\{F\}$ is generally a function that varies slowly with time in comparison with the free structural vibration. Consequently, unless a vibration is excited, the first three terms in Eq. (4.1) can be discarded, leaving us with the equation:

$$K(u) + Q(u) = \{F\} \tag{4.2}$$

Here K and Q are nonlinear algebraic operators, containing terms of first through third degree in u. The application of these operators to a function results in a vector with the number of elements N equal to that of the load vector $\{F\}$. Consequently, we can write

$$K_i(u) + q\, Q_i(u) = F_i \qquad i = 1, N \tag{4.3}$$

For reasons that will be clear from the subsequent discussion, we make the substitution

$$\{u\} = \{u_o\} + \{u_1\} \tag{4.4}$$

in which we assume that $\{u_o\}$ represents an equilibrium configuration and that $\{u_1\}$ is so small that all terms of higher than the first order in u_1 may be discarded.

After substitution of Eq.(4.4) into Eq.(4.2), we can subtract the equation:

$$K(u_o) + q\ Q(u_o) = \{F\} \qquad (4.5)$$

Then Eq.(4.2) takes the form

$$[\bar{K}]\ \{u_1\} + q\ [\bar{Q}]\ \{u_1\} = 0 \qquad (4.6)$$

The elements of the matrices $[\bar{K}]$ and $[\bar{Q}]$ are in general functions of the displacement vector $\{u_o\}$. That is,

$$\bar{K}_{ij} = (\partial K_i/\partial x_j) \text{ at } u = u_o$$

and

$$\bar{Q}_{ij} = (\partial Q_i/\partial x_j) \text{ at } u = u_o \ .$$

$$\qquad (4.7)$$

For Eq.(4.7) to have nonzero solutions

$$\text{Det}\ \left([\bar{K}] + \bar{q}_\infty\ [\bar{Q}]\right) = 0\ . \qquad (4.8)$$

If $\{F\} = 0$ (no thermal effects, symmetric wing profile, and zero angle of attack), then $[\bar{K}]$ is represented by the linear stiffness matrix $[K]$, and Eq. (4.8) represents the classical formulation of the divergence problem (static aeroelasticity). With a symmetric wing profile thermal effects cause only in-plane displacement components. The eigenvector obtained from Eq. (4.8) contains normal displacement components only. In that case the solution represents a bifurcation in the equilibrium path. The matrix $[\bar{K}]$ represents the linear stiffnes matrix for the prestressed structure. That is, it includes the effects of thermal stresses on the stiffness properties.

If the fundamental solution $\{u\} = \{u_o\}$ of Eq. (4.2) contains normal displacement components, the vanishing of the determinant (Eq. (4.8)) generally represents a vertical tangent in a displacement/velocity diagram rather than

a bifurcation point. In that case the eigenvalue approach to the divergence problem is not rigorous. It is possible to linearize Eq. (4.2) for computation of $\{u_o\}$ but the solution obtained from Eq. (4.8) represents a more or less unconservative estimate of the critical velocity. We refer to the solution of Eq. (4.8) as linear and the direction solution of Eq. (4.2) as nonlinear static aeroelasticity. The choice between the methods is discussed in subsection 4.4.

Dynamic aeroelastic instability is said to occur if the flight conditions are such that the amplitude of a vibration will increase with time. Solution to that problem, of course, requires that the "dynamic" terms in Eq. (4.1) are included. The structural damping is often discarded since its magnitude is not well known and its exclusion results in only slightly conservative results for lifting surfaces such as the missile fins considered in the present analysis.

The time step in the integration procedure must be relatively small in comparison to the period for important vibration modes. Since the duration of the trajectory is very large in comparison to a vibration period, the direct approach is impractical. It is possible to "compress" the trajectory into a shorter time period as long as q and $\{F\}$ remain slowly varying. This leads to some difficulties with the thermal terms. Better efficiency may be achieved if the quasistatic solution first is obtained (Eq. (4.2)). The analysis can then be restarted with excitation of a small amplitude vibration at appropriately selected points along the trajectory. The trajectory is safe if the vibration amplitude is decaying at all points along the trajectory. The direct integration of Eq. (4.1) will be referred to as nonlinear dynamic aeroelasticity.

A linearization of the dynamic solution can be obtained in the following way. In Eq. (4.1) is substituted

$$\{u\} = \{u_o\} + a_i \{u_i\} \sin \omega_i t \tag{4.9}$$

where $\{u_o\}$ represents the quasistatic solution and a_i, $\{u_i\}$ and $\{\omega_i\}$ represent amplitude, deformation pattern, and frequency of the i-th vibration mode. It is assumed that the a_i are so small that terms of higher than first order in a_i can be discarded. After subtraction of the terms representing quasistatic equilibrium, we obtain a homogeneous equation system from which frequencies and modes can be determined as eigenvalues and eigenvectors.

Frequencies and generalized masses corresponding to a finite number of modes can be determined at appropriately chosen points along the trajectory. These results can be used in a classical flutter analysis as described in numerous text books. We refer to this procedure as linear dynamic aeroelasticity analysis.

The information obtained from the linear eigensolution to extract the flutter speed is somewhat limited since it does not indicate the rate of growth of the vibration amplitude. However, it does not seem likely that a vehicle can be subjected to supercritical condition for a significant time interval without structural failure.

It is true also that the linearization of the analysis precludes effects of stiffening of the structure with finite deformation. For the cantilevered plates considered such structural stiffening is insignificant within the range of tolerable deformation. In most cases the stiffening of the "aerodynamic spring" will also be insignificant. Thus, it appears that the linear dynamic aeroelasticity analysis is quite satisfactory for the present purpose.

All options discussed above have been retained as capabilities in the computer program for aeroelastic analysis, STAGS-MOFA. In the case of linear divergence analysis the problem defined by Eq. (4.8) is not solved directly. The nonconservative nature of the aerodynamic matrices results in a matrix that is not symmetric. Eigenvalue routines for such problems are not available for problems of the size that may be required for an accurate solution of the lifting surface with thin leading and/or trailing edges. As the development of such procedures could not be contained within the scope of the present program, the aeroelastic analysis was based on the modal approach.

That is, nonlinear terms in Eq. (4.1) are discarded. Linearized equations gives quasi static solutions that define the prestress for a free vibration analysis. The vibration modes and frequencies are used in a modal analysis of linear divergence.

The building blocks for the aeroelastic analysis then are

TRR1D   for thermal analysis

STAGS   for elastic analysis

FLAM   for computation of aerodynamic forces

MODIV   for linear static aeroelastic analysis

MOFA   for linear dynamic aeroelastic analysis

The manner in which those programs work together is indicated by the Flow Chart in Fig. 4.1. Auxiliary storage is used for intermediate results, such as temperatures from TRR1D. However, by proper choice of control cards it is possible to exercise the programs in sequence during the same computer run.

The temperatures are first computed in TRR1D at a number of time steps over the trajectory. The results are stored in a file and accessible so that the temperature distribution at any fixed value of time can be obtained by inter-polation. Subsequently, the values of the aerodynamic force matrices are determined in FLAM as discussed in subsection 4.3. The information is available to STAGS as needed during a nonlinear quasi static or nonlinear transient analysis. The quasi static analysis gives the solution to the nonlinear di-vergence problem as well as a complete picture of stresses and strains in the structure during the trajectory.

For linear static aeroelasticity analysis the user will ask STAGS for a linear analysis. Modes and frequencies will be computed and stored so that for each preselected time step a computed critical velocity can be obtained by use of the MODIV program. The trajectory is safe if the computed critical velocity at all points exceeds the actual velocity.

Unless the STAGS analysis consists of direct integration of the nonlinear form of Eq. (4.1), a separate dynamic aeroelastic analysis is also needed. For this purpose the user can select to obtain either a linear or a nonlinear quasi static solution. If the user chooses the option of nonlinear dynamic aeroeleasticity analysis, the transient analysis will be restarted at pre-selected steps with excitation of the vibration modes. If he chooses linear dynamic aeroelasticity analysis, modes will be stored on file and utilized by MOFA in a classical flutter analysis. If the computed flutter velocity exceeds the actual velocity at all time steps, the trajectory is safe.

Some results obtained by the analysis system discussed here are presented in subsection 4.4. Based on those results recommendations for an optimum procedure in using the program will be made in Section 5.

4.2 The Aerodynamic Input

The present study represents a first step toward the development of a complete, integrated system for aeroelastic analysis of flight vehicles with thin lifting surfaces (wings and fins) operating in the lower hypersonic regime. It is limited to small angles of attack. Thus, much of the basic theory is already available since only the fin strip aerodynamics is considered. However, the moderate nose tip bluntness usually necessary in a hypersonic missile design generates a nonuniform flow field over the fins. Analytic means have been developed to account for these effects, as was discussed in the previous section. The capability is presently limited to hemispherical nose tips. However, the nonuniform dynamic pressure distribution generated over the fins by such a nose tip can be computed and is included in the program.

A significant simplification is introduced in inviscid hypersonic theory by the fact that the pressure at a point is a function of the local angle of attack only. This reduces the aerodynamic calculations to consideration of chordwise strips. It was shown in Section 3 that for the very small angles of attack considered in the present study, Third Order Piston Theory will provide a simple means for calculation of the inviscid aerodynamic influence coefficients with sufficient accuracy.

4.2.1 Calculation of Third Order Piston Theory Aerodynamic Influence Coefficients

The geometry of a typical two-dimensional strip will be discussed with reference to Fig. 3.18 in which the important variables are illustrated. The derivation follows closely that of Ref. 109. It is noted that the slope at any point is the sum of five components; namely, initial angle of attack of the airfoil, camber, control surface increment, variation in thickness, and structural deformation. Since this study excludes rigid body motions, the first four components can be determined at the start of the analysis. All changes of the effective angle of attack are due to flexibility and are the thermoelastic perturbations in the analysis from the rigid body steady state condition. With the usual small angle assumption, Eq. (3.36) can be written

$$(V_\perp/U)_U = \upsilon_U - (\alpha + \delta_f)$$

$$(V_\perp/U)_L = \upsilon_L + (\alpha + \delta_f)$$

(4.10)

Here υ_U and υ_L are upper and lower surface slopes with respect to the velocity vector, $\alpha = \alpha_o + \theta$ is the rigid body angle of attack, and $\delta_f = \partial h/\partial x$ is the change of surface slope due to structural flexibility for a thin airfoil.[#]   The pressure difference normal to a lifting surface is

$$\frac{\Delta p}{q} = (C_{pL} - C_{pU})$$

(4.11)

in which the pressure coefficient C_p is expressed in terms of the total slope at a point as

$$C_p = (\frac{p - p\infty}{q}) = \frac{2\delta}{M_\infty} + (\frac{\gamma + 1}{2})\, \delta^2 + (\frac{\gamma + 1}{6})\, M_\infty\, \delta^3$$

(4.12)

On substituting Eq. (4.12) into Eq. (4.11) and distinguishing between upper, and lower surface slopes one obtains

$$\frac{\Delta p}{q} = \frac{2}{M_\infty}\, (\delta_L - \delta_U) + (\frac{\gamma + 1}{2})(\delta_L^2 - \delta_U^2) + (\frac{\gamma + 1}{6})\, M_\infty\, (\delta_L^3 - \delta_U^3)$$

(4.13)

Inserting Eq. (4.10) into Eq. (4.13) and expressing the result in ascending powers of the slope $(\alpha + \delta_f)$ gives

$$\frac{\Delta p}{q} = Q_o + Q_1\, (\alpha + \delta_f) + Q_2\, (\alpha + \delta_f)^2 + Q_3\, (\alpha + \delta_f)^3$$

(4.14)

in which the Q_i are the Aerodynamic Influence Coefficients (A.I.C.) as function of the total slope.

[#] $(\delta_f)_U = (\delta_f)_L = \delta_f$

$$Q_0 = \frac{2}{M_\infty} (\upsilon_L - \upsilon_U) + (\frac{\gamma + 1}{2})(\upsilon_L^2 - \upsilon_U^2) + (\frac{\gamma + 1}{6}) M_\infty (\upsilon_L^3 - \upsilon_U^3)$$

$$Q_1 = \frac{4}{M_\infty} + (\gamma + 1)(\upsilon_L + \upsilon_U) + (\frac{\gamma + 1}{2}) M_\infty (\upsilon_L^2 + \upsilon_U^2)$$

$$Q_2 = (\frac{\gamma + 1}{2}) M_\infty (\upsilon_L - \upsilon_U)$$

$$Q_3 = (\gamma + 1) M_\infty / 3$$

Charts of these coefficients are given in Ref. 109 for many profiles. Expanding Eq. (4.14) to obtain an expression for the lifting pressure in terms of the perturbation or flexibility components of the streamwise surface slope gives

$$\frac{\Delta p}{q} = \overline{Q}_0 + \overline{Q}_1 \, \delta_f + \overline{Q}_2 \, \delta_f^2 + \overline{Q}_3 \, \delta_f^3 \qquad (4.15)$$

in which the A.I.C.s as functions of the rigid body surface slopes are

$$\overline{Q}_0 = Q_0 + Q_1 \, \alpha^2 + Q_3 \, \alpha^3$$

$$\overline{Q}_1 = Q_1 + 2Q_2 \, \alpha + 3Q_3 \, \alpha^2$$

$$\overline{Q}_2 = Q_2 + 3Q_3 \, \alpha$$

$$\overline{Q}_3 = Q_3$$

The Q_i are discussed in some detail and given graphically for zero angle of attack in Ref. 109, showing that a significant increase in complexity results for a nonsymmetric section or nonzero initial angle of attack. In the nonsymmetric case $\upsilon_U \neq \upsilon_L$ and all terms in Eq. (4.13) must be computed. For a symmetric section, $\upsilon_U = \upsilon_L$ so $Q_0 = Q_2 = 0$, and there is no justification for retaining Q_3. Thus, the aerodynamic formulation reduces to a linear one.

In what has been said up to now, no distinction has been made between dynamic (unsteady) and static behavior. All inviscid pressures are known in terms of the local slope and the distinction between the two lies in a different interpretation of "slope". For static flow, the chordwise slope is simply that due to static structural flexibility.

$$\delta_f = \frac{\partial h}{\partial x} \tag{4.16}$$

where h represents lateral displacement and the x the distance along the chord. Lateral motion introduces an additional component equal to the lateral velocity divided by the freestream velocity, so that the effective slope becomes

$$(\delta_f)_{eff} = \frac{\partial h}{\partial x} + \frac{1}{U_\infty} \frac{\partial h}{\partial t} \tag{4.17}$$

A discussion of generalized aerodynamic forces is included here for completeness.

4.2.2 Computation of Generalized Aerodynamic Forces

The aeroelastic analysis as discussed above includes the use of generalized aerodynamic forces. It is assumed that the lateral displacement h, of a thin platelike lifting surface can be defined in terms of its first L normal modes.

$$h(x,y,t) = \sum_{\ell=1}^{L} \emptyset_\ell (x,y) \, q_\ell (t) \tag{4.18}$$

$\phi_\ell(x,y)$ is the mode shape and $q_\ell(t)$ is the deflection amplitude at a reference point. Then, as is well known, the equations of motion can be written

$$M \{\ddot{\xi}\} + D \{\dot{\xi}\} + M \omega_n^2 \{\xi\} = \{G\} \qquad (4.19)$$

in which the $\omega_{n\ell}$ are the natural frequencies with M_ℓ the generalized mass, and D_ℓ the structural damping. The components of the generalized force $\{G_\ell\}$ are

$$G_\ell = \iint_S F_z (x,y,t) \, \phi_\ell (x,y) \, dxdy$$

where S is the area of the lifting surface and F_z is the normal force for the case of a thin surface

$$F_z (x,y,t) = (p_L - p_U) = \Delta p (x,y,t) \qquad (4.20)$$

where Δp is the pressure difference between upper and lower surfaces.

In a linear analysis at $\alpha = 0$, the only term contributing to the lifting pressure is that containing the first power of δ_f, i.e.,

$$\Delta p (x,y,t) = \bar{q}_\infty Q_1 (x,y) \, \delta_f (x,y,t) . \qquad (4.21)$$

The streamwise effective slope is given by

$$\delta_f (x,y,t) = \frac{\partial h}{\partial x} + \frac{1}{U_\infty} \frac{\partial h}{\partial t} \qquad (4.22)$$

For simple harmonic motion of frequency ω, Eq. (4.22) can be written in terms of the reduced frequency $k = c\omega/2U_\infty$.

$$\delta_f(t) = \bar{\delta}_f e^{i\omega t} = (\frac{\partial \bar{h}}{\partial x} + 2ik \frac{\bar{h}}{c}) e^{i\omega t} .$$

Introducing matrix notation and expressing the displacements and streamwise slopes in terms of their respective modal matrices gives

$$\{\delta_f\} = \{[D\Phi] + 2\frac{ik}{c}[\Phi]\}\{q\} \tag{4.23}$$

in which $[D\Phi]$ and $[\Phi]$ are the modal slope and modal deflection matrices, respectively. The former is usually written as an operator matrix times the modal deflection matrix

$$[D\Phi] = [D][\Phi] .$$

We can now write the aerodynamic force vector as follows for $\alpha = 0$

$$\{F_z\} = \bar{q}_\infty \lfloor Q_1 \rceil \lfloor A \rceil \{\delta_F\} \tag{4.24}$$

A is the diagonal matrix of element planform areas. The generalized forces are defined by the vector $\{G\} = [Q]\{\bar{q}\}$ where

$$[Q] = \bar{q}_\infty [\Phi]^T \lfloor Q_1 \rceil \lfloor A \rceil [D\Phi[+ \frac{ik}{b}[\Phi]$$
$$= \bar{q}_\infty [\Phi]^T \lfloor Q_1 \rceil \lfloor A \rceil \lfloor [D] + \frac{ik}{b}\lfloor 1 \rceil \rceil [\Phi] . \tag{4.25}$$

Using the definitions of dynamic pressure and reduced frequencies, we have

$$\bar{q}_\infty = \frac{\rho U_\infty^2}{2} = \rho \frac{c^2 \omega^2}{8k^2} \tag{4.26}$$

On substituting Eq. (4.26) into Eq. (4.25) the final matrix $[\bar{Q}]$ needed to represent the generalized aerodynamic forces in the flutter program can be written in a form consistent with that in Ref. 32, namely

$$[\bar{Q}_1] = \frac{\rho c^2}{8k^2}\left[[BR] + \frac{ik}{b}[BI]\right] \tag{4.27}$$

in which

$$[BR] = [\Phi]^T \lfloor Q_1 \rceil \lfloor A \rceil [D][\Phi]$$

and

$$[BI] = [\Phi]^T \lfloor Q_1 \rfloor \lceil A \rceil [\Phi] \ .$$

These are the two components of the $[\overline{Q}_1]$ matrix found in Eq. (4.1.12) of
Ref. 32. Once they are computed, along with the generalized mass matrix and
the natural frequencies of the lifting surface, these data are fed into the
MOFA program (Ref. 32) to obtain the flutter speeds according to the linearized
formulation.

4.3   Program Capabilities

A computer program ICAM has been derived in which aerodynamic influence co-
efficients and generalized aerodynamic forces are determined for use in the
STAGS and MOFA programs. The programs include the chordwise thickness
variation of wedge, diamond and parabolic sections, and it is very easy to
modify a subroutine PRØFIL to account for any other thickness distribution.
The Mach number is assumed to be sufficiently high so the correction for
sweepback (Ref. 32) is negligible.

4.4   Numerical Results

4.4.1 Linear Static Aeroelasticity

Some classic divergence results have been obtained by use of STAGS and MODIV
in combination. With the prestress from a linear analysis STAGS computes vibra-
tion modes for use in MODIV.

The effective[#] dynamic pressure as a function of the distance from the root chord
was determined by use of the method discussed in Section 3. The dynamic pressure
for a straight wing with the leading edge 42.0 inches behind the spherical nose
of the missile body is shown in Figure 4.2. In Figure 4.2a results are shown for
one body with a 2.0 inch and one with a 6.0 inch diameter. Figure 4.2b shows the
effect of increasing angle of attack from zero to $\alpha = 6^{\circ}$ for the 6.0 inch body
diameter. In all cases the effect of the body reduces considerably the dynamic
pressure over a large portion of the fin. Thus, the presence of the missile body
should result in an increase of the free stream dynamic pressure at which aero-
elastic instability occurs.

\# The distribution at the quarter chord of the diamond airfoil section.

The results presented in Table 4.1 apply to a rectangular wing with a 10.0 in. chord and 8.0 in. span. The cross-section of the wing is "diamond-shaped" as shown in Fig. 2.1. In Table 4.1A are shown the results for a wing that has only partial support along the root chord, i.e., all displacements are constrained at nodes 7, 8, 9 but the other nodes are free (see Fig. 2.1). It is seen that the critical velocity increases, as expected, when the effect of the missile body is taken into account. The slight decrease in critical velocity with angle of attack is due to the changes in the generalized aerodynamic forces. For the wing alone this simply reflects the nonlinear aerodynamics described by piston theory. In the presence of the missile body the effect is reinforced by the increase with α of the local dynamic pressure[#] (see Fig. 3.13).

If the same wing is clamped along the entire root chord, the critical free stream pressure increases dramatically, as can be seen from Table 4.1B. Again, the presence of the missile body results in an increase of the critical pressure. Most of the results presented in Table 4.1B include the effect of aerodynamic heating. They correspond to a parabolic temperature distribution with $450^{\circ}F$ at the leading and trailing edges and $0^{\circ}F$ at midchord.

4.4.2 Nonlinear Static Aeroelasticity

It was indicated in subsection 4.1 that the linear static aeroelastic analysis presents a rigorous solution only if no component of the divergence mode (eigenfunction) is contained in the precritical deformation pattern. This generally is the case only if the precritical mode is free from lateral displacement, that is, if the wing profile is symmetric and the angle of attack is zero. If a component of the divergence mode is present at subcritical velocity, then this component will grow nonlinearly from the outset. Rigorously correct deformations and stresses in the structure can only be determined from the nonlinear quasistatic solution. The traditional linear solution is adequate for small dynamic pressures but becomes progressively less credible as dynamic pressure increases.

[#] The shear flow Effect at $\alpha \neq 0$ (Profile A-A in Fig. 1-2), which is not included, could amplify this α-effect significantly.

TABLE 4.1

LINEAR DIVERGENCE RESULTS

RECTANGULAR PLANFORM WING 10.IN. CHORD, 8.IN. SPAN. 4.5% T/C DIAMOND SECTION

A) 3 Node Root Support. Room Temperature.

BODY	ANGLE OF ATTACK (DEG)	DIVERGENCE DYNAMIC PRESSURE (LBS/IN^2)
None	0.	410.
	2.	404.
	4.	391.
	6.	370.
6 In. Dia.	0.	566.
	2.	553.
	4.	510.
	6.	447.

B) Same Wing but Clamped Along the Root.

BODY	ANGLE OF ATTACK (DEG)	L.E.& T.E. TEMP. (DEG. F.)	DIVERGENCE DYNAMIC PRESSURE (LBS/IN^2)
None	0.	0.	2400.
6 In. Dia.	0.	0.	3550.
None	0.	450.	2200.
	2.		2180.
	4.		2150.
	6.		2110.
6 In. Dia.	0.		2670.
	2.		2620.
	4.		2490.
	6.		2260.

The shortcomings of the linear static aeroelastic analysis were first noted by Padlog, Donato, and Batt (Ref. 19). With a simple but still representative model of a wing susceptible to divergence it is shown that the classical linear analysis may give nonconservative results. The reason for this is that the nonlinear contribution to the aerodynamic forces is such that the twisting moment grows with the angle of twist at a rate that exceeds the linear rate. Consequently, the curve representing the secondary equilibrium form bends back from the maximum at the critical dynamic pressure. The equilibrium on this secondary path is unstable so the situation is analogous to the well known and much discussed problem with imperfection sensitivity in elastic stability analysis. Of course, the nonlinear structural terms should also be accounted for. If the structure were stiffening under increasing deformation, the situation could be reversed, resulting in a stable secondary equilibrium path. However, at moderate deformation structural nonlinearities are insignificant for the cantilever plate. If a disturbance is present that will cause a lateral displacement, this displacement will grow at an accelerated rate, until at some point the slope of the curve is infinite. At that point the equilibrium becomes unstable and the existence of a vertical slope may be considered to be a nonlinear divergence condition. The dynamic pressure corresponding to aeroelastic instability is below that determined by the linear theory and decreases with increasing size of the disturbance.

It should be noted that the vertical tangency point may correspond to very large deformations. Excessive stresses may confine flight to a narrower range. Therefore, it seems that in the majority of applications it is necessary to carry out a nonlinear analysis. In addition to the need to assess structural integrity, there is a need to consider the effects of wing deformation on flight mechanics. In particular, the aerodynamic stability derivatives are affected by such deformations. It is demonstrated in Ref. 14 that relatively small aerodynamic nonlinearities can sometimes produce dramatic changes in the stability derivatives at high values of the dynamic pressure.

For code verification and to illustrate the relationship between linear and nonlinear static aeroelastic analysis STAGS was again applied to the rectangular

planform wing with diamond shaped profile (Fig. 2.1). The same finite difference grid was used and the wing was attached only at the grid points 7, 8, and 9. No thermal or missile body aerodynamic effects were included. The linear divergence velocity was determined by use of STAGS - computer vibration modes in MODIV. The critical dynamic pressure so computed is shown in Fig. 4.5. The imperfection causing lateral displacements was introduced in the form of a small lateral force at the tip of the leading edge or by flight with a nonzero angle of attack. Three values of this perturbation force were considered as shown in the figure. For these three cases the angle of attack was zero. In a fourth case no imperfections were introduced, but the initial angle of attack was 2.0 degrees.

The stiffness properties of aluminum was used in the analysis. Even for a high performance alloy, the stresses will be well into the inelastic range when the wing displacement reaches a value of 0.5 in. Consequently, at flight with an initial angle of attack of 2.0^o, the critical dynamic pressure is less than one-third of that computed from the linear theory.

It may be observed here that the effect of the missile body is to reduce the dynamic pressure on a large part of the wing. For a given maneuver this may have to be compensated for by an increase in the angle of attack. In view of decreasing body effect with increasing angle of attack and the additional shear flow effect at $\alpha \neq 0$, the presence of the missile body may on the balance have an unfavorable effect on the static aeroelastic stability of the wing even in inviscid flow. When the viscous wing-body interaction is considered, the adverse effect of the presence of the missile body will be much greater, as was discussed earlier in connection with Fig. 3.22.

4.4.3 Dynamic Aeroelasticity

The flutter speed was computed for a number of cases by use of the STAGS-MOFA combination. The flutter analysis in MOFA was based on the three lowest frequencies and corresponding modes, as computed by use of STAGS. As a first example the rectangular wing with a 10.0 in. chord and 8.0 in. span was considered (see Fig. 2.1). The wing was clamped along the entire root chord. It

4-18

was assumed to have its leading edge 42.0 in. aft of the missile body nose tip. The flight was assumed to be at 10,000 ft. altitude and at a Mach number of 5.0. Results are shown in Table 4.2. As in the static divergence case, the critical velocities are seen to increase significantly due to the missile body effect, and to decrease slowly with increasing angle of attack. To assess the importance of thickness on the aerodynamic forces and the resulting flutter condition results were also obtained using the "Mach Box" theory of Ref. 32. The resulting flutter dynamic pressure of 1600 lbs/in^2 is markedly unconservative relative to the 900 lbs/in^2 computed accounting for thickness effects. This evidence of the destabilizing influence of thickness is consistent with the majority of available literature, such as Refs. 110, 111, 112, and 113.

Table 4.3 shows some results for a clipped delta wing. Planform and cross-section of the wing are shown in Fig. 4.4. The results shown in Table 4.3A do not include effects of aerodynamic heating. The effects of the missile body and of angle of attack are similar to those for the rectangular wing. The slight decrease in flutter speed with angle of attack agrees with Refs. 76, 114, 115 and 116. Table 4.3B shows results corresponding to a parabolic temperature distribution with 600°F at leading and trailing edges and 0°F at midchord.

The body effect is greater for the thermally stressed clipped delta wing at isothermal conditions. This is due to the fact that at high temperatures the structural stiffnesses are being reduced, tending to amplify the relative importance of the aerodynamic terms which are temperature invariant. Thus we have reason to believe that in general, the hotter the structure is, the more important do the aerodynamic terms become.

As was discussed above, solution of the nonlinear equations of motions including displacement dependent aerodynamic loads would yield a complete solution to the aeroelastic problem. While the flutter analysis only indicates the velocity at which a small vibration will grow with time, the integration of Eq. (4.1) will also show the rate of growth of the oscillation. It may show, for example, that a maneuver that includes a short time at a speed slight above the flutter velocity still is safe.

TABLE 4.2A

BINARY FLUTTER RESULTS-RECTANGULAR PLANFORM WING

10.IN. CHORD, 8.IN. SPAN, 4.5% T/C DIAMOND SECTION. ROOM TEMPERATURE.

CLAMPED ROOT, MACH NO. = 5.0 AT 10,000 FT. ALTITUDE

WING L.E. AT 42.0 IN. AFT OF BODY NOSE

BODY	ANGLE OF ATTACK (DEG)	FLUTTER DYNAMIC PRESSURE (LBS/IN^2)
None	0.	900.
	2.	850.
	4.	800.
	6.	750.
6 In. Dia.	0.	1200.
	2.	1100.
	4.	950.
	6.	850.

TABLE 4.3

BINARY FLUTTER RESULTS-CLIPPED DELTA PLANFORM WING

10.IN. ROOT CHORD, 2.5 IN. TIP CHORD, 8.0 IN. SPAN, 4.5% T/C DIAMOND SECTION
MACH NO. 5.0 AT 10,000 FT. ALTITUDE,
WING L.E. AT ROOT CHORD AT 42.0 IN. AFT OF BODY NOSE

A) Room Temperature

BODY	ANGLE OF ATTACK (DEG)	FLUTTER DYNAMIC PRESSURE (LBS/IN^2)
None	0.	1900.
	2.	1880.
	4.	1840.
	6.	1810.
6 In. Dia.	0.	2840.
	2.	2730.
	4.	2530.
	6.	2340.

B) Leading and Trailing Edges at 600 DEGREES FAHRENHEIT

BODY	ANGLE OF ATTACK (DEG)	FLUTTER DYNAMIC PRESSURE (LBS/IN^2)
None	0.	1020.
	2.	980.
	4.	930.
	6.	850.
6 In. Dia.	0.	1720.
	2.	1620.
	4.	1500.
	6.	1300.

Data may be saved from a quasi static analysis and STAGS can be restarted at
some points along the trajectory with dynamic terms included together with
an excitation of a small amplitude vibration. For demonstration of such a
solution the rectangular wing with a diamond profile was selected. At room
temperature, zero angle of attack and body effect on the dynamic pressure
excluded, the critical velocity is found to be 155,000 in/sec. The transient
analysis with STAGS was started with a vibration excited by application of a
load of 0.1 lbs at the tip and the leading edge of the wing. This load was
applied instantaneously and then held constant. Restarts were made at
12,000, 140,000, and 160,000 in/sec (Fig. 4.5). It is seen that dynamic
instability occurs somewhere between 140,000 and 160,000 in/sec. The oscilla-
tion is not centered around zero since the load at the wing tip is retained
and produces a nonsymmetric effect that grows with the velocity of the free
air stream (see Fig. 4.3).
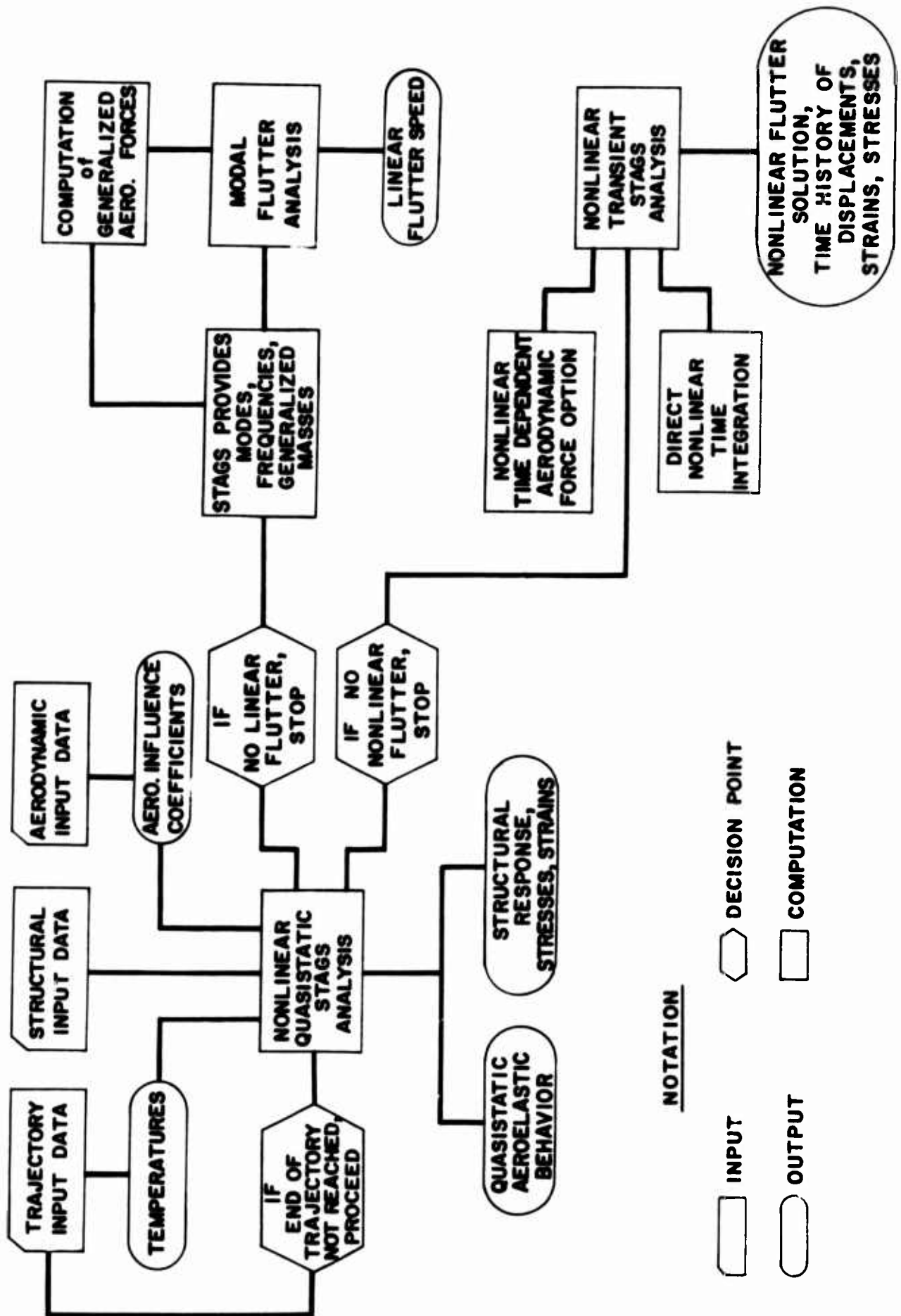
Figure 4.1 Chart Demonstrating Suggested Strategy for the Digital Program.

(a) Effect of Body Diameter

(b) Effect of Angle of Attack

10.IN. CHORD (ROOT 2.5 IN. TIP CHORD FOR THE CLIPPED DELTA WING. 8.IN. SPAN. WING ROOT LEADING EDGE AT 42.5 IN. BEHIND MISSILE BODY NOSE. MACH NUMBER IS 5.0.

Figure 4.2 Missile Body Influence on Spanwise Dynamic Pressure Variation
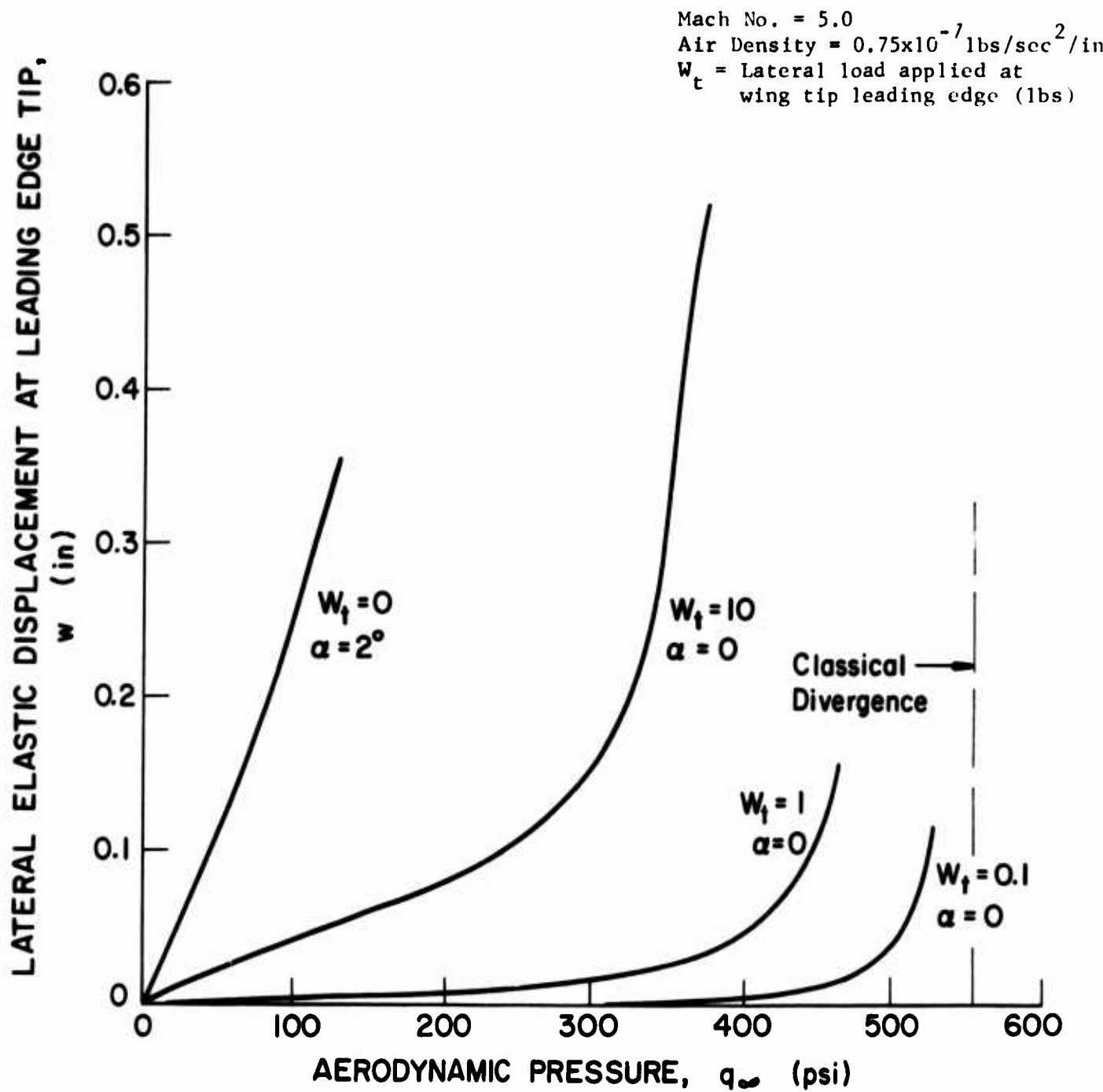
Figure 4.3 Static Aeroelastic Behavior of the Rectangular Planform, Diamond Section Wing Supported at Nodes 7, 8 and 9 along Root Chord
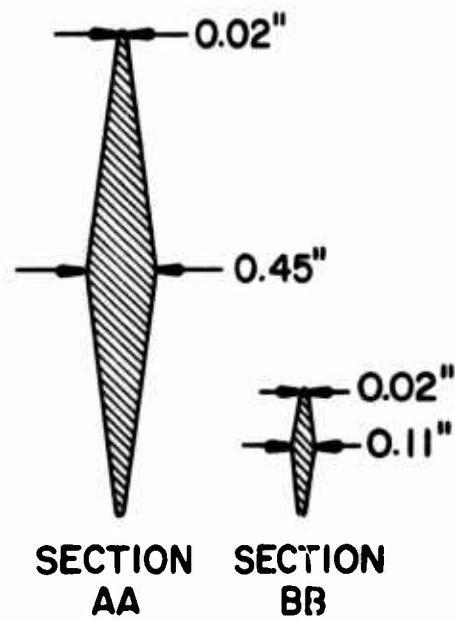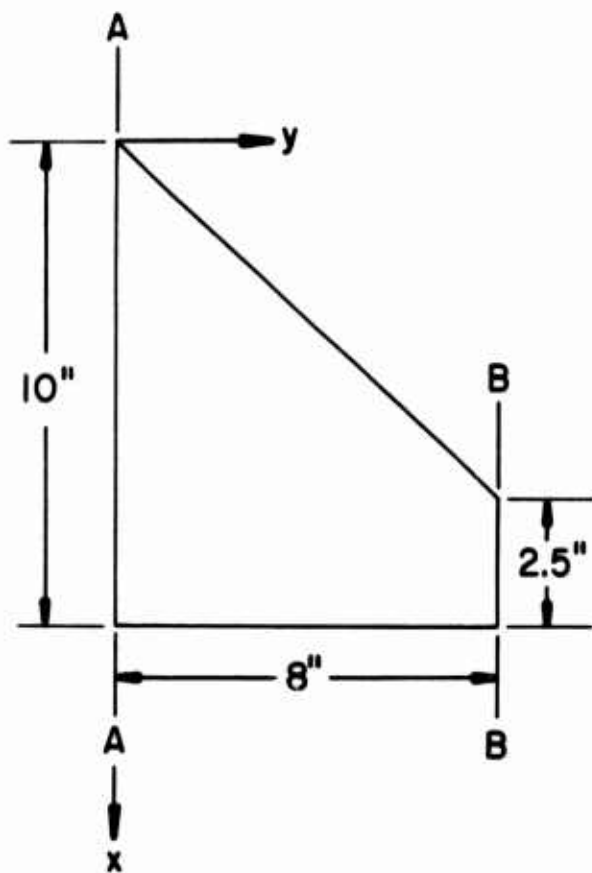
Figure 4.4 Geometry of Clipped Delta Wing
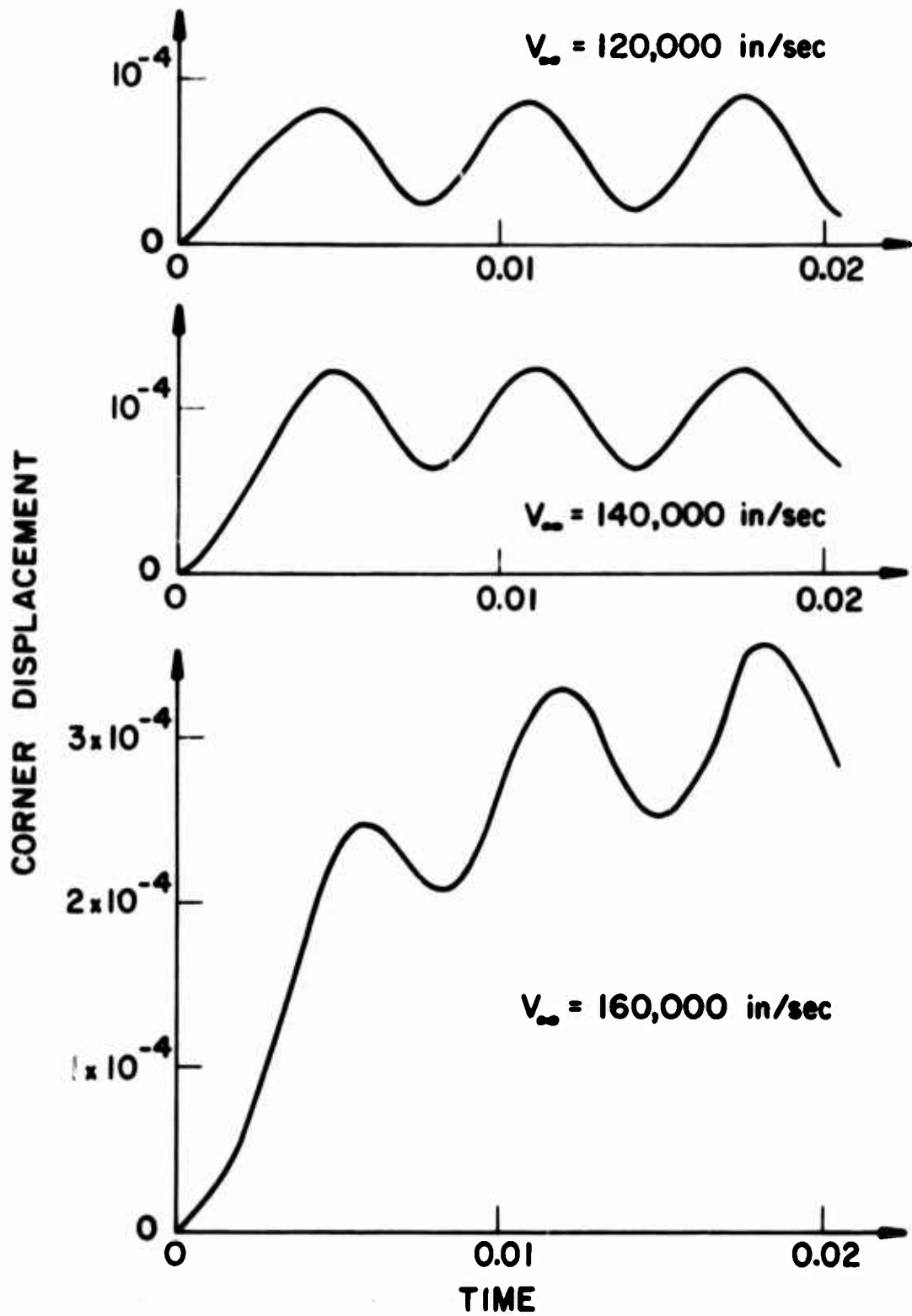
Figure 4.5 Transient Response Analysis for Rectangular Wing

Section 5
RECOMMENDED PROCEDURE

It is not claimed that the work presented in the preceding sections provides
a completely satisfactory solution of the problem of aeroelastic stability
of lifting surfaces in hypersonic flight. However, it is believed to advance
the state of the art in such analysis considerably. The computer program de-
veloped under the contract is somewhat limited, and more development is needed
before accurate analysis of a tactical missile is possible. The code contains
many options with respect to the choice of strategy in the aeroelastic analy-
sis. These are all left open to the user. However, some recommendations are
made for the choice of procedures. The recommendations are primarily based
on the experience acquired during the development and limited application of
the code.

The first question that arises is whether the linearized options may be used
or whether it is necessary to solve the complete nonlinear equations (quasi-
static or transient). A few points relevant to this question are listed here:

(1) It has long been realized that for thin lifting surfaces a rigorous defi-
nition of stresses and deformations can be obtained only if such nonlinear
effects are included as deformation dependent loads. It has also been shown
that nonlinearities in the aerodynamic formulation are important within a
practical range of flight parameters. In a linear analysis, the term $Q(u)$
(Eq. (4.2)) degenerates into $[\bar{Q}]\{u\}$.   It is sometimes assumed
that such an analysis gives a good estimate of deformations and stresses as
long as the flight velocity is somewhat below the classical divergence velo-
city. For the lifting surfaces and flight conditions typical for hypersonic
tactical missiles this does not appear to be the case. Therefore, unless
special circumstances dictate differently, it is necessary to obtain the non-
linear quasistatic solution (Eq. 4.2)). In that case there is no need for a
solution to the linearized aeroelastic problem as divergence will be indi-
cated by a rapidly increasing wing tip deflection.

(2) The nonlinear transient analysis is somewhat more accurate than the linearized flutter analysis since it retains a much larger number of degrees of freedom. In addition, it provides some additional information, such as the rate of growth of the vibration modes in the post critical condition. For structural configurations for which the stiffness grows with increasing deformation the linearized analysis may be unduly conservative. However, these objections appear to be slight in comparison to the computational advantages that are offered by the linearized flutter analysis.

(3) The linearized dynamic aeroelasticity analysis is executed by MOFA, using frequencies and virtual masses computed by STAGS and generalized aerodynamic forces computed by FLAM. It is clear that within the range of flight parameters of interest thermal effects are important. It is not equally clear, however, how important the effects of structural deformation on the aerodynamic forces are ($Q(u)$ in Eq. (4.2)) or if aerodynamic and geometric nonlinearities need be included in the STAGS analysis. However, in the general case it is necessary, as stated above, to obtain the nonlinear quasistatic solution. In that case vibration modes are, of course, obtained for use in the flutter analysis at the time when this solution is established. In fact, the whole aeroelastic problem can then be solved in one computer run. Likewise, whether or not geometrically nonlinear terms in the prestress analysis need to be retained is not clear at this point. Such terms can easily be suppressed by use of the standard input cards in STAGS. Suppression of these terms may lead to better convergence with little sacrifice in accuracy. The most important effect of structural nonlinearity is probably the coupling between in-plane stress (thermal) and torsional stiffness of the plate.

(4) The capability to evaluate the linear divergence speed may be useful as a first estimate. Some idea of when divergence is going to occur is needed for selection of the time steps at which vibration analysis is to be carried out. The nonlinear flutter option can be used after a preliminary linear flutter analysis. A restart with excitation of small amplitude vibrations can be executed at a time step previous to that at which flutter was indicated.

Based on these arguments, it seems that the following approach can be recommended:

o Perform a complete nonlinear quasistatic analysis covering a pertinent part of the trajectory.

o At a number of intervals obtain vibration modes and frequencies from STAGS for use in a linearized flutter analysis with MOFA.

o If the aeroelastic characteristics of the lifting surface is relatively well known, this may be achieved in one run. If not, it is recommended that some preliminary analysis is made, such as a linear divergence or flutter analysis based on linear prestress and an approximate temperature field.

o Before an extensive study (parameter variation) is performed, it may be advisable to perform some comparative analyses to determine if structural and/or aerodynamic nonlinearities may be neglected in the analysis.

The problem of leading or trailing edge buckling deserves some consideration. Presently it seems that the best recommendation is that it be treated with benign neglect. Buckling caused by controlled displacement, as is the case if stresses are thermally induced, is generally a stable phenomenon. The gradually increasing amplitude of the buckle relieves the compressive stress. In Section 2 it was observed that the development of leading edge buckling had little effect on the basic stiffness of the plate. It seems likely that this behavior is typical and that the observation can be extended to similar configurations. Two different procedures for assessing thermal buckling effects are available. One is to introduce a small perturbation. In that case the quasistatic solution corresponds to stable equilibrium for all levels of the temperature. In some temperature range the lowest vibration modes will include the very localized modes corresponding to leading edge buckling. In view of the results discussed above, it is not likely that the presence of these modes will significantly affect the flutter velocity.

If no perturbation is introduced to trigger thermal buckling, convergence will be considerably easier. In that case the quasistatic solution obtained beyond the point of thermal buckling will represent unstable equilibrium. The coefficient matrix used in the vibration analysis has at least one negative root, and the corresponding eigenvalue is negative. Such solutions to the vibration analysis are ignored in the aeroelastic analysis. If, as expected, leading edge buckling has little effect on the flutter characteristics, the two approaches should give very similar results. There is presently insufficient experience available on which to base more definitive recommendations regarding the problem of leading edge buckling.

Section 6
CONCLUSIONS

A study of the aerothermoelastic characteristics of a tactical missile operating at near zero angle of attack in the Mach number range $3 \leq M_\infty \leq 6$ has produced the following results:

o An integrated digital program has been developed for the static and dynamic linear and nonlinear aeroelastic response of sharp edge, aerodynamically heated, cantilevered lifting surfaces representative of a wide range of tactical missile wings and fins. The program utilizes a one-dimensional "through the thickness" flat plate solution for computation of the structural temperature effects, third order piston theory aerodynamics modified to account for the nonuniform flow generated by a hemispherically blunted missile body, and the STAGS nonlinear finite difference program for the structural (response) calculations.

o In general it is found to be desirable to run a full nonlinear quasistatic analysis for each trajectory till its completion or the onset of divergence. Flutter analyses, linear or nonlinear, should be performed only at selected discrete times within each trajectory using the appropriate prestress conditions from the quasistatic solution. The nonlinear flutter solution provides a direct numerical solution of the coupled nonlinear equations but is in its present form markedly less efficient than the eigenvalue solution obtained through standard type linear flutter analyses.

Important results obtained in the analyses are:

o Thermostructural analyses conducted to compare with existing (closed form) solutions show excellent agreement where such could be expected and the numerical results follow well established trends where the problems become too complex for closed form solutions. Computed results illustrate the thermally induced stiffness changes in wings and demonstrate the importance of boundary conditions, temperature sensitive elastic moduli, initial imperfections, planform and thickness variations.

o A simple analytic theory has been developed that can predict the non-uniform flow characteristics produced by spherical nose bluntness on slender axisymmetric bodies at supersonic and hypersonic speeds, $M_\infty \geq 3$. It is shown that nose bluntness has adverse effects on the rigid body vehicle dynamics. The theoretical predictions are in excellent agreement with available experimental data.

o Missile nose bluntness generates a large spanwise dynamic pressure gradient over the fin, and will at nonzero angle of attack also create an inviscid shear flow which makes the aerodynamic forces on the fin displacement dependent. Cylindrical leading edge roundness, however, is found to have insignificant influence on the two-dimensional unsteady fin aerodynamics.

o A simple viscous perturbation theory has been developed which gives results that agree well with available numerical and experimental results. It is found that for flight conditions of present interest viscid-inviscid interaction effects on the fin are small in the absence of boundary layer transition and flow separation.

o Although boundary layer transition and flow separation will have significant effects on the two-dimensional aerothermoelastic characteristics of the fin (strips), it is the three-dimensional flow separation caused by the interaction between the fin and the fuselage boundary layer that is of most concern. It can cause negative aerodynamic damping of movable fins for typical axis locations, and will in general

destroy the applicability of the simple piston theory, as the aerodynamic forces no longer are dependent only upon local deflections. This should be considered when interpreting results from the aeroelastic analysis with the present version of the program.

Section 7
RECOMMENDATIONS FOR FUTURE WORK

The present study represents a first step toward development of the needed analytic capability. A tactical missile has to perform high g maneuvers. Thus, further analytic efforts are needed.

In the field of unsteady aerodynamics the following analytic efforts would appear to be most urgent:

o Define the aerodynamic environment of the fins in the angle of attack range of interest for a maneuvering missile. The highly nonlinear aerodynamic characteristics can be defined by further extension of the embedded Newtonian analysis technique. The effects of elastic perturbations of small amplitude can often be determined by local linearization techniques, such as were demonstrated in the present study. However, based upon the results in Ref. 14 the nonlinear aerostructural coupling effects can be very large and a full nonlinear analysis may be necessary.

o Extend present analytic capability to include realistic missile body geometrics by considering biconic nose tips and ogival forebody geometrics in addition to the hemisphere-cylinder and hemisphere-cone geometric investigated in the present study.

o Extend the developed analytic theory for viscid-inviscid interaction to include the effects of boundary layer transition. Asymmetric transition can have a significant effect on the fin aerodynamics even when thermal effects are ignored, and can be expected to have a greater influence when the full aerothermoelastic coupling is included.

o Develop means for determining how trailing edge flow conditions and
   leeside flow separation affect the unsteady two-dimensional airfoil
   aerodynamics of a finite chord fin.

o Conduct an investigation of the interaction between the fin and the
   fuselage boundary layer which will lead to a better unstanding of
   the "real life" unsteady fin aerodynamics. The goal is, of course,
   to develop means by which the separated flow effects, which always
   will be present for realistic fin thicknesses (Ref. 117) can be in-
   cluded in an aerothermoelastic analysis.   Due to the complexity
   of the flow field, this can be accomplished only through a powerful
   combination of analytic and experimental techniques. An experimental
   approach to this problem, which also could define the nose bluntness
   generated entropy wake effects, is discussed in Ref. 87.

o Develop means for determination of the rigid body unsteady aerodynamics
   in the angle of attack range of interest for a maneuvering tactical
   missile. In the inviscid flow field the difficulties are caused by
   the large nonlinear effects of nose bluntness. It is believed that
   the embedded Newtonian theory can be extended to describe these
   effects for realistic missile geometries. In addition to this invis-
   cid flow investigation it is important that some means be developed to
   assess the potentially large effects of viscous cross flow on the
   vehicle dynamics, in particular the cross flow effects on boundary
   layer transition and (near) base flow recirculation.

o It may be desired that all the fin problems discussed above are con-
   sidered also for canard surfaces. Because of the close proximity to
   the nose tip, the canard surfaces will have their own unique aero-
   thermoelastic problems.   In addition, their presence will change the
   flow environment experienced by the fins. Although the full coupling
   between the flow fields cannot be considered for some time, some pre-
   liminary, exploratory investigation probably should be made at a rather
   early stage to get an assessment of how large these coupling effects are.

In the field of structural and aeroelastic analysis a number of tasks appear to be of considerable interest. Among the more important are the following:

o Exercise the developed capability in the field of hypersonic aeroelasticity to improve our general understanding of the problems encountered and give some direction for continued research in the area.

   The following items may be mentioned as worthy of special attention:

   . Effects of leading edge buckling

   . The accuracy of the aeroelastic analysis as a function of the number of modes included in the analysis

   . Effect of structural nonlinearity (in kinematic relations)

   . Effect of wing plan form and profile on the aeroelastic characteristics.

o In the completed study the lifting surface was considered fixed at the root in one way or another so that all rigid body motions are constrained. Ultimately it may be deemed necessary to include in the analysis the rigid body modes of the vehicle. Before a substantial effort along those lines is planned, it seems prudent to acquire more experience by exercising presently available computer codes and consulting with experts in pertinent areas.

o Modification of the extrapolation method for initial estimates of the unknowns can lead to considerable improvements in computer time for the quasi-static solution. By reorganizing the procedures for computing partial derivatives of the strain energy with respect to the discrete variables, considerable reduction in computer time can be achieved. It is expected that the computer time for a typical transient response analysis may be reduced by a factor from two to five, depending on the problem parameters.

o The thermal gradients of the leading and trailing edges of a typical wing structure, as based on solutions of the one-dimensional heat equation, are extremely sharp. It appears that a much more favorable distribution would be obtained if chordwise heat conduction were accounted for. Therefore, a computer code should be developed and integrated in STAGS that is based on the more realistic two-dimensional solution.

o Solving the transient nonlinear response requires a large (3 times the number of nodes) order system of coupled differential equations and is expensive in computer time. Alternative, more economic methods should be developed to handle the nonlinear flutter problem. An obvious contender for this task is the method of modalizing the equations. The approach here will naturally be more complex than the linear procedure used in the past. This is due to the coupling of the equations introduced by the nonlinear terms, which also causes the number of differential equations to be solved to exceed the number of normal modes chosen. Nevertheless, for practical wing structures the reduction of the number of equations will be many-fold and the resulting savings in computer costs is significant. It is also important to note that the linear eigenvalue method is subject to some approximations.

     . The displacement pattern is restricted so that it can be defined as the sum of displacement modes. Generally, the flutter analysis is restricted to four modes or less.

     . The solution gives the point in time at which an infinitesimal disturbance will begin to grow.

     . The analysis does not indicate the rate of growth of the amplitude of the vibration.

If a modal transient analysis is developed in which the nonlinear terms are retained, the last two approximations are eliminated. This is not believed in itself to be too important. However, if the nonlinear transient analysis is reduced by the modal approach to entail only a few degrees of freedom, the direct solution of the equations of motion (Eq. 4.1) will probably be more efficient than the linearized approach. Hence, no price is paid for the additional information yielded.

o In its present form the computer program does not provide a complete output
   of all the quantities, e.g., the aerodynamic derivatives of concern to
   aeroelasticians. It is highly desirable that the program be modified to
   post-process the data in order to extract the maximum information from
   each analysis.

Section 8

REFERENCES

1   Collar, A. R., "The Expanding Domain of Aeroelasticity", J. R. Aero. Soc., Vol. 1, August 1946, pp 613-636.

2   Rogers, M., "Aerothermoelasticity", Aero/Space Engineering, Vol. 17, No. 10, October 1958, pp 34-43.

3   Zisfein, M. B., Donato, V. W., and Farrell, R. F., "Supersonic Aeroelastic Effects on Static Stability and Control, Part I, Aerodynamics", WADC TR-58-95. December 1958.

4   Rattinger, I., and Gallagher, R. H., "Supersonic Aeroelastic Effects on Static Stability and Control, Part II, Structures", WADC TR-58-95, April 1960.

5   Donato, V., "Supersonic Aeroelastic Effects on Stability and Control, Part III, Aeroelastic Interaction", WADC TR-58-95. July 1960.

6   Blessing, A. H., and Honawalt, A. J., "Thermal Effects on Static Aeroelastic Stability and Control, Part I, Methods of Predicting Structural Temperatures due to Aerodynamic Heating", WADC TR-58-378, Part 1, June 1959.

7   Batt, J. R., and Farrell, R. F., "Thermal Effects on Static Aeroelastic Stability and Control, Part II, Aerodynamics". WADC TR-58-378, Part 2, December 1959.

8   Bisplinghoff, R. L., "Some Structural and Aeroelastic Considerations of High Speed Flight", J. Aero. Sci., Vol. 23, No. 4, April 1956, pp 289-329.

9   Bisplinghoff, R. L., and Dugundji, J., "Influence of Aerodynamic Heating on Aeroelastic Phenomena" in High Temperature Effects in Aircraft Structures. Edited by N. J. Hoff. Pergamon Press. 1958. pp 288-312.

10 Mills, W. R., Schmit, L. A., Balmer, H. A., Cener, D. and Foss, K. A., "Procedures for Including Temperature Effects in Structural Analysis of Elastic Wings, Parts I, II, III, and IV. January 1958 to March 1960.

11 Harder, R. L., et al, "Supersonic Flutter Analysis Including Aerodynamic Heating Effects", WADC TR 59-553, February 1960.

12 Ashley, H., and Zartarian, G., "Piston Theory - A New Aerodynamic Tool for the Aeroelastician", J. Ae. S., Vol. 23, No. 12, December 1956, pp 371-381.

13 Ashley, H., and Zartarian, G., "Supersonic Flutter Trends as Revealed by Piston Theory Calculations", WADC TR-56-74, May 1958.

14 Zartarian, G., Hsu, P. T., and Ashley, H., "Dynamic Airloads and Aero-elastic Problems at Entry Mach Numbers", J. Ae. S., Vol. 28 No. 3, March 1961, pp 209-222.

15 Zartarian, G., and Hsu, P. T., "Theoretical and Experimental Studies on Airloads Related to Hypersonic Aeroelastic Problems of General Slender Pointed Configurations", ASD-TR-61-7, April 1961.

16 Zartarian, G., and Sauerwein, H., "Further Studies on High Speed Unsteady Flow", ASD-TDR-62-463, September 1962

17 Brunelle, E. J., "Transient and Nonlinear Effects on High Speed Vibratory Thermoelastic Instability Phenomena", WADC TR-60-484, December 1960

18 Batt, J. R., Gallagher, R. H., et al, "Thermal Effects on Static Aero-elastic Stability and Control", WADC-TR-58-378, Numerous Volumes published in 1959.

19 Padlog, J., Donato, W. W., and Batt, J. R., "Thermoelastic Effects on Hypersonic Stability and Control", ASD-TR-61-287, Numerous Parts and Volumes published 1961-1963.

20 Batt, J. R., and Gallagher, R. H., "Nonlinear Thermoelastic Effects on Hypersonic Stability and Control", Various Parts and Volumes of RDL-TDR-64-16, 1964 and 1965.

21 Ericsson, L. E., "Unsteady Aerodynamics of an Ablating Flared Body of Revolution Including Effects of Entropy Gradient", AIAA J., Vol. 6, No. 12, December 1968, pp 2395-2401.

22 Ericsson, L. E., "Effect of Nose Bluntness, Angle of Attack, and Oscillation Amplitude on Hypersonic Unsteady Aerodynamics of Slender Cones", AIAA Jr., Vol. 9, No. 2, February 1971, pp 297-304.

23 Ericsson, L. E., "Unsteady Embedded Newtonian Flow", Astronautics Acta, Vol. 18, 1973, pp 309-330.

24 Ericsson, L. E., "Effects of Boundary Layer Transition on Vehicle Dynamics", J. Spacecraft and Rockets, Vol. 6, No. 12, pp 1404-1409, December 1969

25 Ericsson, L. E., "Transition Effects on Slender Vehicle Stability & Trim Characteristics", J. Spacecraft & Rockets, Vol. 11, No. 1, Jan. 1974, pp 3-11.

26 Ericsson, L. E., and Reding, J. P., "Ablation Effects on Vehicle Dynamics", Journal of Spacecraft & Rockets, Vol. 3, No. 10, pp 1476-1483, Oct 1966.

27 Korkegi, R. N., "Survey of Viscous Interactions Associated with High Mach Number Flight", AIAA Journal, Vol. 9, No. 5, May 1971, pp 771-784.

28 Almroth, B. O., Brogan, F. A., User Manual for STAGS, Lockheed Report No. LMSC-D358197, 1974.

29 . Compton, W. R., and Schultz, L. D., "Transient Thermal Response One-Dimensional", provided by Aerothermodynamics Branch (Code 4061) N.W.C. China Lake 1974.

30 Compton, W. R., and Schultz, L. D., "A FORTRAN IV Program for the Solution of One-Dimensional Heat Conduction Problems in Multilayer Plate Cylinders and Spheres Subject to Arbitrary Aerodynamic Heat Transfer". TN 4061-124, N.W.C. China Lake, July 1965.

31 VanDriest, E. G., "The Problem of Aerodynamic Heating", Aeronautical Engineering Review, Vol. 15, No. 10, October 1956.

32 Hughes Aircraft Company, "Modal Flutter Analysis Study", Report No. SD 15204, April 1971.

33 Budiansky, B., and Mayers, J., "Influence of Aerodynamic Heating on the Effective Torsional Stiffness of Thin Wings", J. Aero. Sci., Vol. 23, No. 12, p 1081, 1956.

34 Heldenfels, R. R., and Vosteen, L. F., "Approximate Analysis of Effects of Large Deflections and Initial Twist on Torsional Stiffness of a Cantilever Plate Subjected to Thermal Stress", NACA TR 1361, 1958.

35 Biot, M. A., "Influence of Thermal Stress on the Aeroelastic Stability of Supersonic Wings", J. Aero. Sci., Vol. 24, No. 6, p 418-421, June 1957.

36 Kochanski, S. L., and Argyris, J. H., "Some Effects of Kinetic Heating on the Stiffness of Thin Wings", Aircraft Engineering, Oct 1957, Feb 1958, March 1958, and April 1958.

37 Mansfield, E. H., "Combined Flexure and Torsion of a Class of Heated Thin Wings - A Large Deflection Analysis", R&M 3195, March 1958.

38 Van der Neut, A., "Buckling Caused by Thermal Stresses", Chapt. 11 of High Temperature Effects in Aircraft Structures, edited by N. J. Hoff, Pergamon Press, 1958.

39 Singer, J., "Thermal Buckling of Solid Wings of Arbitrary Aspect Ratio", J. Aero/Space Sci., Vol. 25, No. 9, Sept 1958, pp 573-580.

40   Mansfield, E. H., "Leading Edge Buckling due to Aerodynamic Heating",
      R&M 3197, May 1959.

41   Hayes, W. D., and Probstein, R. F., Hypersonic Flow Theory, Academic
      Press, New York and London, 1959.

42   Fink, M. R., "Comparison of Static Pressures on Flared Bases in Non-
      Uniform Hypersonic Flow as Calculated by Exact and Approximate Methods",
      Journal of the Aerospace Sciences, Vol. 29, No. 8, Aug 1962, pp 1012,
      1013

43   Hoult, C. P., "On the Inviscid Tail Efficiencies of Slender Configura-
      tions at Hypersonic Speeds", Journal of the Aerospace Sciences, Vol. 29,
      No. 6, June 1962, p. 748.

44   Seiff, A., and Whiting, E. E., "Calculation of Flow Fields from Bow-
      Wave Profiles for the Downstream Region of Blunt-Nosed Circular
      Cylinders in Axial Hypersonic Flight", TND-1147, Nov 1961, NASA

45   Seiff, A., "Secondary Flow-Fields Embedded in Hypersonic Shock Layers",
      TND-1304, May 1962, NASA

46   Gravalos, F. G., Edfelt, I. H., and Emmons, H. W., "The Supersonic
      Flow about a Blunt Body of Revolution for Gases at Chemical Equilibrium",
      Proceedings of the IX International Astronautical Congress, Amsterdam,
      Aug. 25-30, 1958, pp 312-332

47   Seiff, A., Whiting, E. E., "A Correlation Study of the Bow-Wave Pro-
      files of Blunt Bodies", TND-1148, Feb 1962, NASA.

48   Faye-Peterson, R., "Theoretical Aerodynamic Studies of Missiles with
      Flared Skirts in Supersonic Upstream Flow", S.M.F. Fund Paper FF-31,
      Aerospace Forum II Session, IAS, 30th Annual Meeting, New York,
      Jan. 22-24, 1962.

49   Katz, J. R., "Pressure and Wave Drag Coefficients for Hemispheres,
      Hemisphere-Cones, and Hemisphere-Ogives", Report 5849, March 21, 1958,
      Naval Ordnance Research Lab.

50   Lin, S. C., "Cylindrical Shock Waves Produced by Instantaneous Energy
      Release", J. Applied Physics, Vol. 25, No. 1, Jan 1954, pp 54-57.

51   Keuhn, D. M., "Experimental and Theoretical Pressures on Blunt
      Cylinders for Equilibrium and Non-Equilibrium Air at Hypersonic
      Speeds", TND-1979, 1963, NASA.

52   Lukasiewicz, J., "Blast-Hypersonic Flow Analogy Theory and Application",
      ARS Journal, Sept 1962, pp 1341-1346

53   Chernyi, G. G., "Effect of Slight Blunting of Leading Edge of an
      Immersed Body on the Flow Around It at Hypersonic Speeds", TT F-35,
      1969, NASA.

54   Cheng, H. K., "Hypersonic Flow with Combined Leading-Edge Bluntness
      & Boundary Layer Displacement Effect", Rep. No. AF-1285-A-4 (Contract
      Nonr-2653(00)), August 1960, Cornell Aero. Lab. Inc., Buffalo, N.Y.

55   Wagner, Jr., R. D., and Watson, R., "Induced Pressures and Shock Shapes
      on Blunt Cones in Hypersonic Flow", TND-2182, March 1964, NASA.

56   Roberts, J. F., Lewis, C. H., and Reed, M., "Ideal Gas Spherically
      Blunted Cones Flow Field Solutions at Hypersonic Conditions", AEDC-
      TDR-66-121, Aug 1966, ARO Inc., Tullahoma, Tenn.

57   Maslowe, S. A., and Benson, J. L., "Computer Program for the Design and
      Analysis of Hypersonic Inlets", Report No. 18079, Aug 1964, Lockheed
      Aircraft Corporation, Burbank, California (also NASA CR 114344)

58   Ames Research Staff, "Equations, Tables, and Charts for Compressible
      Flow", Report 115 (1953), NACA

59   Walchner, O., and Clay, J. T., "Nose Bluntness Effects on the Stability
      Derivatives of Cones in Hypersonic Flow", Trans. of the Second Technical
      Workshop on Dynamic Stability Testing, Vol. 1, Paper 8, April 20-22, 1965,
      Arnold Engineering Development Center, Arnold Air Force Station, Tenn.

60   Clay, J. T., "Nose Bluntness, Cone Angle, and Mach Number Effects on
      the Stability Derivative of Slender Cones", ARL 67-0185, Sept 1967,
      Aerospace Research Lab, Wright Patterson AFB, Ohio.

61   Ward, L. K., and Uselton, B. L., "Dynamic Stability Results for Sharp
      and Blunted 10-Deg. Cones at Hypersonic Speeds", Trans. of the 3rd
      Technical Workshop on Dynamic Stability Problems, Vol. III, Paper 2,
      Nov. 4-7, 1968, NASA Ames Research Center, Moffet Field, Ca.

62   Rie, H., Linkievicz, E. A., and Bosworth, F. D., "Hypersonic Dynamic
      Stability, Part III, Unstead Flow Field Program", FDL TDR-64-149,
      Part III, Jan 1967, Flight Dynamics Lab, Wright Patterson AFB, Ohio.

63   Reding, J. P., and Ericsson, L. E., "Dynamic Support Interference",
      J. Spacecraft & Rockets, Vol. 9, No. 7, May 1972, pp 547-553.

64   Orlik-Rückemann, K. J., "Dynamic Viscous Pressure-Interaction in Hyper-
      Flow", Aeronautical Report LR-535, July 1970, National Research Council
      of Canada, Ottawa.

65   Orlik-Rückemann, K. J., "Oscillating Slender Cone in Viscous Hypersonic
      Flow", AIAA Journal, Vol. 10, No. 9, Sept 1972, pp 1139-1140.

66   Ericsson, L. E., and Reding, J. P., "Boundary Layer Transition and
      Dynamic Sting Interference", AIAA Journal, Vol. 8, No. 10, Oct 1970,
      pp 1886-1888.

67   Peterson, C. W., and Bogdonoff, S. M., "An Experimental Study of Laminary Hypersonic Blunt Cone Wakes", AIAA Paper No. 69-174, June 1969.

68   Walchner, O., Private communication of unpublished data, June 1968, Aerospace Research Lab, Wright Patterson AFB, Ohio

69   Ericsson, L. E., and Guenther, R. A., "Dynamic Instability Caused by Forebody Blowing", AIAA Journal, Vol. 11, No. 2, Feb 1973, pp 231-233.

70   Ericsson, L. E., and Reding, J. P., "Dynamic Stability Problems Associated with Flare Stabilizers and Flap Controls", J. Spacecraft and Rockets, Vol. 7, No. 2, Feb 1970, pp 132-137.

71   Edney, B. E., "Effects of Shock Impingement on the Heat Transfer Around Blunt Bodies", AIAA Journal, Vol. 6, No. 1, Jan 1968, pp 15-21.

72   Lighthill, M. J. "Oscillating Airfoils at High Mach Number", Journal of Aerospace Sciences, Vol. 20, No. 6, June 1953, pp 402-406.

73   VanDyke, M. D., "Supersonic Flow Past Oscillating Airfoils Including Nonlinear Thickness Effects", Report 1183, 1954, NACA

74   Pugh, P. G., and Woodgate, L., "Measurements of Pitching-Moment Derivatives for Blunt-Nosed Aerofoils Oscillating in Two-Dimensional Supersonic Flow, R&M No. 3315, July 1961, Aeronautical Research Council, Great Britain

75   Scruton, C. Woodgate, L. Lapworth, K. C., and Maybrey, J., "Measurement of Pitching-Moment Derivatives for Aerofoils Oscillating in Two-Dimensional Supersonic Flow", R&M No. 3234, Jan 1959, Aeronautical Research Council, Great Britain

76   Yates, E. C., and Bennett, R. M., "Analysis of Supersonic-Hypersonic Flutter of Lifting Surfaces at Angle of Attack", J. Aircraft, Vol. 9, No. 7, July 1972, pp 481-489.

77   Bertram, M. H., "Hypersonic Laminar Viscous Interaction Effects on the Aerodynamics of Two-Dimensional Wedge and Triangular Planform Wings", TND-3523, Aug 1966, NASA.

78   East, R. A., "A Theoretical and Experimental Study of Oscillating Wedge Shaped Airfoils in Hypersonic Flow", A.A.S.U. Report No. 228, Nov 1962, University of Southhampton, Hampshire, England.

79   VanDyke, M. D., "The Combined Supersonic-Hypersonic Similarity Rule", Journal of Aerospace Sciences, Vol. 18, No. 7, July 1951, pp 499-500.

80   Orlik-Rückemann, K. J., and LaBerge, J. G., "Oscillatory Experiments
     in a Helium Hypersonic Wind Tunnel", Advances in Hypervelocity Techniques,
     Plenum Press, N.Y., 1962, pp 187-209

81   Hulchʳʸ, G. D., and Behren, W., "Viscous Hypersonic Flow over a Flat
     Plate at Angle of Attack with Leeside Boundary Layer Separation", Pro-
     ceedings of the 1972 Heat Transfer and Fluid Mechanics Institute,
     Northridge, Calif., June 1972, pp 108-127.

82   Beastall, D., and Pallant, R. J., "Wind-Tunnel Tests on Two-Dimensional
     Supersonic Aerofoils at M=1.86 and M=2.48", R&M No. 2800, July 1950,
     Aeronautical Research Council, Great Britain.

83   Ericsson, L. E., "Dynamic Effects of Shock-Induced Flow Separation",
     Journal of Aircraft, Vol. 12, No. 2, Feb 1975, pp 86-92.

84   Ericsson, L. E., and Reding, J. P., "Aerodynamic Effects of Bulbous
     Bases", NASA CR-1339, Aug 1969.

85   Ericsson, L. E., and Reding, J. P., "Re-Entry Capsule Dynamics",
     Journal of Spacecraft and Rockets, Vol. 8, No. 6, Journal of Space-
     craft and Rockets, Vol. 8, No. 6, June 1971, pp 575-586

86   LaBerge, J. G., and Orlik-Rückemann, K. J., "Dynamic Stability Tests
     of Sharp Slender Wedges at M=9 and M=18 in Helium", Lab. Memo No. HG
     2-29, July 1968, National Aeronautical Establishment, Ottawa, Canada.

87   Orlik-Rückemann, K. J., "Measurements of Hypersonic Moment Derivatives
     on Fins of a Missile-Like Configuration", Private Communication,
     15 August 1974.

88   Peake, D. J., Rainbird, W. J., and Atraghj, E. G., "Three-Dimensional
     Flow Separations on Aircraft and Missiles", AIAA Journal, Vol. 10,
     No. 5, May 1972, pp 567-580

89   Ericsson, L. E., and Reding, J. P., "Dynamic Stall Simulation Problems",
     J. Aircraft, Vol. 8, No. 7, July 1971, pp 579-583.

90   Kipke, K., "Unterschungen an Längsangeströmten Ecken in Hyperschallbereich",
     Bericht 7314, Sept 1973, Tech. N. Braunschweig, W. Germany.

91   Watson, R. D., and Weinstein, L. M., "A Study of Hypersonic Comer Flow
     Interactions", AIAA Journal, Vol. 9, No. 7, July 1971, pp 1280-1286.

92   Windelmann, A. E., "Aerodynamic Interaction Phenomena Produced by a Fin
     Protuberance Partially Immersed in a Turbulent Boundary Layer at
     Mach 5", AGARD CP 71-71 Specialists Meeting on Aerodynamic Interference,
     Silver Spring, Maryland, 28-30 Sept 1970

93   Morkovin, M. V., Donohue, J. C., and Larson, H. K., "Exploratory Investigations of the Effects of Gas Injection through a Porous Model on Separation, Transition, Static Stability and Control Effectiveness of a Blunt Entry Body at Mach Number 7.3", AIAA Paper No. 68-27, Jan 1968.

94   Morkovin, M. V., and Donohue, J. C., "Exploratory Investigations of the Effects of Gas Injection through a Porous Model on Separation, Transition Static Stability and Control Effectivenss of a Blunt Entry Body at Mach 7.3", Report No. ER 14598, Contract NAS2, 3873, Martin Marietta Corporation, Baltimore, Maryland.

95   Ericsson, L. E., "Transition Effects on Slender Vehicle Stability and Trim Characteristics", AIAA Paper No. 73-126, Jan 1973.

96   Ericsson, L. E., "Entropy Gradient Effects on Blunted Cone Transition", AIAA Paper No. 75-195, Jan 1975.

97   Sliski, N. J., "An Analytical and Experimental Investigation of Hypersonic Viscous Interaction Premise Effects", AFFDL-TR-73-58, Nov 1973, Air Force Flight Dynamics Laboratory, Wright-Patterson, Air Force Base, Ohio.

98   Orlik-Rückemann, K. J., "Stability Derivation of Sharp Wedges in Viscous Hypersonic Flow", AIAA Journal, Vol. 4, No. 6, June 1966, pp 1001-1007.

99   Schaaf, S. A., Moulic, E. S., Chahine, M. T., and Maslach, G. J., "AERO-dynamic Characteristics of Wedges in Low Density Supersonic Flow", ARS Journal, Vol. 31, 1961, pp 194 -

100   Tellep, D. M., and Talbot, L., "Normal Forces on Flat Plates in Low-Density Supersonic Flow", J. Aero-Sci., Vol. 23, No. 12, Dec 1956, pp 1099-1108

101   Macha, J. M., Norton, D. J., and Yong, J. C., "Surface Temperature Effect on Subsonic Stall", AIAA Paper No. 72-960, Sept 1972.

102   Bertram, M. H., and Blackstock, T. A., "Some Simple Solutions to the Problem of Predicting Boundary-Layer self-Induced Pressures", NASA TND-798, April 1961.

103   Mandl, P., "Effect of Small Surface Curvature on Unsteady Hypersonic Flow over an Oscillating Thin Wedge", CASI Transactions, Vol. 4, No. 1, March 1971, pp 47-57.

104   Mandl, P., "Unsteady Hypersonic Flow over a Slightly Curved Oscillating Thin Airfoil", Report Ltr-US-15, Sept 1970.

105   Mandl, P., "Errata, Effect of Small Curvature on Unsteady Hypersonic Flow over an Oscillating Thin Wedge", Vol. 8, No. 2, Sept 1975.

106   Sullivan, P. A., "Inviscid Hypersonic Flow on Cusped Surfaces", Journal of Fluid Mech., Vol. 24, Jan 1966, pp 99-112.

107   McIntosh, S. C., Jr., "Hypersonic Flow over an Oscillating Wedge", AIAA Journal, Vol. 3, No. 3, March 1965, pp 433-440.

108   Bailie, J. A., and McFeely, J. E., "Binary Flutter of Wedges in Hypersonic Flow", J. Spacecraft and Rockets, Vol. 3, No. 7, July 1966, pp 1130-1132.

109   Babb, J. R., "Thermoelastic Effects on Hypersonic Stability and Control - Part 1: Hypersonic Aerodynamics", ASD-TR-61 287, May 1963.

110   Bennett, R. M., and Yates, E. C., "A Study of Several Factors Affecting the Flutter Characteristics Calculated for Two Swept Wings by Piston Theory and by Quasi Steady Second-Order Theory and Comparison with Experiment", NASA TN D-1794, May 1963.

111   Yates, E. C., and Bennett, R. M., "Use of Aerodynamic Parameter from Nonlinear Theory in Modified-Strip-Analysis Flutter Calculations for Finite Span Wings at Supersonic Speeds, NASA TN D-1824, July 1963.

112   Hanson, P. W., and Levy, G. M., "Experimental and Calculator Results of a Flutter Investigation of Some very Low Aspect Ratio Flat Plate Surface at Mach Numbers from 0.62 to 3.00", NASA TN D-2038, October 1963.

113   Hurley, S. R., "Hypersonic Flutter Model Tests of Advanced Wing Configurations at Initial Angles of Attack", RTD TDR-63-4219, October 1964.

114   Chawla, J. P., "Aeroelastic Instability at High Mach Number", J. Aero. Sci., Vol. 24, No. 4, April 1958, pp 246-258.

115   Runyan, H. L., and Morgan, H. G., "Flutter at Very High Speeds", NASA TN D-942, August 1961.

116   Goetz, R. C., "Hypersonic Flutter Analysis Using Measured Static Aerodynamic Derivatives and Comparison with Experiment", NASA TN D 5233, May 1969.

117   Korkegi, R. H., "Comparison of Shock-Induced Two- and Three-Dimensional Incipient Turbulent Separation", AIAA Journal, Vol. 13, No. 4, April 1975, pp 534-535

Appendix A
NOMENCLATURE

$\{1\}$	unit vector
a	speed of sound
a_i	deformation amplitude in i^{th} vibration mode
a, b	parameters defined in Eq. (3.16)
$[A]$	surface area matrix (Eq. (4.24))
A_1, A_2	constants defining f* (Eq. (3.6))
ΔA	surface area element
A, B	parameters in Eq. (3.16)
$\bar{B}, \bar{B}_1, \bar{B}_2$	viscous parameters defined in Eq. (3.57)
$[BI], [BR]$	matrices defined in Eq. (4.27)
c	reference length, cylinder caliber or base diameter for bodies, chord length for air foils
C^*	Chapmen-Rubesin parameter based on reference temperature
D	plate stiffness, Et $[12 (1 - \nu^2)]$
$[D]$	damping matrix
D_N	nose drag

$$C_{D_N} = D_N / (\rho_\infty U_\infty^2/2) \, (\pi d_N^2/4)$$

d_N	nose drag of airfoil strip

$$c_{d_N} = d_N / (\rho_\infty U_\infty^2/2) \, d_N{}'$$

d_B	base diameter

d_N	diameter of axisymmetric nosebluntness
d_B'	base height of wedge
d_N'	diameter of cylindrical leading edge
$[D\Phi]$	modal slope matrix
E	Young's Modulus
f, F	pressure correlation functions
f^*	dynamic pressure ratio, $\rho U^2 / \rho_\infty U_\infty^2$
F_z	lift component (Eq. (4.20))
$\{F\}$	total force vector
$\{F_z\}$	aerodynamic force vector
g^*	velocity ratio, U/U_∞
G_1, G_2, G_e	parameters defined in Eqs. (3.61) and (3.77)
h	surface displacement
i	imaginary unit, $i^2 = -1$
k	reduced frequency, $c\omega/2U_\infty$
k_f and k_g	parameters in Eq. (3.16) and Eq. (3.17) respectively
$K, \bar{K}$	nonlinear algebraic stiffness operators (Section 4)
K	hypersonic similarity parameters (Eqs. (2.23) and (3.33))
$K_{sh}, k(\gamma)$	shock parameters (Eqs. (3.4) and (3.9))
ℓ	sharp cone body length
M	Mach Number, U/a
$[M]$	mass matrix

M_p pitching moment

$$C_m = M_p/(\rho_\infty U_\infty^2/2)\, Sc$$

m_p pitching moment for an airfoil strip

$$c_m = m_p/(\rho_\infty U_\infty^2/2)\, c^2$$

$M \times N$ size of matrix

N normal force

$$C_N = N/(\rho_\infty U_\infty^2/2)\, S$$

n normal force for an airfoil strip

$$c_n = n/(\rho_\infty U_\infty^2/2)\, c$$

p static pressure

$$C_p = (p - p_\infty)\,/\,(\rho_\infty U_\infty^2/2)$$

p_0 blast wave pressure

$$C_{p_0} = (p_0 - p_\infty)/(\rho_\infty \, U_\infty^2/2)$$

P   aerodynamic operator

$|P|$ pressure force vector

Pr   Prandtl number

q   rigid body pitch rate (Section 3)

q_ℓ deflection amplitude in ℓ'th mode

$\bar{q}$ dynamic pressure, $\rho \, U^2/2$

$Q, \bar{Q}$ aerodynamic operators

Q_i aerodynamic influence coefficients (Eq. (4.14))
r   body radius (Fig. 3.1)

R   radial distance from bow shock centerline (Fig. 3.1)

$|R|$ thermal forces

R_b longitudianl body radius of curvature

R_e Reynolds number, $Re_x = x \, U_e/\nu_e$ and

$$Re_{x_\infty} = x \, U_\infty/\nu_\infty$$

S   reference area, $\pi \, c^2/4$ for bodies and projected wing area for air foils

t   time

t   plate thickness (Eq (2.5))

T   temperature

T*   reference temperature

ΔT_{crit} critical temperature difference

u	displacement field (Section 4)
u_i	deformation pattern in ith vibration mode
U	strain energy (Eq (2.1))
U	axial velocity
V	total potential energy (Eq (2.1))
$V_\perp$	velocity normal to body surface
W	airfoil sink velocity, normal to free stream
W_t	lateral load applied at the wing tip
x	axial coordinate (Fig. 3.1)
x, y, z	cartesian coordinates (Eq (2.4))
x_g, y_g, z_g	global coordinates in STAGS
x_o	centroid location of equivalent nose bluntness (x_o = 0 for spherical or cylindrical nose bluntness)
$\overline{\Delta x}$	cone center of gravity location forward of base
X_i	displacement component (Eq (2.1))
X, Y	surface coordinates (Eq (2.4))
y/d_N	spanwise fin coordinate (Fig. 3.13)
y_L, y_U	distance from chord centerline to lower and upper airfoil surface (Fig. 3.18 a)
y_b	wind-fixed surface coordinate (Fig. 3.34)
z	translatory coordinate (Fig. 3.1)

α	thermal expansion coefficient
α	angle of attack
α_0	trim angle-of-attack
β	angular body coordinate (Fig. 3.1)
γ	constant in Eg (4.12)
γ	ratio of specific heats (γ = 1.4 for air)
δ	local flow inclination to airfoil surface. For small inclination angles $\delta = V_{\perp}/U$
δ_f	change in δ due to deformation
ζ^*	boundary layer displacememt thickness
Δ	bending deformation
ϵ	density ratio across bow shock
θ	body perturbation in pitch
θ_c	cone half angle
θ_F	flare angle
θ_w	wedge half angle
κ	dimensionless surface curvature, $c/R_b \theta_w$
$\bar{\kappa}$	κ for airfoil center chord
Λ	nose bluntness parameter (Eq. (3.9))
μ	Mach angle
ν	Poisson's ratio
ν	kinematic viscosity of air (Section 3)
$\bar{\nu}$	viscous hypersonic similarity parameter, $\bar{\nu} = \bar{\chi} / M_e^e$
ξ	dimensionless x-coordinate, $\xi = x/c$
ξ	temperature parameter in Eg(2.5)
ξ, η	coordinates for grid generation in STAGS

ξ	shape parameter for temperature distribution (Eg (2.5))
ξ	amplitude of vibration mode (Eg (4.19))
ρ	air density
σ	anguler surface coordinate (Fig 3.5)
υ	surface inclination to free stream velocity
ϕ	azimuth (Fig. 3.1)
ϕ_ℓ	mode shape of ℓ'th mode.
Φ	modal displacement natrix
$\bar{\chi}, \chi^*$	inviscid hypersonic similarity parameters defined in Eg. (3.7 and (3.11) respectively.
$\bar{\chi}$	viscous hypersonic similarity parameter defined in Eg. (3.57)
ω_i	natural vibration frequency of i'th mode
Ω	work done by external forces (Eg. (2.1))

Subscripts

A	aft half
AC	aerodynamic center
b	body surface
B	base
B	Busemann correction
c	centrifugal pressure corrrection
crit	critical
CG	center of gravity or oscillation center
d	deformation
e	boundary layer edge
E	total elastic deformation effect
f	flexibility effect
F	forward half
FP	flat plate
L	lower surface
LE	leading edge
i	inviscid flow (Section 3)
i	initial imperfection (Section 2)
M	main airfoil
N	nose
N and NEWT	Newtonian value
γN	γ- corrected Newtonian value
PT	piston theory

sh	bow shock
SHARP	sharp leading edge or pointed nose
t	total or stagnation value
TE	trailing edge
TW	tangent wedge
U	upper surface
v	viscosity effect
w	wall
o	initial value or constant parameter value
0, 1, 2, 3	parameter values bounding different regions (Eq. (3.16))
∞	free stream conditions
2D	two-dimensional value

Superscript

'	prime superscript indicates two-dimensional value
—	barred symbols indicate absolute value: e.g., $\bar{h} = |h|$

Derivative Symbols

$$\dot{\theta} = \frac{\partial \theta}{\partial t}$$

$$C_{N_\alpha} = \frac{\partial C_N}{\partial \alpha} \; ; \quad C_{m_\theta} = \frac{\partial C_m}{\partial \theta}$$

$$C_{m_q} = \frac{\partial C_m}{\partial \left(\frac{cq}{U_\infty}\right)} \; ; \quad C_{m_{\dot{\alpha}}} = \frac{\partial C_m}{\partial \left(\frac{c\dot{\alpha}}{U_\infty}\right)}$$

$$C_{m_{\dot{\theta}}} = C_{m_q} + C_{m_{\dot{\alpha}}}$$

$$C_{p_K} = \frac{\partial C_p}{\partial K}$$

A-9

APPENDIX B   UTILIZATION OF THE STAGS HYPERSONIC AEROELASTICITY PACKAGE

B.1   Program Organization

In order to perform a complete hypersonic aeroelastic analysis of an "aerodynamic" structure, such as a wing or a wing-fuselage assembly, two approaches are currently available. The first approach is to perform a STAGS nonlinear "quasi-static" analysis including the effects of both aerodynamic heating and transverse forcing functions, while at the same time computing and saving vibration modes at selected pre-stress states along the flight trajectory. In this way a determination of divergence and/or thermal buckling conditions may be obtained directly, while a prediction of flutter behavior, i.e., critical speed, may be obtained in a subsequent modal analysis with a post-processor. The second approach is to include inertial effects at the outset by performing transient (time integration) analysis. This of course obviat   the need for the modal flutter post-processor but at a significantly greater expense to the user. In either case, two external programs, HYPATH (Hypersonic Aerodynamic Thermal Analysis) and HYPALM (Hypersonic Aerodynamic Load Matrices) should be executed in preparation for STAGS, while the optional "post"-processor; FLAM (Flutter Analysis Modal) may be executed when using the first approach. The integration of these programs, which is based on a peripheral data structure, as well as their individual input/output require-ments and those adjustments additionally required by STAGS for such an analysis are described in the following sections. The general organization is summarized in Figure B.1.
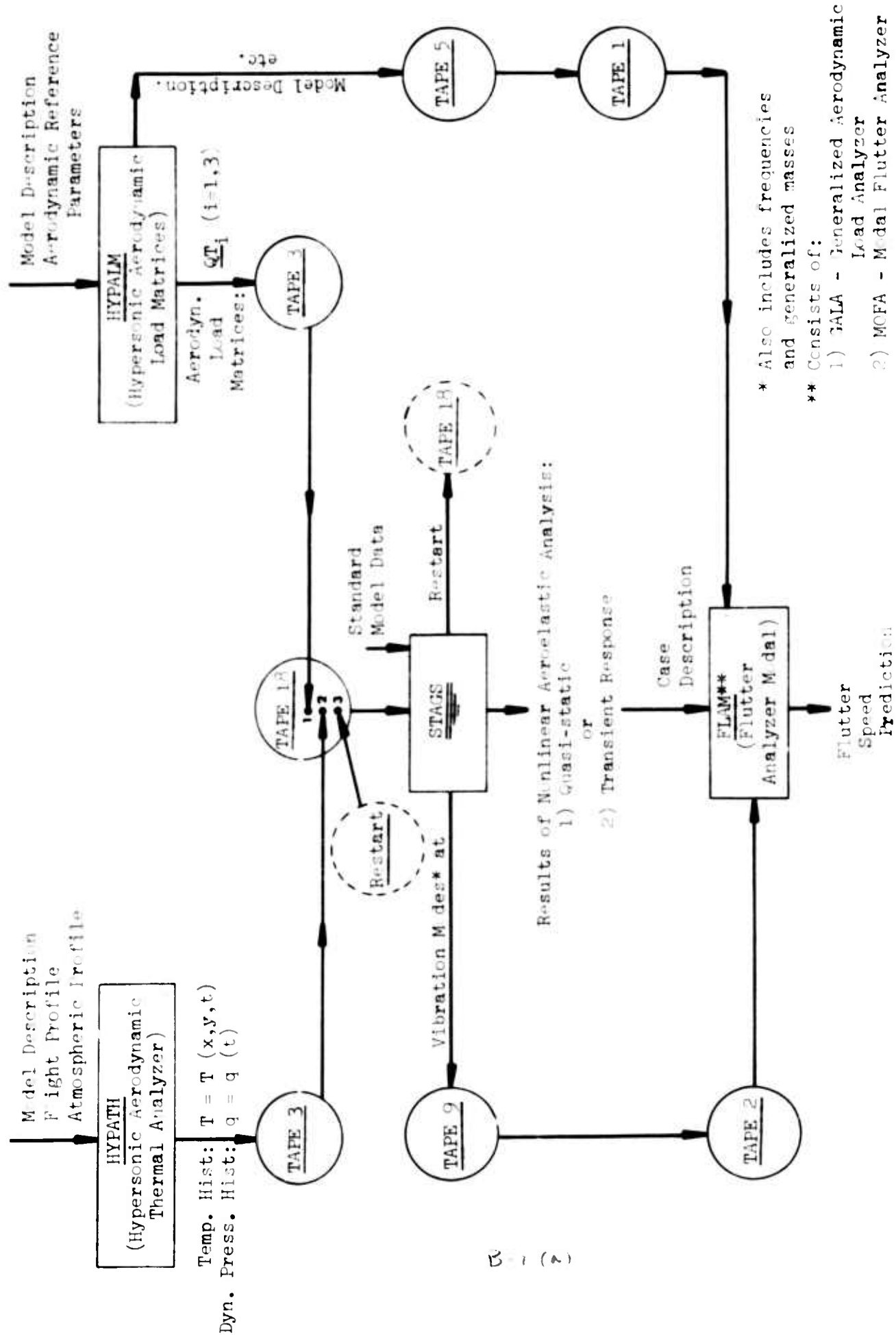
Fig. B.2 STAGS Hypersonic Aeroelastic Analysis: Program Organization and Interaction

B-1 (a)

B.2   Program   HYPALM (Hypersonic Aerodynamic Load Matrices)

B.2.1 Function

Prepares for a STAGS aeroelastic analysis by creating an aerodynamic load matrix file, QT0, QT1, QT2, QT3, for each "aerodynamically active" branch. These matrices, in addition to the dynamic pressure and elastic rotations of the structure (i.e., wing) are incorporated by STAGS in the formation of the aerodynamically equivalent forcing function.

B.2.2 Data Card Input

GENERAL CONTROL CARDS.

A-1 Case Title Card

Variable	Format	Columns	Description
Label	12A6	1-5	Case title.

B-1 I/O Summary Card

Variable	Format	Columns	Description
ISTEER	I5	1-5	0 - Thickness/chord ratios at span-wise stations to be input from cards. 1 - Thickness/chord ratios to be defined in user written subroutine PSTEER.
ISTAGS	I5	6-10	0 - Print results only. 1 - Save QT matrices on tape for STAGS analysis.

Variable	Format	Columns	Description
NBRNCH	I5	11-15	Total number of branches in STAGS model.

B-2 Active Branch Summary Card

Variable	Format	Columns	Description
LAB (I) (I=1, NBRNCH)	16I5	1-80	List of aerodynamically active branches. -1 - inactive, do not perform analysis on branch. +1 - active, perform analysis on branch.

THE REMAINING CARDS ARE REPEATED ONCE FOR EACH "ACTIVE" BRANCH AS DEFINED ON THE B-2 CARD.

GEOMETRY

C-1 Shell Type Definition Card

Presently, the shell geometry for each active branch is restricted to that of a quadrilateral plate, as representative of a wing. Due to the nature of the analysis the quadrilateral is further restricted such that two of its sides must be parallel to the local x axis (see description of coordinate systems in STAGS user's manual). This ensures a unique "span-wise" station for each column in the branch.

Variable	Format	Columns	Description
NSHELL	I5	1-5	Basic shell geometry. 3 - Plate.
NCART	I5	6-10	0 - Rectangular grid. 1 - Isoparametric mapping to a quadrilateral.

C-2 Surface Constants Card #1

Corresponds to rectangular dimensions L_1 and L_2 in STAGS manual for NSHELL=3, if NCART=0. If NCART=1, L_1 and L_2 represent maximum "natural" coordinates.

Variable	Format	Columns	Description
PRØP1	E10.6	1-10	Length parallel to local x axis. Use 1.0 if NCART=1.
PRØP2	E10.6	11-20	Length parallel to local y axis. Use 1.0 if NCART=1.

C-3 Surface Constants Card #2

This card is included only if NCART=1. It represents local coordinates of the quadrilateral branch corner points corresponding to the system established in the STAGS user's manual.

Variable	Format	Columns	Description
X(I), Y(J) (J-1, 4)	8E10.6	1-80	Local cartesian coordinates of branch corner points. Must be defined in clockwise order starting with the coordinates (0., 0.).

DESCRETIZATION

D-1 Grid Definition Card

Variable	Format	Columns	Description
NR	I5	1-5	Number of rows. NR positive, spacing is constant. NR negative, spacing is variable, read in X or ξ values on card D-2.

Variable	Format	Columns	Description
NC	I5	6-10	Number of columns. NC positive, spacing is constant. NC negative, spacing is variable, read in Y or η values on card D-3.

D-2 X- or ξ- Coordinate Card

Include this card only if NR < 0 on the D-1 card.

Variable	Format	Columns	Description
X(I) (I=1, NR)	8E10.6	1-80	X or ξ value for row I.

D-3 Y- or η- Coordinate Card

Include this card only if NC < 0 on the D-1 card.

Variable	Format	Columns	Description
Y(J) (J=1, NC)	8E10.6	1-80	Y or η value for Column J.

AERODYNAMIC PARAMETERS

E-1 Aerodynamic Analysis Type Summary

Variable	Format	Columns	Description
NTHK	I5	1-5	1 - Include thickness effects.
NCAM	I5	6-10	1 - Include camber effects.
NCON	I5	11-15	1 - Include control surface effects.
NDYN	I5	16-20	1 - Include fuselage nose effects.
MODAL	I5	21-25	1 - Save input file for subsequent modal flutter analysis.

E-2 Flight Parameter Card

Variable	Format	Columns	Description
ALPHA	E10.6	1-10	Angle of attack (deg.)

Variable	Format	Columns	Description
PR	E10.6	11-20	Ambient pressure (psi)
RHO	E10.6	21-30	Ambient density $\left(\dfrac{lb\text{-}sec^2}{in^4}\right)$
AMACH	E10.6	31-40	Representative Mach no.
GAM	E10.6	41-50	Ratio of specific heats ($=1.4$)
BREF	E10.6	51-60	Ref. semi-chord (in.)

E-2 Section Profile Card

Variable	Format	Columns	Description
NSYM	I5	1-5	0 - Symmetric profile 1 - Nonsymmetric profile
NPROF	I5	6-10	1 - Diamond profile 2 - Wedge profile 3 - Parabolic profile

E-4 Thickness/Chord Ratios, Upper Profile

Include this card only if NTHK=1 on the E-1 card and ISTEER=0 on the

B-1 card.

Variable	Format	Columns	Description
TU(J) (J=1, NC)	8E10.6	1-80	Thickness/chord ratio at span-wise station J, upper profile.

E-5 Thickness/Chord Ratios, Lower Profile

Include this card only if

1) ISTEER=0 on the B-1 card,
2) NTHK=1 on the E-1 card, and
3) NSYM=0 on the E-3 card.

Variable	Format	Columns	Description
TL(J) CJ=1, NC)	8E10.6	1-80	Thickness/chord ratio at span-wise station J, lower profile.

E-6 Local Chord Lengths

Include this card only if NCAM=1 on the E-1 card.

Variable	Format	Columns	Description
CB(J) (J=1, NC)	8E10.6	1-80	Local chord lengths.

E-7 Control Surface Parameter Card #1

Include this card only if NCON=1 on the E-1 card.

Variable	Format	Columns	Description
XH(J)	8E10.6	1-80	Distance of leading edge from hinge-line.

E-8 Control Surface Parameter Card #2

Include this card only if NCON=1 on the E-1 card.

Variable	Format	Columns	Description
BETA(J) (J=1, NC)	8E10.6	1-80	Control deflection in radians.

E-9 Fuselage Nose Parameter Card

Variable	Format	Columns	Description
DN	E10.6	1-10	Fuselage nose diameter
XN	E10.6	11-20	Distance from leading edge to
CDN	E10.6	21-30	Nose drag coefficient body

B.2.3   User Written Subroutines

At present, a user written subroutine is available for defining the maximum thickness/chord ratios (i.e., profile) as a function of span-wise station. It is called when ISTEER=1 and is referred to as subroutine PSTEER:

SUBROUTINE PSTEER (J, Y, C, TU, TL)	PSTEER.2
END	PSTEER.3

where:

Given $\begin{cases} J = \text{Span-wise station (i.e., column).} \\ Y = \text{Coordinate (local) of span-wise station.} \\ C = \text{Chord length.} \end{cases}$

Returned $\begin{cases} TU = \text{Maximum thickness/C (upper profile).} \\ TL = \text{Maximum thickness/C (lower profile).} \end{cases}$

> Note: TL may be neglected when the
> profile is symmetric (NSYM=1).

B.2.4   Output File Creation

Two peripheral files are created by HYPALM:

1) The $\underline{QT_i}$ matrices are written to $\underline{TAPE3}$ in preparation for a STAGS aeroelastic analysis (if ISTAGS=1 on the B-1 card).

B-8

2)   The entire input file is written to <u>TAPE5</u>
in preparation for FLAM, the post-STAGS
flutter analyzer (if MODAL=1 on the E-1 card).

It is therefore necessary to save these files either on disk, or
a physical tape unit should the user decide to execute the program package
in stages rather than within the same runstream.

B.3   Program HYPATH (Hypersonic Aerodynamic Thermal Analysis)

B.3.1   Function

HYPATH prepares for a STAGS analysis by creating a temperature history file, based on aerodynamic heat convection, radiation and one dimensional conduction theory, for a given flight profile. The analysis includes all "aerodynamically active" STAGS branches.

B.3.2   Data Card Input

GENERAL CONTROL CARDS

A-1 Case Title Card

Variable	Format	Columns	Description
Title	12A6	1-72	Case Title

B-1 Execution Summary Card

Variable	Format	Columns	Description
ISTEER	I5	1-5	0 - Nodal properties to be input on cards. 1 - Nodal properties to be defined in user written subroutine STEER.
ISTAGS	I5	6-10	0 - Suppress temperature history file. 1 - Create temperature history file.
NBRNCH	I5	11-15	Total number of branches in STAGS model.
NCHK	I5	16-20	0 - Perform analysis. 1 - Verify input data only.

B-2 Branch Summary Card

For correct file utilization by STAGS, it is necessary that every STAGS branch is represented in this summary card(s).

Variable	Format	Columns	Description
NROB(I), IROC(I) (I = 1, NBRNCH)	15I5	1-75	Number of rows in branch I, number of columns in branch I, and row-or-column only switch:

0 - Every node in branch is to be analyzed.
1 - Only one node per row need be analyzed.
2 - Only one node per column need be analyzed.
3 - Only one node is necessary to represent entire branch.
-1 - Ignore branch in analysis (i.e., "inactive").

B-3 Input Data Summary Card

Variable	Format	Columns	Description
NLAY	I5	1-5	Number of layers thru thickness to be considered. Maximum = 6. Note: NLAY + 1 temperatures are computed. If symmetry is later specified, 2 * NLAY + 1 temperatures are implicitly obtained.
JFMAX	I5	6-10	Number of data cards in flight profile deck.
IATM	I5	11-15	Atmospheric data specification.

0 - Atmospheric profile deck will be read.
1 - 1966 U.S. standard Atmospheric data will be used.
2 - Mil. Std. 210-A Std. Hot day data will be used.
3 - Mil. Std. 210-A std. Cold day data will be used.

Variable	Format	Columns	Description
JAMAX	I5	16-20	Number of data cards in atmospheric profile deck (only necessary if IATM=0).
IMORV	I5	21-25	0 - Flight profile velocity defined in terms of Mach number. 1 - Flight profile velocity defined in ft./sec.
ITIME	I5	26-30	0 - Time in flight profile given in seconds. 1 - Time in flight profile given in minutes.
IGRAD	I5	31-35	0 - Initial temperatures are uniform thru thickness. 1 - Initial temperatures vary thru thickness.
IPLOT	I5	36-40	IPLOT negative, temperature vs. thickness plots are required. IPLOT zero or positive, no plots are required. (Note: plots are only allowed when ISTAGS=0 on B-1 card.

B-4 Time Step and Computation Summary Card

Variable	Format	Columns	Description
TIME 1	E10.6	1-10	Initial time to be considered in analysis. (Must lie within range specified in flight profile deck, card).
TIME 2	E10.6	11-20	Final time to be considered in analysis. (Must lie within range specified in flight profile deck).
NSTEPA	I5	21-25	Number of time steps to be computed in finite difference analysis. The maximum allowed is 100.

Variable	Format	Columns	Description
NSTEPW	I5	26-30	Number of time steps to be saved on STAGS temperature history file. The maximum allowed is 50. (In addition the initial values are always saved.)
ICOM	I5	31-35	Equation solution type. 0 - Tri-diagonal solution. 1 - Cholesky solution.

C-1 Plot Specification Card

Include this card only if IPLOT < 0 on the card and ISTEER=0

on the card.

Variable	Format	Columns	Description
Arg, XTLME(I) (I=1, 5)	8E10.6	1-80	Number of times at which plots are desired and their values, respectively. The maximum allowed is 5.

D-1 Flight Profile Deck Header Card

Variable	Format	Columns	Description
FLIGHT	12AG	1-72	Flight profile.

D-2 Flight Profile Deck

The flight profile deck consists of JFMAX cards (as specified

on the B-3 card), each card prescribing the flight velocity and altitude

at a given time along the trajectory. Linear interpolation is used at

computation steps falling between the prescribed times.

Variable	Format	Columns	Description
TF(J), CF(J), FF(J) (J=1, JFMAX)	3E10.6	1-30	Time, velocity and altitude, respectively, at various points along the flight trajectory.

B-13

E-1 Atmospheric Profile Deck Header Card

Include this card only if IATM=0 on the B-2 card.

Variable	Format	Columns	Description
ATMOS	12A6	1-72	Atmospheric profile title.

E-2 Atmospheric Profile Deck

Include these cards only if IATM=0 on the B-2 card.   The
atmospheric profile deck prescribes the ambient pressure and temperature
as a discrete function of altitude. JAMAX cards (as specified on B-2 card)
each representing an individual altitude are used.   As with the flight profile
deck, the independent variable (i.e., altitude) must be monotonically increas-
ing as linear interpolation is used for intermediate stations.

Variable	Format	Columns	Description
TA(J), CA(J), FA(J) (J=1, JAMAX)	3E10.6	1-30	Altitude (ft.), pressure (psf.) and temperature (DEG. R), respectively, at JAMAX separate altitudes.

THE REMAINING INPUT SECTION IS REPEATED ONCE FOR EACH

"ACTIVE" (I.E., IROC $\geq$ 0) BRANCH

GEOMETRY

F-1 Shell Type Definition Card

Variable	Format	Columns	Description
NSHELL	I5	1-5	Shell type.
			3 - Plate

Variable	Format	Columns	Description
NCART	I5	6-10	0 - Rectangular grid. 1 - Quadrilateral grid, isoparametric mapping.

F-2 Aerodynamic Flow Description Card

This card prescribes the branch configuration in terms of the aerodynamic problem class.

Variable	Format	Columns	Description
ISHAPE	I5	1-5	1 - Flat plate 2 - Cylinder (not operational) 3 - Sphere (not operational)
IFLCN	I5	6-10	1 - Flat plate, perfect gas. 2 - Flat plate, cabrically imperfect gas. 3 - Stagnation point, perfect gas. 4 - Wedge reattachment (cubic solution) 5 - 17 "Reserved for future use."
DIA	E10.6	11-20	Diameter for cylindrical or spherical geometry (reserved for future use).

F-3 Surface Constants Card #1

Corresponds to rectangular dimensions L_1 and L_2 in STAGS manual for NSHELL=3, if NCART=0. If NCART=1, L_1 and L_2 represent maximum "natural" coordinates.

Variable	Format	Columns	Description
PRØP1	E10.6	1-10	Length parallel to local x axis. Use 1.0 if NCART=1.
PRØP2	E10.6	11-20	Length parallel to local y axis. Use 1.0 if NCART=1.

F-4 Surface Constants Card #2

This card is included only if NCART=1. It represents local coordinates of the quadrilateral branch corner points corresponding to the system established in the STAGS user's manual.

Variable	Format	Columns	Description
X(I), Y(J)	8E10.6	1-80	Local cartesian coordinates of branch corner points. Must be defined in clockwise order starting with the coordinates (0., 0.).

DISCRETIZATION

G-1 Grid Definition Card

Variable	Format	Columns	Description
NR	I5	1-5	Number of rows. NR positive, spacing is constant. NR negative, spacing is variable, read in X or ξ values on card G-2.
NC	I5	6-10	Number of columns. NC positive, spacing is constant. NC negative, spacing is variable, read in Y or η Values on card G-3.

G-2 X- or ξ- Coordinate Card

Include this card only if NR < 0 on the G-1 card.

Variable	Format	Columns	Description
X(I) (I=1, NR)	8E10.6	1-80	X or ξ value for row I.

G-3 Y- or η- Coordinate Card

Include this card only if NC < 0 on the G-1 card.

Variable	Format	Columns	Description
Y(J) (J=1, NC)	8E10.6	1-80	Y or η value for Column J.

- -

*In the event that the steering subroutine is not used (i.e., ISTEER=0 on the B-1 card, the following cards are required for each node being considered within an "active" branch.

H-1 Nodal Information Card #1

Variable	Format	Columns	Description
NSN	I5	1-5	Number of node being considered (must be sequential).
TT	E10.6	6-15	Total thickness (in.) characteristic re no. distance (in.).
EM	E10.6	26-35	Emissivity
DELTA	E10.6	36-45	Sweep angle (deg.)
ALPHA	E10.6	46-55	Heat transfer coefficient at midplane. 0. - symmetric section only one-half considered.

H-2 Nodal Information Card #2

Include this card only if IGRAD=0 on the B-3 card.

Variable	Format	Columns	Description
T0	E10.6	1-10	Initial temperature, uniform thru thickness (DEG. F).

H-3 Nodal Information Card #3

Include this card only if IGRAD=1 on the B-3 card.

Variable	Format	Columns	Description
TZER(I) (I=1, NLAY+1)	8E10.6	1-80	Initial temperature distribution thru thickness (or to mid-surface if ALPHA=0. on the H-1 card).

H-4 Nodal Information Card #4

Variable	Format	Columns	Description
NMAT(I) (I=1, NLAY)	16I5	1-80	Material type of each layer thru thickness (or half of thickness if ALPHA=0. on the H-1 card).

1 - 2024T Al
2 - 701 Al
3 - Beryllium
4 - Copper
5 - SAE 1010 Steel
6 - SAE 1020 Steel
7 - SAE 4130 Steel
8 - 300 Maraging Steel
9 - 301 Stainless Steel
10 - 403 Stainless Steel
11 - 410 Stainless Steel
12 - G-18-8 Stainless Steel
13 - 17-7 PH Stainless Steel
14 - Iconel - X
15 - Magnesium (DCW-HK-31XA-F)
16 - Tungsten
17 - Fiberglass
18 - Avcoat No.1
19 - Insulcork
20 - Titanium
21 - TMC Propellant

B.3.3 User Written Subroutine

The user has the option of specifying all of the nodal parameters appearing in data cards H-1 to H-4 within a single user written subroutine, STEER. In this way, functional relationships with branch, row and column numbers, transverse station and spacial coordinates as independent variables may be conveniently established.

```
SUBROUTINE STEER (NSN, IB, X, Y, ETA, ZETA, IP        STEER.2
1, TZER, T, NMAT, ALE, DELTA, EM, ALPHA)              STEER.3
DIMENSION TZER(7), NMAT(6)                            STEER.4
(INSERT STEERING CODE)                                STEER.5
END
```

WHERE:

NSN = Number of structural node. This number is incremented consecutively through the entire set of "active" branches. Depending upon the value of IROC(I) (see B-2 card) it may be incremented only once per row, once per col., etc.

Given: {
IB = Branch number

x = Local x coordinate of node

y = Local y coordinate of node

ETA = "Natural" x coordinate (meaningful only when NCART=1)
}

ZETA = "Natural" y coordinate (meaningful only for NCART=1).

IP = Number of points defined thru the thickness (=NLAY+1)

Returned:

TZER(I) (I=1, IP)	See H-1 card for definition
T	Equivalent to TT on H-1 card
NMAT(I) (I=1, IP-1)	See H-1 card
ALE	See H-1 card
DELTA	See H-1 card
EM	See H-1 card
ALPHA	See H-1 card

B.3.4 Output File Creation

A thermal history file containing, essentially, T=T (x, y, t) and q = q(t) is written to TAPE3 when ISTAGS=1 on the B-1 card. Due to the data reorganization necessary to produce this file, it is advised that a preliminary run with NCHK=1 is made for model verification before attempting the file creation run with ISTAGS=1 and NCHK=0. As with program HYPALM, it will also be necessary to save TAPE3 on a peripheral device if the STAGS analysis is to be performed in a separate run.

B.4 The "STAGS" Interface

B.4.1 Data File Input

Assuming the aeroelastic pre-processors, programs HYPALM and HYPATH, have been executed, the following data files will have been created:

1) Aerodynamic Load Matrices
   (written to TAPE3 by HYPALM)

2) Thermal History *
   (written to TAPE3* by HYPATH)

3) Aerodynamic Model Description
   (written to TAPE5 by HYPALM)

As shown in Figure B.1, two of these files are usually required for a STAGS aeroelastic analysis and therefore must be copied to TAPE18 (in the order depicted) before execution. In the case of a "restart" analysis a third file must also be copied to TAPE18. This refers to the "restart" file which is automatically written to TAPE18 in a previous analysis and which, of course, must be "saved" at the time and then copied to TAPE18 (in the position depicted in Fig. B.1) before executing a restart run. Note that files 1) and 2) above do not have to include the entire flight trajectory at the outset, as the files may be re-created with programs HYPALM and HYPATH to account for different intervals in the trajectory prior to successive STAGS "restart" runs.

---

* It is worth emphasizing that TAPE3 refers to a local file. If HYPALM and HYPATH are to be executed consecutively within the same runstream, the contents of TAPE3 must therefore be copied to an intermediate file and TAPE3 "unloaded" before executing the second program and "re-creating" a new TAPE3.

B.4.2 Data Card Modifications

The data card requirements for the various possible types of STAGS analyses are described in the STAGS user's manual. Those particular entries which are affected in a STAGS aeroelastic analysis are:

1) Two additional parameters have been included on the B-1 card -

Variable	Format	Columns	Description
IAERO	I5	31-35	1 - Aeroelastic analysis. Aerodynamic load matrices are to be read from TAPE18. 0 - Not an aeroelastic analysis.
ITHERM	I5	36-40	1 - Hypersonic thermal analysis has been performed. Thermal history is to be read from TAPE18.

B-2 Aerodynamic Load Matrix Selection Card

Include this card only if IAERO=1 on the B-1 card.

Variable	Format	Columns	Description
IQT0	I5	1-5	1 - Read QT0 matrix.
IQT1	I5	6-10	1 - Read QT1 matrix.
IQT2	I5	11-15	1 - Read QT2 matrix.
IQT3	I5	16-20	1 - Read QT3 matrix.
IPQT	I5	21-25	1 - Print QT matrices.
RHOINF	E10.6	26-35	Ambient air density.

3) Note that when performing a quasi-static STAGS aeroelastic analysis INDIC should be set equal to 3 for a basic nonlinear analysis, and to 5 if a subsequent modal flutter analysis is anticipated. In the latter case a number of vibration modes about various pre-stress states are computed and saved as described under the F-2 and F-3 data cards in the STAGS user's manual.

4) As long as the thermal history file is to be considered (i.e., ITHERM=1) the dynamic pressure as a function of time is directly accessible. Therefore, when performing a quasi-static nonlinear analysis the load multipliers on the F-1 card (system A) represent actual values of the time (in seconds) and correspond to the flight profile deck used as input to program HYPATH. When performing a transient response analysis the flight profile time is then identical with the times specified on the H-1 data card. One potential complication arises when the hypersonic thermal effects are omitted and an aeroelastic analysis is attempted with IFLU=1 and ITHERM=0 on the B-1 card. In this case the consequences are as follows:

a) For a nonlinear static analysis, since the dynamic pressure history is no longer accessible, the load multipliers on the F-1 card represent actual values and increments of the dynamic pressure in psi.

b) For a transient analysis, the time parameter is specified as usual, but the flight velocity must be specified as a function of time in subroutine VINF.

B.4.3 Output File Creation

Potentially, two data files are created during a STAGS aeroelastic analysis:

1) A restart file is written to TAPE18 in all cases.

2) A vibration mode file containing displacement mode vectors, natural frequencies and generalized masses for each[*] of the selected pre-stress states is written to TAPE9 if INDIC=5 and IAERO=1 on the B-1 card.

These files, of course, must be saved on a peripheral device for use in a subsequent execution of STAGS and/or the flutter post-processor (FLAM).

B.5 Program FLAM (Flutter Analysis Modal)

B.5.1 Function

FLAM performs a linearized modal flutter analysis about a series of nonlinear pre-stress states along a flight trajectory, incorporating the vibration modes computed by STAGS at these prescribed states. Internally, program GALA employs the displacement mode vectors to obtain generalized

---

[*] The data for each pre-stress state is separated by an END-OF-FILE mark, which must be considered when copying TAPE9 from one logical file to another.

aerodynamic forces which are utilized (in addition to the natural frequencies, generalized masses and selected "reduced" frequencies) by program MOFA to solve a reduced (complex) eigenvalue problem and hence predict the critical, i.e., flutter, speed in an iterative manner.

B.5.2 Data File Input

Two data files are prerequisite to performing a FLAM analysis, in addition to a minimal number of data cards:

1) "Model description" file created by program HYPALM previously on TAPE5. This file must be copied (or attached) to TAPE1 before FLAM execution.

2) "Vibration mode" file created by STAGS in a previous analysis and containing eigenvectors, eigenvalues and generalized masses for a number of modes evaluated at a number of pre-stress states (i.e., times along flight trajectory). This file, originally saved on TAPE9 must be copied (or attached) to TAPE2 before FLAM execution. Note: Each pre-stress state constitutes an individual sub-file on TAPE9 and hence more than one "copy" command may be required in transferring the contents to TAPE2.

B.5.3 Data Card Input

A-1 Case Title Card

Variable	Format	Columns	Description
TITLE	12A6	1-72	Case title.

aerodynamic forces which are utilized (in addition to the natural frequencies, generalized masses and selected "reduced" frequencies) by program MOFA to solve a reduced (complex) eigenvalue problem and hence predict the critical, i.e., flutter, speed in an iterative manner.

B.5.2 Data File Input

Two data files are prerequisite to performing a FLAM analysis, in addition to a minimal number of data cards:

1) "Model description" file created by program HYPALM previously on TAPE5. This file must be copied (or attached) to TAPE1 before FLAM execution.

2) "Vibration mode" file created by STAGS in a previous analysis and containing eigenvectors, eigenvalues and generalized masses for a number of modes evaluated at a number of pre-stress states (i.e., times along flight trajectory). This file, originally saved on TAPE9 must be copied (or attached) to TAPE2 before FLAM execution. Note: Each pre-stress state constitutes an individual sub-file on TAPE9 and hence more than one "copy" command may be required in transferring the contents to TAPE2.

B.5.3 Data Card Input

A-1 Case Title Card

Variable	Format	Columns	Description
TITLE	12A6	1-72	Case title.

B-1 Case Summary Card

Variable	Format	Column	Description
NLD	I5	1-5	Number of pre-stress states (i.e., points along flight trajectory) at which a flutter analysis is desired.

B-2 Load/Time Step Specification Card

Variable	Format	Column	Description
PLD(I) (I=1, NLD)	8E10.6	1-80	Times (or load multipliers) denoting pre-stress states to be evaluated. Vibration modes from STAGS analysis for each must be present on TAPE2. It is not necessary to request all of the pre-stress states resident on TAPE2, but PLD(I) must be requested in a monotonically increasing order.

THE REMAINING CARDS ARE REPEATED <u>NLD</u> TIMES.

C-1 Reduced Frequency Summary Card

For each pre-stress state a modal flutter analysis is actually performed for each of a number of selected "reduced" frequencies and a tentative flutter speed is obtained graphically by means of an interpolative procedure described elsewhere in the text.

Variable	Format	Columns	Description
NREF	I5	1-5	Number of "reduced" frequencies to be considered. The maximum currently permitted is 8.

B-1 Case Summary Card

Variable	Format	Column	Description
NLD	I5	1-5	Number of pre-stress states (i.e., points along flight trajectory) at which a flutter analysis is desired.

B-2 Load/Time Step Specification Card

Variable	Format	Column	Description
PLD(I) (I=1, NLD)	8E10.6	1-80	Times (or load multipliers) denoting pre-stress states to be evaluated. Vibration modes from STAGS analysis for each must be present on TAPE2. It is not necessary to request all of the pre-stress states resident on TAPE2, but PLD(I) must be requested in a monotonically increasing order.

THE REMAINING CARDS ARE REPEATED NLD TIMES.

C-1 Reduced Frequency Summary Card

For each pre-stress state a modal flutter analysis is actually performed for each of a number of selected "reduced" frequencies and a tentative flutter speed is obtained graphically by means of an interpolative procedure described elsewhere in the text.

Variable	Format	Columns	Description
NREF	I5	1-5	Number of "reduced" frequencies to be considered. The maximum currently permitted is 8.

C-2 Reduced Frequency Specification Card

Variable	Format	Column	Description
REF(I) (I=1, NREF)	8E10.6	1-80	Reduced frequency values (rad./sec.).